Synthesis and technological processing of hybrid organic-inorganic materials for photonic applications

Dissertation zur Erlangung des naturwissenschaftlichen Doktorgrades
der
Julius-Maximilians-Universität Würzburg

vorgelegt von
Pélagie Declerck

aus Chambray-lès-Tours, Frankreich

Würzburg 2010

i. Index of abbreviations

2PP	**t**wo-**p**hoton **p**olymerization
3D	**t**hree-**d**imensional
ACAC	**ac**etyl**ac**etone
AIBN	2,2-**a**zobis**i**so**b**utyro**n**itril
AOM	**a**cousto-**o**ptical **m**odulator
APTMS	**a**cryloxy**p**ropyl**trim**ethoxy**s**ilane
BAF	9,9-**b**is(4-**a**minophenyl) **f**luorine
BAPS	2,2-**b**is(4-[4-**a**minophenoxy]**p**henyl)**s**ulfone
BPADA	**b**isphenol **A di**anhydride
BS	**b**eam **s**plitter
BU	**bu**tanone
CCD	**c**harge-**c**oupled **d**evice
CL	**c**omplexing **l**igand
CTE	**c**oefficient of **t**hermal **e**xpansion
Eq.	**e**quation
dB	**d**eci**b**el
DC	**d**egree of **c**onversion
DEPT	**d**istortionless **en**hancement by **p**olarization **t**ransfer
dil.	**di**lution
DLW	**d**irect **l**aser **w**riting
DMDMS	**dim**ethyl**dim**ethoxysilane
DMDES	**dim**ethyl**di**ethoxysilane
DPD	**dip**henylsilane**d**iol
DPDMS	**dip**henyl**dim**ethoxysilane
DPPA	**dip**henyl**p**hosphinic **a**cid
DPDMS	**dip**henyl**dim**ethoxysilane
ECET	[2-(3,4-**e**poxy**c**yclohexyl)**e**thyl]**tri**metoxysilane
FT-	**F**ourier-**t**ransform
GLYMO	3-(**gly**cidyloxypropyl)tri**me**th**o**xysilane
HSP	**H**ansen **s**olubility **p**arameters
ID	**id**endification numbers
IR	**i**nf**r**a**r**ed
ISC	Fraunhofer-**I**nstitut für **S**ili**c**atforschung, Würzburg

LO	**l**ongitudinal **o**ptical
MA	**m**ethacrylic **a**cid
MAS-NMR	**M**agic **a**ngle **s**pinning **n**uclear **m**agnetic **r**esonance
MAEAA	2-(**me**th**a**cryloyloxy)**e**thyl **a**ceto**a**cetate
MEMO	[3-(**me**th**a**cryloyloxy)propyl]tri**me**th**o**xysilane
MEMS	**m**icro**e**lectro**m**echanical **s**ystem(s)
MEPA	2-(**me**th**a**cryloyloxy)**e**thyl **ph**osph**a**te
mol-%	**mol**ar percentage
MP	4-**m**ethyl-2-**p**entanone
no.	**n**umber
NA	**n**umerical **a**perture
n.d.	**n**ot **d**etermined
NIR	**n**ear-**i**nf**r**a**r**ed
NMR	**n**uclear **m**agnetic **r**esonance
ODA	**o**xy**di****a**niline
PA	**p**ropyl**a**cetate
PC	**p**hotonic **c**rystal
PMDA	**p**yro**m**ellitic **di**a**n**hydride
PMMA	**p**oly**m**ethyl**m**eth**a**crylate
PPA	**p**henyl**p**hosphonic **a**cid
ppm	**p**arts **p**er **m**illion
p-VBPA	**p**ara-**v**inyl**b**enzyl**p**hosphonic **a**cid
ref.	**ref**erence
RIE	**r**eactive **i**on **e**tching
SEM	**s**canning **e**lectron **m**icroscopy
SETMS	**s**tyryl**e**thyl**t**ri**m**ethoxy**s**ilane
SMDES	**s**tyryl**m**ethyl**di**eth**o**xy**s**ilane
TBAF	**t**etra**b**utyl**a**mmonium **f**luoride hydrate
TEOS	**t**etra**e**th**o**xy**s**ilane
THF	**t**etra**h**ydrofurane
Ti(OBu)$_4$	**ti**tanium **bu**toxide
Ti(OEt)$_4$	**ti**tanium **et**hoxide
Ti(OPr^i)$_4$	**ti**tanium **iso**pr**o**poxide
Ti(OMe)$_4$	**ti**tanium **me**thoxide
Ti(OPr)$_4$	**ti**tanium **pr**opoxide

TM	transition metal
TMO	transition metal oxide
TMS	tetramethylsilane
TO	transversal optical
UV	ultraviolet
VIS	visible
WP	wave plate
wt.-%	weight percent
$Zr(OEt)_4$	zirconium ethoxide
$Zr(OPr)_4$	zirconium propoxide

ii. Definitions

ii.1 Water ratio r

In order to perform hydrolysis reactions necessary for some of the syntheses, water was added directly or mixed with the catalyst e.g. hydrochloric acid. The water content used in the syntheses is defined by the water ratio r. It is equal to the molar quantity of water added with respect to the molar quantity of water needed for a complete condensation reaction. For example, in a mixture based on 1 mol [3-(methacryloyloxy)propyl]trimethoxysilane (MEMO) and 1.5 mol H_2O, the water ratio is equal to 1.

For titanium, the coordination number may range from 4 to 6. Within the framework of this thesis, the calculation of the water ratio was based on a coordination number equal to 4. For example, in a mixture based on 1 mol titanium ethoxide ($Ti(OEt)_4$) and 2 mol H_2O, the water ratio is then close to 1.

ii.2 NMR notations for silicon species

^{29}Si-NMR spectroscopy was used for the refinement of the chemical environment of Si atoms by analyzing the chemical shifts of the signals. Notably, information on the silicon species such as their degree of condensation or hydrolysis can be determined. Since many different styles of notation have been used for polyorgano-alkoxysilanes in the literature, the notation style used in this thesis for the analysis of the ^{29}Si NMR spectra will be described.

Widely accepted are the notations M, D, T, and Q (mono, di, tri, and quaternary), which denote the number of oxygen substitutions at the silicon atom. For example, MEMO which contains three methoxy groups, is labeled T, or diphenylsilanediol (DPD), which contains two hydroxyl groups, is labeled D. The degree of condensation of the silicon species M, D, T, and Q with other silicon species is given by a superscript. For example, for a given organo-alkoxysilane, T^1 symbolizes a silicon atom linked to one organic group. Three sites are available for possible condensation reactions, whereas one of them forms siloxane bonds. The symbol D^2 is assigned to a silicon atom linked to two organic groups, and the two remaining sites are fully condensed (i.e., the species contains two siloxane bonds). Additionally, the remaining groups (i.e., the groups which are not condensed) are written as subscript in brackets. Hydroxyl, methoxy, ethoxy, and titanium oxide groups are labeled (OH), (OMe),

(OEt), and (OTi), respectively. For example, $T^1_{(OH)(OMe)}$ refers to a species containing one siloxane bond, one hydroxyl and one methoxy group, and one organic group linked to the silicon atom. This explicit notation (see also [1]) was chosen in this work due to the numerous possibilities encountered with signals recorded during the condensation of siloxane entities with titanium alkoxide which is not possible to point out with other notations used in the literature.

Other notations are a variant of the one chosen in this work. Instead of explicitly labeling the remaining groups, a number is written as subscript in order to specify the number of hydroxyl groups attached to the silicon atom. For example, T^1_1 represents a T species containing a siloxane bond, a hydroxyl group linked to the silicon atom, and another group, which can be, for example a methoxy, an ethoxy, or a titanium oxide group. The major disadvantage of this notation is the lack of information concerning the remaining groups. The chemical shift of silicon species condensed with a titanium alkoxide and the chemical shift of the same silicon species containing an alkoxy group are different, the distinction of the remaining group has to be underlined.

Some authors used a similar notation as the latter one described, but with inversed indices (see, e.g., Oubaha et al.[2]).

ii.3 NMR notations for ^{13}C and ^{1}H NMR spectroscopy

In order to simplify the interpretation of ^{13}C-NMR spectra, the carbon associated to a chemical shift is underlined in a group of atoms. For example, in a molecule or species containing an ethoxysilane group, the carbon of the -CH$_2$- of the ethoxide group is represented as follows: -Si(OC$\underline{H}$H$_2$CH$_3$).

In the same way, in ^{1}H NMR spectroscopy, the proton underlined represents the proton, which is pointed out. For example, in a molecule or species containing an ethoxysilane group, the protons of the -CH$_2$- of the ethoxide group are represented as follows: -Si(OC$\underline{H_2}$CH$_3$).

1.   Introduction

Tomorrow's data transmission needs an increase of the packaging density and higher level integration in order to obtain fast access to data at any time and any location. Another aspect is the continuous miniaturization; the components have to be smaller, lighter, and have to have a higher functionality. The electrical technology (Cu technology) is limited by impedances and capacitances, and many efforts have to be carried out to overcome those. Due to the frequency-dependent signal, runtime and cross-talk the data transmission can affected. Moreover, the quality factor (bite rate/length) is limited to approximately 0.5 GHz m[3]. Optical technologies can overcome the disadvantages of the electrical technology, whereas almost no cross-talk occurs, and the quality factor is much higher than for electrical technology[4].

In optical technology, the transmission of information is carried out with light. Optical fibers guiding light have revolutionized the telecommunication industry [5]. For an optical fiber or waveguide (cf., Figure 1), two materials with a certain index step have to be used in order to guide the light. The light is totally reflected at the interface of the higher to the lower index material, whereas the fiber or waveguide core has to have the higher refractive index, and the surrounding cladding material has to have a lower refractive index[4]. Waveguides can be produced in two dimensions such as, as plane (slab) waveguide, or as optical fiber (Figure 1)[6].
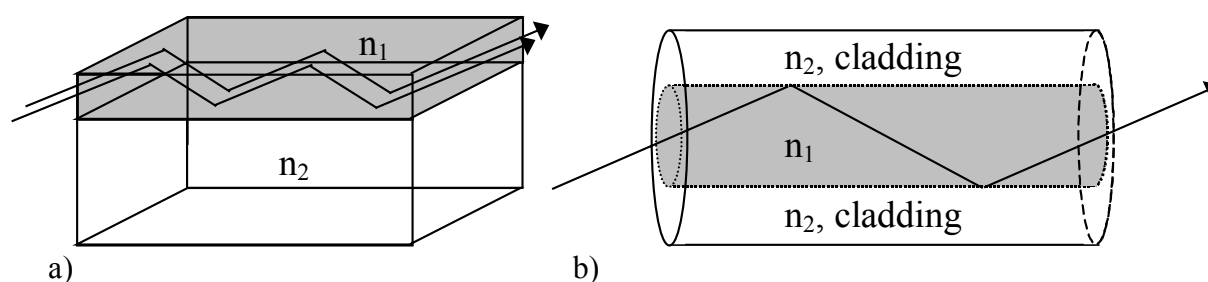
Figure 1: Optical waveguides. (a) Planar (slab) waveguide, and (b) optically waveguiding fiber (with $n_1 > n_2$)[6].

Beside waveguides, other optical structures can be used for transmission of information or switching using light. In 1987, Yablonovivh[7] and John[8] were the first who suggested that structures with a periodic variation in the refractive index (or the dielectric permittivity) can influence the nature of photonic modes in a material[5], and introduced the concept of a photonic bandgap of one to three dimensions[9]. This generalization inspired the name of "**p**hotonic **c**rystal" (PC), and should allow the fabrication of optical circuits similar to semiconductor circuits devices such as, for example optical transistors[10].

PC are optical structures in which two media with different refractive indices (or dielectric permittivities) are periodically arranged[7,8]. In a certain range of photon energy (or frequency), propagation is forbidden (in analogy to an electronic bandgap in a semiconductor), which is called photonic bandgap. The bandgap resulting from a PC structure can be tuned in a certain range of wavelengths by changing the periodicity of the lattice constant[6]. In case of a high refractive index contrast, a suitable lattice constant and crystal

symmetry formed by the PC building blocks, an omni-directional photonic bandgap can be achieve, whereas also bandgaps of higher order are of application relevance[6,9,11].

Figure 2 shows a schematic representation of one-, two- and three-dimensional PC. The simplest form of a photonic crystal is a one-dimensional (1D) periodic structure (cf., such as a multilayer film). 1D periodic systems were continuously studied and are applied, for example in reflective coatings, or distributed feedback (DFB) lasers[11].

Figure 2: Schematic representation of one-, two-, and three-dimensional photonic crystals[9].

In addition to the high refractive index variation between the two media, the fabrication of higher dimensional photonic crystal structu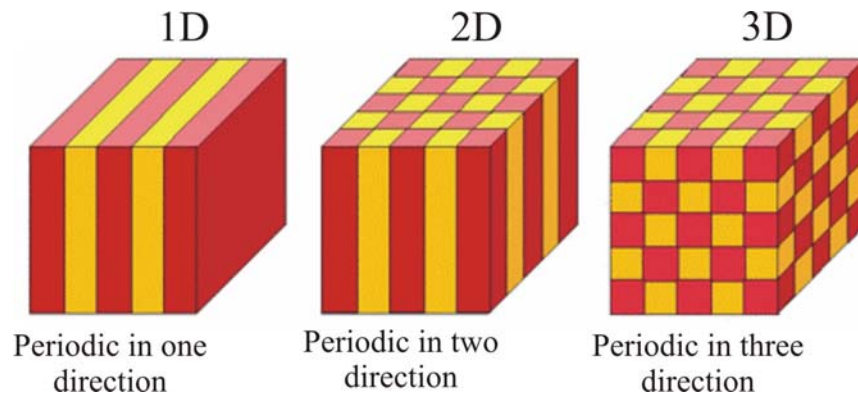res is a challenge, because the structure has to be fabricated with high precision in order to not affect the optical properties. A wide variety of methods have been used to fabricate photonic crystal structures for all kinds of applications. In the following, three different methods allowing the fabrication of 3D PC structures are briefly reported.

The direct semiconductor fabrication by using a layer by layer method allows the micro-fabrication of a photonic bandgap material at infrared frequencies through the combinations of advanced planar semiconductor techniques for the individual layers. In order to combine the different layers into a 3D PC, ultra-precise alignment and stacking procedures are needed[12]. Two other methods can also be used: self-assembly, which is based on organized building blocks, generally monodispersed silica or polystyrenes nanospheres[6], and **d**irect **l**aser **w**riting (DLW)[12,13]. For both methods, the refractive indices of the nanospheres or polymers are too low. In order to overcome this, the created PC structure is used as template, and is then infiltrated with a higher refractive index material. The infiltration of opal-type templates by self-assembly methods has been successfully demonstrated[14-16]. The major drawback of this method is the formation of defects such as, for example, missing particles leading to cavities, or dislocations. Recently, it was demonstrated that DLW by two- **p**hoton **p**olymerization (2PP) processing allows one to fabricate complicated 3D microstructures[17]. This method has emerged due to the rapid, cheap, and flexible fabrication of photonic micro- and nanostructures[12,18]. For example, PC structures were successfully created based on multifunctional inorganic-organic hybrid polymers (ORMOCER®s[1]) by 2PP. These hybrid

---

[1] ORMOCER®:trademark of Fraunhofer-Gesellschaft zur Förderung der angewandten Forschung e.V. in Germany

polymers, synthesized by a sol-gel process using organo-alkoxysilane precursors, are based on organically functionalized inorganic oxidic units, whereas the organic moiety can be organically cross-linked by light or thermally induced processes[19-22]. The resulting materials are typically highly transparent in the visible wavelength regime, having exceptional thermal and mechanical properties, high chemical resistance, and they can be produced at low cost. However, the refractive index reported up to now does not exceed 1.6[23].

In order to fabricate optical elements, a suitable material with a high refractive index combined with a suitable technology is needed. The 2PP polymerization process has the advantage to flexibly allow the fabrication of 2- or 3D structures on the micro- and nanometer scale using purely organic or organically modified inorganic materials[19,20,24]. The major objective of this work is to increase the refractive index of ORMOCER® materials beyond 1.6, which then can be patterned by the 2PP process to create complex 3D structures. New syntheses had to be developed in order to use this 3D method as a simple method to create arbitrary PC structures, and the structure of the resulting materials had to be characterized and correlated to the material's refractive index. First lithography experiments were carried out by one and two photon polymerization processes.

This work is organized as follows. In chapter 2, the sol-gel process for the synthesis of inorganic-organic materials generally described. This is followed by a survey of the refractive indices of organic, inorganic, and hybrid materials. Some selected techniques for the determination of the refractive index which were used for this thesis are described as well. Finally, the organic polymerization process by one- and two- photon polymerization is explained.

In chapter 3, the syntheses and characterization methods and instrumentation used in the framework of this thesis are described. The synthesis protocols for each resin are described (ordered by resin identification numbers). Many other resins have been synthesized during this work (cf., Annex 1). Only selected resins, characterized in details and processed by one or/and two photon polymerization processes are described. Three groups of syntheses are reported: resins based on organo-alkoxysilanes and titanium alkoxide precursors, resins based on titanium alkoxide precursors modified with a complexing ligand (CL) and organo-alkoxysilanes, and resins based on organo-alkoxysilanes, titanium alkoxides, and organo-phosphorus precursors. These three groups were chosen in order to correlate the chemical composition of the materials to their refractive indices. This is followed by a survey on the technological processing, which was used for the fabrication of patterned coatings with the novel materials.

In chapter 4, the syntheses by hydrolysis and polycondensation reactions of the developed hybrid organic-inorganic materials are reported. In a first part, the resins are characterized chemically and discussed with respect to their optical properties. Particularly, the evolution of the refractive index of the materials with selected syntheses parameters is discussed. In addition, the patterning process of selected, novel organic-inorganic hybrid polymers by one- and two-photon polymerization is described, whereas some processing parameters were studied, demonstrating the feasibility of the novel materials for these technologies.

2. Theoretical background

In order to synthesize a high refractive index material by wet chemical methods which can be patterned in 3D, knowledge in the three following fields are necessary: the sol-gel process, the refractive index, and the photo-induced organic polymerization. Thus, a state of the art of each field and their interconnections are reported in this chapter.

In the first part, the chemistry of the sol-gel process is described, and particularly the different ways which can be used in order to synthesize hybrid organic-inorganic materials. The second part deals with the refractive index, which is a further main topic of this thesis. The correlation between the chemical composition of materials and their refractive indices is exhibited and some methods, which are used to measure the refractive index, are briefly described. Finally, a third part relates to the patterning of the materials, and shows how it can affect the refractive index of the material.

2.1 Sol-gel process

This chapter is divided into three parts. In the first part, the general background of the sol-gel chemistry is briefly described. The basic reactions which occur during the formation of the inorganic network followed by the reactivity of the precursors towards nucleophilic reactions are considered. The latter one can be controlled by the use of catalysts (acidic, basic, or nucleophilic), or **c**omplexing **l**igands (CL) which affect the kinetics of the hydrolysis and condensation reactions. Then, the second part is devoted to hybrid organic-inorganic materials, which have the advantage to combine properties of organic and inorganic materials. They are divided into two general classes (class I and II), depending on the nature of the bond between the organic and inorganic phases[25]. The third part deals with organically modified silicon alkoxides which belong to class II. Their chemistry and processing are described in more detail separately, since they have been synthesized for this thesis. Inorganic-organic hybrid polymers (ORMOCER®s) developed at the Fraunhofer **I**nstitut für **S**ili**c**atforschung (ISC) are described as an example of organically modified silicon alkoxides. Moreover, syntheses and characterizations of organically modified silicon alkoxides containing heteroelements such as titanium are reported from the literature.

The sol-gel process yields oxidic networks based on $-[Si-O]_n-$ or $-[M-O]_n-$[26] (where M is a metal) by progressive polycondensation reactions of molecular precursors in a liquid medium. Ceramic-based materials can be synthesized via a **sol** preparation, **gel**ation of this sol, and finally removal of the solvent[27]. The chemical route is based on hydrolysis and condensation reactions, and enables one to obtain pre-ceramic materials at low temperature with a high degree of chemical homogeneity. The interest in sol-gel materials is not only related to their physical and chemical properties, but also to the possibilities of very different material processing. Figure 3 presents a scheme of different processing routes leading to a variety of materials such as powders, fibers, films, gels, aerogels, xerogels, or dense ceramics issued from the same sol[28]. Each modification can be used in a wide range of applications, for example, sol-gel films can be used as optical coatings (e.g., colored, antireflective coatings), coatings for electronic applications, and protective coatings (e.g., corrosion and mechanical resistant), respectively[28].
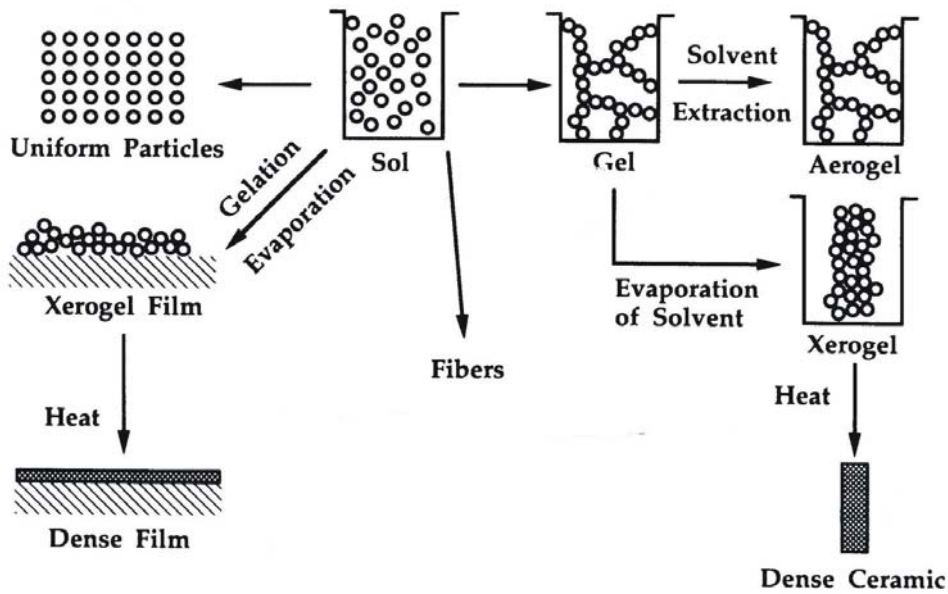
Figure 3: Overview of the different sol-gel processing routes [28].

2.1.1 Background of the sol-gel chemistry

2.1.1.1 Chemical reactions

The chemistry of the sol-gel process is based on inorganic polymerization reactions of metallo-organic compounds such as alkoxides $M(OR)_z$, where M can be Sn, Ti, Zr, Al, etc. or $Si(OR)_4$, where OR is OC_nH_{2n+1}. The first reaction is a hydrolysis reaction (Figure 4 (a)). The sol-gel process occurs in three steps: (i) nucleophilic attack of the metal M by the oxygen atom of a water molecule, (ii) transfer of a proton from the water to an -OR group linked to the metal, and (iii) release of the resulting ROH molecule. As soon as reactive hydroxyl groups are generated, the formation of branched oligomers takes place by a polycondensation process, in which two competitive mechanisms occur: water and alcohol condensation (Figure 4 (b),(c)).
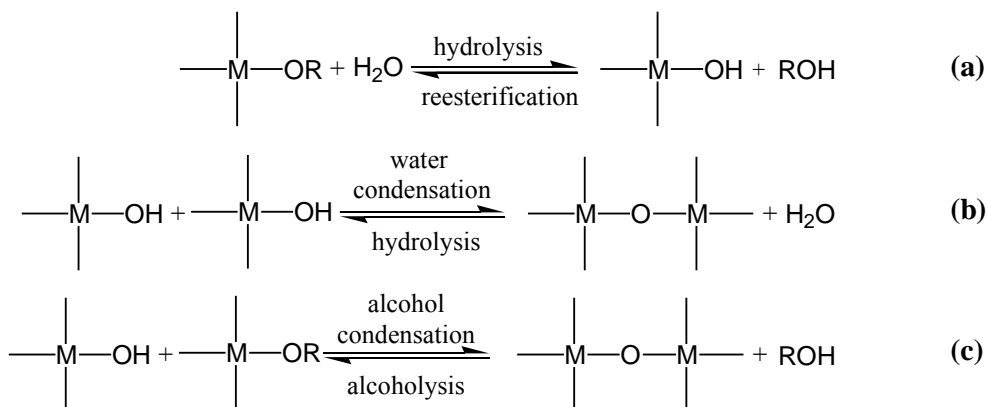
Figure 4: Chemical reactions during sol-gel processing, where M can be Si or a transition metal (TM) atom.

The characteristics and the properties of the final inorganic network are related to the factors, which influence the hydrolysis and condensation reactions such as pH value, temperature, reaction time, concentration of precursors, nature and concentration of the catalyst, the use of complexing ligands, water ratio, and/or solvent.

2.1.1.2 Chemical reactivity of metal alkoxides

The chemical reactivity of metal alkoxides towards nucleophilic attack, i.e., towards hydrolysis, mainly depends on the strength of the nucleophile, the electrophilic character of the metal atom (the electronegativity), and its ability to increase its coordination number N (Table 1).

Table 1: Electronegativity (χ), coordination number (N), and degree of unsaturation (N-Z) for some tetravalent metals having the oxidation state Z, (Z=4)[25,29].

Alkoxides	χ	N	N-Z
$Si(OPr^i)_4$	1.74	4	0
$Sn(OPr^i)_4$	1.89	6	2
$Ti(OPr^i)_4$	1.32	6	2
$Zr(OPr^i)_4$	1.29	7	3
$Ce(OPr^i)_4$	1.17	8	4

Silicon has a low electrophilicity and remains four-coordinated in monomeric $Si(OR)_4$ alkoxide precursors as well as in silica (SiO_2). Thus, silicon alkoxides are not very reactive. Catalysts have to be used in order to increase the hydrolysis and condensation reaction rate[25,28,29].

On the other hand, transition metals have an electronegativity lower than silicon and, in addition, their oxidation state is lower than their usual coordination number in the corresponding oxide. Therefore, they are very sensitive to moisture, and have to be handled in a dry atmosphere in order to avoid precipitation of the metal precursor. Additionally, chemical additives may be used to decrease the reactivity of metal alkoxides towards nucleophilic additions.

The reactivity of metal alkoxides and $Si(OR)_4$ is reported in the literature as followed[30,31]: $Si(OR)_4 <<< Sn(OR)_4$, and $Ti(OR)_4 < Zr(OR)_4 < Ce(OR)_4$.

The electronegativity of a metal is not the key parameter to determine its chemical reactivity. For example, in the case of tin, its electronegativity is higher than that of silicon. But the oxidation state is lower than its coordination number. Therefore, the oxidation state associated to the coordination number, i.e., the degree of unsaturation (defined in Table 1) should be considered as the driving parameter.

In the following, the influence of the catalyst will be considered. In order to increase the hydrolysis and condensation rates of silicon alkoxides, acidic, basic, or nucleophilic catalysts can be used[28]. Acidic and basic conditions notably affect the inorganic network. Under acidic conditions, the hydrolysis reaction is raised, whereas with a basic catalyst both,

hydrolysis and condensation reactions occur simultaneously. The difference in selectivity between basic or acidic catalysts leads to the formation of different network shapes and textures. By using basic catalysts, aggregation occurs, leading to a more compact and highly branched silica network, whereas a weakly branched polymer is obtained with acidic catalysts[25,28].

The reactivity of non-silicate tetravalent metal alkoxides towards nucleophilic reagents, mainly driven by the degree of unsaturation of the metal, is higher than those of silicon alkoxides. They also have to be handled in a dry atmosphere. Additionally, chemical modifications through the addition of inorganic acids, ß-diketones, carboxylic acids, or other CL can be performed in order to inhibit the condensation reaction, and to prevent precipitation[28]. Such chemical modifications have been carried out for the syntheses of the hybrid organic-inorganic materials developed in the framework of this thesis.

The simplest inhibitors for condensation reactions are protons (H^+ ions). According to the acid concentration and oxygen coordination (terminal or bridging oxygens), nucleophilic species (e.g., Ti-OH) are more or less protonated causing selective inhibition of condensation reactions[32-34].

The reactivity of non-silicate tetravalent metal alkoxides is moderated by using complexing ligand (CL), leading to a new precursor $M(OR)_{x-y}(CL)_y$ (Eq. 1)[35-41]. Figure 5 illustrates examples of new precursors synthesized from the complexation of titanium alkoxide with different CL.

$$M(OR)_x + y\,CL\text{-}H \longrightarrow M(OR)_{x-y}(CL)_y + y\,ROH \qquad\qquad (Eq.\ 1)$$
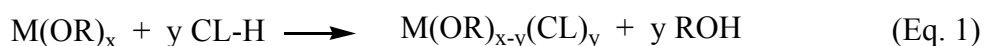
In the case of strong complexing ligands such as ß-diketonates or acid derivatives, where the complexes are hydrolyzed, the alkoxy groups are removed, thus causing the formation of metal-oxo polymers, while some of the ligands are still bonded to the metallic center. The stability of complexes against the hydrolysis reaction depends on the metals and also on the ligands. The stability of carboxylic acid derivatives towards hydrolysis is poor, and the organic ligands are more or less removed from the metal atoms during the hydrolysis reaction[29]. With ß-diketones, the stability of acetylacetonate derivatives towards water depends on the pH value. In acidic media (pH < 1.5), the acetylacetonate groups are easier removed from the titanium[42].

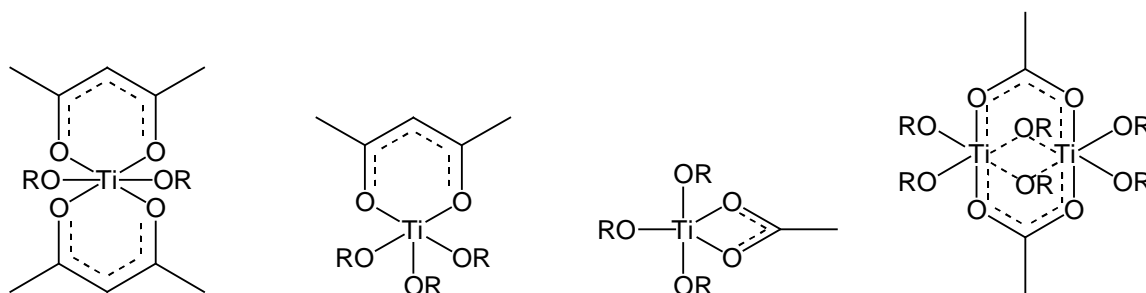Figure 5: Examples of few precursors formed from Ti(OR)$_4$ and complexing ligands[27,28,35].

Acetic acid and acetylacetone are the most common complexing ligands used to moderate the reactivity of non-silicate metal alkoxides[37,43-49]. In principle, any carboxylic acid and ß-diketone may be used. Diols and phosphonic acids (R'PO$_3$H$_2$) are also reported in the

literature[41,50-52]. Figure 6 depicts some complexing ligands, which can be used for the chemical modification of metal alkoxides.
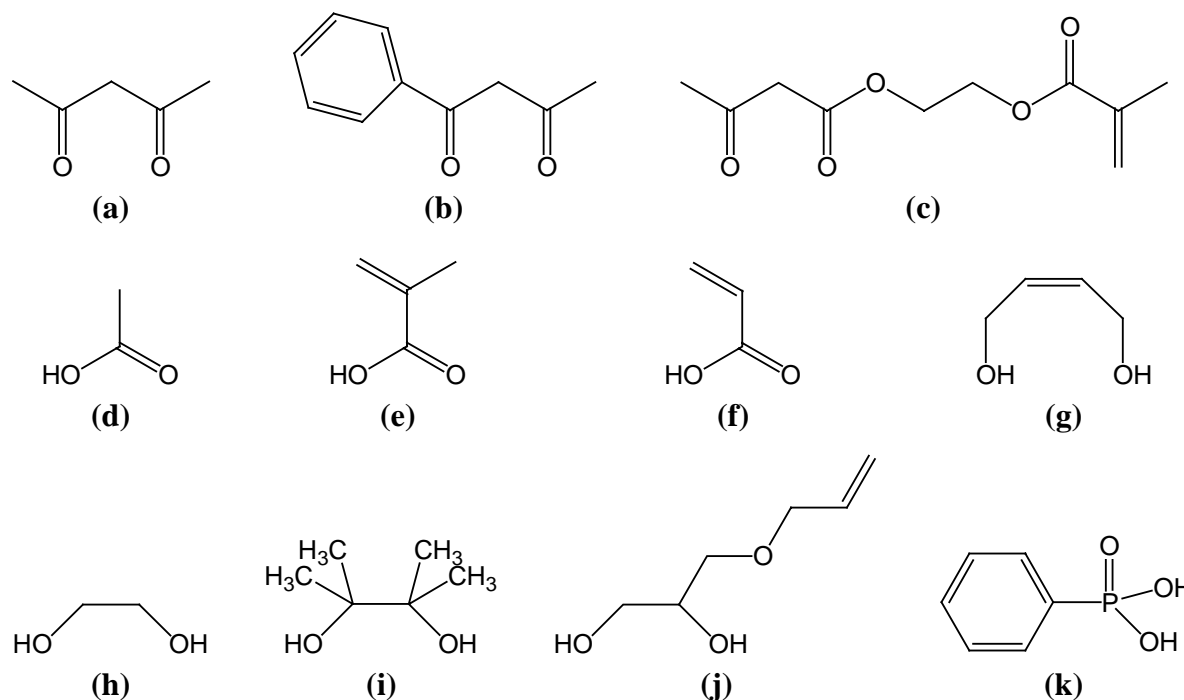

Figure 6: Some organic compounds used for the chemical modification of metal alkoxides. (a) Acetylacetone[42,44-47], (b) benzoylacetone[46], (c) 2-(methacryloyloxy)ethyl acetoacetate[40,50,53,54], (d) acetic acid[37,48,49,55], (e) methacrylic acid[36,39,56], (f) acrylic acid[39], (g) cis-2-butene-1,4-diol[41,50], (h) ethylene glycol[51], (i) pinacol[51], (j) 3-allyloxypropane-1,2-diol[50], and (k) phenylphosphonic acid[52,57,58].

The hydrolysis and condensation reactions of the modified precursor depend on its stability, which is not always possible to predict on the basis of the stability of the parent compounds[28].

2.1.2   Hybrid organic-inorganic materials

Beside the synthesis of purely organic or inorganic materials, the sol-gel process offers the possibility to synthesize hybrid organic-inorganic materials in which the properties of organic and inorganic materials can be combined. The inorganic part of the material contributes to its mechanical and thermal strength and also allows, for example, the modulation of the refractive index (cf., chapter 2.2). On the other hand, the organic part, where the thermal stability is often limited to 250°C, may contribute to specific properties such as optical or electrical properties, electrochemical reactions, chemical, or biochemical reactivity. Sanchez et al.[25] have divided the hybrid organic-inorganic materials into two classes. Class I corresponds to hybrid systems in which the organic molecules are simply embedded in an inorganic matrix. Hybrid systems in which organic and inorganic molecules are bonded through stronger chemical bonds (e.g., covalent or iono-covalent bonds) belong to class II hybrid materials[25,29]. In the following, general synthesis aspects of class I and II hybrid materials are described, followed by a particular emphasis of ORMOCER®s as special example for class II organically modified silicon alkoxide hybrid materials. Then, the syntheses of organically modified silicon alkoxides condensed with transition metal

16

alkoxides, on which major emphasis is in this work, are reported from the literature.

2.1.2.1 Class I materials

In class I materials, organic and inorganic compounds are embedded, and the cohesion of the final structure is obtained by weak bonds such as hydrogen, van der Waals, or ionic bonds. These materials present a large diversity in their structures, and also in their final properties (mechanical, optical, electrical, ionic, sensors, bio-sensors, catalyst,...). Some examples of class I materials are described in the following.

Organic dyes can be embedded in sol-gel matrices. Small organic molecules are entrapped in an inorganic network (Figure 7). This corresponds to the doping of sol-gel matrices by organic dyes, or inorganic ions or molecules, resulting in fluorescence, photochromic, or non-linear optical properties[59-61]. Organic molecules such as rhodamines, coumarins, porphyrins, and spiropyrans have been introduced as non-linear optical dyes into an inorganic network such as silica, aluminosilica, titanium dioxide, or zirconium dioxide[62-65]. Basically, the alkoxide precursor, the dye, and the catalyst are mixed in a common solvent. Water is then added to the mixture, inducing the polycondensation reactions, and the dye molecules are uniformly trapped in the growing polymer.

H_2O

catalyst
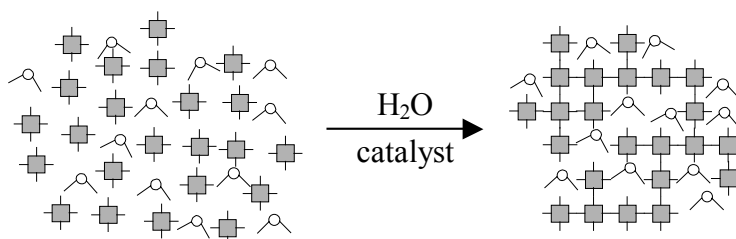
Figure 7: Organic dyes embedded in sol-gel matrices[29].

The key symbols used in all figures are given in Figure 8.

 inorganic precursor (metal alkoxide)

 bis (silicon end-capped) polymer

 inorganic cluster

 bis (organically modified) silicon alkoxide

 alkoxide functionalized by a non-labile polymerizable group

 alkoxide functionalized by labile polymerizable groups

 organic molecule (e.g., dye)   organic monomer   organic monomer

 polymer chain

 polymer chain

Figure 8: Key symbols used for the schematic description of hybrid materials.

The introduction of organic monomers can be also performed by embedding them in sol-gel matrices. Porous inorganic matrices may be filled with molecules by immersing the bulk material into a solution containing polymerizable organic monomers (e.g., methylmethacrylate, butadiene, and derivatives thereof), and a catalyst. In a second step, the organic polymerization is initiated either by UV irradiation, or by heating, and the polymer is formed (Figure 9). Due to the difference of the density of the monomer and the polymer, strong mechanical stresses may occur in the final material, and as a result the formation of many optical defects is an obvious problem[59-61,66,67].
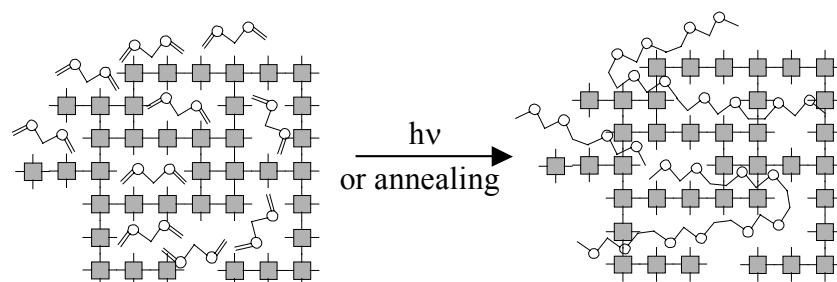
Figure 9: Organic monomers embedded in sol-gel matrices followed by UV or thermally initiated polymerization[29].

Another method to produce class I hybrid materials is to embed inorganic particles into a polymer matrix[27]. For that, the polymer (or prepolymer) is mixed with inorganic particles (Figure 10). Due to agglomeration of particles, non-homogenous materials are often obtained. By using suitable solvents and further drying steps, better homogeneity can be achieved.
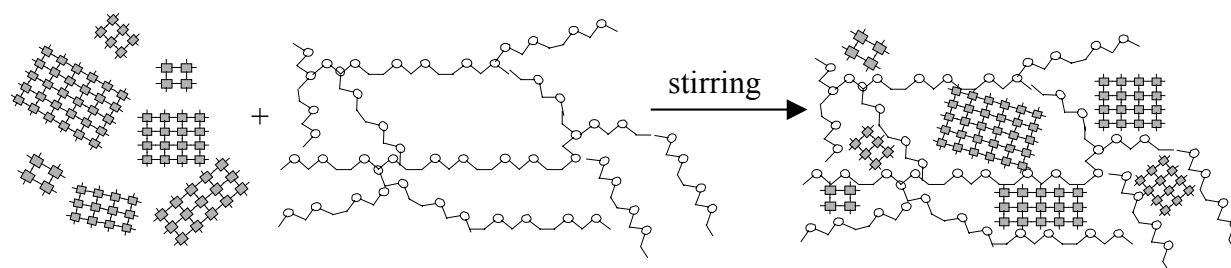
Figure 10: Inorganic particles embedded in a polymer matrix[29].

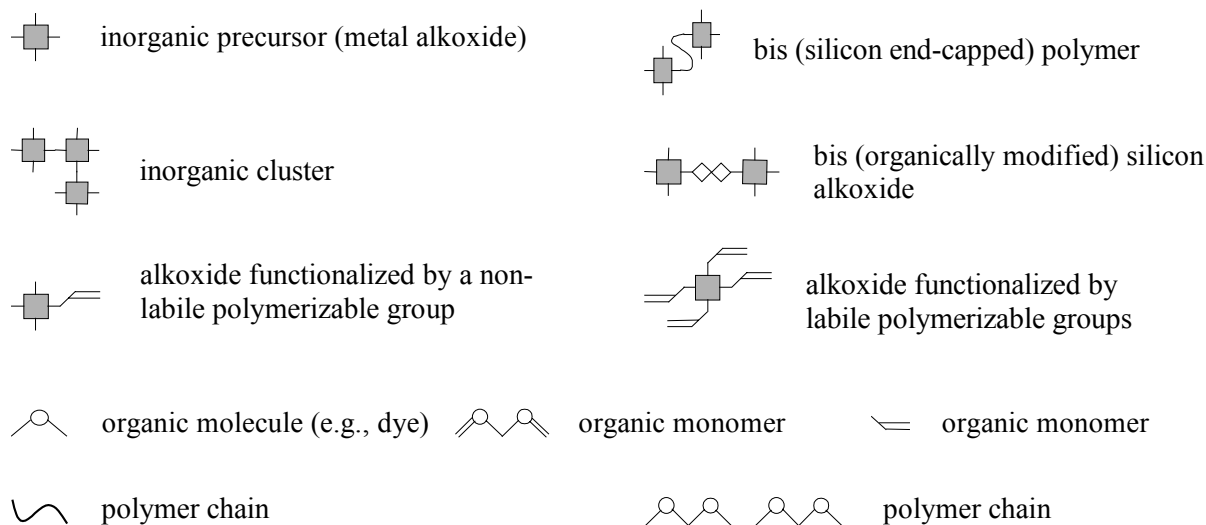Organic molecules can be also introduced into the sol-gel matrices by filling the polymers using an in-situ generation of inorganic particles[68,69]. In order to overcome the inhomogeneity of the materials obtained by embedment of inorganic particles in polymers, the formation of inorganic clusters can be performed *inside* the polymer structure. A typical method consists in the mixing of the polymer with a metal alkoxide in a suitable solvent. By adding a catalyst and water, the inorganic polycondensation is performed (Figure 11).
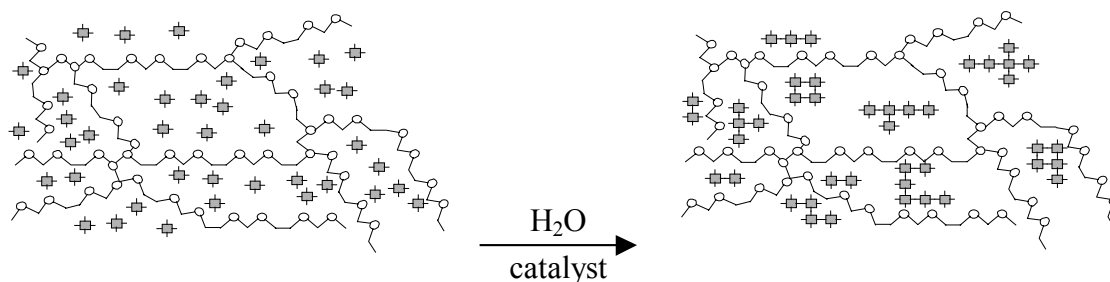
Figure 11: Polymers filled with in-situ grown inorganic particles or clusters[29].

In order to avoid shrinkage of the material during the evaporation of the solvent, and also to avoid an inhomogeneity of the resulting composite material, simultaneous formation of an interpenetrating organic-inorganic network was proposed as alternative synthesis route [70,71] (Figure 12). Modified silicon alkoxides containing two distinct entities are used as starting units. In addition to the possibility to hydrolyze the silicon alkoxide, they contain also organically polymerizable entities. Thus, their hydrolysis leads to the formation of an oxide network (SiO_x), and simultaneously an organically polymerizable alcohol is released. The latter one can be polymerized either by UV light or heating (T) in the presence of a catalyst, resulting in interpenetrating organic-inorganic networks.
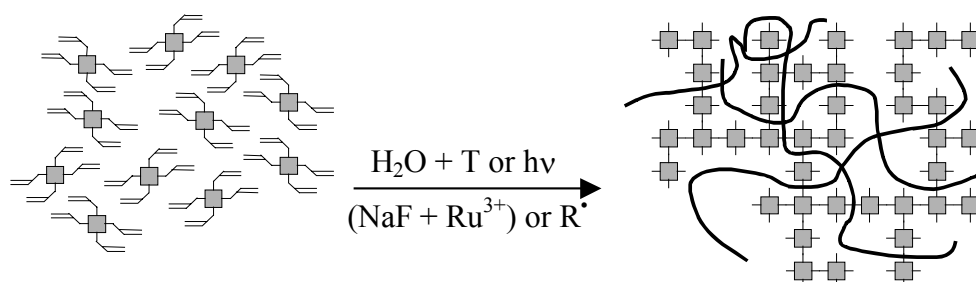
Figure 12: Simultaneous formation of interpenetrating organic and inorganic networks (with R$^{\bullet}$ as a free-radical)[29].

2.1.2.2   Class II materials

Class II materials correspond to hybrid organic-inorganic compounds where both, the organic and the inorganic compounds are connected together through strong chemical bonds such as covalent or iono-covalent bonds[25,29].

The molecules used as starting building blocks possess two distinct functionalities: alkoxy groups (R-OM bonds) which react by hydrolysis and condensation reactions, forming the inorganic network, and metal carbon bonds (M-C) which are stable towards a hydrolysis reaction. This stability is achieved, when M is silicon, tin, mercury, lead, or phosphorus. When M is a transition metal, the M-C bond is not stable. However, the organic part can be linked to the transition metal by its complexation with a ligand leading to M-O-C bonds (section 2.1.1.2).

The most common way to introduce an organic group R' in a silica network is to use organo-alkoxysilane precursors R'$_x$Si(OR)$_{4-x}$ (with x=1, 2 or 3, Si-OR as a hydrolysable bond, and Si-

R' as a stable group), in which the Si-C bond is stable towards hydrolysis in most sol-gel conditions. If the R' groups have a reactive function such as vinyl, amide, or isocyanate, organic reactions can be performed.

In order to synthesize hybrid materials based on organically modified silicon alkoxides, three methods are described in the literature: sequential syntheses, syntheses issued from polyfunctional alkoxysilanes, and syntheses from alkoxysilanes functionalized by a polymer.

A sequential synthesis is separated into two steps: the first one consists in the formation of an inorganic network by polycondensation reactions of the alkoxysilanes moieties, while the second step is the organic cross-linking by photochemical or thermal curing leading, for example to materials referred to as ORMOCER®s[22,72-77] (cf., Figure 13). Since ORMOCER®s are the materials synthesized in the framework of this thesis, their syntheses, properties, and applications are described separately below (see section 2.1.3).
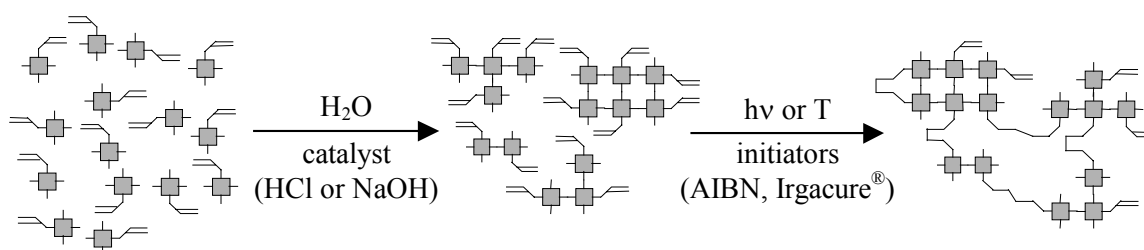
Figure 13: Syntheses of hybrid materials from organically modified silicon alkoxides[29]. AIBN (2,2-**a**zobis**iso**butyro**n**itril) and Irgacure® (from Ciba-Geigy) are used as thermal and UV initiators, respectively.

The syntheses based on polyfunctional alkoxysilanes are also used to synthesize hybrid materials from organically modified silicon alkoxides[78,79]. Polyfunctional alkoxysilanes are based on organic units R' which are linked to two or more $Si(OR)_3$ groups. When two trialkoxysilane groups are bonded to the R' unit, the generic formula is $(RO)_3Si-R'-Si(OR)_3$. By hydrolysis in the presence of a catalyst, the inorganic condensation can be performed (Figure 14). Depending on the nature of the precursor, the solvent and the catalyst, microporous materials are obtained. By high temperature treatments, the organic groups can be removed, and materials suitable as membranes are obtained[79,80].
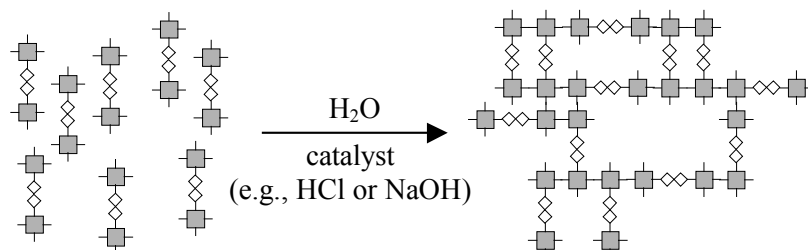
Figure 14: Syntheses of hybrid materials from polyfunctional alkoxysilanes[29].

Hybrid materials containing organically modified silicon alkoxides can be synthesized from alkoxysilanes functionalized with a polymer[69,81]. The syntheses of these hybrid materials are based on reactive alkoxysilane groups [$-Si(OR)_3$] which are grafted to oligomers or polymers

by different reactions[81] (Figure 15). For example, an oligomer or polymer containing hydroxy groups can react with metal-oxo polymers which are in-situ formed. The final materials may be tailored to enhance thermal, mechanical, optical, and ionic properties[82].
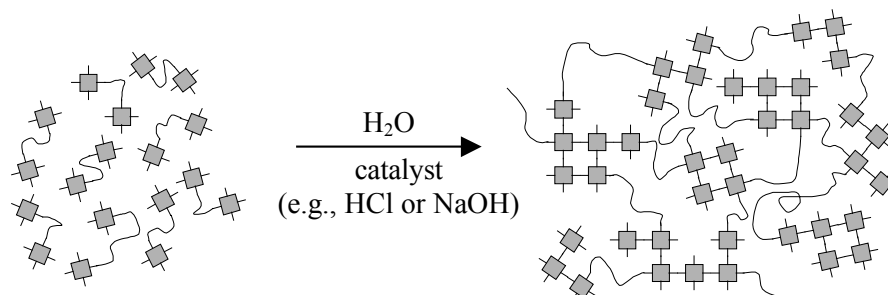
Figure 15: Syntheses of hybrid materials from alkoxysilanes functionalized by polymers[29].

Class II hybrid organic-inorganic materials can be also synthesized from **t**ransition **m**etal **o**xides (TMO). Different methods of syntheses have been performed in order to synthesize hybrid organic-inorganic materials containing transition metal alkoxides.

A silica layer can be grafted on the **t**ransition **m**etal (TM) oxide network. The first simplest way to implement this is to use an intermediate silica layer[29]. The surface of TM-oxo polymers or colloids has a high density of hydroxyl groups (M-OH), which can react with silicon alkoxides or organo-alkoxysilanes leading in the formation of M-O-Si bonds. This process is used to link a vinyl-, epoxy-, or methacryl-modified silanes to zirconia or titania[83,84]. Subsequently, the organic layer can react with the organic monomer, and an organic layer around the metal oxo-polymer is formed (Figure 16).
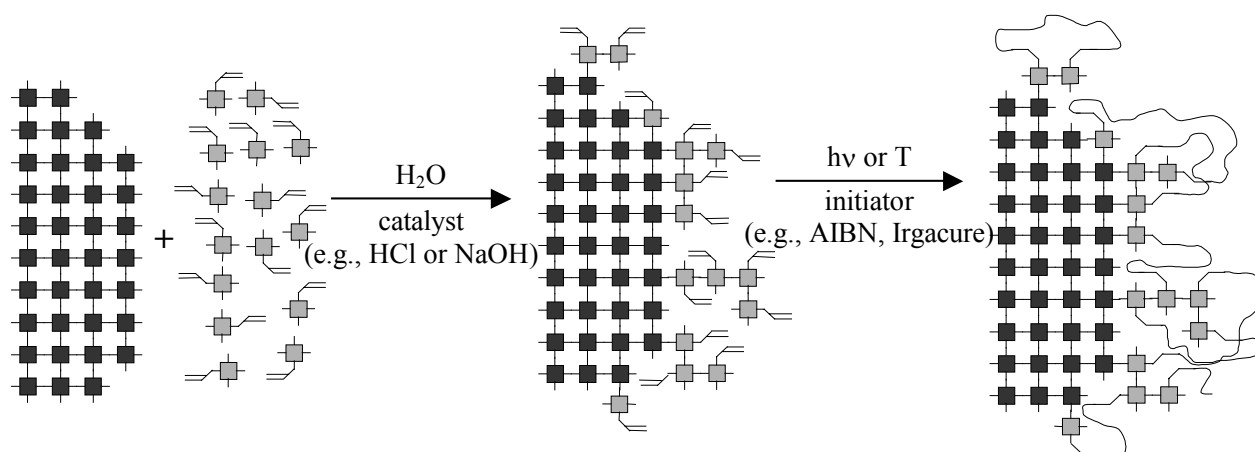
Figure 16: Silica layer grafting on TMO[29].

The complexation of transition metal alkoxides allows one to further synthesize organic-inorganic hybrid materials. **C**omplexing **l**igands (CL) are often used to modify the reactivity of a metal alkoxide (cf., section 2.1.1.2), involving ionic M-C bonds which can be easily cleaved by water. For the synthesis of organic-inorganic structures containing a polymerizable function (vinyl, allyl, methacryl, etc.), the behavior of some of these chelates

has been recently studied with titania- or zirconia-based materials. For example, 2-(methacryloyloxy)ethyl acetoacetone (Figure 6 (c)) which is a ß-diketone ligand with a methacrylate moiety, was chelated to zirconium propoxide. Both, organic and inorganic polymerizations were performed leading to milky sols[47]. The synthesis scheme is generally the same than that of organically modified silicon alkoxides (cf., Figure 13).

Template building blocks can be used as starting units in order to obtain hybrid organic-inorganic structures (Figure 17). The most studied building blocks are based on silicilic acid clusters ($H_8Si_8O_{20}$) from which functional organic silicilic acid derivatives can be obtained[85]. Syntheses of TM-oxo clusters containing polymerizable moieties synthesized from different TM such as, for examples, titanium, zirconium, or tin, were reported in the literature [86].
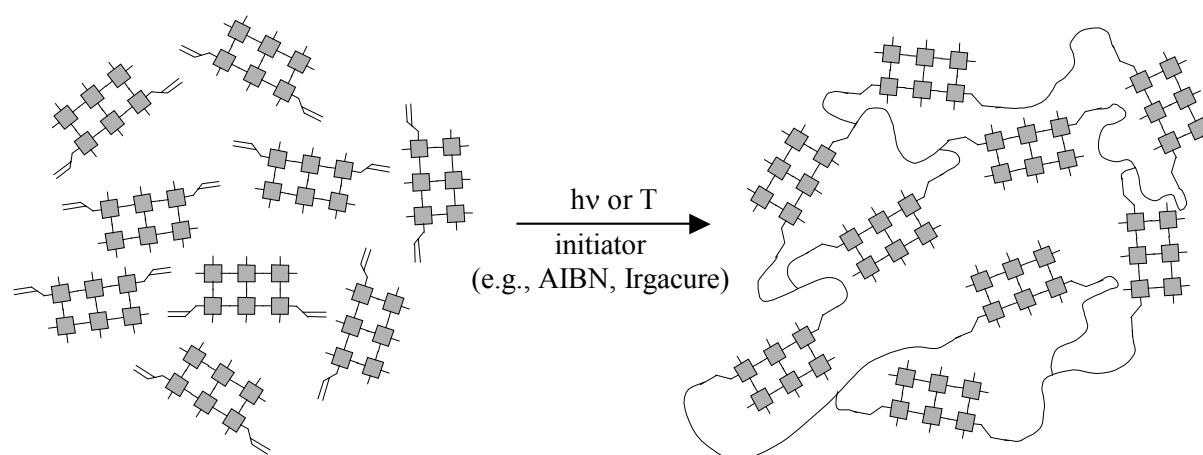
Figure 17: Hybrid material based on template building blocks[29].

Depending on the TM employed, the M-C bonds can be broken in the presence of water. Thus, such building blocks are often introduced in polymerizable matrices such as, for example, ORMOCER®s[86], or polymerizable monomers such as, for example, styrene or methylmethacrylate monomers[87].

2.1.3   Organically modified silicon alkoxides

For more than two decades, the Fraunhofer ISC has been working on inorganic-organic hybrid polymers, registered as ORMOCER®s for all kinds of applications. They are an example of organically modified silicon alkoxides, and belong to the class II hybrid organic-inorganic materials, where the organic and inorganic molecules are bonded through strong chemical bonds. In this section, their preparation and applications are described, followed by a survey about syntheses and characterization of organically modified silicon alkoxides containing heteroelements. The latter were also synthesized in the framework of this thesis.

2.1.3.1 Organic-inorganic hybrid polymeres

ORMOCER®s are prepared from organo-alkoxysilane molecular precursors or oligomers of the general formula R'$_n$Si(OR)$_{4-n}$ or (OR)$_{4-n}$Si-R''-Si(OR)$_{4-n}$, with n = 1, 2, 3. Figure 18 shows

a general schematic of the individual precursors, and their function in the network.
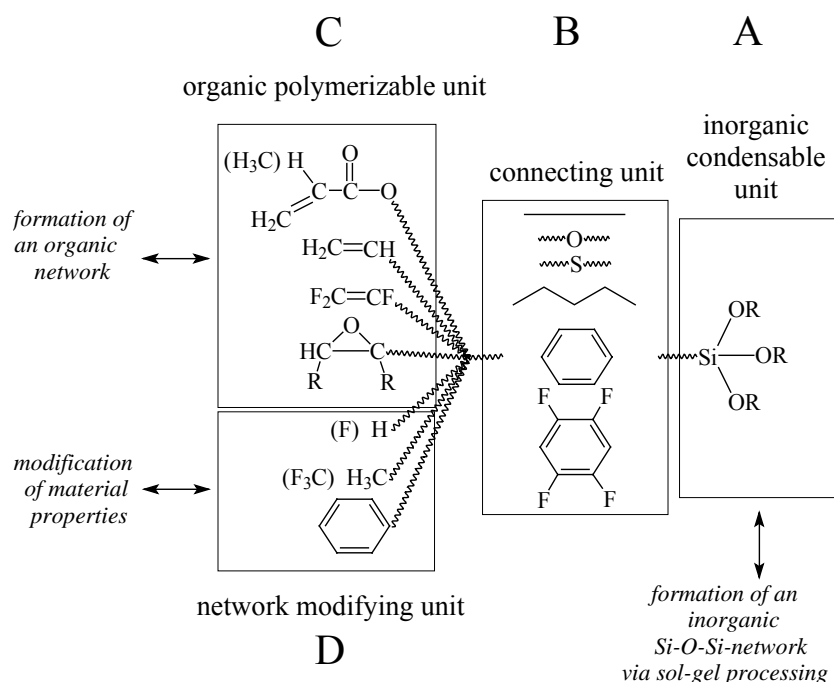
Figure 18: General schematic of organo-alkoxysilanes and their function for the network[73].

The inorganic condensable unit (-Si-OR) is used to form an -Si-O-Si- network by hydrolysis and polycondensation reactions via a sol-gel process. The introduction of heteroelements into the inorganic-organic network can be also performed (see section 2.1.3.2). The organic unit R' is used as network modifier and/or network former. If R' possesses an organic polymerizable unit, it reacts with itself or with polymerizable monomers, then being a network former. If R' does not contain an organic polymerizable moiety, it acts as a network modifier. For example, the optical properties of the final material can be adjusted in this way. The refractive index of a silane based on fluorinated phenyl is lower than its unfluorinated analog[88]. In addition, a connecting unit can influence the resulting material properties. An increase of the length of the connecting unit will decrease the Young's modulus and, at the same time, will increase the coefficient of thermal expansion (CTE).

The organic polymerization can be induced photochemically and/or thermally. Thus, patterning can be achieved by many different methods, among which photolithography or direct laser writing by 2PP were used for the experiments described in chapter 4.2.

The range of applications for ORMOCER®s is very broad. They can be used in decorative applications, but also as protective coatings. ABRASIL® and CLEANOSIL® are successful examples of such ORMOCER® commercially available from T-O-P GmbH[89]. A few micrometer thick layer of ABRASIL® improves, for example, the scratch and abrasion resistance of a material[72]. ORMOCER® materials are also used as barrier systems against water vapor for the passivation of electronic circuits and devices[90]. ORMOCER®s may also be used as filling composite material for dental applications[91,92], where the materials have appropriate properties for teeth such as, for example, abrasion resistance and low shrinkage. Moreover, for dental applications the material has to be non-toxic, has to have a sufficiently

high X-ray opacity compared to dental tissue, and to be easy to use for the dentist. Dental ORMOCER[®] systems such as Definite[®] and Admira[®] are also commercially available[93]. ORMOCER[®]s were also used for applications in microelectronics. For example, a complete Pentium™ multi-chip module (133 MHz) was realized (Figure 19 (a))[73]. The substrate of this module consists of metal interconnections separated with ORMOCER[®] dielectric layers on a FR-4 laminated board. Sputtered aluminum layers were used for the signal interconnections. Vias were fabricated by direct photo-patterning by UV lithography using a mask aligner. Due to the adhesion properties of ORMOCER[®]s, they can be applied on flexible substrates, e.g. even as optical waveguides (cf., Figure 19 (b))[94]. ORMOCER[®]s can be found in industrial applications for micro-optics. By combining UV lithography and soft-embossing, micro-optical elements, for example the incoupling into optical fibers from vertical cavity surface emitting lasers (VCSEL), can be fabricated as shown in Figure 19 (c)[77]. At least, the use of ORMOCER[®]s in energy storage systems should be also mentioned, whereas ORMOCER[®]-based electrolytes are used for thin film lithium-polymer batteries (Figure 19 (d))[95].
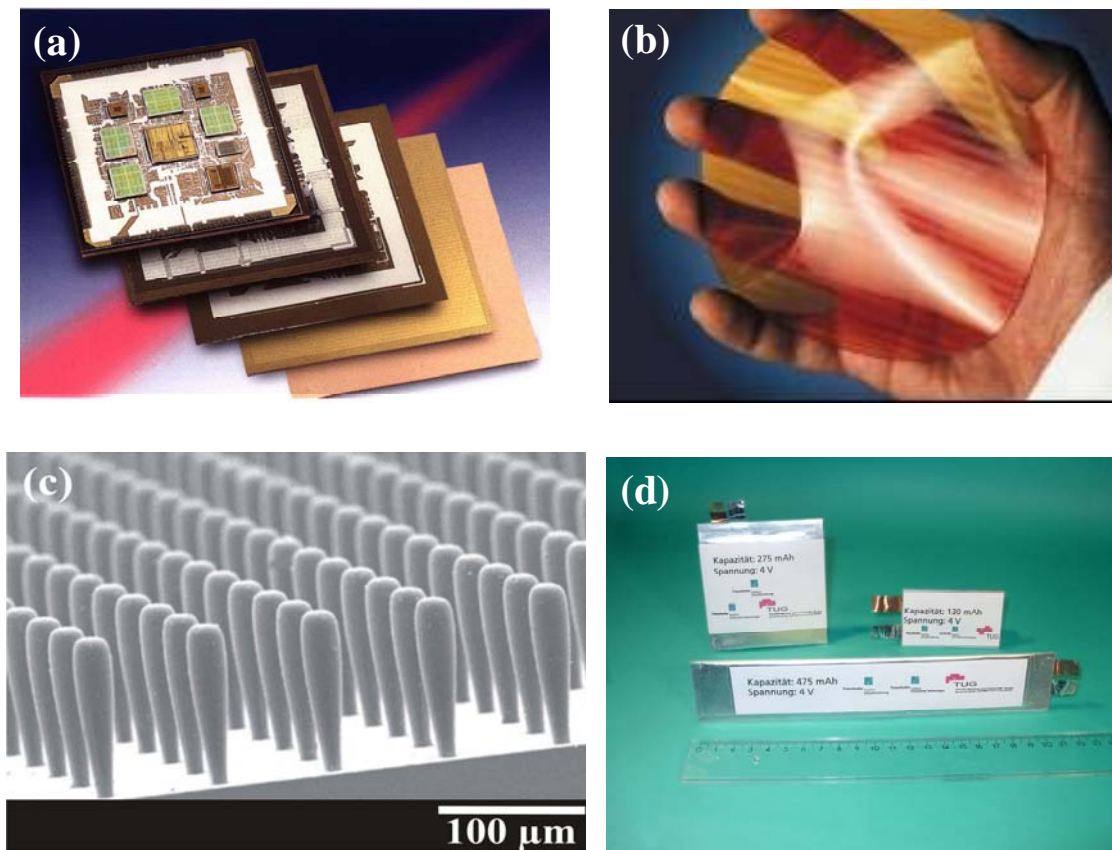

Figure 19: Examples of applications of ORMOCER[®]s, (a) Pentium™ multi-chip module[73], (b) waveguides on a flexible foil[94], (c) replicated microlenses [77], and (d) demonstrators of flexible thin-film batteries[95].

2.1.3.2 Organically modified silicon alkoxides and transition metal alkoxides

In addition, the siloxane-based hybrid organic-inorganic compounds can be co-condensed with $Si(OR)_4$, and metal alkoxides, mainly $Ti(OR)_4$, $Zr(OR)_4$, and $Al(OR)_4$, respectively. The incorporation of titanium and zirconium alkoxides has attracted considerable interest[96-103] due to the possibilities of adjusting the physical properties (such as refractive index, thermal and mechanical resistance) of the resulting hybrid materials. It will be proven in the framework of this work that the refractive index of the resulting ORMOCER® increases significantly by the introduction of titanium alkoxide, and structural aspects will be discussed and correlated to the material properties.

Since titanium alkoxides are quickly hydrolyzed compared to silicon alkoxides (cf., chapter 2.1.1.2), the hydrolysis of these two different metal alkoxides in one synthesis can generate a segregation, resulting in solutions containing Si-O-Si and Ti-O-Ti rich areas, leading to non-transparent solutions. A clear solution is obtained for specific synthesis conditions, for example by limiting the amount of water, prehydrolysing the alkoxysilanes, and controlling the acidity/basicity of the medium[104-106]. The co-condensation of organo-alkoxysilanes and metal alkoxide, such as titanium alkoxide, leads to the formation of Si-O-Si, Ti-O-Ti, and Ti-O-Si bonds.

Most authors postulated the existence of Si-O-Ti and Zr-O-Ti bonds by **F**ourier-**t**ransform **i**nfra**r**ed (FT-IR) spectroscopy, whereas this has been proven by **n**uclear **m**agnetic **r**esonance (NMR) spectroscopy and single crystal X-Ray diffraction by only a few authors. The stability of these bonds with the storage conditions and/or the addition of water is another problem which is often discussed in the literature[104,107-112]. In the following section, a literature survey of methods used to characterize Si-O-Ti bonds are reported. In addition, the evolution and the stability of this bond with the storage conditions are summarized from the literature.

FT-IR spectroscopy is often used to characterize the presence of an Si-O-Ti band, whose vibrational mode is observed between 910 and 950 cm^{-1}[110,113-116]. However, this band is overlapped with the vibrational mode of Si-OH bonds. Thus, FT-IR spectroscopy is not the best suited method to investigate the presence of Si-O-Ti bonds in hybrid materials.

The formation of Si-O-Ti as well as Zr-O-Si bonds was clearly evidenced using ^{17}O-and ^{29}Si-NMR spectroscopy by Babonneau et al.[107] and Hoebbel et al.[108,109] with solutions based on hydrolyzed **di**methyl**die**thoxysilane (DMDES) and $Ti(OPr^i)_4$ (or $Zr(OPr)_4$), and, DPD and $Ti(OPr^i)_4$, respectively. For ^{17}O-NMR spectroscopy, an isotopic enrichment of the sample due to the low sensitivity of this isotope (10^{-5} compared to ^1H) is necessary. ^{29}Si- and ^{17}O-NMR spectra were recorded before and after the addition of the metal alkoxide. After its addition, new pronounced peaks were detected which were assigned to Si-O-Ti and Si-O-Zr bonds[107,108]. In small quantities, titanium alkoxide acts as catalyst for the condensation of silanols in addition to the Si-O-Ti bond formation[109,112]. By increasing the quantity of $Ti(OPr^i)_4$, new signals were detected corresponding to Si-O-Ti bonds[108].

Single crystal X-Ray diffraction was used in order to characterize titanodiphenylsiloxane crystals[117] which have been synthesized by reacting DPD with $Ti(OPr^i)_4$, or $Ti(OPr^i)_4$ complexed with acetylacetonate ligands. Figure 20 shows two structural schematics presentations of titanodiphenylsiloxanes among the six obtained from Hoebbel et al.[117].
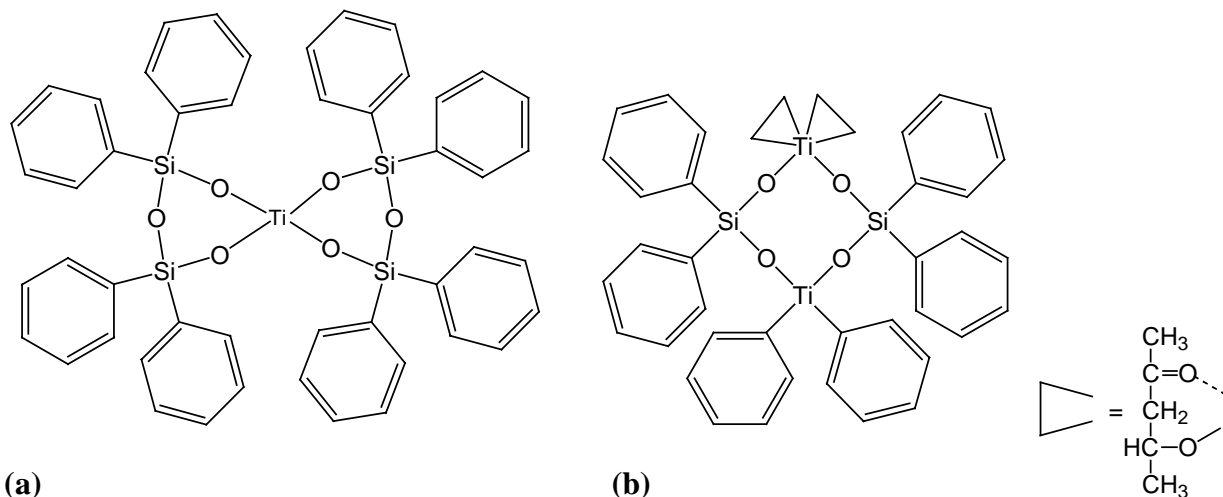
Figure 20: Examples of titanodiphenylsiloxanes synthesized by Hoebbel et al.[117] (a) Spirocyclic, and (b) cyclotetrameric titanodiphenylsiloxane.

Since the materials synthesized in the framework of this thesis might possess Si-O-Ti bonds, the evolution of the Si-O-Ti bonds during the aging process, different storage conditions, or by adding water, is summarized in the following from the literature.

Babonneau et al.[107] studied the effect of the aging process on the Ti-O-Si and Zr-O-Si bonds by ^{17}O-NMR spectroscopy. By increasing the storage time (in air dried at room temperature, in an open flask), it was shown that the intensity of peaks from Si-O-Si and Ti-O-Ti (or Zr-O-Zr) bonds increased, while the intensity of the signal from Si-O-Ti (or Zr-O-Ti) bonds decreased, and even almost disappeared after 32 hours storage. The authors reported that the Si-O-Ti peak disappeared faster than the Zr-O-Si peak. Hoebbel et al.[108] investigated also the evolution of the Si-O-Ti bonds in a closed flask stored at 25°C. They noticed that the intensity of the signal of the Si-O-Ti bonds decreased with time as already found by Babonneau et al.[107]. On the other hand, the signal of the Si-O-Ti bonds did not disappear after 21 days, which is different from the observations of Babonneau et al.[108]. The cleavage of the Ti-O-Si bonds, leading to the formation of Si-O-Si and Ti-O-Ti bonds by adding water to the sol was clearly demonstrated[108,114]. The molecular homogeneity of the material decreases due to the increase of the phase separation between silica-rich and titania-rich phases. Hoebbel et al.[117] investigated the hydrolytic stability of the Si-O-Ti bonds in titanodiphenylsiloxanes by hydrolyzing six different titanodiphenylsiloxanes with various amounts of water. In addition, the effect of the H$^+$ concentration was also investigated. The results show that no matter how much water was used, a hydrolytic degradation of the Si-O-Ti bonds occurred.

Moreover, simultaneous exposure at elevated temperatures and to relative humidity has been also reported to affect the Si-O-Ti bonds. For example, Matsuda et al.[110] showed that high temperature (135°C) and high humidity (90%) storage led to the dissociation of Si-O-Ti bonds in the coating due to the attack from water vapor, then to the formation of Ti-O-Ti bonds, and finally to the nucleation and growth of anatase. The same phenomenon was also observed by Imai et al.[111], who transformed TiO_2 gel films into anatase by exposing the coatings to water vapor at temperatures between 80 and 180°C, while in dry atmosphere, a temperature treatment beyond 400°C was required for the anatase crystallization.

2.2 Refractive index

Materials having a high refractive index, synthesized from patternable organo-alkoxysilanes and co-condensed with titanium alkoxides are one of the main topics of this thesis. This chapter relates to the refractive index of a material and its chemistry. The refractive index of a material depends on its composition, its structure, but also on, external parameters such as the temperature and the humidity[118]. Crystalline materials have higher refractive indices than amorphous ones. The refractive index of a material is also related to its density and its polarizability. In this part, the refractive indices of inorganic oxides are firstly described and followed by those of organic components, such as organic polymers. The last part focuses on the refractive index of inorganic-organic hybrid materials, especially on those having an organically cross-linkable moiety.

The refractive index n of a transparent material is given by (Eq. 2), where C_0 is the velocity of light in vacuum, and C is the velocity of the light in a medium[119]:

$$n = \frac{C_0}{C}.$$
(Eq. 2)

The complex refractive index n* (cf., (Eq. 3)) includes the absorption index k, which is related to the energy absorbed by the medium from the light wave as it propagates through the medium, thus being also related to the absorption coefficient α[119].

$$n^*(\lambda) = n - i\left(\frac{\alpha\lambda}{4\pi n}\right).$$
(Eq. 3)

n*(λ) is referred to as dispersion relation. Usually, n decreases for increasing λ (from the UV to the IR regime) which is called normal dispersion. This is due to the fact that photons of higher energy (low wavelength/high frequency) interact more strongly with a medium than photons of lower energy[120]. Since n also depends on the temperature of the material, it is denoted by the symbol n_D^{20}. The superscript indicates the temperature in degree Celsius, and the subscript the wavelength of the light (in this case, D indicates the Na_D line at 589 nm, unless otherwise stated).

2.2.1 Refractive index of materials

2.2.1.1 Inorganic oxidic materials

It is well-known that crystalline materials have a higher refractive index than amorphous ones. Typically, silica crystallized in the quartz structure has a refractive index close to 1.553[121], whereas the refractive index of the amorphous phase is close to 1.51[119]. Anisotropic crystals possess two or three refractive indices, depending on their crystal symmetry, where the refractive indices are different for various crystal orientations with respect to the incident light. Crystals having a cubic symmetry and amorphous materials are isotropic, and possess only one refractive index[119,122].

Table 2 summarizes typical values of average refractive indices, and the densities of inorganic oxides associated to their crystalline phases[121]. For example, among the three crystalline phases of TiO_2 (brookite, anatase, and rutile), anatase and rutile are the most investigated crystalline phases. Both of the latter are crystallized in the tetragonal phase, however, rutile shows a significantly higher refractive index than anatase (2.903 for rutile

compared to 2.554 for anatase).

Table 2: Average refractive indices n_D^{20} of selected oxides, their crystalline phases, and associated densities [121].

Oxide formula	Oxides name	Crystalline system	Refractive index	Density (g/cm³)
Al_2O_3	aluminium oxide	hexagonal	1.768 - 1.760	3.965
$\alpha-Al_2O_3$	corundum	rhombic	1.765	3.97
CuO	tenorite	monoclinic	2.63	6.49
NiO	busenite	cubic	2.1818	6.67
Fe_2O_3	hematite	trigonal	3.01	5.24
Fe_3O_2	magnetite	cubic	2.42	5.18
SiO_2	cristobalite	cubic or tetragonal	1.487 - 1.484	2.32
	quartz	hexagonal	1.553	2.66
SnO_2	cassiterite	tetragonal	1.997 - 2.093	6.95
TiO_2	brookite	rhombic	2.583 - 2.741	4.17
	anatase	tetragonal	2.554 - 2.493	3.84
	rutile	tetragonal	2.616 - 2.903	4.26
ZnO	zincite	hexagonal	2.008-2.029	5.606
ZrO_2	baddeleyite	monoclinic	2.13 - 2.20	5.89

The density of a material affects also the refractive index as predicted by the Lorenz-Lorentz formula ((Eq. 4), also known as Clausius-Mossotti equation[123,124]:

$$\frac{n^2-1}{n^2+1} = \frac{\rho N_A \alpha}{3\varepsilon_0 M}, \tag{Eq. 4}$$

where M is the molecular weight, ρ the density, α the material's polarizability, N_A the Avogadro number, and ε_0 the dielectric constant of vacuum. Solving (Eq. 4) leads to (Eq. 5)[124]:

$$n = \sqrt{\dfrac{1 + 2\left(\dfrac{\alpha N_A \rho}{3\varepsilon_0 M}\right)}{1 - \left(\dfrac{\alpha N_A \rho}{3\varepsilon_0 M}\right)}} \ . \qquad\qquad\qquad (\text{Eq. 5})$$

Thus, an increase of the material's density leads to an increase of the refractive index of the final material. However, oxides having the same density can have different crystalline structures. For example, aluminium oxide structures which nearly have the same density show the same refractive index (n = 1.76). This means that a different crystalline structure does not necessarily correlate with the refractive index, and that the material density has larger impact.

Crystalline inorganic oxidic materials have the advantage of high refractive indices, which are needed for photonic applications. Particularly, titanium dioxide, whose refractive index ranges from 2.49 to 2.90 depending on its crystalline phase, is very promising due to its high refractive index. On the other hand, inorganic oxidic materials are not directly patternable, and 3D structures require fabrication in a layer-by-layer assembly, where each layer has to be fabricated with a complete series of lithography and etching steps.

2.2.1.2 Organic materials

Based on the solution of the Lorenz-Lorentz formula (Eq. 4), one can notice that not only the density of the material affects the refractive index, but also its polarizability α. Three modes of polarization contribute to the total polarization: the electronic, the atomic, and also the dipole orientation polarization[118,123]. The dipole orientation polarization takes place when a molecule has a permanent dipole. In the presence of an external electrical field, a redistribution of the electronic charges occurs within the molecule, resulting in a reorientation of the dipole. Atomic polymerization results from the rearrangement of nuclei in response to an electrical field. Electronic polarization originates from a redistribution of the electron density within the molecule without affecting its nuclear backbone or directional orientation. Electronic polarizability is important in the presence of π-systems such as conjugated olefins or aromatic systems. Due to the high electron mobility in such systems, the exposure to an external electric field leads to quick redistributions of electronic densities within the molecule. Therefore, aromatic systems possess higher refractive indices than aliphatic ones[118].

The presence of halogens in an organic molecule also considerably influences its refractive index. Except for fluorine, the substitution of a hydrogen by a halogen leads to an increase of the refractive index[123,125]. Halogens are known to be very electron-rich. They possess a high electronegativity χ ($\chi_{(F)}$ = 4.10; $\chi_{(Cl)}$ = 2.83, $\chi_{(Br)}$ = 2.69, and $\chi_{(I)}$ = 2.23; electronegativity from the Allred-Rochow scale[126]), resulting in a polar carbon-halogen bond. The bond between carbon and halogen is made up mainly by the overlapping of an sp^3 hybrid orbital of carbon with a p orbital of the halogen. From fluorine to iodine in the halide series, the size of the halogen p orbital increases, and the electron cloud around the halogen atom becomes more diffuse leading to an increase of the polarizability of the halogen[127]. From the Lorenz-Lorentz formula (Eq. 4), an increase of the polarizability of the halogens suggests an increase of the refractive index. Hougham et al.[123,125] showed that the replacement of hydrogen with fluorine always lowers the dielectric permitivity/refractive index increment because of the

lower electronic polarizability of the C-F bond relative to the C-H bond. Furthermore, the increase of free volume in a molecule or material with fluorine substitution contributes to the decrease of the refractive index (atomic radius of hydrogen and halogens: $r_H = 0.79$ Å, $r_F = 0.57$ Å, $r_{Cl} = 0.97$ Å, $r_{Br} = 1.12$ Å, and $r_I = 1.32$ Å). This is attributed to the larger steric volume of fluorine relative to hydrogen, which may interfere with efficient chain packing[118].

Thus, polymers can have a broad refractive index distribution depending on their composition. Their refractive indices vary between 1.3 to 1.78[128-132]. A summary of refractive indices of representative optical polymers is given in Table 3.

Table 3: Refractive indices of conventional optical polymers [118,133].
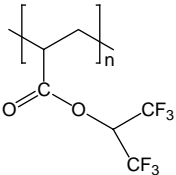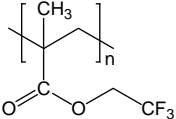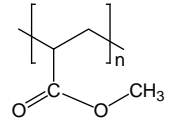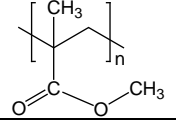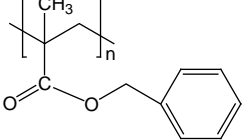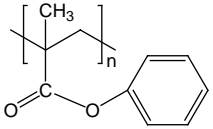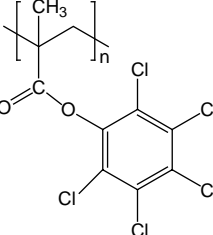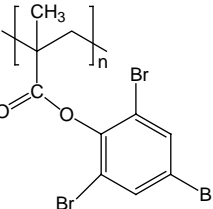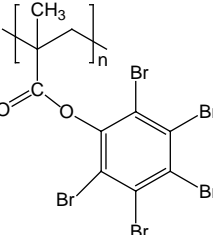
Polymers	Refractive indices
Poly(methylmethacrylate)	1.49
Polystyrene	1.59
Polycarbonate	1.58
Polyurethane	1.56
Epoxy resin	1.58
Polyimide (BPADA/ODA)*	1.78

* BPADA/ODA: **b**is**p**henol **A** **di**anhydride/**o**xy**di**aniline

The optical properties such as the refractive index and the optical loss, and also the thermal stability vary significantly related to the polymer structure. In the past three decades, novel optical polymers have been developed in academic and industrial laboratories, and some of them are commercially available[128]. Two families of well-known organic polymers are selected, as example for their high refractive indices depending on their chemical structure: polyacrylates and polyimides (cf., Table 4).

Most of previous work was concentrated on the use of polymethylmethacrylate (PMMA) as waveguide material in optical applications. The refractive index of PMMA reported in the literature is 1.49 at 589 nm, and the optical losses are 0.3 dB/cm at 1300 nm and 0.8 dB/cm at 1550 nm[134,135]. On the other hand, the stability of PMMA was reported to be between 90 and 105°C[136,137]. Depending on the composition of the polymer, the refractive index can be as high as 1.71 (Table 4). High refractive index polymers are based on brominated aromatic acrylate or methacrylate monomers, commercially available from Sigma Aldrich.

Table 4: Refractive indices of some acrylate polymers.

Polymer	Structure	n_D^{20}	Ref
Poly(1,1,1,3,3,3-hexafluoroisopropyl acrylate)		1.375	[138]
Poly(2,2,2-trifluoroethyl methacrylate)		1.418	[138]
Poly(methyl acrylate)		1.472	[139]
Poly(methyl methacrylate)		1.49	[118,139]
Poly(benzyl methacrylate)		1.568	[133]
Poly(phenyl methacrylate)		1.5706	[139]
Poly(pentachlorophenyl methacrylate)		1.608	[138,139]
Poly(2,4,6-tribromophenyl methacrylate)		1.66	[138]
Poly(pentabromobenzyl methacrylate)		1.71	[138]

AlliedSignal[140,141] has developed highly-crosslinked halogenated and non-halogenated acrylate monomers. Fluorinated acrylates exhibit lower loss values (0.001, 0.03, and 0.06 dB/cm at 840, 1300, and 1550 nm, respectively) than the non-fluorinated ones (0.02, 0.15,

and 0.45 dB/cm at 840, 1300, and 1550 nm, respectively). By blending and copolymerizing selected miscible monomers, the refractive index ranges from 1.3 to 1.6. The materials have been processed by conventional mask photolithography and direct laser writing.

Bromination or iodination can increase the refractive index of the polymer[142] . Depending on the degree of halogenation and the presence of aromatic groups in the material, series of photopatternable acrylate-based polymers were developed (cf., Table 4). As mentioned above, high refractive index materials are obtained for polymers containing a high content of bromide or iodine. Refractive index up to 1.77 was reported on iodinated polymers[142] . It has to be mentioned, however, that halogenated organic molecules are often healthy hazardous, and some of them are even known as human carcinogens. Therefore, they should be avoided for industrial applications.

Polyimides contain imide groups, -OC-N(R)-CO-. They have the advantage to offer superior thermal resistance (up to 400°C[136]) compared to the acrylate polymers (< 300°C), but their optical losses are slightly higher[118,143]. Their refractive indices range between 1.54 and 1.78[130-132] due to their chemical structures. The most familiar polyimide is widely known as Kapton H® (Figure 21), developed by DuPont during the 1960s[144]. As it is synthesized from **p**yro**m**ellitic **di**anhydride (PMDA) and **o**xy**di**aniline (ODA), it is also called PMDA-ODA.
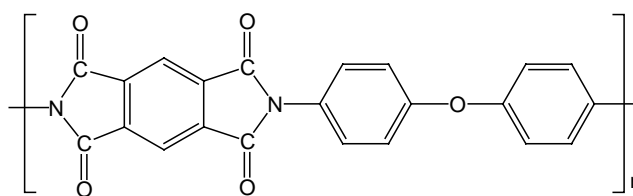
Figure 21: Chemical structure of PMDA-ODA (Kapton H®), developed by DuPont[131,144].

Based on PMDA-ODA, many other polyimides with some modified properties are commercially available such as, for example, Kapton®HN[145] which has a refractive index of 1.70[130], but a high optical absorption loss value of 2.9 dB/cm at 1310 nm[146]. However, it is insoluble and highly colored, like many other fully aromatic polyimides[144]. Eichstadt et al.[147] reported that the fully aromatic polyimide (Figure 22), synthesized from **bisp**henol **A di**anhydride (BPADA) and ODA monomers, has a refractive index of 1.662 (at 632 nm).
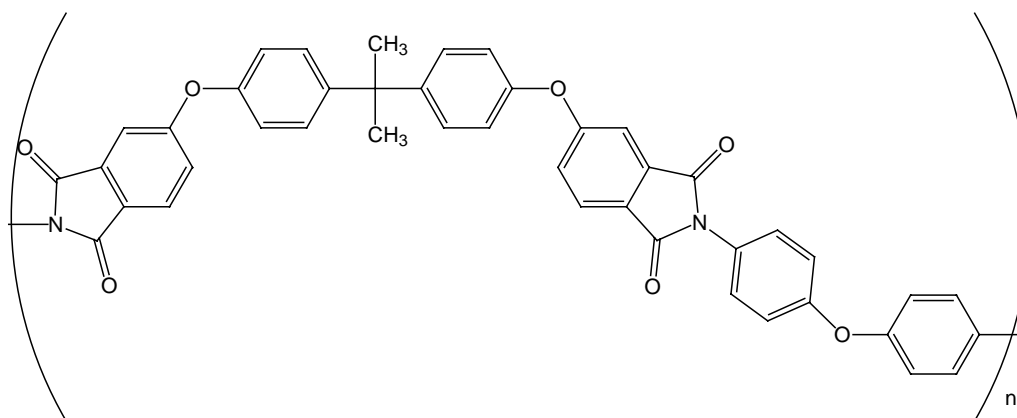
Figure 22: Chemical structure of the polyimide synthesized from BPADA and ODA[147].

Based on these results, Flaim et al.[130] synthesized a new variety of polyimides from BPADA, 2,2-**b**is(4-[4-**a**mino**p**henoxy]phenyl)**s**ulfone (BAPS), and 9,9-**b**is(4-**a**minophenyl)**f**luorene (BAF). The refractive indices of the resulting polyimides were compared to those of Eichstadt et al.[147] (Figure 23). The BPADA/BAF shows a higher refractive index value than the compounds from Eichstadt[147], while the BPADA/BAPS exhibits slightly lower values.
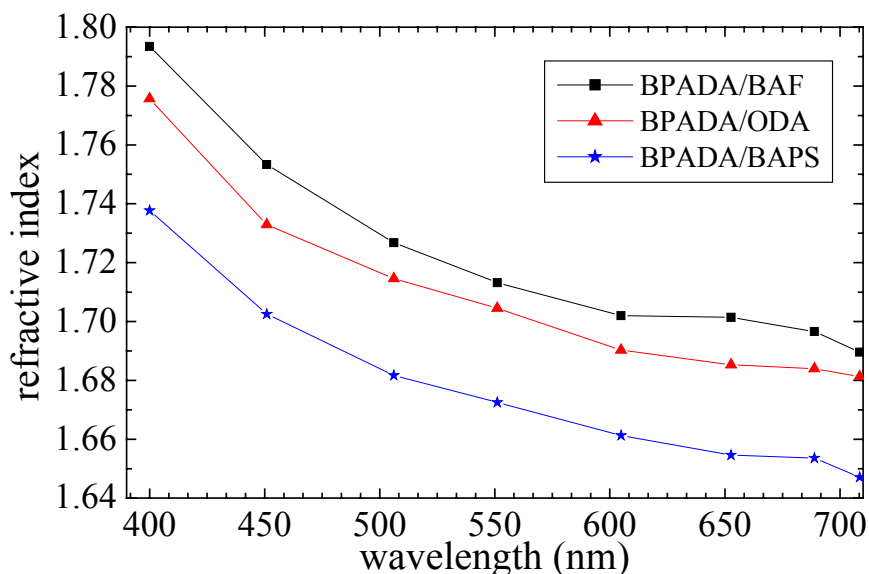
Figure 23: Refractive index of polyimides synthesized from Eichstadt et al. [147] (BPAD/ODA) and Flaim et al.[130] (BPAD/ BAF and BPAD/BAPS).
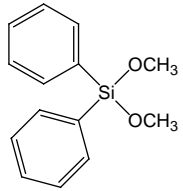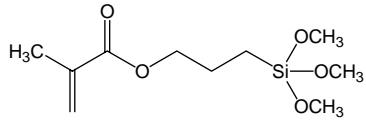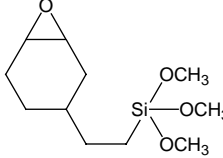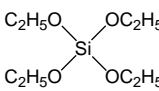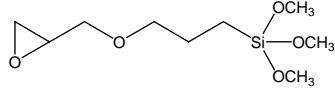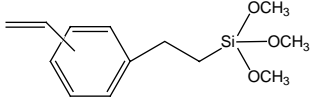
High refractive indices of polyimides containing sulfur substituents, up to 1.769 were also reported[142]. Although polyimides have the advantage to have high refractive indices which would increase the possible application scenarios for photonic applications, they are colored, and most of them are not directly photo-patternable. Optical integrated circuits are mostly obtained by reactive ion etching (RIE) process which has the disadvantage to produce rough surfaces, leading to an increase of scattering losses[128,131]. Some photosensitive polyimides have been reported in the literature[148-150]. Many negative photosensitive polyimides are commercially available by DuPont[136] and Fujifilm[151]. However, the pattern resolution of the negative tone resist materials is typically lower in resolution than positive tone materials, because of swelling during the development[144,148]. The resolution of a 4 μm thick positive photosensitive polyimide film has been reported to be 8 μm[148]. On the other hand, due to their highly aromatic nature, their solubility is limited to a few harmful solvents such as N-methylpyrrolidinone, dimethylformamide, dimethylacetamide, or α-butyrolactone[130]. Moreover, most of the films obtained with polyimides are highly colored due to charge transfer interactions, and processing conditions (curing temperature, monomer purity, kind of solvents, and atmosphere in the thermal curing process)[130,144].

2.2.1.3 Organic-inorganic hybrid polymers

Hybrid organic-inorganic materials (cf., chapter 2.1.2) synthesized by sol-gel processing have the advantage to combine the properties of organic and inorganic compounds to some extent. The inorganic part of the materials may allow, for example, modulation of the refractive index, and contributes to its mechanical and thermal strength. On the other hand, the organic part may contribute to specific properties (optical, electrical properties) and provides a polymerizable moiety which offers the possibility to micro-pattern the film with photolithography or laser techniques.

As already described in chapter 2.1.3.1, ORMOCER®s as special class of organic-inorganic hybrid materials are prepared from organo-alkoxysilane precursors with the general formula $R'_nSi(OR)_{4-n}$. The formation of an Si-O-Si network is obtained by hydrolysis/polycondensation reactions via sol-gel process of the inorganic condensable unit (-Si-OR). The composition of the ORMOCER® notably affects its refractive index. For ORMOCER®s synthesized from organo-alkoxysilanes, the refractive indices ranging from 1.47 to 1.60 have been reported[22,76,152]. Table 5 gives a list of the refractive indices of some commercially available organo-alkoxysilanes.

Table 5: Refractive indices n_D^{20} of selected organo-alkoxysilanes commercially available from ABCR[153] which are used as precursors in the literature.

Name	Formula	n_D^{20}
DPDMS		1.545
MEMO		1.431
ECET		1.449
TEOS		1.382
GLYMO		1.429
SETMS		1.505

The incorporation of metal alkoxides into organo-alkoxysilanes by co-condensation reactions is often used in order to increase the refractive index of the material. The effect of the co-condensation of titanium and zirconium alkoxide on the refractive indices was widely studied in the literature[96-100,102,154,155] (cf., Table 6), and the co-condensation with titanium alkoxide seems to affect the refractive index more than that with zirconium alkoxide.

Table 6: Variation of the refractive index of resins synthesized from organo-alkoxysilanes co-polymerized with titanium or zirconium alkoxides.

Composition of resins (mol-%)				n	Ref.
epoxysilane, 90	Ti(OEt)$_4$, 10			1.50	
epoxysilane, 65	Ti(OEt)$_4$, 35			1.54-1.55	
epoxysilane, 90	Zr(OPr)$_4$, 10			< 1.50	
epoxysilane, 65	Zr(OPr)$_4$, 35			1.52-1.53	
DPD, 80	Ti(OEt)$_4$, 20			1.62-1.63	[97]
DPD, 50	Ti(OEt)$_4$, 50			1.67-1.68	
DPD, 90-70	Zr(OPr)$_4$, 10-30			1.60-1.61	
DPD, 60	Zr(OPr)$_4$, 20	epoxysilane, 20		1.58-1.59	
DPD, 30	Zr(OPr)$_4$, 50	epoxysilane, 20		1.60	
DPD, 40	Ti(OEt)$_4$, 60			1.68	
DPD, 50	Zr(OPr)$_4$, 50			1.59	[96]
DPD, 40	Zr(OPr)$_4$, 40	GLYMO, 20		1.58	
TEOS, 80	Ti(OPr)$_4$, 20			1.46	[154]
MEMO, 60	(Ti(OPr)$_4$:MA)=(1 :1) 40			1.55	[155]
GLYMO, 40	(Ti(OBu)$_4$: ACAC)=(1 :1) 60			1.54-1.55	[102]
GLYMO, 60	(Ti(OBu)$_4$: ACAC)=(1 :1) 40			1.54-1.55	
MEMO, 91	(Ti(OPr)$_4$:MA)=(1 :2) 9			1.51	[98,99]
MEMO, 71	(Ti(OPr)$_4$:MA)=(1 :2) 29			1.53	
MEMO, 60	Ti(OEt)$_4$, 40			1.5685	
MEMO, 50	Ti(OEt)$_4$, 30	DPDMS, 20		1.5580	[100]
MEMO, 50	Ti(OEt)$_4$, 20	DPDMS, 25	DMDMS, 5	1.5420	
MEMO, 50	Ti(OEt)$_4$, 10	DPDMS, 15	DMDMS, 25	1.5295	

For materials based on $Ti(OEt)_4$ and DPD, high refractive indices up to 1.68 were obtained [96,97]. The latter high refractive index is not only due to the presence of titanium alkoxide, but also due to the presence of DPD which is known to improve the refractive index of the material due to the π-system in the aromatic groups (cf., chapter 2.2.1.2). However, DPD does not contain an organically polymerizable moiety. In the last decade, more attention was paid to materials synthesized from organo-alkoxysilanes containing a polymerizable moiety and co-condensed with titanium alkoxides. Indeed, these materials can be organically polymerized and, additionally, have higher refractive indices than the inorganic-organic material as ORMOCER$^®$s solely based on organo-alkoxysilanes[98-100,102,155,156].

The direct incorporation of anatase titania nanocrystals into silica sol based on GLYMO was reported. Depending on the weight content of TiO_2, refractive indices from 1.5017 to 1.6630, for 10 and 50 wt.-% TiO_2, respectively, were measured at 632.8 nm[157].

Organic-inorganic hybrid polymers synthesized by sol-gel process were prepared from soluble polyimides and titanium precursors. Chang et al.[158] reported an increase of the refractive index from 1.66 to 1.82 (at 633 nm) with the incorporation of 40 wt.-% of TiO_2. Whereas, high refractive index coatings up to 1.943 (at 633 nm) were reported by Su et al.[159] with the incorporation of 90 wt.-% of TiO_2. No patterning process was reported for these polyimide-titania hybrid films.

The photopolymerization which induces a densification of the material due to the organic cross-linking of the suitable moieties also affects the refractive index of a material. To our knowledge, the organic polymerization process of materials synthesized from organo-alkoxysilanes co-condensed with titanium alkoxides has been seldomly reported in the literature. Recent investigations on the influence of the UV irradiation on the refractive index of Ti-containing layers showed that a UV irradiation can promote a significant refractive index increase[99,155]. For films free from UV initiator, a slow linear increase of the refractive index of about 0.008 after 120 s UV irradiation is observed. For materials containing a photoinitiator, the refractive index variations follow a bidirectional kinetics, with a first jump by about 0.009-0.01 after 10 min UV irradiation, and then an increase of about 0.012 after 60 and 120 min, depending on the initiators introduced into the material[99]. A similar behavior was observed by Trejo-Valdez et al.[155]. The organic polymerization and the different steps of the UV lithography process are described in more detail in chapter 2.3.1.

2.2.2 Refractive index measurement

The refractive index of a material can be determined by many different techniques. The main instrument used for liquids is the Abbé refractometer. In addition, by combination with an immersion liquid with a known refractive index, the refractive index of a coating can be determined. Ellipsometry and prism coupler methods are the most used methods to determine the refractive index and the thickness of coatings. Another method is the calculation of the refractive index and the thickness of a thin-film coating from the interference fringes in its transmittance spectrum. In the following, each method is briefly described, since they were applied to characterize the materials and coatings within this work.

2.2.2.1 Abbé refractometer

The Abbé refractometer is an instrument used to determine the refractive index of liquids, named after its inventor Abbé (1840-1905)[160]. It is based on the concept of a critical angle θ_c. A liquid sample is sandwiched between an illuminating and a refracting prism (Figure 24). The refracting prism, which has a known high refractive index (e.g., 1.75), is used to measure samples having only lower refractive indices. A light source is projected through the illuminating prism. Since the bottom surface of the latter one is rough, each point on the surface can generate light rays traveling in all directions up to grazing incidence. The light at grazing incidence is refracted into the prism at the critical angle as shown in Figure 24. Then, a telescope is used to view this light leaving the prism. The resulting picture is a shadow boundary starting at the critical angle, where no more light can pass through this angle. Finally, the dark region is superposed on a pre-calibrated scale and the refractive index can be easily read[160-162].
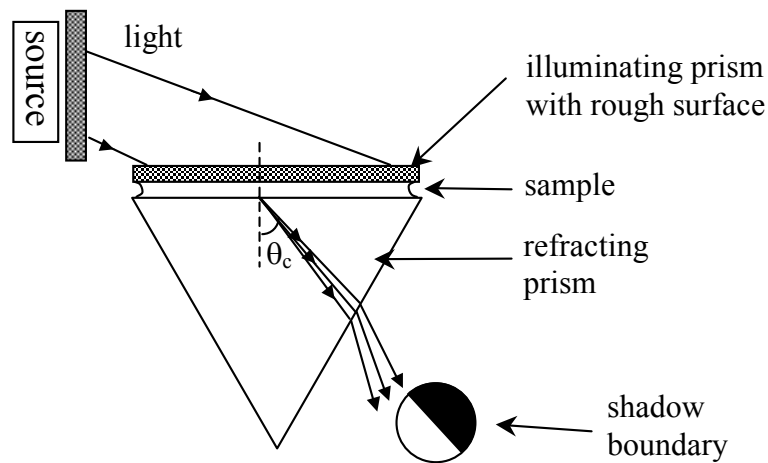
Figure 24: Schematic cross-section of a part from an Abbé refractometer showing the optical path[160-162]. The sample thickness has been exaggerated for clarity.

Due to the simple utilization of the Abbé refractometer, a quick determination of the refractive index can be done. On the other hand, the refractometer is designed to be used for samples having a lower refractive index than this of the refracting prism, and the measurements are typically performed only at the sodium D line at 589 nm.

2.2.2.2 Prism coupler

The general theory of prism coupling was introduced by Ulrich et al.[163]. A film which is coated onto a substrate is brought into contact with the base of a prism by means of a coupling head, creating a small air gap between the film and the prism (Figure 25). A laser beam strikes the base of the prism, and is totally reflected at the base of the prism onto a photodetector.
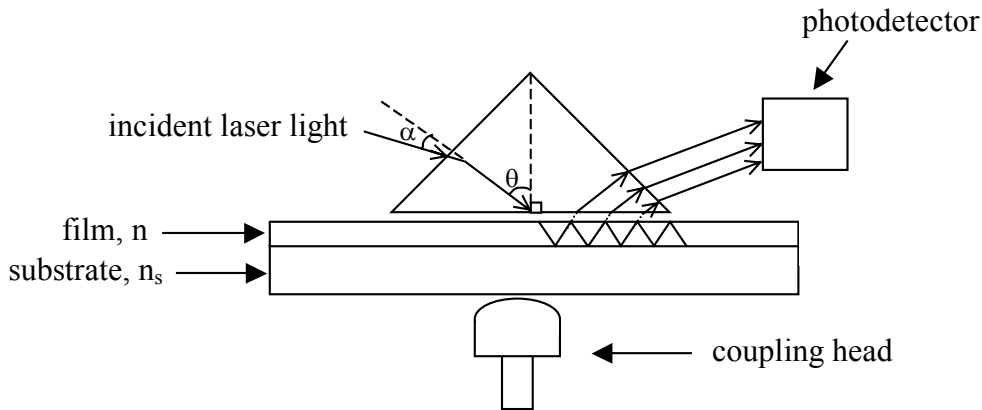
Figure 25: Schematic view of a prism coupler.

For discrete values of the incident angle θ (mode angles), evanescent light is coupled into the film, and enters into a guided optical propagation mode, causing a sharp drop in the intensity of light reaching the detector. To a rough approximation, the angular location of the first two modes determines the film index, whereas the angular difference between the modes determines the thickness. It allows one to measure the thickness and the refractive index completely independently using an iterative method. Measurements are performed using a computer-driven rotary table which enables a variation of the incident angle θ, and to locate each propagation mode of the film.

This method has two major advantages. It requires only the measurement of angles which can be taken conveniently and with high precision. The film has to be thick enough to observe at least two or more modes of the same polarization, in order to determine the refractive index and the thickness of the film with a high accuracy. For thin films (less than 1 μm), the refractive index and thickness cannot be determined, since one cannot detect at least two modes. The refractive index can be determined for films having a lower refractive index than that of the prism at the wavelength of the light source, similar to an Abbé refractometer.

2.2.2.3 Ellipsometry

The technique of ellipsometry was invented in 1887 by Paul Drude, who used it to determine the dielectric function of various metals and dielectrics[164]. This technique is applied for determining optical properties of surfaces and thin films. It measures the changes of the polarization reflected off a surface of a sample, and allows one to determine all optical constants, i.e., refractive index, absorption coefficient, as well as porosity and thickness of a coating[164,165].

A typical setup of an ellipsometry experiment is sketched in Figure 26. A linearly polarized incident light beam with a known polarized orientation (finite field components E_p and E_s in the plane of incidence (p) and perpendicular to the plane of incidence (s)) is reflected off a sample surface. The interaction of the light with the sample causes a polarization change from linearly to elliptically polarized light. The elliptically polarized light is then detected with an analyzer[165].
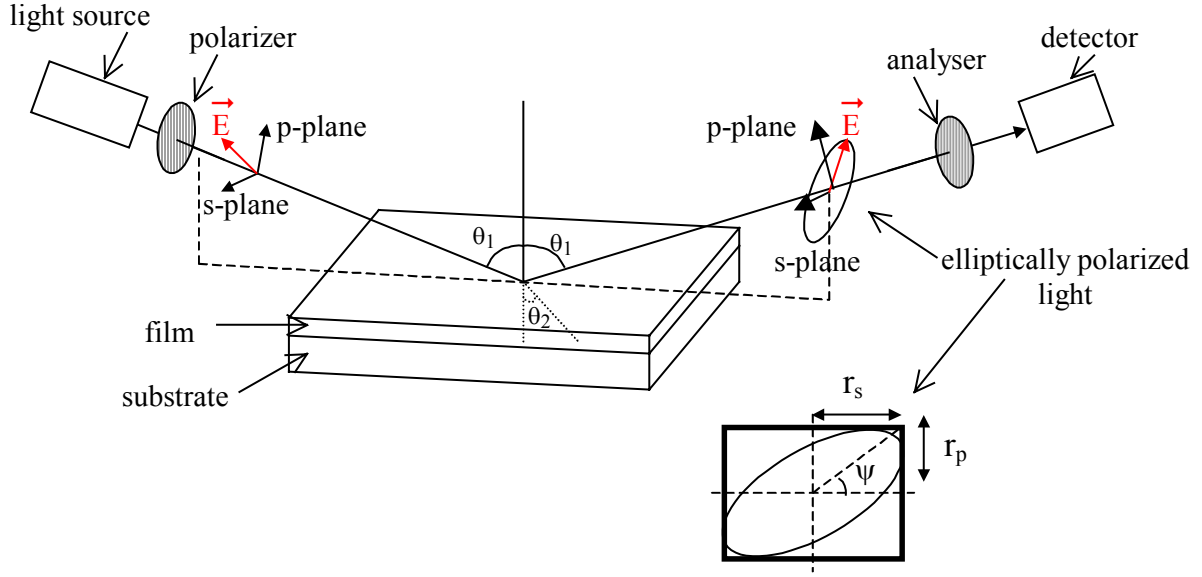
Figure 26: Schematic presentation of an ellipsometry experiment[166,167]. $\vec{E}$ is the electric field of the polarized light.

Ellipsometry measures two values, ψ and Δ, which determine the differential changes in the light amplitude and phase. They are related to the ratio of Fresnel reflection coefficients r_p and r_s for *p* and *s*-polarized light (Eq. 6)

$$\frac{r_p - \text{polarized}}{r_s - \text{polarized}} = e^{i\Delta} \tan\psi \, ,$$ (Eq. 6)

where r_s and r_p are expressed as

$$r_s = \frac{E_s}{E_o} = \frac{\cos\theta_1 - n^* \cos\theta_2}{\cos\theta_1 + n^* \cos\theta_2} \quad , \text{ and } \quad r_p = \frac{E_p}{E_o} = \frac{n^* \cos\theta_1 - \cos\theta_2}{n^* \cos\theta_1 + \cos\theta_2} \, ,$$

respectively .

θ_1 is the angle of incidence, and θ_2 is the angle of refraction which can be related to θ_1 using Snellius' Law of refraction (Eq. 7), where n^* is the complex index of refraction, already defined in chapter 2.2 (Eq. 3):

$$\sin\theta_1 = n^* \sin\theta_2$$ (Eq. 7)

The measured quantities ψ and Δ are used in various equations and algorithms to create a model which describes the interaction of the light with the sample[164,165]. The film thickness and the optical constants have to be extracted through a model-based analysis using optical physics. The modeling process is illustrated in Figure 27.
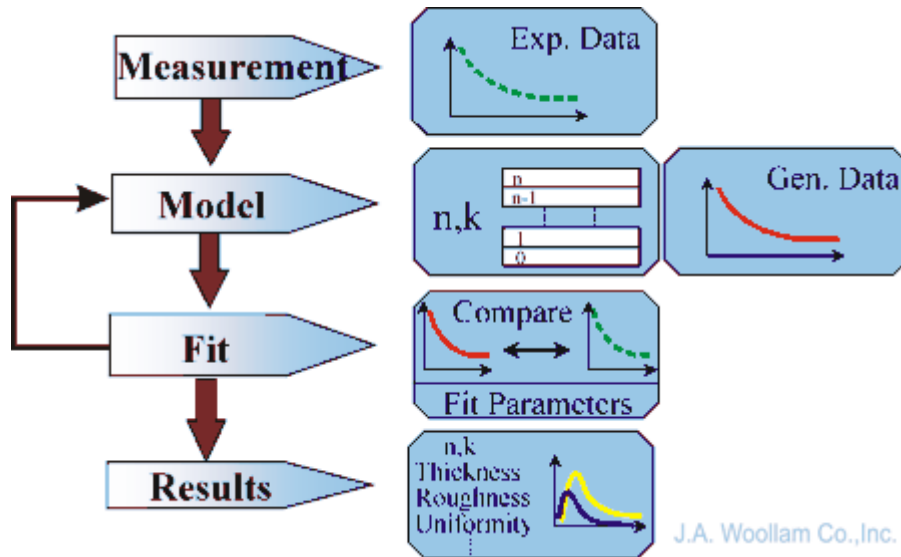
Figure 27: Modeling process used to extract the optical constants and the thickness of a coating[168].

2.2.2.4 Transmission spectroscopy

Another method to determine the refractive index and the thickness of a coating is to use transmission spectroscopy. Monochromatic light passes through a thin sample, and the intensity transmitted as function of the wavelength $T(\lambda)$ by using a spectrophotometer is measured. For thin layers on thick transparent substrates, the transmission spectrum shows wavelength-dependent oscillations (interference fringes) within the thin film[169-173]. This method is commonly called Swanepoel's technique[172,174].

A schematic view for a weakly absorbing thin-film with a refractive index n_c and a thickness d on a transparent substrate having a thickness several orders of magnitude larger than d and a refractive index n_s is shown in Figure 28. Incident light with an angle of incidence θ_0 leads to the generation of reflected and transmitted light waves. The superposition of the transmitted or the reflected waves leads to interferences which are generated by the difference in phase between the light paths.

40
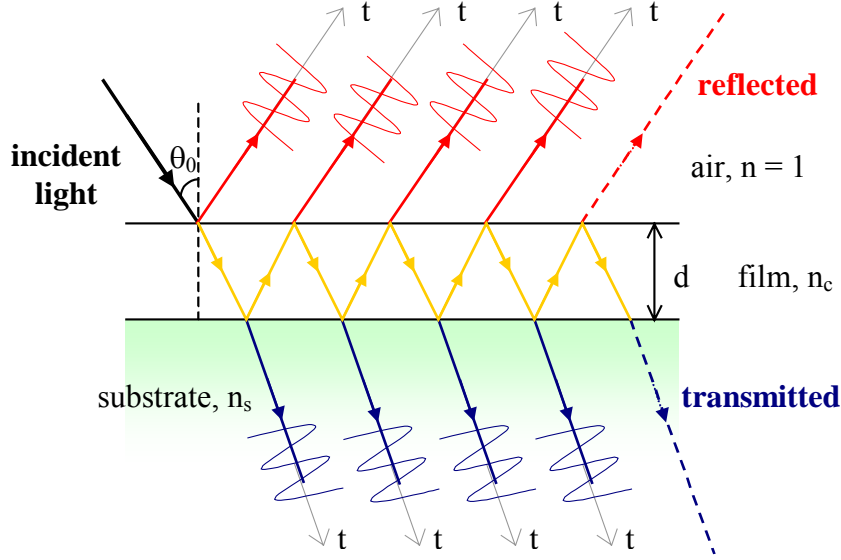
Figure 28: Schematic view of a thin-film with a refractive index n_c and a thickness d, sandwiched between air (n = 1) and a substrate with a refractive index n_s.

Considering a thick substrate without a film, its reflection R_s (free from interference) is given by (Eq. 8). Using the transmission spectra of the substrate T_s, the refractive index of the substrate n_s can be calculated at a definite wavelength λ_1 with equations (Eq. 8 and 9):

$$R_s(\lambda_1) = \frac{1 - T_s(\lambda_1)}{1 + T_s(\lambda_1)} \text{ and} \tag{Eq. 8}$$

$$n_s = \frac{1 + \sqrt{R_s(\lambda_1)}}{1 - \sqrt{R_s(\lambda_1)}}. \tag{Eq. 9}$$

If $T(\lambda_1)$ is the measured transmission of the coated substrate at a wavelength λ_1, the reflection of the coating at the wavelength $\lambda_1, R(\lambda_1)$, is defined by (Eq. 10). The refractive index of the coating n_c at the wavelength λ_1 can be calculated with (Eq. 11) or (Eq. 12). If the refractive index of the coating is higher than that of the substrate ($n_c > n_s$), it can be only calculated at minima of the interference of the transmission spectrum.

$$R(\lambda_1) = \frac{1 - T(\lambda_1) - R_s(\lambda_1)}{1 - T(\lambda_1).R_s(\lambda_1) - R_s(\lambda_1)}, \tag{Eq. 10}$$

with,

$$n_c = \begin{cases} \sqrt{n_s \dfrac{1+\sqrt{R(\lambda_1)}}{1-\sqrt{R(\lambda_1)}}} & \text{for } n_c \geq \sqrt{n_s} \qquad\qquad \text{(Eq. 11)} \\[3em] \sqrt{n_s \dfrac{1-\sqrt{R(\lambda_1)}}{1+\sqrt{R(\lambda_1)}}} & \text{for } n_c \leq \sqrt{n_s} \, . \qquad\quad \text{(Eq. 12)} \end{cases}$$

The thickness of the coating d can be calculated for $n_c > n_s$ from (Eq. 13) and (Eq. 14) at distinct wavelengths λ_0 which correspond to maxima or minima, where k and k' correspond to integer numbers larger than 0.

$$dn_c = \begin{cases} dn_c = k' \dfrac{\lambda_0}{2} & \text{at the maxima} \qquad\qquad \text{(Eq. 13)} \\[3em] dn_c = (2k+1)\dfrac{\lambda_0}{4} & \text{at the minima.} \qquad\quad \text{(Eq. 14)} \end{cases}$$

By calculating the ratio between two positions of two maxima or minima, and by comparison with Table 62 in Annex 2, k and k' can be calculated at particular wavelengths of the transmission spectrum of the coating and, consequently, the thickness of the coating can be calculated as well.

The technique of Swanepoel has the advantage to measure the refractive index and the thickness of the coating very quickly. This technique is simple to handle and less expensive than conventional methods (i.e., ellipsometry, prism coupler). Moreover, the refractive index and the thickness of the coating are calculated with an accuracy better than 1%[172]. On the other hand, this technique has the disadvantage to allow the determination of refractive indices only at particular wavelengths (such as, e.g., at the minima). Thus, the dispersion curve n(λ) cannot be determined with this technique. Moreover, the comparison of the refractive indices of different coatings can be performed only at the same wavelength. For that, the thicknesses of the coatings have to be exactly the same, which is nearly impossible to achieve with different materials where the processing is not known. Furthermore, this technique can be used only for highly transparent coatings. For absorbing coatings, for example, for coatings containing particles, the determination of the refractive index cannot be performed directly with the transmission spectrum.

2.3 Photon-induced organic polymerization

In the last years, the three dimensional microfabrication techniques have attracted a great attention because of their various applications such as, for example for **m**icro**e**lectro**m**echanical **s**ystems (MEMS), 3D optical waveguide circuitry, 3D optical data storage[6], only to mention some of which. Up to now, photolithography is one of the major techniques to fabricate microstructures in electronic devices. 3D structures such as, for example **p**hotonic **c**rystal (PC) structures can be fabricated by using a layer by layer method[6]. However, it is based on many sophisticated and time-consuming steps. Recently,

two-**p**hoton **p**olymerization (2PP) was established as process which allows one to fabricate arbitrary three-dimensional micro- and nano structures at time scale far below that of standard lithography[6,77].

In the framework of this thesis, 3D structures were written by means of a 2PP process using newly developed ORMOCER® resins. In order to evaluate the feasibility of the organic cross-linking of these resins, first experiments were carried out by UV lithography, and the knowledge was then partly transferred to the 2PP process. Thus, the chapter is organized as followed. In a first part, the one-photon polymerization process (UV lithography) of hybrid organic-inorganic materials is described. The parameters which affect the organic polymerization are reported from the literature. Particular emphasis was focused on the effect of the presence of titanium heteroelement in hybrid organic-inorganic materials. The second part of the chapter describes the 2PP process, and its parameter space relevant for the patterning process.

2.3.1   One-photon polymerization process

The one-photon lithography process (UV lithography) is used in semiconductor device fabrication to transfer a pattern form from a mask to a coating. Upon UV lithography, a photoresist material can act either as positive or negative photoresist. In a positive photoresist, a backbone cleavage in the UV-exposed areas takes place, and the UV-exposed part is removed during the development step. For negative photoresists, the organic cross-linking occurs in the UV-exposed part, which remains on the substrate after the development step.

As soon as oxygen is present in the atmosphere, it can react with the free radicals formed during the photochemical reactions (cf., Figure 29). The efficiency of the initiation species is reduced[175,176] due to these oxygen inhibition reactions. Thus, the degree of conversion (DC) of C=C bonds also referred to as degree of organic polymerization, which represents the rate of vinyl functions converted to aliphatic functions is low, and the polymerization at the coating surface does not take place even for long irradiation times[177].

$$P \xrightarrow{h\nu} P*$$
$$P* + MH \xrightarrow{h\nu} PH^\bullet + M^\bullet$$
$$M^\bullet + O_2 \xrightarrow{h\nu} MO_2^\bullet$$
$$PH^\bullet + O_2 \xrightarrow{h\nu} P + HO_2^\bullet$$
$$2\ HO_2^\bullet \xrightarrow{h\nu} H_2O_2 + O_2$$
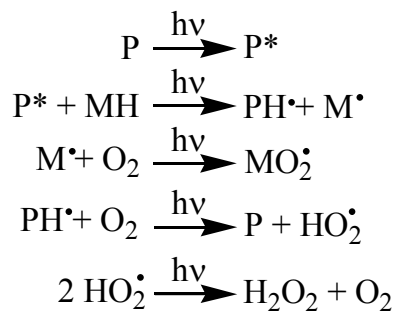
Figure 29: Photopolymerization reactions in the presence of oxygen. P corresponds to the photoinitiator, whose excitation energy is denoted by *, and MH is a monomer[176].

Oxygen acts as a radical scavenger by interfering with the initiation and propagation rate. These reactions can be avoided by preconditioning the material in a carbon dioxide atmosphere, and by utilizing a surface layer which has an oxygen impermeability[176].

The degree of organic polymerization is also influenced by the nature of the photopolymerizable group. Hybrid organic-inorganic materials based on acrylate moieties have shown a higher degree of polymerization than those based on methacrylate[178].

Moreover, it has been reported that the reactivity of **a**cryloxy**p**ropyl**trim**ethoxy**s**ilane (APTMS) is so high that radicals produced under UV irradiation react much faster with the monomers than with O_2, even at the surface of the coating[179].

The initiator type has been also reported to affect the polymerization reactions[180,181]. For a good efficiency of the photo-polymerization process, a wide overlap between the emission spectrum of the light and the absorption spectrum of the photoinitiator, short excited state lifetimes of the initiator, and high quantum yields of reactive radicals from excited state are required[181]. Figure 30 shows some examples of commercially available photoinitiators which have been used for the photo-polymerization of hybrid organic-inorganic materials.
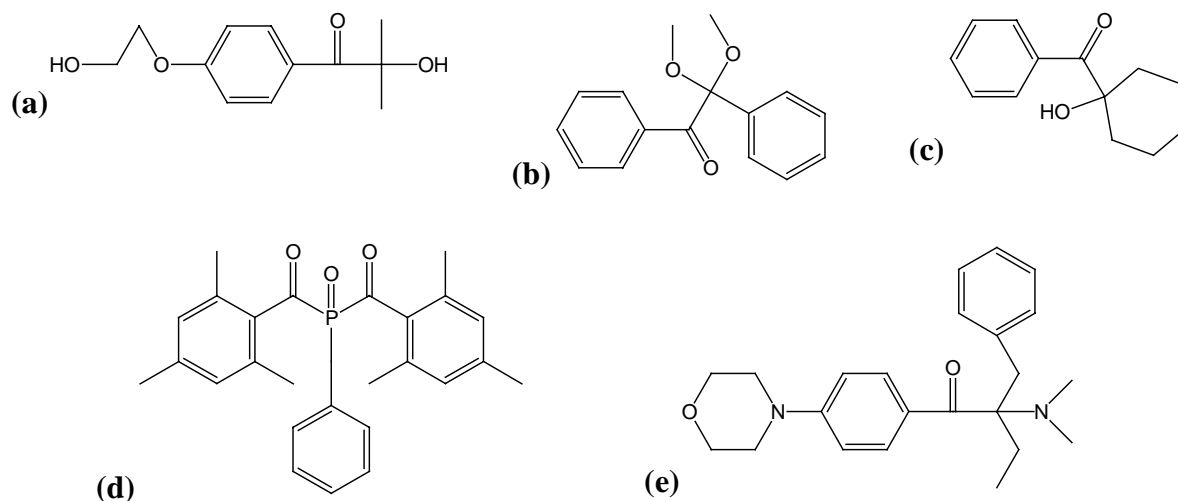
Figure 30: Examples of photoinitiators employed for organic cross-linking reactions (commercially available from Ciba-Geigy): (a) Irgacure 2959 (2-hydroxy-1-[4-(2-hydroxyethoxy)phenyl]-2-methyl-1-propanone), (b) Irgacure 651 (alpha-dimethoxy-alpha-phenylacetophenone), (c) Irgacure 184 (1-hydroxy-cyclohexyl-phenyl-ketone), (d) Irgacure 819 (phosphine oxide, phenyl bis (2,4,6-trimethyl benzoyl), and (e) Irgacure 369 (2-benzyl-2-(dimethylamino)-1-[4-(4-morpholinyl) phenyl]-1-butanone).

Soppera et al.[181] studied the effect of photoinitiators on the degree of polymerization on hybrid organic-inorganic materials based on MEMO, and the highest polymerization efficiency was obtained with Irgacure 819 (phosphine oxide, phenyl bis (2,4,6-trimethyl benzoyl). However, the latter one has been reported to be not stable in materials based on titanium and zirconium alkoxides[182]. Irgacure 651 (alpha-dimethoxy-alpha-phenylacetophenone) showed a good compromise between stability in the lacquer formulations and good reactivity, whereas Irgacure 184 (1-hydroxy-cyclohexyl-phenyl-ketone) and Irgacure 2959 (2-hydroxy-1-[4-(2-hydroxyethoxy)phenyl]-2-methyl-1-propanone) yielded a low reactivity.

The increase of the concentration of the photoinitiator has been also reported to increase the degree of polymerization[180]. For example, Houbertz et al.[183,184] showed that the degree of polymerization of an ORMOCER® material has increased from 62 to 78% by increasing the initiator concentration from 0.25 to 3 wt.-%, respectively. Beyond 3 wt.-%, the degree of polymerization is saturated at about 78 %. The same effect was also observed by Croutxé-Barghorn et al.[178], who reported that for initiator concentrations higher than 2 wt.-%, no significant increase of the final degree of polymerization was observed.

The UV polymerization process is based on different steps (Figure 31). Firstly, a photopatternable resin containing a photoinitiator is deposited onto a substrate (step 1, Figure 31). The coating is often thermally treated (Figure 31, step 2) prior to an exposure to UV light through a mask (Figure 31, step 3). After that, the coating might be again thermally treated at moderate temperatures (Figure 31, step 4). The pre- and the post-exposure bake steps are performed in order to improve the adhesion of the coating on the substrate, and to already remove process solvents. Subsequently, a development step is carried out by dipping the coating into an appropriate solvent (Figure 31, step 5) in order to remove non-UV-exposed parts. Finally, a thermal curing step can be performed (Figure 31, step 6).
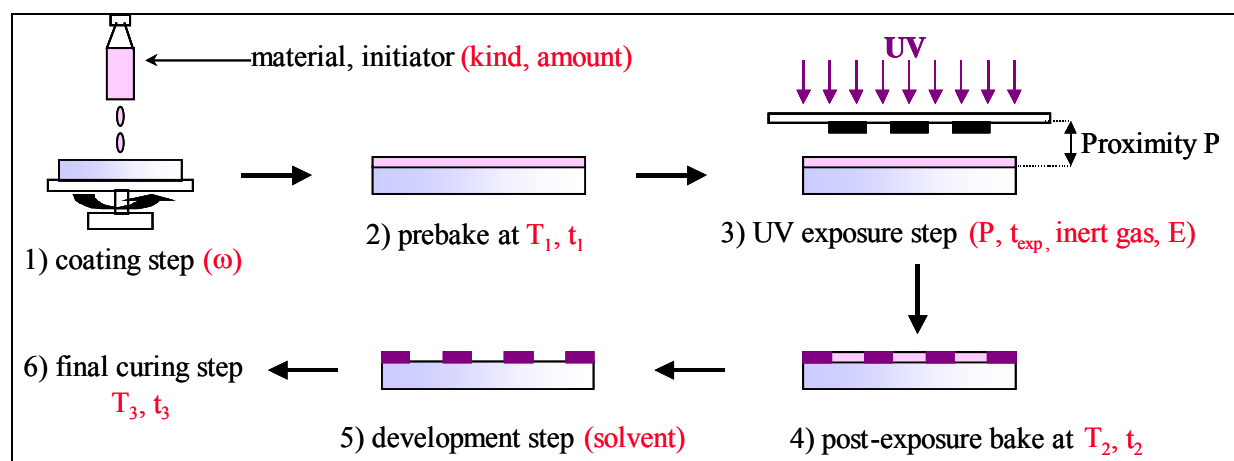
Figure 31: Steps involved in the photolithography process for a negative photoresist. Adjustable parameters are: ω (coating speed), T_1, T_2, and T_3 (temperature), t_1, t_2, and t_3 (curing time), P (proximity distance), t_{exp} (exposure time).

Of course, parameters such as light intensity and exposure time also affect the photo-polymerization, and they have to be determined in order to pattern the material[180]. Thus, the pattern formation is influenced by the different steps of the UV lithography process, but also by the polymer type (i.e., by the photopatternable resin), the kind and the quantity of the chosen photoinitiator, the atmosphere, and the exposure dose. Beside these listed parameters, the introduction of heteroelements by co-condensation reactions can considerably affect the organic cross-linking of the material upon UV irradiation.

Photochromic properties of titanium clusters and amorphous TiO_2 gels have been described in the literature. Under UV irradiation, they became dark green or dark blue[54,55,185,186]. This coloration has been attributed to a transition assigned to a Ti^{4+}-Ti^{3+} intervalence band[55]. It was reported that the coloration remains stable for several weeks and disappears in the presence of oxygen. Soppera et al.[182] assumed that Ti^{4+}-Ti^{3+} can act as reducing species leading to the formation of radicals upon irradiation. By FT-IR spectroscopy, they found a decrease of intensity of the vibration band of a polymerizable unit upon UV irradiation of a material without photoinitiator. Castellano et al.[186] assumed a decomposition process in TiO_2 amorphous gels involving in the reduction of trace impurities such as O_2, or electron recombination with trapped holes. Moreover, it was reported that an irradiation of coatings by UV light based on titanium (or zirconium) alkoxides and ß-diketones leads to a dissociation of chelate bonds in the coating causing a solubility change between the non-UV- and UV-exposed parts. Thus, patterned layers were obtained by this

photolysis process.[46,187].

Beside the UV irradiation of titanium clusters and amorphous TiO_2 gels, the effect of UV irradiation on materials based on titanium alkoxide co-condensed with organo-alkoxysilanes has been recently investigated. Hybrid coatings based on MEMO (71%) and titanium isopropoxide complexed with methacrylic acid ($(Ti(^iPrO)_4:MA)=(1:2)$) were UV-exposed with and without photoinitiator[99]. In both cases, an increase of the refractive index and of the degree of polymerization was observed. In the presence of the photoinitiator, the degree of polymerization jumped about 50%, and after 10 minutes a slower increase was reported, reaching a value close to 80 % after 60 and 120 min UV irradiation time with Irgacure 651 and Irgacure 1700, respectively. For coatings without photoinitiator, the degree of polymerization increased more slowly and continuously, reaching only 65% after 120 min UV irradiation. These effects have been attributed to a possible photocatalytic mechanism induced by titanium oxo-polymer species, i.e., small Ti-O-Ti species incorporated within the organic/inorganic network. Moreover, it was suggested that in the presence of a photoinitiator, the UV irradiation of these coatings leads to the combination of the photocatalytic and photopolymerization mechanisms. Recently, Luo et al.[100,188] patterned hybrid inorganic-organic materials based on MEMO and $Ti(OEt)_4$ by a UV lithography process, and they showed that for high TiO_2 concentrations, the coatings were patternable without adding a photoinitiator. They suggested that TiO_2 can initiate the polymerization upon UV light absorption. Moreover, additional UV irradiation was performed on a completely processed coating, and FT-IR spectroscopy has shown a decrease in the peak intensity corresponding to the vibrational modes of the organic compounds, a decrease in the intensity of the Si-O-C bending mode, and a significant increase of the peak of the Si-O-Si symmetric stretching mode. They have attributed the FT-IR results to the UV-induced decomposition of the organic components, and to a UV-induced densification of the hybrid network.

From the literature, the reactions which occur during the UV irradiation of materials based on titanium heteroelements introduced by the co-condensation of titanium alkoxide and organo-alkoxysilane can affect the efficiency of the organic polymerization. Until now, these reaction pathways are still not completely understood. Some authors suggest that the presence of titania can initiate the photopolymerization[99,100,188]. On the other hand, it has been also reported that titania induces the reduction of impurities, leading to a decomposition of the organic compounds, analogously to TiO_2 nano-crystals which were found to decompose the organic substances adsorbed on the titanium oxide surfaces[189]. In the following, a brief description of the photocatalytic activity of TiO_2 is described.

TiO_2 was shown to be an excellent material for photocatalytically breaking down organic compounds[190]. Among the three crystal structures anatase, rutile, and brookite, anatase has been reported to be the most photoactive phase[189,191]. The reaction mechanism of the TiO_2 photocatalysis is schematically depicted in Figure 32.

46
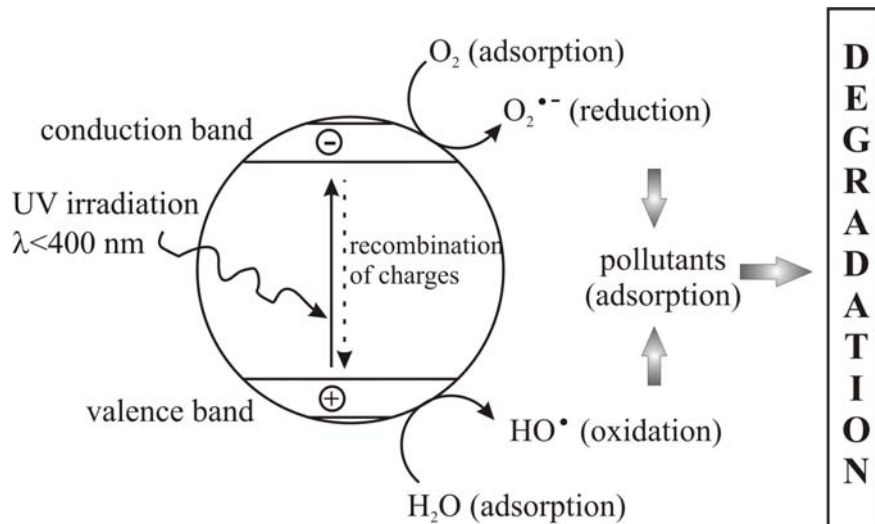
Figure 32 : Reaction mechanisms of TiO$_2$ photocatalysis[189,192].

The photocatalysis process can be for simplicity expressed by (Eq. 15)[192]:

$$\text{organic compound} \xrightarrow[\text{h}\nu \geq \text{E}_\text{g}]{\text{TiO}_2} \text{CO}_2 + \text{H}_2\text{O} + \text{mineral acid}$$

(Eq. 15)
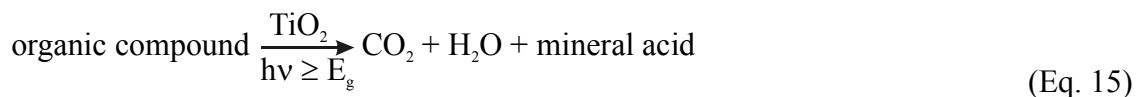
The absorption of photons with their energy equal or higher than bandgap leads to the generation of electrons (e$^-$) and holes (h$^+$) in the conduction and the valence band, respectively. Typically, the bandgaps of anatase and rutile were reported to be close to 3.2 and 3.0 eV, which corresponds to light wavelengths of 388 and 413 nm, respectively[191]. The oxidation of water molecules adsorbed at the surface of a film by the holes produces hydroxyl radicals (HO$^\bullet$). These radicals have a strong oxidizing power, and they can react with organic compounds, leading to free radicals which further react with oxygen, producing organic peroxyl radicals. The latter can participate in a chain reaction, leading to a complete degradation of organic compounds on a short time scale, where the organic compounds are converted into carbon dioxide and water[191] (cf., (Eq. 15)).

At the same time, the electrons generated in the conduction band (Figure 32) are used to reduce oxygen in the air, producing the superoxide radical anion (O$_2^{\bullet-}$). This is an effective oxygenation agent that attacks either surface adsorbed radicals and/or radical ions, leading to the production of carbon dioxide molecules. However, the detailed mechanism of the reaction of the photocatalytic process on the TiO$_2$ surface is still not completely clear[191,192].

2.3.2   Two-photon polymerization process

In the 2PP process, a droplet of a photosensitive resin is sandwiched between two glass substrates (cf., zoom in Figure 33). An immersion oil is used between the objective and the glass substrate. The sample is mounted into the instrument and then exposed to femtosecond laser pulses focused into the material's volume. With the tightly focused laser irradiation, the polymerization process can be initiated by two-photon absorption within the focal

volume[193,194], such that the energy of the molecule excitation is equal to the sum of the energies of the photons $E = h\nu_1 + h\nu_2$ [195]. Since the process of multi-photon absorption depends non-linearly on the light intensity, the interaction region is strictly limited to the focal volume, while in the outer focal regions the material stays unaffected. By moving the focus in x, y, and z direction, arbitrary 3D structures can be written. Then, the 3D structure is developed by dipping the material into an appropriate solvent also used in conventional UV lithography. For positive tone resist materials, the exposed part is dissolved in a developer, while for negative tone resists the non-UV-exposed part is removed by the developer. Since the photons used to excite the initiator have half of the nominal energy required to excite the absorbing material, it is possible to initiate the reaction at wavelengths, where the material is transparent to one-photon excitation. At the focus, the intensity is high enough and the excitation of two photons occurs[6].

The schematic representation of the experimental setup which was used for the fabrication of 3D structures in the framework of this thesis is shown in Figure 33[193,196]. A 100x immersion-oil microscope objective (Zeiss, **n**umerical **a**perture (NA) of 1.4) is used to focus laser pulses into the materials. 2PP is initiated by near-IR ultra-short laser pulses from a Ti:Sapphire oscillator. The central emission wavelength, repetition rate, and duration of the laser pulses were 780 nm, 94 MHz, and 120 fs. A **w**ave **p**late (WP) together with a polarizing **b**eam **s**plitter (BS) is used to attenuate the average power of the transmitted beam. An **a**cousto-**o**ptical **m**odulator (AOM) in combination with an aperture is used as a fast shutter. The beam is expanded by a telescope, and then coupled into x-y galvo scanner, whereas the x, y, z stage can also used for patterning the materials in 3D. The sample is mounted onto a 3D piezo stage for sample positioning in all directions, whereas x,y,z stage can also be used for patterning the materials in 3D. A **c**harge-**c**oupled **d**evice (CCD) camera placed behind the dichroic mirror is used for online monitoring of the 2PP process.
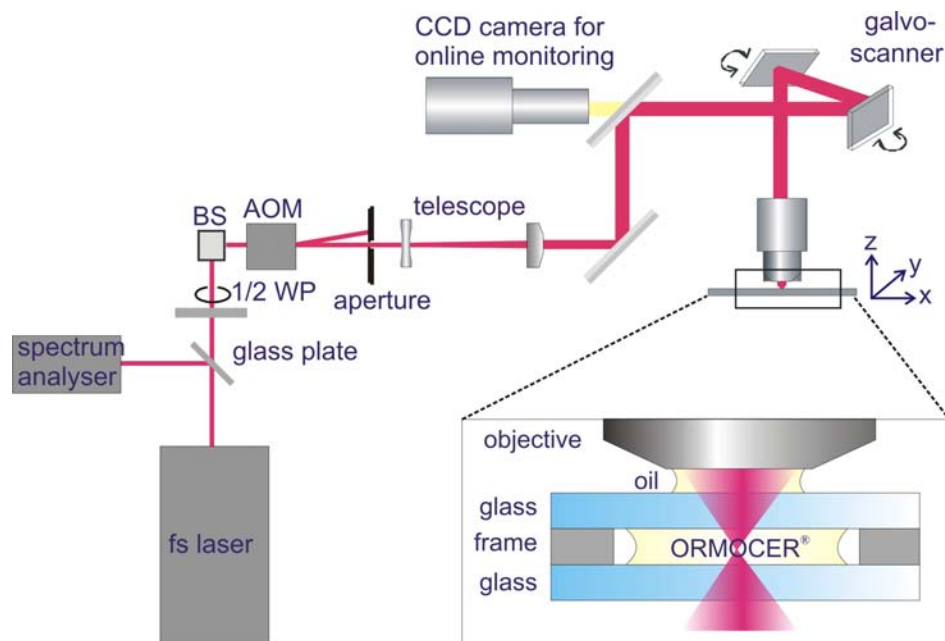
Figure 33 : Schematic sketch of the experimental setup with a zoom of the sample holder[193,196].

The 2PP process can generate arbitrary 3D structures, such as, for example, a Venus statue or a dragon, which were written using an ORMOCER® resin (Figure 34). The time taken to generate such 3D structures is correlated to the complexity of the 3D structures. For example, the Venus statue from Figure 34 was written in 5 minutes[19,77], since only the outer shell was irradiated.
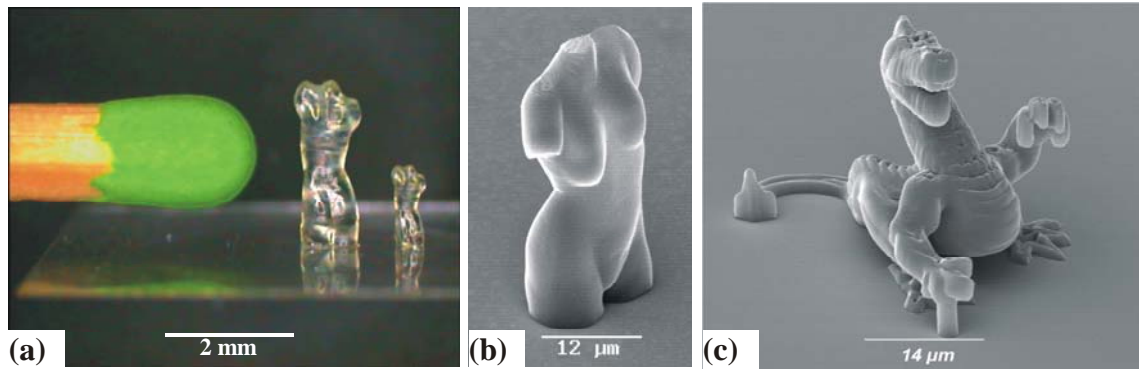
Figure 34: Example of structures generated in an ORMOCER® from (a) mm to (b) µm scale: Venus statue, and (c) microscopic dragon with 2PP using femtosecond laser pulses[19,77,197].

3D PC structures have been also written by 2PP. For example, Figure 35 shows a 3D PC structure generated by 2PP from an ORMOCER® resin in only one minute. The periodicity of the crystal is about 450 nm, while the individual rods are approximately 220 nm in diameter.
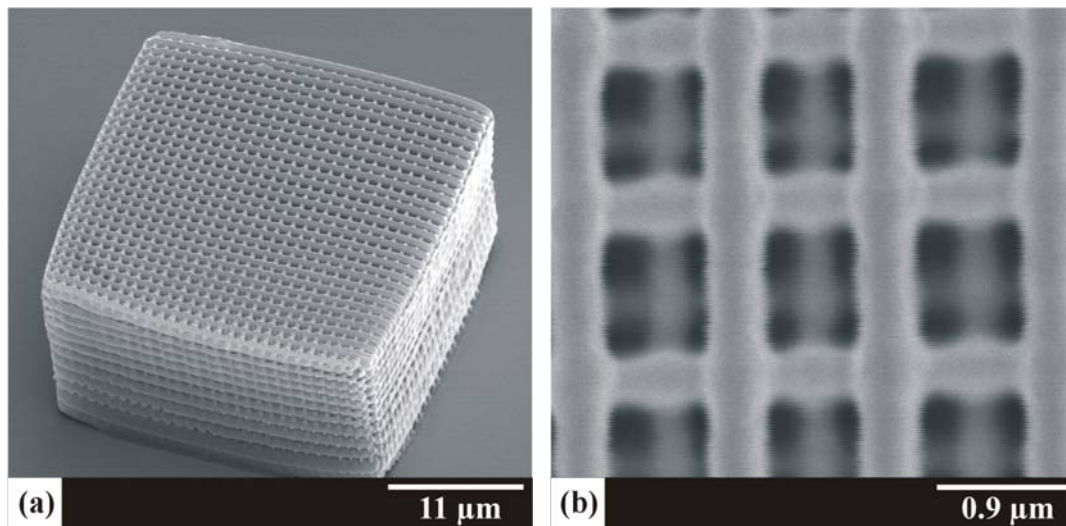
Figure 35 : SEM images of (a) a photonic crystal structure generated by 2PP in an ORMOCER®. (b) Zoom into the structure presented in (a), where up to 4 individual layers are clearly visible[193].

The structure obtained by the 2PP process depends on the laser parameters (pulse duration, wavelength, energy, repetition rate), material parameters (optical properties), and numerical aperture (NA) of the focusing objective[198]. The type of laser affects notably the resolution of the structure. For example, by decreasing the wavelength of the laser into the visible range

(Ar-ion laser or frequency doubled Nd-YAG laser) smaller 3D structures and higher resolution can be achieved[199]. Haske et al.[200] have reported nanoscale features as small as (65 ± 5) nm by using 520 nm femtosecond pulse excitation. Moreover, elliptical focal volumes are obtained with low NA objectives due to the confocal parameter which is much larger than the radius of the focal spot. On the other hand, with very high NA objectives, the focal volume becomes more symmetric[198]. Furthermore, in order to focus the laser into the volume of a liquid resin, the material has to be transparent in the near IR, especially at the laser wavelength[17].

The polymerization of the material can be initiated as soon as the density of the initiator radicals exceeds a certain concentration. From experiments by Serbin et al.[17], with UV light the lowest measured density of radicals required of ORMOCER® is approximately 0.25 wt %. This density depends on the two-photon absorption cross-section of the photoinitiator[17]. The efficiency of the photoinitiator is linked to its cross-section, which is expressed in Goeppert-Mayer (GM) units with $1 GM = 1 \times 10^{-50} cm^4$ s photon^{-1}. Unfortunately, the majority of known organic molecules has a very small value of non-linear absorption cross-sections, typically of $\sigma_2 \sim 1$ GM[195], and some commercially available UV-visible photoinitiators have even σ values on the order of more than 100 GM[201]. For example, the cross-sections of Irgacure 184, 369 and 819 (UV photoinitiator commercially available by CIBA) have been reported to be close to 23, 7, and < 4 GM at wavelengths of 246, 324, and 295 nm, respectively[202]. Thus, even with high-intensity pulsed laser illumination, the probability of exciting an molecule by simultaneous absorption of two photons remains inefficiently small[195]. The increase of the absorption cross-section could be achieved by an extension of the π-conjugated length, the introduction of electron-donating (D) and electron-accepting (A) groups at the chain termini, and throughout the conjugation sequence[195,199,201,203]. In the last decades, efforts have been made to prepare novel photoinitiators with high values of absorption cross-sections[195,199,203-206], where it is expected that larger cross-section values will allow one to lower the power and to enable shorter irradiation times, resulting in minimal optical damage to materials[199]. Besides, this will significantly increase the process window. For example, Cumpston et al.[203] reported a class of conjugated organic stilbene-based π-conjugated compounds that exhibit large cross-sections as high as 1250×10^{-50} GM at a wavelength of 448 nm, and enhance the two-photon sensitivity relative to conventional UV initiators[202]. Higher cross-section initiators (σ = 11 000 GM at 419 nm), have been reported by Drobizhev et al.[195] for a new molecule comprising 29 repeat units of 4,4'-bis(diphenylamino)stilbene chromophore.

3.   Experimental part

3.1   Methods and instrumentation

3.1.1   Nuclear magnetic resonance spectroscopy (NMR) in solution

^{1}H-, ^{13}C-, and ^{29}Si-NMR spectroscopy in solution was carried out at room temperature using a Bruker Avance DPX 400 NMR spectrometer with a 9.4 T magnetic field and equipped with a quaternary nuclear probe head. The resins were dissolved in deuterated solvents such as deuterochloroform ($CDCl_3$) or deuterated acetone (d6-acetone). The solutions were mixed with a small amount of **t**etra**m**ethyl**s**ilane (TMS) used as internal reference, and transferred into NMR sample glass tube of 5 mm in diameter and 178 mm in length. The detected chemical shifts are given in **p**arts **p**er **m**illion (ppm) referred to the TMS signal. Table 7 shows a selection of typical acquisition parameters in routine ^{1}H-, ^{13}C-, and ^{29}Si-NMR spectroscopy measurements.

Table 7: Typical parameters for routine solution NMR spectroscopy.

Parameters	^{1}H	^{13}C	^{29}Si
Frequency	400 MHz	101 MHz	79.5 MHz
Number of scans	64	1024	512
Delay time D1	1.00 s	2.00 s	30.0-60.0 s
Decoupling frequency	___	400 MHz	400 MHz

In some cases, due to the complexity of the mixture (e.g., the use of different silanes and titanium precursors), the number of scans was increased up to 2048 in order to optimize the signal-to-noise ratio.

Distortionless **e**nhancement by **p**olarization **t**ransfer (DEPT) ^{13}C-NMR spectra were also recorded giving additional information about the number of protons attached to the carbon atoms in the structure. DEPT-135 was used in this work. The signals of primary (CH_3) and tertiary (CH) carbons have positive intensity, the signals of secondary (CH_2) carbons have negative intensity, and quaternary carbon atoms (C) are not detected by DEPT.

Time-resolved ^{1}H-, ^{13}C-, and ^{29}Si-NMR spectra were obtained by sequential analysis of reaction mixtures at low temperatures. A small quantity of a sample (0.3 ml) was extracted from the mixture at pre-defined reaction times, and immediately frozen in liquid nitrogen in order to stop the reactions. For the NMR measurements, the samples were briefly allowed to liquefy at room temperature, and mixed to a chromium(III) acetylactetonate solution (30.3 mmol/L) and TMS (816 mmol/L) in $CDCl_3$. The addition of chromium(III) acetylacetonate has the advantage to considerably accelerate the relaxation of the exited nuclei cloud, and therefore to reduce the delay time D1 to 5-10 s delay between two pulses. The NMR measurements were performed at -20°C, and 200-500 pulses were applied for each spectrum employing a delay time of 10 s for the ^{29}Si nuclei.

In order to assign the ^{1}H-, ^{13}C-, and ^{29}Si-NMR peaks in the spectra, the notation style used during this work is reported in part ii.2.

3.1.2 ^{31}P solid-state Magic Angle Spinning NMR

^{31}P solid-state MAS NMR spectra were recorded at the University of Montpellier 2, with a Bruker Avance DPX300 spectrometer, using high power proton decoupling (flip angle 45°C, and recycling delay 10 s).

3.1.3 Fourier-transform infrared spectroscopy

Fourier-transform infrared (FT-IR) spectra were recorded with a Nicolet Magna-IR 760 FT-IR spectrometer in absorbance, with a resolution of 4 cm^{-1}. Liquid samples were analyzed as films placed between two sodium chloride crystal plates, while solid samples were mixed directly with potassium bromide (KBr) and analyzed on pellets.

3.1.4 Micro-Raman spectroscopy

Micro-Raman spectra of coatings were measured by a confocal Raman spectrometer (Model LabRam, Horiba). The samples were excited at 632.8 nm with a He-Ne laser through a microscope objective (x100). Raman spectra were obtained with the following conditions: confocal hole: 200, slit: 100. The irradiation and accumulation times as well as the use of a filter were optimized for each sample.

The degree of organic polymerization DC (already mentioned in section 2.3.1) was calculated by measuring the decrease of the area of the peak attributed to the vibrational bands of the C=C stretching mode (A_{uv}, cf., (Eq. 16)) relative to its area on the non-exposed coating ($A_{no\ uv}$, cf., (Eq. 16)).

This method which was well described by Shin et al.[207] and commonly used in order to study the organic polymerization[178,179,208], is described in the following. After a baseline correction of the spectra, they were analyzed using a curve fitting program (LabSpec 3.01c from Dilor), where each vibrational band is a mixture of Lorentzian and Gaussian peak shape. After fixing the position of the peaks, the program was run to optimize the calculation of Lorentzian and Gaussian combination from the experimental spectra. By comparing the area of the vibrational bands of the polymerizable C=C stretching mode to the area of the vibrational band of an internal standard, the degree of polymerization was estimated from (Eq. 16).

$$DC(\%) = 100 \times \left(1 - \frac{A_{uv}}{A_{no\ uv}}\right),$$

(Eq. 16)

where $A_{no\ uv}$ and A_{uv} are the peak areas of the vibrational bands of the polymerizable C=C stretching mode of the non-UV-exposed and UV-exposed coating, respectively. As internal standard reference for these experiments, the vibrational mode from a C=C stretching mode from the phenyl groups was used since they have been reported to be not affected by the UV irradiation.

Since the DC values were calculated in order to study how the UV exposure time affects the polymerization process, most of the coatings characterized by μ-Raman spectroscopy were not developed. Thus, in order to avoid measurements in the inhibition layer (cf., chapter 2.3.1), spectra were recorded at the surface of the substrate wafers, i.e., by maximizing the intensity of the peaks attributed to the silicon wafer as well as the signals detected from the coating. As the signal recorded corresponds to 3 μm depth, measurements were preferably performed on coatings thicker than 3 μm.

3.1.5   Ultraviolet, visible, and near-infrared spectroscopy

Ultraviolet, visible, and near-infrared (UV-VIS-NIR) spectroscopy was used in order to determine the refractive index and thickness of the coatings.

Transmission spectra of coatings and Borofloat® glass substrates purchased from Schott GmbH were recorded on a Shimadzu UV-3100 spectrophotometer in the wavelength regime between 200 and 2500 nm. The accuracy of the measurement is ± 0.3 % in transmission. From the interference fringes of the transmission spectra of the coatings, the thickness of the coatings as well as the refractive indices at minima of these fringes were calculated using Swanepoel's technique[172,174] (cf., chapter 2.2.2.4).

UV-VIS-NIR spectroscopy was also used in order to measure the optical losses of the resins. The optical losses of the resins were measured in Hellma® 10 mm fused silica vessel. The samples were placed in a Shimadzu UV-3100 spectrophotometer. Prior the measurements, the resins were mixed with a solvent (50% resin/50%solvent), and filtered through a 0.2 μm filter. As reference, the filtered solvent was measured in a 5 mm fused silica vessel. For some resins, the optical losses could not be measured since the dilution ratio has led to saturated solutions,. The losses were specified in dB/cm (± 0.080 dB/cm).

3.1.6   Ellipsometry

The dispersion curve of the refractive index was measured at the Joanneum Research Gesellschaft Institute for Nanostructured Materials and Photonics (Austria) with a J.A.Woollam Comp. Inc ellipsometer (modell VASE variable angle spectroscopic ellipsometer). The Cauchy function (Eq. 17) was used to model the measurement.

$$n(\lambda) = a + \frac{b}{\lambda^2} + \frac{c}{\lambda^4} \quad , \tag{Eq. 17}$$

where λ is the wavelength of the light, and a, b, and c are material dependent specific constants which are determined from a series of algorithms in order to model the measured quantities ψ and Δ obtained from the ellipsometry measurement.

3.1.7   X-ray diffraction

X-ray diffraction (XRD) powder diagrams were recorded on a PW1730 Philips spectrometer. As X-ray source, the copper K_α line (λ = 1.5406 Å) was used. The high voltage of the instrument is set to 45 kV for an intensity of 30 mA. The X-ray detector is a scintillation counter, which moves in order to detect the X-rays reflected from the sample at different angle (theta-theta system). The sample is deposited onto a sample carrier made of steel covered with sapphire, and is analyzed between 2 and 80°. The angle step has been set to

0.02° for a delay time of 1s. The analysis of the data was carried out using the DMA software provided by Wasserman.

3.1.8 Profilometery

The film thickness was measured by a stylus profilometer Alpha Step 200 from the Tencor Instrument, where a stylus is moved across a surface layer and the substrate, the thickness of the layer is measured.

3.1.9 Scanning-electron microscopy

Scanning electron microscopy (SEM) analyses have been performed on a Hitachi S-800 Field Emission Scanning Electron Microscope. Imaging was carried out at high voltages between 6 and 25 kV, and a secondary electron detector has been employed. In order to avoid charging effects, the samples were coated with gold by a sputter-deposition process.

3.1.10 Optical Microscopy

A light microscope (model LEICAINM 20, magnification x5, x20, x50) was used to image the coatings prior to other experiments. In particular, light microscopy was used subsequently to the UV lithography process in order to determine the structural resolution.

3.2 Syntheses of inorganic-organic hybrid materials

The procedures used to synthesize the inorganic-organic hybrid resins in the framework of this thesis are described in the following paragraphs, and are divided into four parts: 1) solvents and chemicals used, and the syntheses of resins based on 2) organo-alkoxysilanes and titanium alkoxides, 3) organo-alkoxysilanes and titanium alkoxides complexed with CL in order to decrease the chemical reactivity of titanium precursor, and 4) titanium alkoxides and organo-alkoxysilanes which were partially and completely replaced by phosphonic acids.

3.2.1 Solvents and chemicals

Commercially available reactants and solvents were purchased from chemical companies (Gelest, Landcaster, Sigma-Aldrich) and employed for syntheses without further purification. All the solvents were dried with molecular sieves, and the water content was controlled by Karl-Fischer titration. The molecular sieves were previously dried in an oven at 250°C for 48h under vacuum in order to avoid water contamination of the solvents.

Styryl**e**thyl**trim**eth**oxys**ilane (SETMS) and [3-(**me**thacryloyloxy)propyl]tri**m**eth**oxy**silane MEMO were purchased from Gelest, titanium precursors, **p**henyl**p**hosphonic **a**cid (PPA), and **di**phenyl**p**hosphinic **a**cid (DPPA) from Sigma-Aldrich, and **di**phenylsilane**d**iol (DPD) was synthesized directly in the competence Team "Hybrid Polymers (ORMOCER®s) for Microsystems and Micromedicine" at the Fraunhofer ISC. Deuterated solvents for NMR experiments were purchased from Deutero, and the UV photoinitiator Irgacure® 369 was provided by Ciba-Geigy. **P**ara-**v**inyl**b**enzyl**p**hosphonic **a**cid (p-VBPA) was kindly synthesized by Dr. H. Mutin and Dr G. Gerrero from the University of

Montpellier 2 (UMR 5637, 34095 MONTPELLIER 5, France).

3.2.2   Resins synthesized without complexing ligands

3.2.2.1 Resins synthesized with one organo-alkoxysilane

Composition of resins PD49, PD79, and PD113:

		(1) 33 mol-% MEMO	9.93 g	(0.04 mol)
		(2) 67 mol-% $Ti(OEt)_4$	18.27 g	(0.08 mol)
PD113	→	(3) Water (HCl 0.01 M aq. sol.)	1.98 g	(0.11 mol), r = 0.5
PD49	→	(3) Water (HCl 2 M aq. sol.)	2.13 g	(0.11 mol), r = 0.5
PD79	→	(3) Water (HCl 12 M aq. sol.)	3.14 g	(0.11 mol), r = 0.5

$Ti(OEt)_4$ (2) is added drop by drop under vigorous stirring to MEMO (1), leading to a viscous and milky solution. Water and hydrochloric acid (3) is slowly added to the mixture. After a reflux at 65°C for 3 days, the viscous milky solution becomes a clear yellow viscous solution. It has to be mentioned that clear transparent solutions are only obtained, if the ratio r_w is below or equal to 0.5. If r is above 0.5, the resulting material is non-transparent which might be due to phase separation, resulting in the formation of large particles, clusters, or agglomeration thereof. Volatile compounds were removed under reduced pressure (40 °C, 1 mbar), and a solid material is obtained. This can be dissolved for further processing.

Composition of resins PD52 and PD60:

		(1) 33 mol-% SETMS	10.71 g	(0.04 mol)
		(2) 67 mol-% $Ti(OEt)_4$	18.37 g	(0.08 mol)
PD52	→	(3) Water (HCl 2 M aq. sol.)	2.13 g	(0.11 mol), r = 0.5
PD60	→	(3) Water (HCl 12 M aq. sol.)	3.14 g	(0.11 mol), r = 0.5

SETMS (1) is mixed with $Ti(OEt)_4$ (2), leading to a milky solution. Then, HCl (3) is dropped into the mixture, the milky solution becomes opaque and slightly yellow. After a reflux step at 65°C for three days, a yellow-orange clear solution is obtained. Volatile compounds are removed under reduced pressure (40°C, 1 mbar), leading to an orange clear viscous resin.

Composition of resin PD77:

	(1) 33 mol-% SETMS	10.71 g	(0.04 mol)
	(2) 67 mol-% $Ti(OMe)_4$	13.76 g	(0.08 mol)
	(3) Water (HCl 12 M aq. sol.)	3.14 g	(0.11 mol), r = 0.5
	Solvent: acetonitrile	15 g	

To a solution of $Ti(OMe)_4$ (2) and SETMS (1) in acetonitril, HCl (3) is added under stirring, leading to a milky solution. A reflux step at 70°C is carried out for 3 days, and an opaque orange solution is obtained. After settling the solution, two phases are obtained: a white

precipitate, and a clear orange phase above. The volatile compounds are removed from the clear orange solution under reduce pressure (40 °C, 1 mbar). An orange clear solid resin is obtained.

Composition of resin PD56:

(1)	10 mol-% SETMS	3.19 g	(0.012 mol)
(2)	90 mol-% Ti(OEt)$_4$	24.64 g	(0.107 mol)
(3)	Water (HCl 12 M aq. sol.)	3.31 g	(0.116 mol), r = 0.5

Ti(OEt)$_4$ (2) is slowly added in a dry argon atmosphere to SETMS (1), leading to a slightly yellow milky mixture. The latter is cooled in an ice bath. HCl (3) is dropped into the solution, which becomes viscous. After one hour reflux at 65°C, a clear fluid yellow solution is obtained. The reflux step was stopped, when the Karl Fischer titration showed that all water is consumed, typically taking place after four days. The volatile compounds formed during the reaction were removed under reduced pressure (40°C, 1 mbar), and a clear orange resin was obtained. The resin is very sensitive to air moisture. So the product is hard exactly to reproduce.

3.2.2.2 Resins synthesized with two organo-alkoxysilanes

Composition of resins PD5, PD92, and PD114:

	(1)	17 mol-% MEMO	5.28 g	(0.02126 mol)
	(2)	50 mol-% DPD	13.52 g	(0.0625 mol)
PD92 **PD5** →	(3)	33 mol-% Ti(OEt)$_4$	9.41 g	(0.04125 mol)
PD114 →	(3)	33 mol-%TEOS	9.41 g	(0.04125 mol)
	(4)	TBAF; 3H$_2$O	0.0395 g (0.125 mmol)	
PD92 **PD114** →	(5)	Water	450 µL	(0.025 mol), r = 0.5
PD5		Solvent: cyclopentanone	29 g	
PD92 **PD114** →		Solvent: THF	25 g	

At room temperature (20°C), MEMO (1) is mixed to a blend based on DPD (2) and solvent. After 15 min stirring, TBAF (4) and water (5) are added (water is added for PD92 and PD114, while no water is used for the synthesis of resin PD5). The solution is then stirred for four hours. Subsequently, Ti(OEt)$_4$ (3) is slowly added in an argon atmosphere. The blend was stirred during 3 (PD5) and 6 days (PD92 and PD114), respectively, leading to an orange and clear solution (PD5) or clear and colorless solutions (PD92 and PD114). Volatile compounds are removed under reduced pressure (40 °C, 1 mbar). A viscous dark orange-brown resin (PD5) or a clear and gel like solid (PD92 and PD114) were obtained.

Composition of resins PD51 and PD109:

	(1) 17 mol-% SETMS	5.66 g	(0.02126 mol)
	(2) 50 mol-% DPD	13.52 g	(0.0625 mol)
	(3) 33 mol-% Ti(OEt)$_4$	9.41 g	(0.04125mol)
	(4) TBAF, 3H$_2$O	0.0395 g (0.125 mmol)	
PD109 →	(5) Water	450 μL (0.025 mol), r = 0.5	
PD51 →	Solvent: cyclopentanone	29 g	
PD109 →	Solvent: THF	25 g	

To a mixture of SETMS (1), DPD (2), and a solvent, TBAF (4) and water are added (water is only used for PD109). After four hours stirring, Ti(OEt)$_4$ (3) is slowly added in an argon atmosphere, leading to a clear orange solution. The volatile components are removed under reduced pressure (40 °C, 1 mbar), and a clear dark orange-brown viscous resin is obtained.

3.2.3 Complexed titanium alkoxide and organo-alkoxysilanes-based resins

Composition of resin PD-CL1:

(1) 55 mol-% DPD	1.3314 g	(6.15 mmol)
(2) 20 mol-% MEMO	0.5603 g	(2.26 mmol)
(3) 25 mol-% Ti$_6$O$_4$(C$_6$H$_5$COO)$_8$(OPr)$_8$	5.0 g	(2.79 mmol)
Solvent: THF	10 g	

DPD (1) which was dissolved in THF is mixed to MEMO (2). Then, the titanium oxo-clusters (3) are added to the blend, and a reflux step was carried out for 48 hours. After the reflux step, the solvent and the volatile compounds are removed under reduced pressure (40 °C, 1 mbar). A pale yellow resin is obtained.

Composition of resin PD-CL76:

(1) 45 mol-% Ti(OEt)$_4$	22.14 g	(0.097 mol)
(2) 45 mol-% ACAC	9.71 g	(0.097 mol)
(3) 10 mol-% SETMS	5.75 g	(0.0215 mol)
(4) Water (HCl 12 M aq. sol.)	3.23 g	(0.113 mol), r = 0.5

Ti(OEt)$_4$ (1) is mixed to **ac**etyl**ac**etone (ACAC (2)), and stirred for one day. FT-IR spectroscopy measurements of the mixture show that Ti(OEt)$_4$ is complexed with ACAC due to the absence of the vibrational mode at 1711 cm^{-1} which characterizes the stretching vibrational mode of the C=O bond from free ACAC. After elimination of 5 g of ethanol (formed in the complexation reaction of Ti(OEt)$_4$) under reduced pressure, the titanate complexed precursor is mixed to SETMS (3). A clear yellow solution is obtained. Subsequently, 12M HCl (4) is added to the mixture as catalyst. A reflux step was performed for 11 days. The water content was determined by Karl Fisher titration which revealed that the hydrolysis reaction takes place very slowly despite the high concentration of the catalyst.

The volatile compounds formed during the reaction were removed under reduced pressure (40 °C, 1 mbar), and an orange and transparent solid material was obtained, which can be dissolved in solution for further processing.

3.2.4   Resins based on organophosphorus precursors

Composition of resin PD-P1 :

(1)	17 mol-% PPA	1.0 g	(6.33 mmol)
(2)	33 mol-% Ti(OEt)$_4$	2.80 g	(12.27 mmol)
(3)	50 mol-% DPD	4.02 g	(18.60 mmol)
	Solvent: THF	20 g	

Ti(OEt)$_4$ (2) is slowly added to a solution of PPA (1) and THF, leading to the formation of a milky, gel. It was not possible to dissolve it by stirring or by heating it up to 60°C.

Composition of resins PD-P4 and PD-P6:

PD-P4 →	(1)	17 mol-% PPA	1.0 g	(6.33 mmol)
PD-P6				
	(2)	33 mol-% Ti(^{i}PrO)$_4$	3.49 g	(12.27 mmol)
PD-P4 →	(3)	50 mol-% DPD	4.02 g	(18.60 mmol)
PD-P6 →	(3)	50 mol-% DPPA	4.06 g	(18.60 mmol)
		Solvent: THF	20g	

Ti(^{i}PrO)$_4$ (2) is slowly added in an argon atmosphere to a solution based on THF and PPA (1), leading to the formation of a milky gel which became a clear slightly yellow solution after three hours stirring. The blend is then stirred for 5 hours, and (3) (DPPA for PD-P6 and DPD for PD-P4) is added. A clear solution is obtained after five minutes. The solution is kept under stirring for two days leading to a viscous solution. After that, the volatile compounds are removed under reduced pressure (40°C, 1 mbar). A solid resin material is obtained, which can be further diluted for processing.

Composition of resin PD-P7:

(1)	17 mol-% p-VBPA	1.25 g	(6.33 mmol)
(2)	33 mol-% Ti(^{i}PrO)$_4$	3.49 g	(12.27 mmol)
(3)	50 mol-% DPD	4.02 g	(18.60 mmol)
	Solvent: THF	20g	

To a solution based on THF and p-VBPA (1), Ti(^{i}PrO)$_4$ (2) is slowly added in an argon atmosphere, leading to the formation of a milky gel which became a clear slightly yellow solution after three hours stirring. After further 5 hours stirring, DPD (3) is added, leading to a clear solution obtained after five minutes. The solution is kept under stirring for two days, leading to a viscous solution. Then, the volatile compounds are removed under reduced

pressure (40°C, 1 mbar). A solid resin material is obtained, which can be further diluted for processing.

3.3 Technological processing

3.3.1 Coatings without UV exposure

Since for most of the resins synthesized in this work solid resin were obtained, the refractive indices of the materials were determined on coatings. The resins were dissolved in an appropriate solvent, filtered, and then spin-coated onto Borofloat® glass substrates with a spin-coater. Due to the high content of titanium in the resins, crack-free coatings were only obtained for thin films (i.e., thicknesses lower than 5 μm). Thus, their refractive indices could not be determined by the prism coupler method. The refractive indices were determined using transmission spectroscopy (UV-VIS) by calculation with the Swanepoel's technique (cf., chapter 2.2.2.4) which required homogenous and highly transparent coatings. Thus, the preparation of the resin such as the solvent used to dissolve the resin, and its dilution rate, but also parameters such as the spin speed and duration had to be individually adapted to the resins, since these parameters can affect the homogeneity of the coatings. The coatings were prepared in a clean room (class 100 to 1000).

The evolution of the refractive index with the curing temperature was also investigated. Suitable curing parameters such as, for example, the annealing rate, the annealing temperature, and its duration were investigated in order to obtain crack-free coatings.

In order to follow the effect of the refractive index with the annealing temperature and without any UV processing, the coatings were cured up to 150°C for three hours, with a heating rate fixed at 5°C/min. This annealing process is reported in the following tables as "directly cured at 150°C". However, in some cases, this annealing process has led to cracks in the coating. Thus, another annealing process had to be performed: a coating was prepared and then cured for different temperatures for one and the same coated sample, beginning with 50°C and the increasing of the temperature stepwise (50°C steps) up to 450°C, where each temperature was reached with an annealing rate fixed at 5°C/min, and kept for 3 hours. However, it has to be mentioned that the temperature treatment was performed on the same sample (i.e., adding time and different temperature levels). This annealing process was used for most of the coatings. In most of the cases, cracks are obtained if the coatings were directly cured at 150°C during three hours, even at a low annealing rate. However, by the modified annealing process described above, for most of the sample, no cracks were observed.

In the following, the parameters which were applied for the preparation of solutions and coatings are described in different tables. For each resin, a solution number, the solvent used for the dilution, the dilution rate notified as weight of resin: weight of solvent, and a coating number are given to identify the individually prepared samples in chapter 3.3. The refractive indices (n) and the thickness of the coatings (d) are reported. As spin speed, 2000 rpm for 40s was used, unless otherwise stated.

Table 8: Parameters used for the preparation of solutions and coatings of resin **PD5**.

Solution n°	Solvent	Dil. rate	Soating n°	Refractive indices (n) and thickness (d)
PD241104/1	PA	0.93 :1	241104/1	not cured n= 1.58 at 1550 nm (d = 4600 nm) cured at 150°C n= 1.60 at 1460 nm (d = 3430 nm)

Table 9: Parameters used for the preparation of solutions and coatings of resin **PD49**.

Solution n°	Solvent	Dil. rate	Coating n°	Refractive indices (n) and thickness (d)
PD300304/1	PA	2.71:1	300304/1	directly cured at 150°C n = 1.62 at 690 nm (d = 1200 nm) n = 1.61 at 1080 nm n = 1.60 at 1500 nm

Table 10: Parameters used for the preparation of solutions and coatings of resin **PD51**.

Solution n°	Solvent	Dil. rate	Coating n°	Refractive indices (n) and thickness (d)
PD070704/1	PA	0.94:1	070704/3	directly cured at 150°C n = 1.61 at 950 nm (d = 2840 nm) n = 1.60 at 1070 nm

Table 11: Parameters used for the preparation of solutions and coatings of resin **PD52**.

Solution n°	Solvent	Dil. rate	Coating n°	Refractive indices (n) and thickness (d)
PD120704/1	PA	0.57:1	120704/1	directly cured at 150°C n = 1.70 at 920 nm (d = 950 nm) n = 1.67 at 1290 nm

Table 12: Parameters used for the preparation of solutions and coatings of resin **PD56**.

Solution n°	Solvent	Dil. rate	Coating n°	Refractive indices (n) and thickness (d)
PD290704/1	PA	0.58:1	040804/2	directly cured at 150°C n = 1.84 at 1820 nm (d = 250 nm)

Table 13: Parameters used for the preparation of solutions and the coatings of resin **PD60**.

Solution n°	Solvent	Dil. rate	Coating n°	Refractive indices (n) and thickness (d)
PD071204/2	PA	(0.62:1)	071204/2	not cured not possible to determine n, the coating was not transparent enough
PD131204/1	PA	(0.25:1)	131204/1	directly cured at 150°C n = 1.70 at 940 nm (d = 410 nm)

Table 14: Parameters used for the preparation of solutions and coatings of resin **PD77**.

Solution n°	Solvent	Dil. rate	Coating n°	Refractive indices (n) and thickness (d)
PD150305/1	THF	0.27:1	150305/1	w = 1000 rpm (40 s) not cured n = 1.61 at 1000 nm (d = 1700 nm) n = 1.60 at 1220 nm n = 1.61 at 1570 nm cured at 100°C n = 1.66 at 1000 nm (d = 1370 nm) n = 1.64 at 1300 nm cured at 150°C n = 1.70 at 930 nm (d = 1230 nm) n = 1.67 at 1200 nm n = 1.68 at 1680 nm cured at 200°C n = 1.70 at 1620 nm (d = 1200 nm) cured at 250°C n = 1.72 at 1550 nm (d = 1120 nm) cured at 300°C n = 1.75 at 1400 nm (d = 1000 nm) cured at 350°C n = 1.75 at 1160 nm (d = 830 nm) n = 1.77 at 1950 nm cured at 400°C n = 1.77 at 860 nm (d = 600 nm) n = 1.73 at 1470 nm cured at 450°C n = 1.78 at 824 nm (d = 580 nm) n = 1.75 at 1360 nm up to 450°C coating cracked

Table 15: Parameters used for the preparation of solutions and coatings of resin **PD79**.

Solution n°	Solvent	Dil. rate	Coating n°	Refractive indices (n) and thickness (d)
PD100105/2	BU	0.3:1	110105/2	directly cured at 150°C n = 1.67 at 1170 nm (d = 520 nm) cured at 200°C cracks
PD100105/5	EtOH	0.3:1	110105/5	directly cured at 150°C n = 1.69 at 700 nm (d = 500 nm) n = 1.68 at 1130 nm cured at 200°C n = 1.71 at 1090 nm (d = 480 nm) cured at 250°C absorbant coating, n not calculable

Table 16: Parameters used for the preparation of solutions and coatings of resin **PD92**.

Solution n°	Solvent	Dil. rate	Coating n°	Refractive indices (n) and thickness (d)
PD030605/2	THF	0.27:1	070605/1	w = 1000 rpm (40 s) not cured n = 1.60 at 950 nm (d = 1930 nm) n = 1.59 at 1120 nm cured at 150°C n = 1.62 at 960 nm (d = 1630 nm) n = 1.60 at 1170 and 1500 nm cured at 200°C n = 1.61 at 1040 nm (d = 1450 nm) cured at 250°C coating cracked

Table 17: Parameters used for the preparation of solutions and coatings of resin **PD109**.

Solution n°	Solvent	Dil. rate	Coating n°	Refractive indices (n) and thickness (d)
PD190106/1	THF	0.27:1	190106/1	w = 1000 rpm (40 s) not cured n = 1.61 at 940 nm (d = 1900 nm) n = 1.60 at 1110 nm cured at 100°C n = 1.62 at 1000 nm (d = 1700 nm) n = 1.60 at 1215 nm cured at 150°C n= 1.63 at 930 nm (d=1580 nm) n= 1.62 at 1240 nm cured at 200°C n = 1.62 at 1000 nm (d = 1400 nm) cured at 300°C n = 1.58 at 1220 nm (d = 960 nm)

Table 18: Parameters used for the preparation of solutions and coatings of resin **PD-CL1**.

Solution n°	Solvent	Dil. rate	Coating n°	Refractive indices (n) and thickness (d)
CL160805/1	toluene	0.25:1	160805/1	not cured n = 1.60 at 1520 nm (d = 1660 nm) cured at 50°C n = 1.63 at 920 nm (d = 1570 nm) n = 1.60 at 1125 nm cured at 100°C n = 1.63 at 1050 nm (d = 1500 nm) cured at 150°C coating cracked

Table 19: Parameters used for the preparation of solutions and coatings of resin **PD-P4**.

Solution n°	Solvent	Dil. rate	Coating n°	Refractive indices (n) and thickness (d)
P270306/1	THF	0.31:1	270306/1	not cured n = 1.61 at 980 nm (d = 1370 nm)

Table 20: Parameters used for the preparation of solutions and coatings of resin **PD-P6**.

Solution n°	Solvent	Dil. rate	Coating n°	Refractive indices (n) and thickness (d)
P270306/2	THF	0.33:1	280306/2	transparent blurred coating

Table 21: Parameters used for the preparation of solutions and the coatings of resin **PD-P7**.

Solution n°	Solvent	Dil. rate	Coating n°	Refractive indices (n) and thickness (d)
P040406/1	THF	0.27:1	040406/1	not cured n = 1.64 at 580 and 680nm (d = 1150 nm) n = 1.62 at 1065 nm

3.3.2 Coatings with UV exposure

The resins were patterned via the UV lithography process. They were diluted in a suitable solvent, and mixed with a photo-initiator (Irgacure® 369) under yellow light. The absorption spectrum of Irgacure® 369 in acetonitrile is shown in Figure 36.
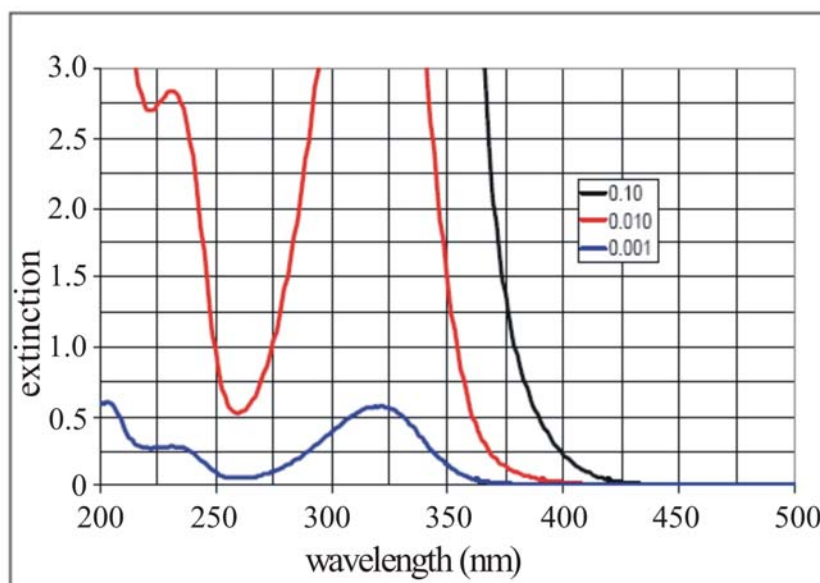

Figure 36: Absorption spectrum of Irgacure® 369 dissolved in acetonitrile at different concentrations, namely 0.1, 0.01, and 0.001 wt.-%[209].

The concentration of Irgacure® 369 was calculated in wt.-% with respect to the weight of the resin. Between 1 and 3 wt.-% initiator were introduced into the resins. These solutions were stirred 24 hours and then filtered through 0.2 µm filter. The resulting mixtures were spin-

coated onto p-Si(100) wafers or Borofloat® glass substrates. For some cases, the substrate surfaces were treated first by spin-coating a silanization solution in order to improve the adhesion between substrate and coating. Typically, this silanization solution is based on hydrolyzed MEMO highly diluted in isopropanol. This treatment is applied depending on the nature of the substrate and the ORMOCER® resin. However, no adhesion improvement was observed with this procedure, and a new surface treatment based on partially hydrolyzed Ti(^{i}PrO)$_4$ complexed with methacrylic acid and highly diluted in isopropanol was developed and employed for some resins. After this optional treatment, the formulation based on resin, solvent, and photo-initiator is spin-coated onto the substrates. Then, a prebake step was performed in order to already remove diluting solvents. After cooling down, the coating was UV-irradiated through a mask with a mask aligner (Karl Süss, MA 6, power density 17 mW/cm^2, lamp spectrum depicted in Annex 3), followed by a post-exposure bake. Finally, the patterned structures were developed by removing the non-exposed areas by dipping the coating into a suitable solvent. A schematic sketch of the processing which shows the different steps is given in Figure 27 (chapter 2.3.1).

The preparation of the different resins, the coating and processing conditions are summarized in the following tables (ordered by resin **id**endification numbers (ID)). These tables of solution preparation summarize the solution number, the used solvent, the dilution rate notified in weight (resin : solvent), and the concentration of the photo-initiator ([I]) in wt.-%. In some cases, the resins were synthesized several times, and in order to distinguish the different batches a letter was added to the resin ID (for example, PD5b is the resin PD5, and batch b). Each table of solution preparation is followed by a table, where the processing conditions are reported. These tables summarize the coating numbers, the spin speed (w) for 40 s, the temperature of the pre- and post-exposure bake (Δ_1 and Δ_2, respectively), whose durations were fixed to 1 min, the UV exposure time (t_{UV}), the solvent (S) used as developer, and remarks. The development times were fixed to 30 s for most of cases. If longer or shorter development times were used, it is separately notified in the remarks column. p-Si(100) wafers were always used as substrates, unless otherwise stated in the remarks column.

Table 22: Solution preparation of resin **PD49**.

Solution n°	Solvent	Dil. rate	[I] (wt.-%)
PD310304/1	PA	0.57:1	1.75

Table 23: Processing conditions of solution **PD310304/1** (Table 22, **PD49**).

Coating n°	w (rpm)	Δ_1 (s)	t_{UV} (s)	Δ_2 (s)	S	Remarks
310304/1	3000	——	180	——	MP	no surface treatment
310304/2	3000	40	180	——	MP	no surface treatment
310304/3	3000	——	180	——	MP	surface treatment: silanization
310304/4	3000	40	30	——	MP	no surface treatment

Table 24: Solution preparation of resin **PD5b**.

Solution n°	Solvent	Dil. rate	[I] (wt.-%)
PD090104/1	PA	0.9:1	1.5

Table 25: Processing conditions of solution **PD090104/1** (Table 24, **PD5b**).

Coating n°	w (rpm)	Δ_1 (s)	t_{UV} (s)	Δ_2 (s)	S	Remarks
171203/4	4000	80°C	30	80	MP	coating removed by development solvent
181203/2	4000	110	30	110	MP	residues in the non-UV-exposed areas
090104/1	4000	110	180	—	MP	for measurement of the refractive index
220104/1a	4000	110	30	—	MP	very thin layer, d = 170 nm
220104/1b	4000	110	30	—	toluol	coating removed by development solvent
220104/2a	4000	110	60	—	MP	d = 540 nm
220104/3a	4000	110	120	—	MP	d = 760 nm
220104/3b	4000	110	120	—	toluol	d = 180 nm
220104/4	4000	110	120	—	MP	surface treatment: silanization d = 760 nm residues in the non-UV-exposed areas
230104/4	4000	110	240	—	MP	d = 970 nm
270104/1a	4000	110	600	—	MP	d = 1150 nm
090204/2	4000	110	180	—	MP	Borofloat® glass substrate, d = 1.10 μm

Table 26: Solution preparation of resin **PD5j**.

Solution n°	Solvent	Dil. rate	[I] (wt.-%)
PD231104/1	PA	0.9:1	1.5

Table 27: Processing conditions of solution **PD231104/1** (Table 26, **PD5j**).

Coating n°	w (rpm)	Δ_1 (s)	t_{UV} (s)	Δ_2 (s)	S	Remarks
251104/1	4000	110	120	—	MP	residues in the non-UV-exposed areas
251104/2	4000	80	120	—	MP	non-UV-exposed removed

Table 28: Solution preparation of resin **PD77**.

Solution n°	Solvent	Dil. rate	[I] (wt.-%)
PD251104/1	THF	0.27:1	3.5

Table 29: Processing conditions of solution **PD251104/1** (Table 28, **PD77**).

Coating n°	w (rpm)	Δ_1 (s)	t_{UV} (s)	Δ_2 (s)	S	Remarks
291104/1	1000	60	120	—	MP	residues in the non-UV-exposed areas
291104/2	1000	40	120	—	MP	residues in the non-UV-exposed areas
291104/3	1000	—	120	—	MP	coating delaminated around the vias, d = 990 nm
291104/7	1000	—	120	—	MP	1 min development, coating completely removed

Table 30: Solution preparation of resin **PD77b**.

Solution n°	Solvent	Dil. rate	[I] (wt.-%)
PD180305/1	THF	0.27:1	1.5
PD210305/1	THF	0.27:1	1.5
PD230305/1	THF	0.27:1	0.5
PD250405/1	THF	0.27:1	1.5
PD280405/1	THF	0.27:1	1.5

Table 31: Processing conditions of solution **PD180305/1** (Table 30, **PD77b**).

Coating n°	w (rpm)	Δ_1 (s)	t_{UV} (s)	Δ_2 (s)	S	Remarks
180305/2	1000	80	120	80	MP	development in an ultrasonic bath, residues in the non-UV-exposed areas

Table 32: Processing conditions of solution **PD210305/1** (Table 30, **PD77b**).

Coating n°	w (rpm)	Δ_1 (s)	t_{UV} (s)	Δ_2 (s)	S	Remarks
210305/2	1000	40	120	40	MP	d ~ 30 μm , cracks near the non-UV-exposed areas
210305/3	1000	80	120	80	MP	residues in the non-UV-exposed areas
210305/4	1000	60	120	60	MP	d ~ 30 μm, cracks near the non-UV-exposed areas
210305/5	1000	70	120	70	MP	uprising of the non-UV-exposed part
210305/6	1000	60	120	60	EA	coating completely removed
210305/7	1000	60	120	60	THF	coating completely removed

Table 33: Processing conditions of solution **PD230305/1** (Table 30, **PD77b**).

Coating n°	w (rpm)	Δ_1 (s)	t_{UV} (s)	Δ_2 (s)	S	Remarks
230305/1	1000	40	120	40	MP	residues in the non-UV-exposed areas
230305/2	1000	50	120	50	MP	residues in the non-UV-exposed areas
230305/3	1000	50	30	50	MP	residues in the non-UV-exposed areas

Table 34: Processing conditions of solution **PD250405/1** (Table 30, **PD77b**).

Coating n°	w (rpm)	Δ_1 (s)	t_{UV} (s)	Δ_2 (s)	S	Remarks
260405/1a	1000	——	——	——	——	for μ-Raman spectroscopy measurements
260405/1b	1000	——	120	——	——	for μ-Raman spectroscopy measurements
260405/1c	1000	——	900	——	——	for μ-Raman spectroscopy measurements

Table 35: Processing conditions of solution **PD280405/1** (Table 30, **PD77b**).

Coating n°	w (rpm)	Δ_1 (s)	t_{UV} (s)	Δ_2 (s)	S	Remarks
280405/2	1000	——	900	——	MP	development in an ultrasonic bath, residues
280405/3	1000	——	900	——	MP	brown residues in the non-UV-exposed part, d = 1.7 μm

Table 36: Solution preparation of resin **PD77c**.

Solution n°	Solvent	Dil. rate	[I] (wt.-%)
PD030505/4	THF	0.27:1	1.5

Table 37: Processing conditions of solution **PD030505/4** (Table 36, **PD77c**).

Coating n°	w (rpm)	Δ_1 (s)	t_{UV} (s)	Δ_2 (s)	S	Remarks
130505/1a	1000	—	900	—	acetonitrile	residues in the non-UV-exposed areas
130505/1b	1000	—	900	—	toluene	residues in the non-UV-exposed areas
130505/1c	1000	—	900	—	CHCl$_3$	residues in the non-UV-exposed areas, UV-exposed area partially removed
130505/1d	1000	—	900	—	heptane	residues in the non-UV-exposed areas
130505/2a	1000	—	900	—	THF	cracks near the non-UV-exposed areas
130505/2b	1000	—	900	—	TBME	residues in the non-UV-exposed areas
130505/2c	1000	—	900	—	xylene	residues in the non-UV-exposed areas
130505/2d	1000	—	900	—	acetone	residues in the non-UV-exposed areas
180505/1a	1000	—	900	—	(THF:xylene)=(1:1)	residues in the non-UV-exposed areas
180505/1b	1000	—	900	—	(THF:xylene)=(2:1)	residues in the non-UV-exposed areas, cracks near the non-UV-exposed areas
180505/1c	1000	—	900	—	(THF: TBME)=(1:3)	residues in the non-UV-exposed areas, cracks near the non-UV-exposed areas
180505/2a	1000	—	900	—	(THF:toluene)=(1:1)	residues in the non-UV-exposed areas, cracks near the non-UV-exposed areas
180505/2b	1000	—	900	—	(THF:heptane)=(1:1)	residues in the non-UV-exposed areas
180505/2c	1000	—	900	—	(THF:heptane)=(2:1)	residues in the non-UV-exposed areas
180505/2d	1000	—	900	—	(THF:heptane)=(3:1)	residues in the non-UV-exposed areas

Table 38: Solution preparation of resin **PD92**.

Solution n°	Solvent	Dil. rate	[I] (wt.-%)
PD270705/1	THF	0.9:1	1.5
PD221105/2	THF	0.39:1	1.5

Table 39: Processing conditions of solution **PD270705/1** (Table 38, **PD92**).

Coating n°	w (rpm)	Δ_1 (s)	t_{UV} (s)	Δ_2 (s)	S	Remarks
290705/1	2000	110	120	—	MP	coating too thin
290705/2	2000	110	120	110	MP	residues in the non-UV-exposed areas d = 1.6 μm
290705/3	2000	110	120	110	MP	non-UV-exposed removed, development >1 min, d = 1.3 μm

Table 40: Processing conditions of solution **PD221105/2** (Table 38, **PD92**).

Coating n°	w (rpm)	Δ_1 (s)	t_{UV} (s)	Δ_2 (s)	S	Remarks
231105/1b	2000	—	120	—	—	for ellipsometer measurements
231105/1d	2000	—	900	—	—	for ellipsometer measurements

Table 41: Solution preparation of resin **PD92b**.

Solution n°	Solvent	Dil. rate	[I] (wt.-%)
PD141205/1	THF	0.87:1	1.5

Table 42: Processing conditions of solution **PD141205/1** (Table 41, **PD92b**).

Coating n°	w (rpm)	Δ_1 (s)	t_{UV} (s)	Δ_2 (s)	S	Remarks
260106/1	2000	—	—	—	—	for μ-Raman spectroscopy measurements
260106/2	2000	—	120	—	—	for μ-Raman spectroscopy measurements
260106/3	2000	—	420	—	—	for μ-Raman spectroscopy measurements
260106/4	2000	—	900	—	—	for μ-Raman spectroscopy measurements

Table 43: Solution preparation of resin **PD92c**.

Solution n°	Solvent	Dil. rate	[I] (wt.-%)
PD300306/1	THF	0.87:1	3

Table 44: Processing conditions of solution **PD300306/1** (Table 43, **PD92c**).

Coating n°	w (rpm)	Δ_1 (s)	t_{UV} (s)	Δ_2 (s)	S	Remarks
310306/1a	2000	—	—	—	—	for μ-Raman spectroscopy measurements
310306/1b	2000	—	120	—	—	for μ-Raman spectroscopy measurements
310306/1c	2000	—	420	—	—	for μ-Raman spectroscopy measurements
310306/1d	2000	—	900	—	—	for μ-Raman spectroscopy measurements

Table 45: Solution preparation of resin **PD92e**.

Solution n°	Solvent	Dil. rate	[I] (wt.-%)
PD210606/1	THF	0.9:1	1.5
PD290606/1	THF	0.9:1	1.5

Table 46: Processing conditions of solution **PD210606/1** (Table 45, **PD92e**)

Coating n°	w (rpm)	Δ_1 (s)	t_{UV} (s)	Δ_2 (s)	S	Remarks
220606/2	2000	110	120	110	MP	non-UV-exposed part removed, delamination and cracks around the UV-exposed areas
220606/3	2000	110	900	110	MP	non-UV-exposed part removed, delamination and cracks around the UV-exposed areas
270606/1	2000	110	120	110	MP	surface treatment: titania solution, d=3 μm
290606/1	2000	110	30	110	MP	surface treatment: titania solution, d=3 μm
290606/2	2000s	110	30	110	MP	surface treatment: titania solution development >1 min, d = 2 μm
290606/3	2000	110	10	110	MP	surface treatment: titania solution development <1 min, d = 1-3 μm

Table 47: Processing conditions of solution **PD290606/1** (Table 45, **PD92e**).

Coating n°	w (rpm)	Δ_1 (s)	t_{UV} (s)	Δ_2 (s)	S	Remarks
040706/1a	2000	110	—	—	—	for μ-Raman spectroscopy measurements
040706/1b	2000	110	30	110	MP	for μ-Raman spectroscopy measurements
040706/1c	2000	110	30	110	MP	additional UV irradiation for 900s for μ-Raman spectroscopy measurements

Table 48: Solution preparation of resin **PD92h**.

Solution n°	Solvent	Dil. rate	[I] (wt.-%)
PD211106/1	THF	0.6:1	1.5

Table 49: Processing conditions of solution **PD211106/1** (Table 48, **PD92h**).

Coating n°	w (rpm)	Δ_1 (s)	t_{UV} (s)	Δ_2 (s)	S	Remarks
231106/4	2000	110	30	110	MP	for ellipsometer measurements

Table 50: Solution preparation of resin **PD109**.

Solution n°	Solvent	Dil. rate	[I] (wt.-%)
PD240106/2	THF	0.9:1	1.5

Table 51: Processing conditions of solution **PD240106/2** (Table 50, **PD109**).

Coating n°	w (rpm)	Δ_1 (s)	t_{UV} (s)	Δ_2 (s)	S	Remarks
240106/1	2000	—	—	—	—	for μ-Raman spectroscopy measurements
240106/2	2000	—	120	—	—	for μ-Raman spectroscopy measurements
240106/3	2000	—	420	—	—	for μ-Raman spectroscopy measurements
240106/4	2000	—	900	—	—	for μ-Raman spectroscopy measurements

Table 52: Solution preparation of resin **PD109c**.

Solution n°	Solvent	Dil. rate	[I] (wt.-%)
PD180706/1	THF	0.9:1	1.5

Table 53: Processing conditions of solution **PD180706/1** (Table 52, **PD109c**).

Coating n°	w (rpm)	Δ_1 (s)	t_{UV} (s)	Δ_2 (s)	S	Remarks
190706/1	2000	40	30	40	MP	delamination of the coating
190706/2	2000	60	30	60	MP	non-UV-exposed removed
190706/3	2000	50	30	50	MP	delamination around the UV-exposed areas
190706/4	2000	40	30	40	MP	Δ_1 and Δ_2:3 min

4. Results and discussion

This chapter is divided into two parts. First, the development of novel inorganic-organic hybrid resins co-condensed with titanium precursors is described. These materials were developed in order to increase the refractive index of ORMOCER®s based solely on organo-alkoxysilane precursors, and to investigate the impact of the hetero-element on the physical properties such as the refractive index. Additionally, they should be patternable by the 2PP process. The optical properties of resins and coatings, i.e., refractive index and optical losses at λ = 780 nm (initiation wavelength for the 2PP process) are discussed depending on the chemical composition of the resins. In a second part, some resins were selected for the UV lithography process. The optical properties of the coatings depending on the UV lithography parameters were investigated as well. Finally, 2PP processing was carried out with some promising resins.

4.1 Characterization of the resins

In this chapter, the characterization of resins based on titanium alkoxides co-condensed with organo-alkoxysilanes containing a polymerizable moiety, and the influence of the synthesis parameters such as, for example, the quantity and the kind of organo-alkoxysilanes, the catalyst concentration, the quantity and kind of titanium alkoxides, and the use of complexing ligands (CL) on the refractive index values were investigated. The syntheses of the resins are described in chapter 3.2.

4.1.1 Characterization of the organo-alkoxysilanes by multi-nuclei NMR spectroscopy

In order to better understand the ^{29}Si- and ^{13}C-NMR spectra of the resins, the organo-alkoxysilane precursors and their hydrolysis products were characterized by NMR spectroscopy. ^{29}Si- and ^{13}C-NMR spectra of the resins synthesized in the framework of this work are very complex due to multiple reactions which can occur upon syntheses of these resins, leading to multiple signals in the spectra. ^{1}H-NMR spectra of the resins could not be analyzed due to an overlapping of the signals which did not allow a complete interpretation of the resin spectra. In order to investigate the material structure, ^{29}Si- and ^{13}C-NMR spectra were recorded. The evolution of the chemical shift of pure organo-alkoxysilanes, their hydrolysis and condensation products as well as the alkoxy exchange reactions were investigated separately. The assignment of the chemical shifts for the ^{29}Si- and ^{13}C-NMR spectra was carried out in several steps. Firstly, ^{13}C- and ^{29}Si-NMR spectra of MEMO and SETMS were studied. Then, the hydrolysis reactions with 10^{-2} M HCl (r =0.5) were investigated at different steps of the synthesis. In addition, the alkoxy exchange reaction was studied.

4.1.1.1 [3-(Methacryloyloxy)propyl]trimethoxysilane and styrylethyltrimethoxysilane

Figure 37 shows a ^{13}C-NMR spectrum of MEMO with the peak assignment. In the ^{29}Si-NMR spectrum (not shown), only one signal at - 42.49 ppm is present which corresponds exactly to the signal of the T^0 MEMO precursor.
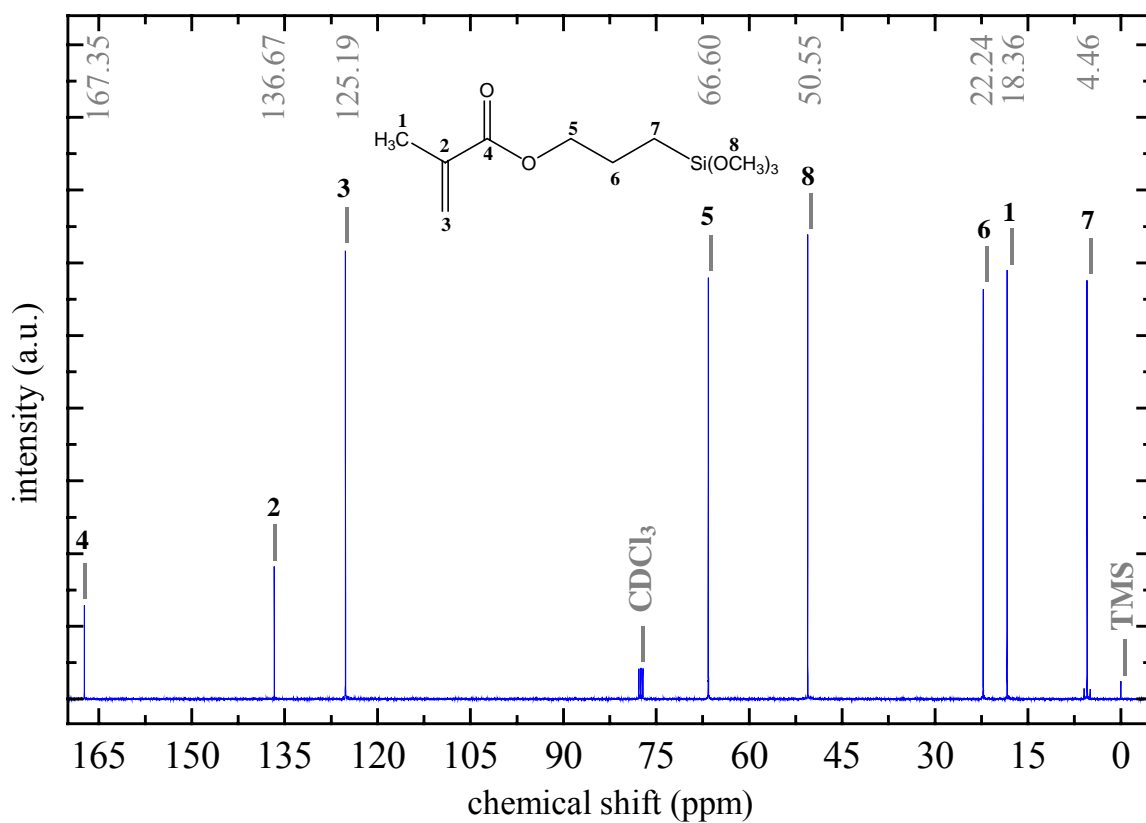
Figure 37: ^{13}C-NMR spectrum of MEMO recorded in CDCl$_3$.

The purity of the precursor SETMS was 95 %. Moreover, it is based on the mixture of the isomers meta and para, and also the isomers *a* and *b* (Figure 38).
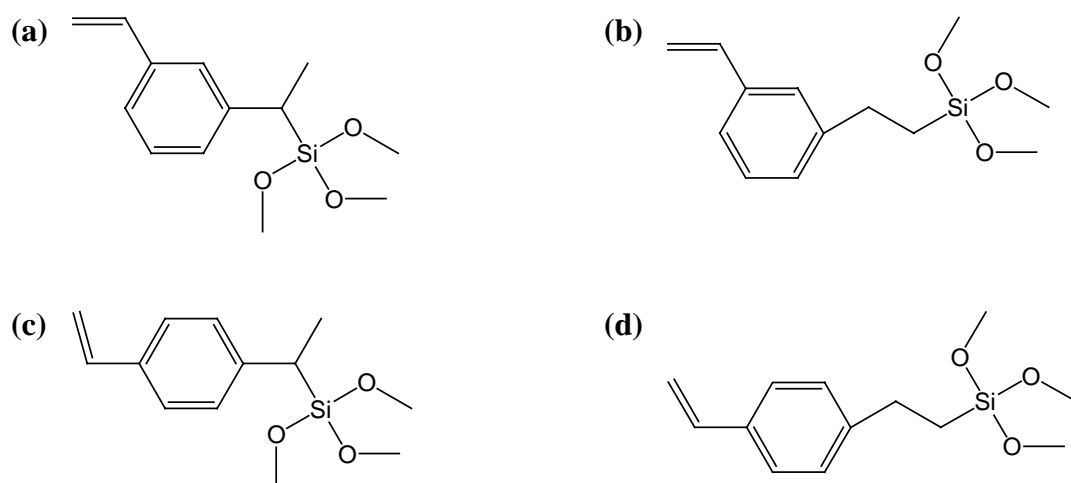
Figure 38: Composition of commercial SETMS. (a) Isomer *a*, and b) isomer *b* meta-substituted, (c) isomer *a*, and d) isomer *b* para-substituted.

Furthermore, SETMS contains t-butylcatechol as inhibitor which is added in order to avoid its polymerization at room temperature. Thus, due to the mixture of the isomers and the t-butylcatechol added, some chemical shifts of the commercially available SETMS could not be attributed. Since this precursor has a high refractive index in comparison to other organo-alkoxysilanes commercially available (cf., section 2.2.1.3), SETMS was used for the syntheses of the inorganic-organic hybrid materials despite its inadequate purity.

In Figure 39, a ^{13}C-NMR spectrum of the commercially available SETMS is shown. Due to the mixture of isomers, multiplet signals are recorded for each carbon addressed by numbers in the inset. In addition, signals recorded by ^{29}Si-NMR spectroscopy (cf., Figure 40) between -49.0 and -50.2 ppm could be attributed to T^1 species or to impurities initially present in the precursor, and thus, can also contribute to the presence of multiple signals recorded for each carbon.

The isomers a and b can be clearly identified by the presence of the multiplets around 15.7, 25.4, and 51.0 ppm and are attributed to the carbons 10, 9 and 11 for the isomer a, and around 11.4, 28.5, and 50.4 for the isomers b, respectively. The peaks around 140 ppm which are not labeled in Figure 39 (a) are attributed to signals from impurities and/or from t-butylcatechol. Around 113.2 and 136.2 ppm, the organic polymerizable CH_2=CH- group is also detected with multiple signals due to the mixture of the different isomers.
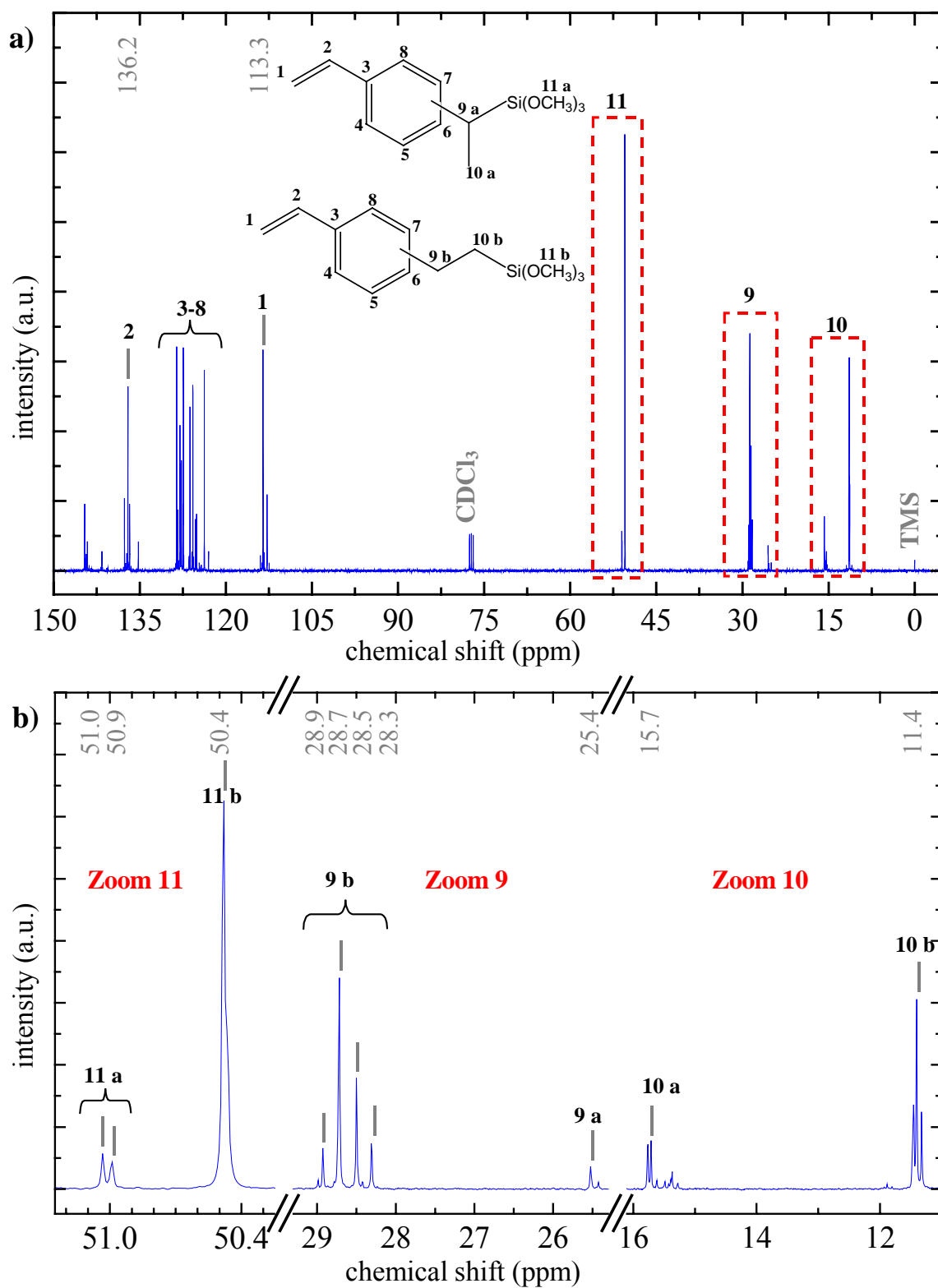
Figure 39: (a) ^{13}C-NMR spectrum of SETMS (purity: 95 %, mixture of isomers, inhibited with t-butylcatechol). The spectrum was recorded in CDCl$_3$. (b) Zooms into the peak structure marked in (a) by dashed rectangles and corresponding peak attribution.

By ^{29}Si-NMR spectroscopy (Figure 40), two regions between -42.5 and -42.8 ppm and between -49.0 and -49.5 ppm are detected. The first region presents four peaks at -42.56, -42.59, -42.63, and -42.78 ppm attributed to the T^0 species of the four isomers shown in Figure 38. In addition, the weak signals recorded around -49 ppm could be attributed to T^1 species, i.e., condensed SETMS, or to impurities within the SETMS precursor.
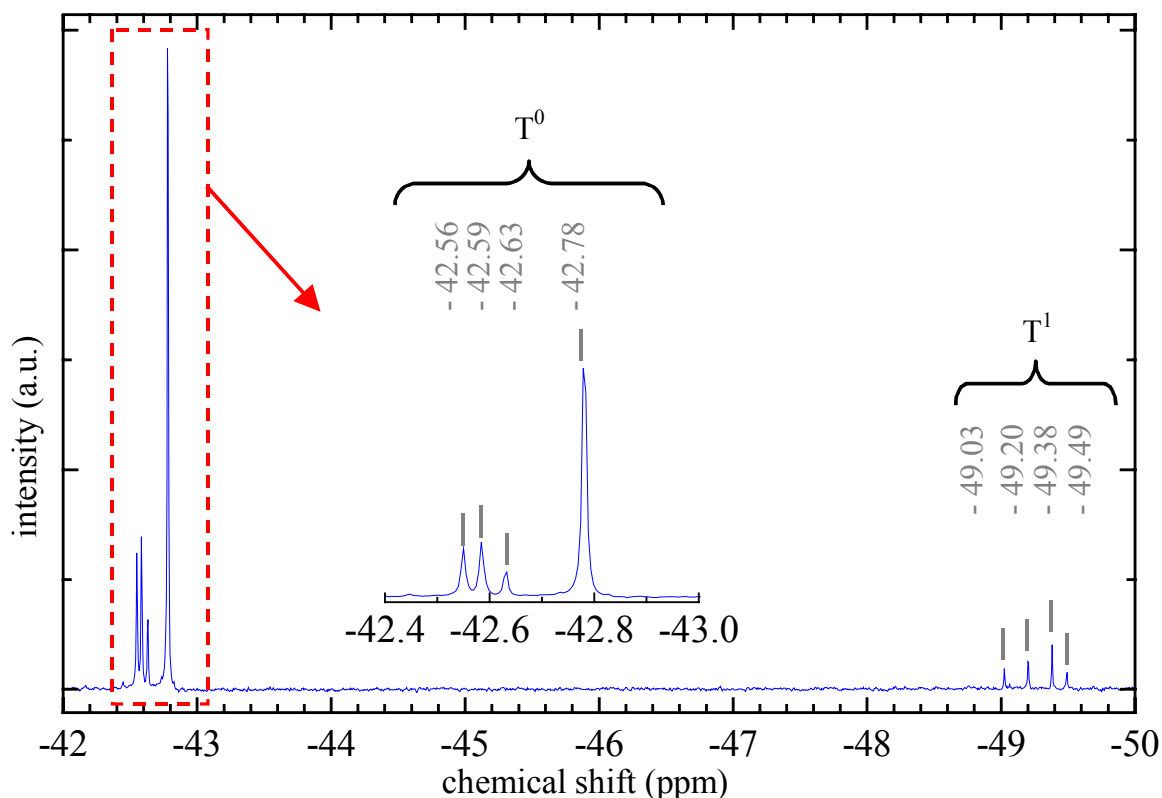
Figure 40: ^{29}Si-NMR spectrum of commercially available SETMS, recorded in CDCl$_3$. The inset shows a zoom into the peak structure marked by the dashed rectangle.

4.1.1.2 The alkoxy exchange reaction

The hydrolysis of titanium ethoxide precursors leads to the formation of ethanol, which may also react with the organo-alkoxysilanes. Thus, organo-alkoxysilanes (25 mol-% MEMO or SETMS) were mixed with ethanol (75 mol-%), and multi-nuclei NMR spectra were recorded after 3 days of stirring.

In Figure 41, the ^{29}Si-NMR spectrum of MEMO mixed with ethanol is displayed. It shows four peaks, uniformly placed at a regular interval of 1.1 ppm, which displays the presence of four different species. The peak corresponding to the pure MEMO at -42.27 ppm is slightly shifted compared to the peak of pure MEMO in the presence of ethanol (-42.49 ppm for the pure MEMO). The three other peaks at -43.37, -44.49, and -45.63 ppm correspond to $T^0_{(OMe)(OMe)(OEt)}$, $T^0_{(OMe)(OEt)(OEt)}$, and $T^0_{(OEt)(OEt)(OEt)}$, respectively, formed by an alkoxy exchange reaction OMe→OEt.
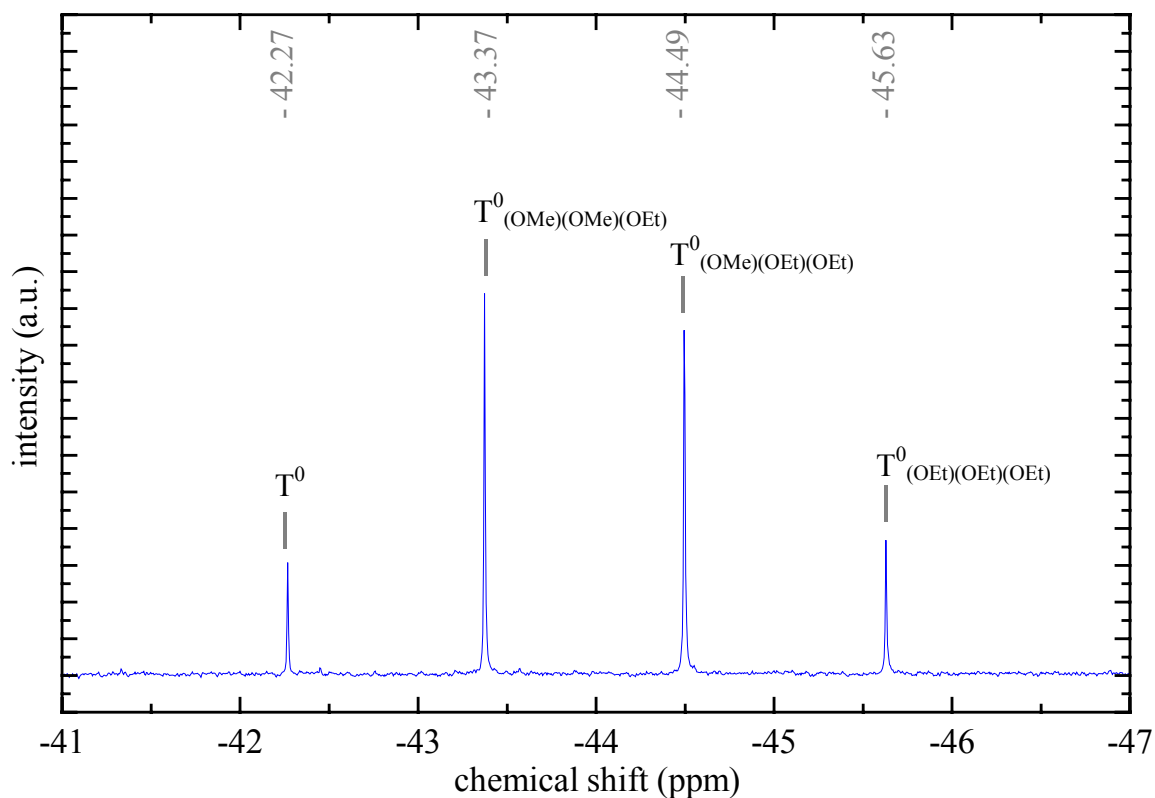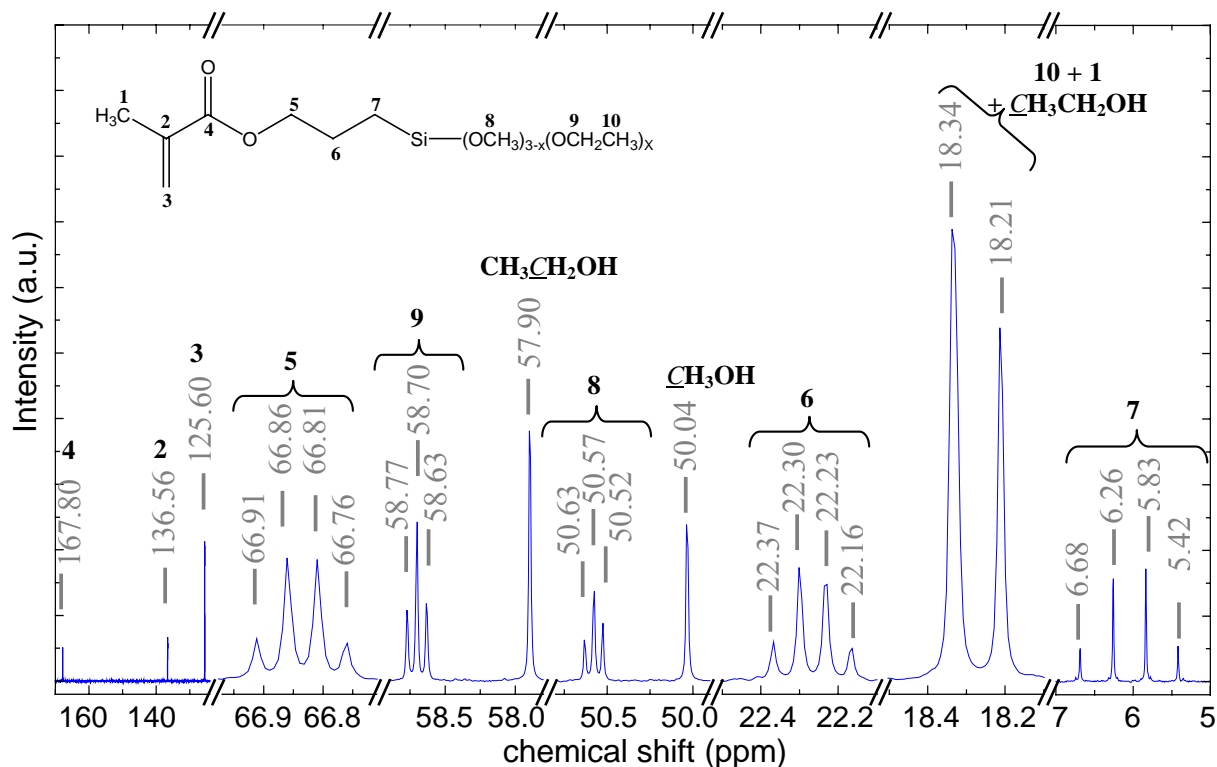
Figure 41: ^{29}Si-NMR spectrum of the mixture MEMO: ethanol (molar ratio 1:3) after three days of stirring at room temperature, recorded in CDCl$_3$.

The same trend is also observed in the mixture SETMS:ethanol (Figure 42). In addition to the group of peaks recorded for the SETMS precursor (Figure 40), three other groups of uniformly spaced peaks between -43.3 and -43.6 ppm, -44.4 and -44.8 ppm, and -45.5 and -45.9 ppm were attributed to $T^0_{(OMe)(OMe)(OEt)}$, $T^0_{(OMe)(OEt)(OEt)}$, and $T^0_{(OEt)(OEt)(OEt)}$, formed by an alkoxy exchange reaction OMe→OEt, like for MEMO.

Since the group of peaks around to -50 ppm, which was supposed to be attributed to T^1 species or impurities was not affected by the presence of ethanol, it supports the hypothesis that it corresponds to the signal of impurities within the SETMS precursor.
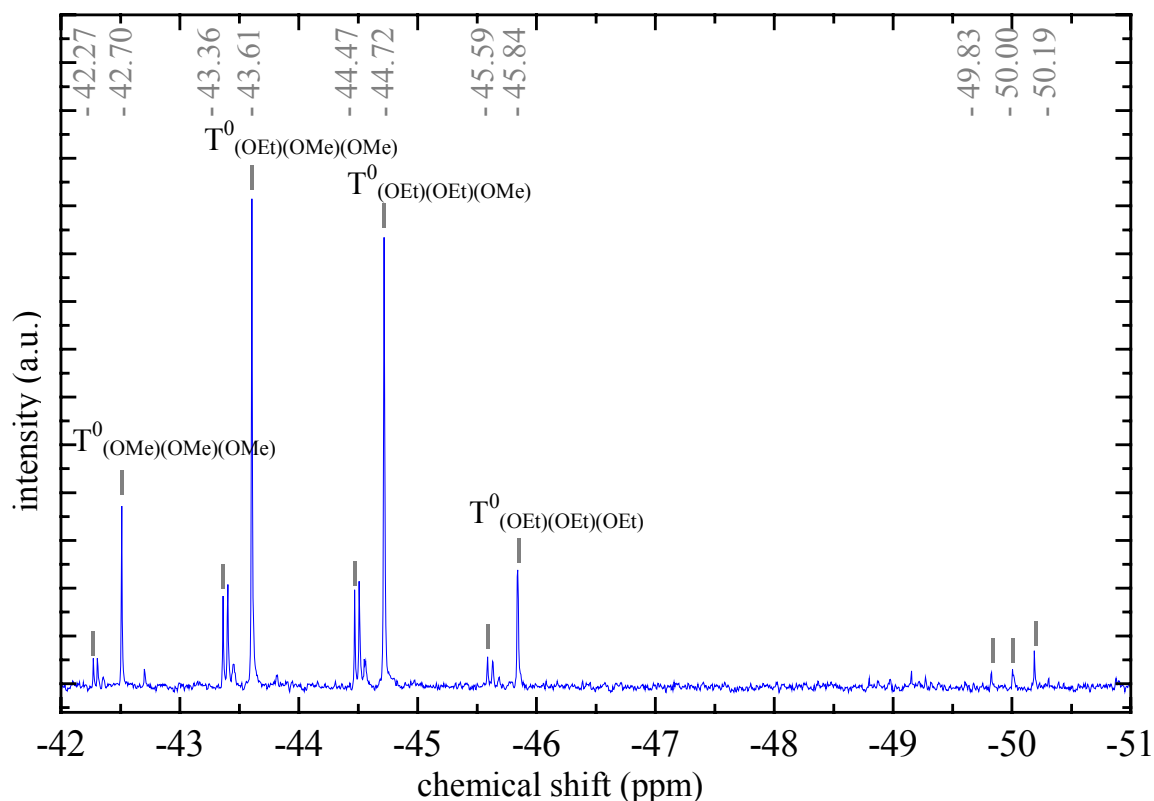
Figure 42: ^{29}Si-NMR spectrum of the mixture SETMS:ethanol (molar ratio 1:3) after three days of stirring at room temperature, recorded in CDCl$_3$.

Alkoxy exchange reactions (OR→OR') of a metal alkoxide M(OR)$_4$ in an alcoholic solution R'OH are already discussed in the literature[210,211]. These reactions were reported to be spontaneous for transition metal alkoxides[212], and might occur with silicon oxide under some specific experimental conditions (acidic catalyzed reactions)[211,212]. However, the results presented in Figures 41 and 42 show that by using MEMO or SETMS, the exchange reaction (OMe→OEt) is spontaneous and occurs without any catalyst.

The ^{13}C-NMR spectrum of the mixture MEMO:ethanol is between 170 and 124 ppm is very similar to the spectrum of the pure MEMO. In this region, the peaks are slightly shifted in the presence of ethanol compared to those of the pure MEMO. According to the alkoxy exchange between ethanol and MEMO, quadruplet signals of the carbons 5, 6, and 7 were detected (Figure 43). The four peaks recorded for each carbon are regularly spaced, and are attributed to the four different alkoxysilane combinations, T^0$_{(OMe)(OMe)(OMe)}$, T^0$_{(OMe)(OMe)(OEt)}$, T^0$_{(OMe)(OEt)(OEt)}$, and T^0$_{(OEt)(OEt)(OEt)}$, also shown in Figure 41. The carbons of the alkoxysilane group (-Si(OCH$_3$)$_{3-x}$(OCH$_2$CH$_3$)$_x$) linked to the oxygen atom (carbon 8 and 9, Figure 43) are detected with three signals having equidistant interspacings. The signal of CH$_3$ of the ethoxy group (-Si(OCH$_2$CH$_3$) is overlapped to that of -CH$_3$ of carbon 1, or ethanol.
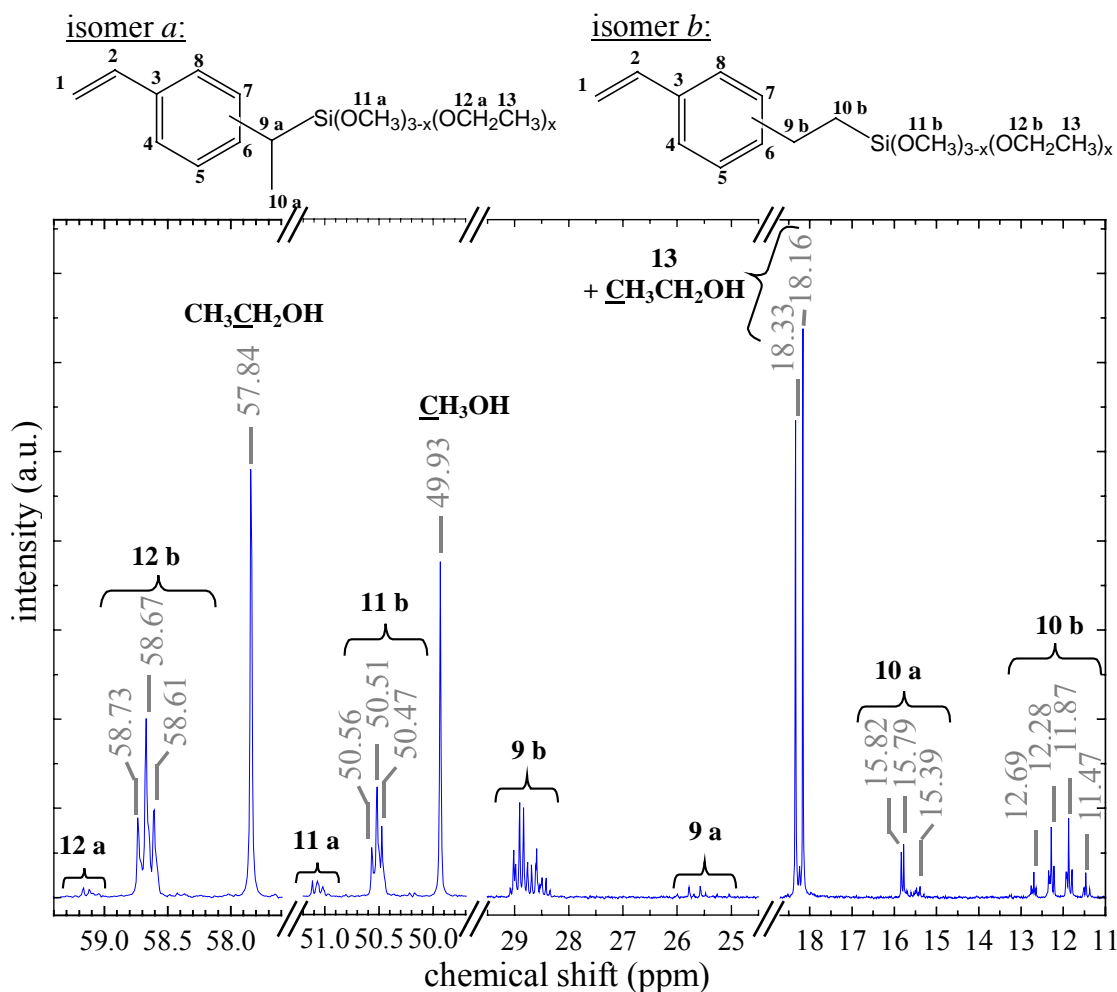
Figure 43: Zooms into the ^{13}C-NMR spectrum (not shown) of the mixture MEMO: ethanol (molar ratio 1:3) after three days of stirring at room temperature.

The ^{13}C-NMR spectrum of the mixture SETMS:ethanol shows the same behavior as the mixture MEMO:ethanol (cf., Figure 44). The chemical shifts of the carbon atoms labeled 9 and 10 are affected by the alkoxy exchange reaction. Since SETMS is a mixture of isomers, the resolution of the signals recorded for the SETMS:ethanol mixture is lower than for those of the MEMO:ethanol mixture. On the other hand, the signals attributed to the alkoxide groups are very well-defined. For example, the carbon atoms linked to the oxygen atom, i.e., carbon atoms 11 and 12,are recorded with three signals.

Figure 44: Zooms into the ^{13}C-NMR spectrum (complete spectrum not shown) of the mixture SETMS: ethanol (molar ratio 1:3) after three days of stirring at room temperature. The carbon atoms are labeled in the structures of isomers *a* and *b*.

4.1.1.3 Hydrolysis reactions of [3-(methacryloyloxy)propyl]trimethoxysilane and styrylethyltrimethoxysilane

Hydrolysis of MEMO or SETMS was performed with 0.01M HCl as catalyst, with the water ratio fixed to $r_w = 0.5$. The mixture MEMO-HCl was miscible only after 25 min of vigorous stirring, whereas 5.5 hours were needed to mix SETMS and HCl. Multi-nuclei NMR spectra were recorded at different steps of the synthesis.

The integration of a series of ^{29}Si-NMR signals of a mixture MEMO-HCl (Figure 45) shows that the hydrolysis has started after 15 minutes stirring time. The ^{29}Si-NMR spectrum shows a strong signal at -41.89 ppm, corresponding to that of MEMO ($T^0_{(OMe)(OMe)(OMe)}$), and a weak signal at -41.01 ppm, corresponding to the hydrolyzed MEMO ($T^0_{(OH)(OMe)(OMe)}$). After 25 min of stirring, four signals are detected between -41.6 and -39.7 ppm, in the $T^0_{(OMe)(OMe)(OMe)}$ region. The signal at -41.68 ppm is attributed to the MEMO ($T^0_{(OMe)(OMe)(OMe)}$) which is shifted due to its environment (-42.49 ppm in pure CDCl$_3$). The three other signals at -40.75, -40.12, and -39.60 ppm are assigned to hydrolyzed MEMO, $T^0_{(OH)(OMe)(OMe)}$, $T^0_{(OH)(OH)(OMe)}$, and $T^0_{(OH)(OH)(OH)}$, respectively. Weak signals between approximately -50.2 and -48.9 ppm

belong to the T^1 region. The latter region is composed of three groups of signals due to the three possibilities of coordination: $T^1_{(OMe)(OMe)}$, $T^1_{(OMe)(OH)}$, and $T^1_{(OH)(OH)}$.
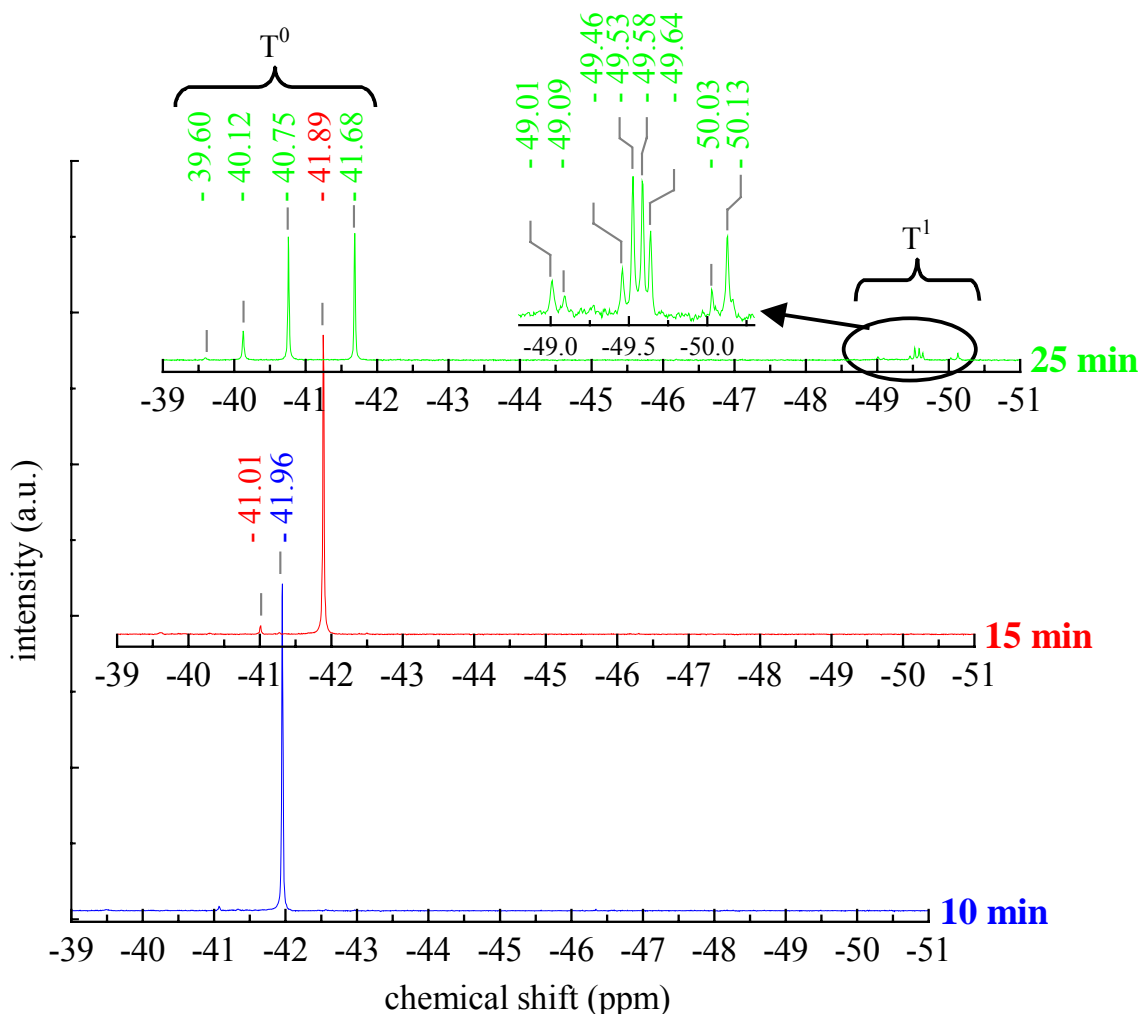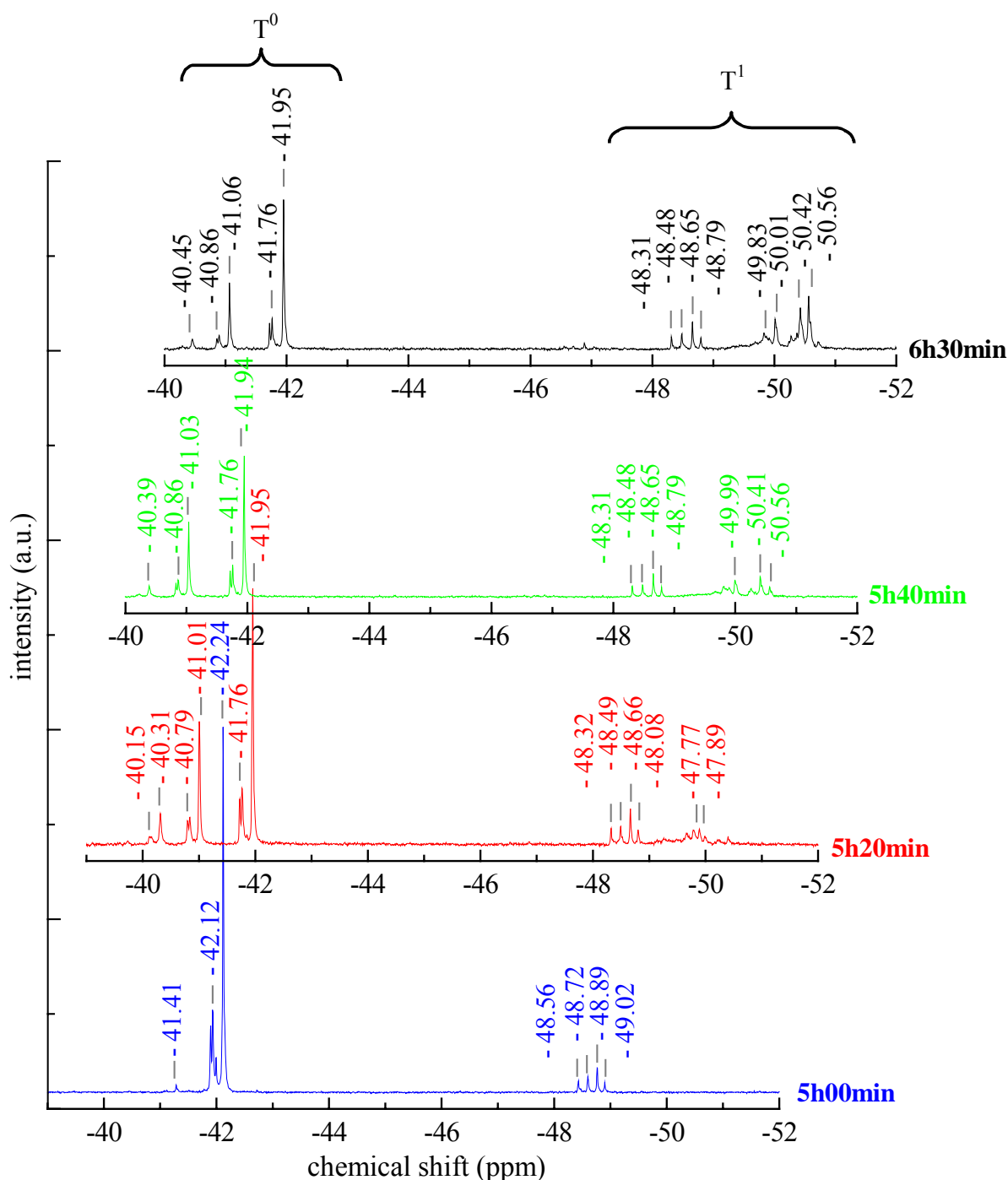

Figure 45: ^{29}Si-NMR spectra at different steps of the hydrolysis/condensation reactions of MEMO with 10^{-2} M HCl, recorded in CDCl$_3$. The inset in the spectrum after 25 min shows a zoom between -49 and -51 ppm.

The hydrolysis reactions of SETMS with 0.01 M HCl were slower than those of MEMO. Thus, the time had to be extended to hours instead of minutes. The first spectrum (Figure 46) was taken after 5 hours, and only the SETMS signals were detected. After 5h20min, a hydrolysis reaction started to take place. In Figure 46, three groups of peaks recorded after 5h20min of stirring time around -41.9, -41.0, and -40.3 ppm are attributed to SETMS coordinated in $T^0_{(OMe)(OMe)(OMe)}$, $T^0_{(OMe)(OMe)(OH)}$, $T^0_{(OMe)(OH)(OH)}$, respectively.

80

Figure 46: ^{29}Si-NMR spectra at different steps of the hydrolysis/condensation reactions of SETMS with 0.01 M HCl, recorded in CDCl$_3$.

The $T^0_{(OH)(OH)(OH)}$ species is firstly recorded after 5h40 min stirring time around -40.39 ppm with a very weak signal. The T^1 species are recorded around -50.4 ppm after 5h40min of stirring. Since the signal initially recorded in the precursor (around -48.8 ppm) is shifted from those of the T^1 species, the latter ones can only be attributed to impurities. After 6h30 min stirring, a very weak and broad peak is recorded between -58 and -60 ppm, attributed to T^2 species.

The chemical shifts of the carbon chain bonds to the silicon atom from MEMO and SETMS are also affected by the hydrolysis reaction (cf., Figures 46 and 47) in the same way as in the alkoxy exchange reaction (Figures 42 and 43). Figure 47 shows zooms of a ^{13}C-NMR spectrum of hydrolyzed MEMO after 25 min, whereas the peaks corresponding to the carbons 1, 2, 3, and 4 (inset of Figure 47) are not shown, since these are not affected by the hydrolysis reaction (except that a slight shift is observed due to the presence of HCl). The carbon directly bonded to the silicon atom (carbon 7 in Figure 47) exhibits three significant regularly spaced signals at 5.14, 6.35, and 7.59 ppm, which correspond to $T^0_{(OMe)(OMe)(OMe)}$, $T^0_{(OH)(OMe)(OMe)}$, and $T^0_{(OH)(OH)(OMe)}$, respectively. Three-fold hydrolyzed MEMO ($T^0_{(OH)(OH)(OH)}$) was not detected by ^{13}C-NMR spectroscopy.
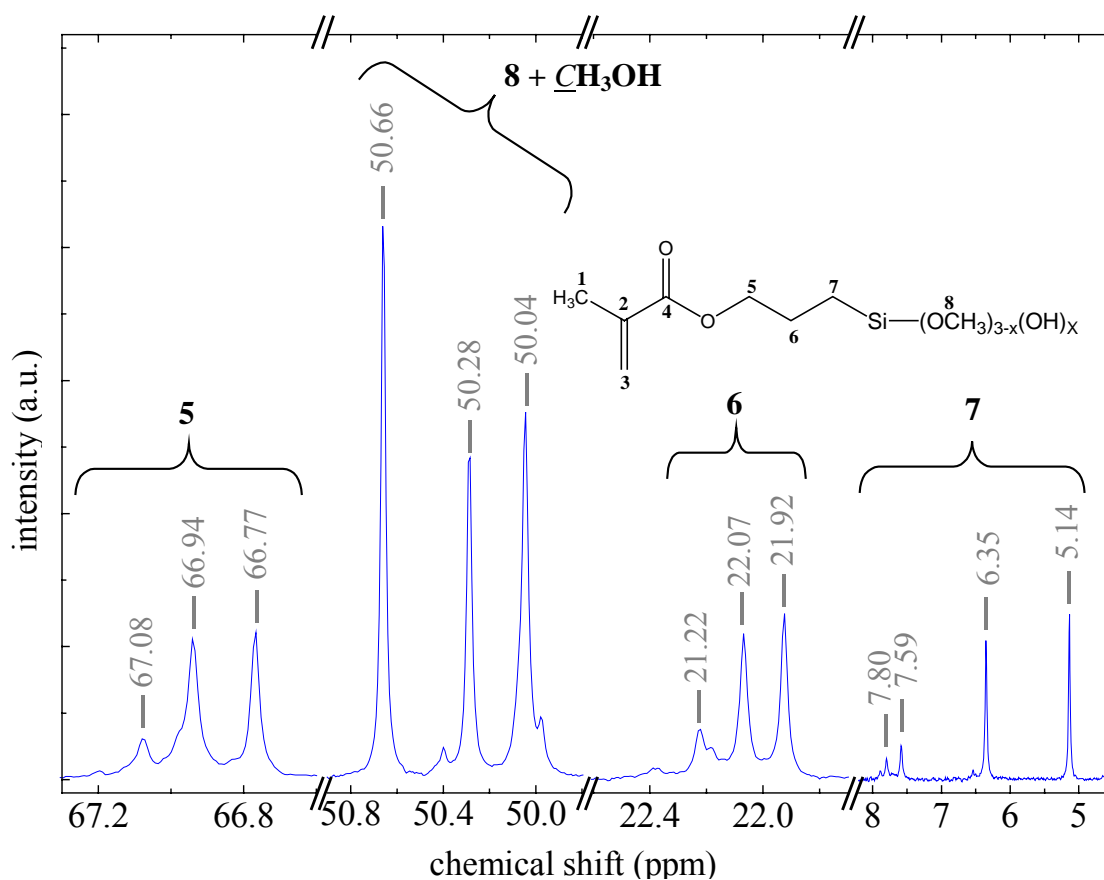
Figure 47: Zooms into the ^{13}C-NMR spectrum of hydrolyzed MEMO between 4.5 and 8.2 ppm, 21.7 and 22.6 ppm, 49.8 and 50.9 ppm, and 66.6 and 67.3 ppm, respectively, after 25 min reaction time. The inset labels the different carbon atoms in the structure. The peak series corresponding to some carbon atoms are marked.

The same behavior is observed for the carbon chain bonded to the silicon atom (carbons 5, 6, 7 and 8, inset of Figure 47). It has to be noticed that the intensity ratios of the carbons 6, 7 and 8 are in good agreement with those of the ^{29}Si-NMR spectrum in the T^0 region. The signals of the carbons 8 of the MEMO unit are detected between 49.8 and 50.9 ppm. The intensity ratio does correspond well to the T^0 region of the respective ^{29}Si-NMR spectrum due to a superposition of the methanol peak resulting from methanol formation during the hydrolysis reaction. In Figure 48, zooms into the ^{13}C-NMR spectrum of the hydrolyzed SETMS are shown. As for the hydrolyzed MEMO, the chemical shift of the carbon in

SETMS directly bonded to the silicon atom is altered by the hydrolysis reaction, but this effect was observed only for the isomer *b*.
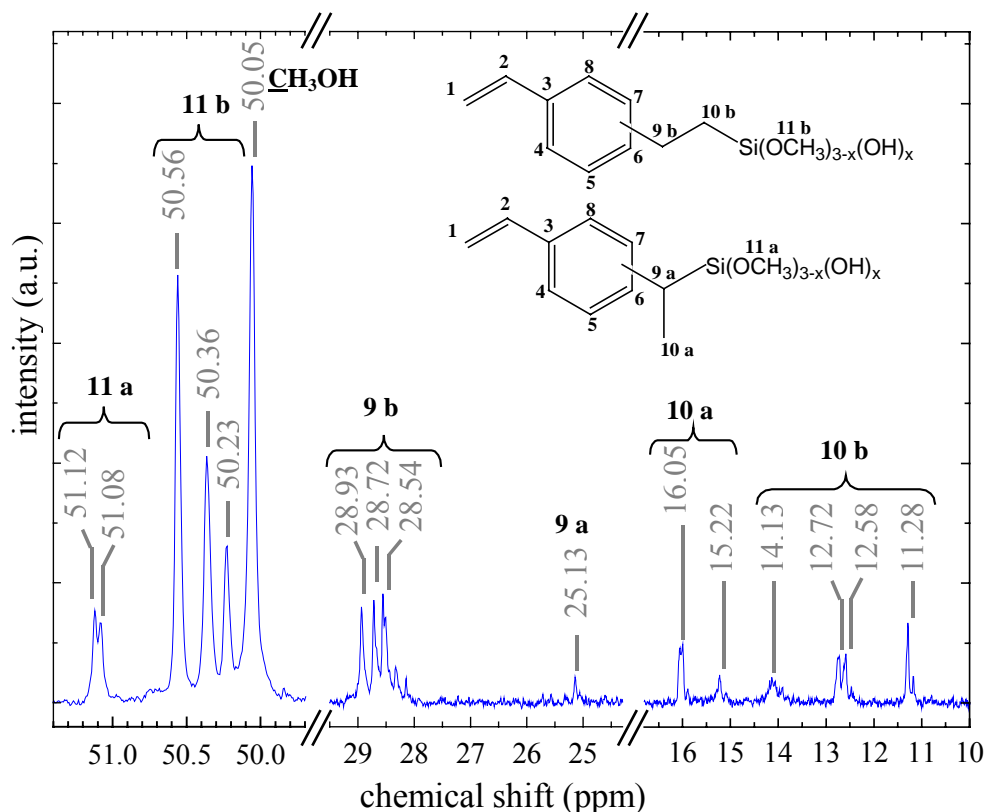

Figure 48: Zooms into the ^{13}C-NMR spectrum of hydrolyzed SETMS between 10 and 16.8 ppm, 24.3 and 29.5 ppm, 49.7 and 51.4 ppm, after 6h30 min reaction time.

The three regularly spaced groups of peaks around 11.3, 12.6, and 14.1 ppm can be attributed to the signal of the carbon directly bonded to the silicon atom (carbon atom 10 b in Figure 48) in the $T^0_{(OMe)(OMe)(OMe)}$, $T^0_{(OH)(OMe)(OMe)}$, and $T^0_{(OH)(OH)(OMe)}$ species, respectively. Moreover, the carbon atoms from the methoxy group in isomer *b* (carbon atom 11 b in Figure 48) were detected with three signals at 50.56, 50.36, and 50.23 ppm, and thus correspond exactly to the three species listed above. The hydrolysis reaction also affects the chemical shift of the carbon atom 9 b, which is shown by the presence of a multiplet around 28.7 ppm. On the other hand, the isomer *a* is not or just slightly affected by the hydrolysis reaction.

It is known that chemical shifts usually are affected by the environment of the investigated species. For example, in ^{29}Si-NMR spectroscopy, pure MEMO has a chemical shift at -42.49 ppm, whereas in presence of ethanol it shifts to -42.27 ppm, or to -41.96 and -41.68 ppm in presence of HCl. Moreover, alkoxy exchange reactions between ethanol and the methoxy group of MEMO or SETMS led to new species detected by ^{29}Si-NMR spectroscopy. Peaks are shifted towards the upfield region, i.e., with the alkoxy exchange reaction, the chemical shift decreases. For example, the chemical shifts for T^0 of MEMO was detected at -42.27 ppm, whereas $T^0_{(OMe)(OMe)(OEt)}$, $T^0_{(OMe)(OEt)(OEt)}$, and $T^0_{(OEt)(OEt)(OEt)}$ were found to be close to -43.37, -44.49, and -45.63 ppm, respectively. In addition, the chemical shifts of new species formed by the hydrolysis reaction of MEMO or SETMS are shifted towards the downfield region, i.e., upon the hydrolysis reaction, the chemical shift increases.

For example, in the ^{29}Si-NMR spectrum of the hydrolyzed MEMO, the chemical shift values recorded are -40.75, -40.12, and -39.60 ppm for the species $T^0_{(OH)(OMe)(OMe)}$, $T^0_{(OH)(OH)(OMe)}$, and $T^0_{(OH)(OH)(OH)}$, respectively, whereas MEMO T^0 was recorded at -41.68 ppm. Depending on the reactions which occur during the synthesis, the chemical shifts of the MEMO T^0 region range from -39.60 to -45.63 ppm. By means of ^{13}C-NMR spectroscopy, it was shown that the signal of the carbon chain linked to the silicon atom is also shifted with the hydrolysis and the alkoxy exchange reactions. Finally, the combination of the hydrolysis and alkoxy exchange reactions lead to a broadening of some signals in the ^{29}Si and ^{13}C-NMR spectra.

By ^{13}C-NMR spectroscopy, the hydrolysis and/or condensation reactions of MEMO (or SETMS) with themselves or with titanium alkoxide precursors generate new signals. These new signals are more or less shifted in comparison to the signals of the respective carbon in the pure organo-alkoxysilane, depending on the new environment of the silicon atom. Moreover, alkoxy exchange between silicon alkoxide ($RSi(OR')_3$ or $Si(OR')_4$) and titanium alkoxide ($Ti(OR'')_4$) has already been pointed out in the literature[212] by multi nuclei-NMR spectroscopy. This reaction may also occur in resins synthesized with organo-alkoxysilanes and titanium alkoxides. Due to the alkoxy exchange, new signals can be detected by ^{29}Si-NMR spectroscopy. The latter one gives information about the environment of silicon, i.e., hydrolysis and/or condensation reaction.

4.1.2 Resins synthesized without complexing ligand

4.1.2.1 Resins synthesized with one organo-alkoxysilane

4.1.2.1.1 [3-(methacryloyloxy)propyl]trimethoxysilane used as organo-alkoxysilane

In the literature, the incorporation of metal alkoxides to organo-alkoxysilanes by co-condensation reactions has been often used in order to increase the refractive index of materials[96-100,102,154,155]. For example, organic-inorganic hybrid materials based on 40 mol-% DPD and 60 mol-% Ti(OEt)$_4$ were synthesized, having a refractive index close to 1.68 [96,97]. On the other hand, these hybrid materials do not contain any polymerizable moiety. In this part of the work, hybrid organic-inorganic materials, which were synthesized from 67 mol-% titanium alkoxide and 33 mol-% of organically polymerizable organo-alkoxysilanes are reported. The influence of the nature of the employed organo-alkoxysilane (MEMO or SETMS) on the refractive index was investigated. In addition, the impact of the catalyst concentration (hydrochloric acid) used for the hydrolysis reactions on the refractive index, the transparency, and the polymerizability of the final material were correlated.

Resins were synthesized from 67 mol-% Ti(OEt)$_4$ and 33 mol-% MEMO using three different HCl concentrations: 0.01 M, 2 M, and 12 M, resulting in resins labeled as PD113, PD49, and PD79 (cf., 3.2.2.1). The HCl concentration generally described in the literature as catalyst for the hydrolysis reaction is close to 0.01 M[98,156,182], and some authors reported the use of HCl concentrations close to 0.2 M[99,101]. In this work, higher catalyst concentrations were used. In fact, highly acidic media (> 2 M) and high temperature reactions have been reported to enhance the formation of anatase and rutile phase[126,213-215]. Particularly rutile possesses high refractive indices between 2.5 and 2.9 (see chapter 2.2.1.1). The water content for the hydrolysis reaction, defined by the ratio r_w, was fixed to 0.5 for the three resins. After removal of volatile components under reduced pressure, solid resins were obtained

independently of the catalyst concentration. The refractive indices of the materials were characterized on coatings using the Swanepoel's technique (cf., chapter 2.2.2.4). For that, the resins were dissolved in solvents, spin-coated on a Borofloat® glass substrate (cf., part 3.3.1), and subsequently cured at 150°C for three hours without any further treatment. Due to the fact that milky solutions were obtained with the resin PD113 for any solvent, the refractive index of this material could not be determined. From Figure 49, the refractive indices and the thicknesses of the coatings from resins PD49 and PD79 (samples 300304/1 and 110105/2, part 3.3.1) were calculated. The refractive indices of the coatings were determined to be 1.61 at 1080 nm and 1.62 at 690 nm (thickness ≈ 1.2 µm) for PD49, whereas an index of 1.67 at 1170 nm (thickness ≈ 520 nm) was obtained for PD79.
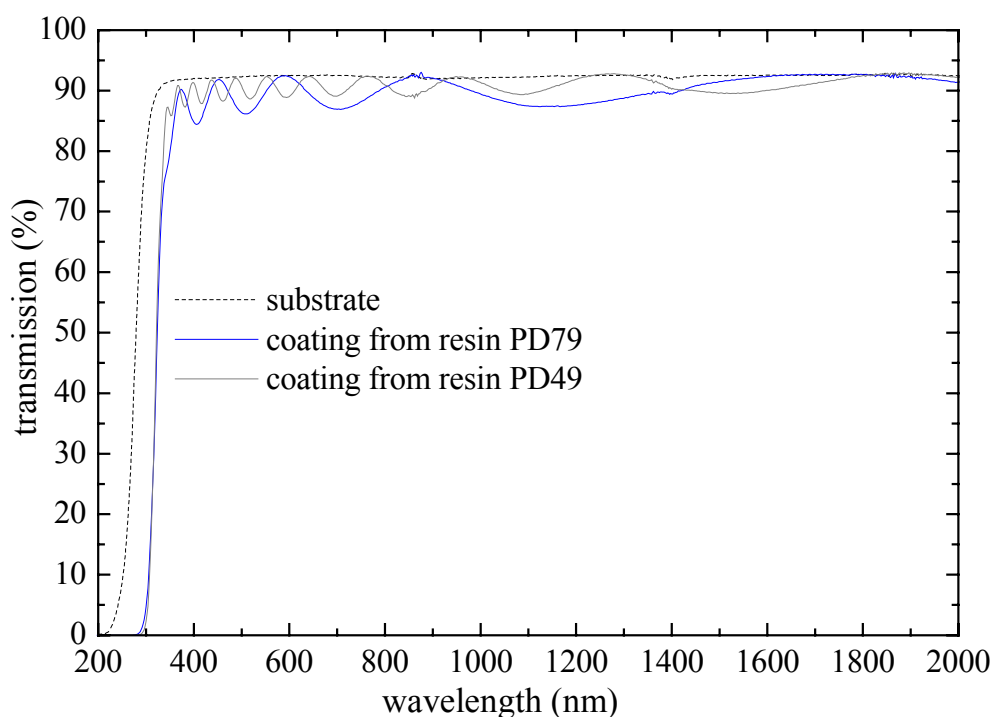
Figure 49: Transmission spectra of a glass substrate, and of resins PD49 and PD79 coated on the glass substrate (labeled 300304/1 and 110105/2, Table 9 and 15, chapter 3.3.1) after curing at 150°C for 3 h.

The optical losses of resins could not be determined, since the dilution of the resins in half volume of solvent has led to saturated solutions (cf., part 3.1.5). The transmission spectra of the coatings show that highly transparent coatings are obtained for the resins PD79 and PD49. Concerning resin PD113 which was synthesized with the lowest HCl concentration, milky solutions were obtained which result from the difference in the reactivity of $Ti(OEt)_4$ and MEMO during the hydrolysis reaction, leading to a phase separation. In the case of PD49 and PD79 synthesized with a very high HCl concentration, the protons from the catalyst act as inhibitors for the condensation reaction. The nucleophilic species (Ti-OH) can be more or less protonated causing selective inhibition of some condensation reactions[32-34].
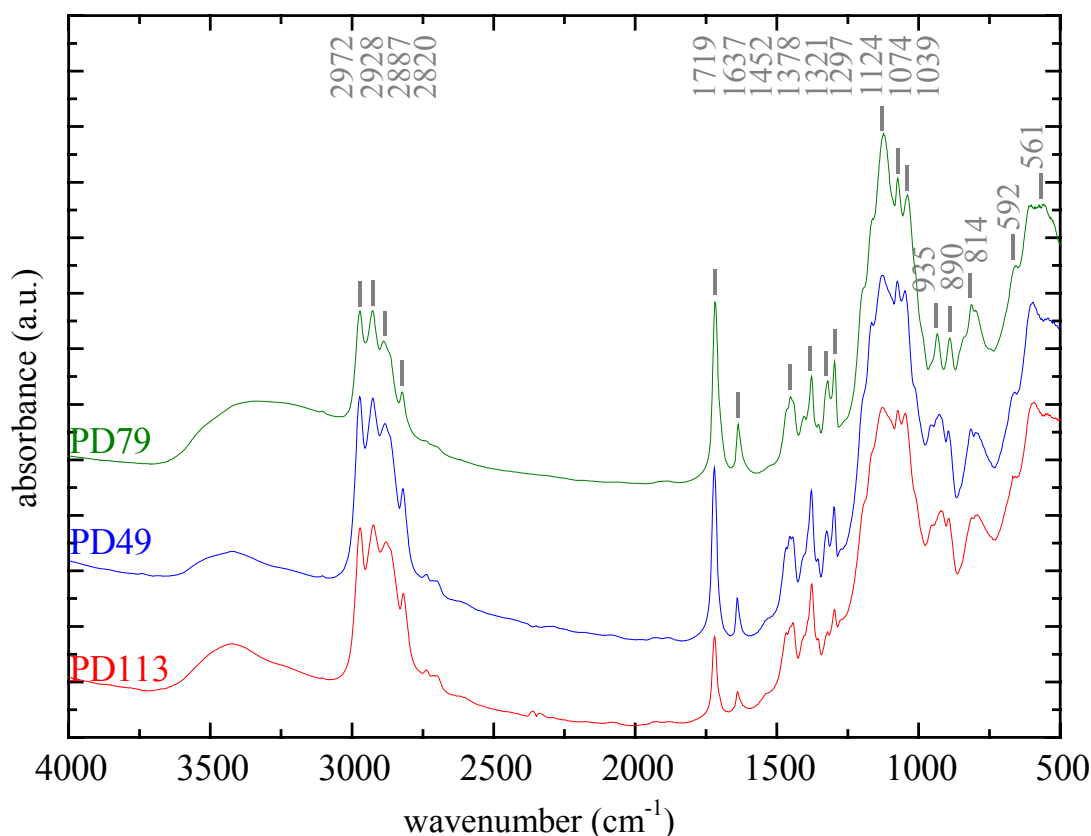
Figure 50: FT-IR spectra of the resins PD113, PD49, and PD79, synthesized with 0.01, 2, and 12 M HCl, respectively, recorded on KBr pellets.

The FT-IR spectra of the resins PD79, PD49, and PD113 are shown in Figure 50. Broad peaks around 3300 cm^{-1} corresponding to the vibrational modes of -OH groups and/or H_2O were observed for the three resins. Between 1400 and 500 cm^{-1}, several broad peaks are observed which are attributed to inorganic oxidic components. In this wavenumber regime, the overlapping of peaks leads to difficulties to assign them to the possible inorganic-oxidic species, which can be Si-O-Si, Si-O-Ti, Si-O-C, Ti-O-C, and Ti-O-Ti bonds, respectively. At 1719 and 1637 cm^{-1}, the stretching vibrational modes corresponding to the C=O and C=C bonds of MEMO are detected. This was confirmed by ^{13}C-NMR spectroscopy (Figure 51). At 167.16 ppm, the **C**=O of MEMO was detected, as well as the CH_2=**C**- and the **C**H_2=C- at 136.38 ppm and 125.19 ppm, whereas the latter should be used for the organic cross-linking reactions.

By increasing the catalyst concentration from 2 to 12 M HCl, an increase of 0.06 in the refractive index was observed. This high increase can be attributed to the presence of chlorides in the material, whose concentration is more than seven times higher in PD79 than in PD49 (33 and 4.23 mmol, respectively). Moreover, considering the variation of the refractive index of, for example, poly(phenyl methacrylate) (n = 1.5706) and poly(pentachlorophenyl methacrylate) (n = 1.6008), the increase of the concentration for hydrochloric acid in PD79 cannot be the only reason which explains the high refractive index jump. Thus, NMR investigations were carried out in order to better explain this high refractive index increase.

The three resins were characterized by ^{13}C- and ^{29}Si-NMR spectroscopy. Since the recorded spectra were independent of the catalyst concentration, only the ^{13}C-NMR spectrum of resin PD79 is shown (Figure 51). The peaks corresponding to the carbon atoms in the -Ti-OEt and -Ti-OCH(CH$_3$)$_2$ groups are still detected in the resin, which means that Ti(OEt)$_4$ containing 10-15% Ti(OCH(CH$_3$)$_2$)$_4$ is not completely hydrolyzed/polycondensed. No peak resulting from the methoxide groups of MEMO was detected, which indicates that MEMO has completely reacted. Two new peaks at 58.28 and 18.32 ppm are assigned to -CH$_2$- and -CH$_3$ from the -Si(OCH$_2$CH$_3$) group. The two well-defined peaks at 14.22 and 60.64 ppm might result from the presence of a new component which could not be assigned with this spectrum. In order to assign these peaks, complementary NMR studies were performed, and they are reported in the following (Figures 52 and 53).
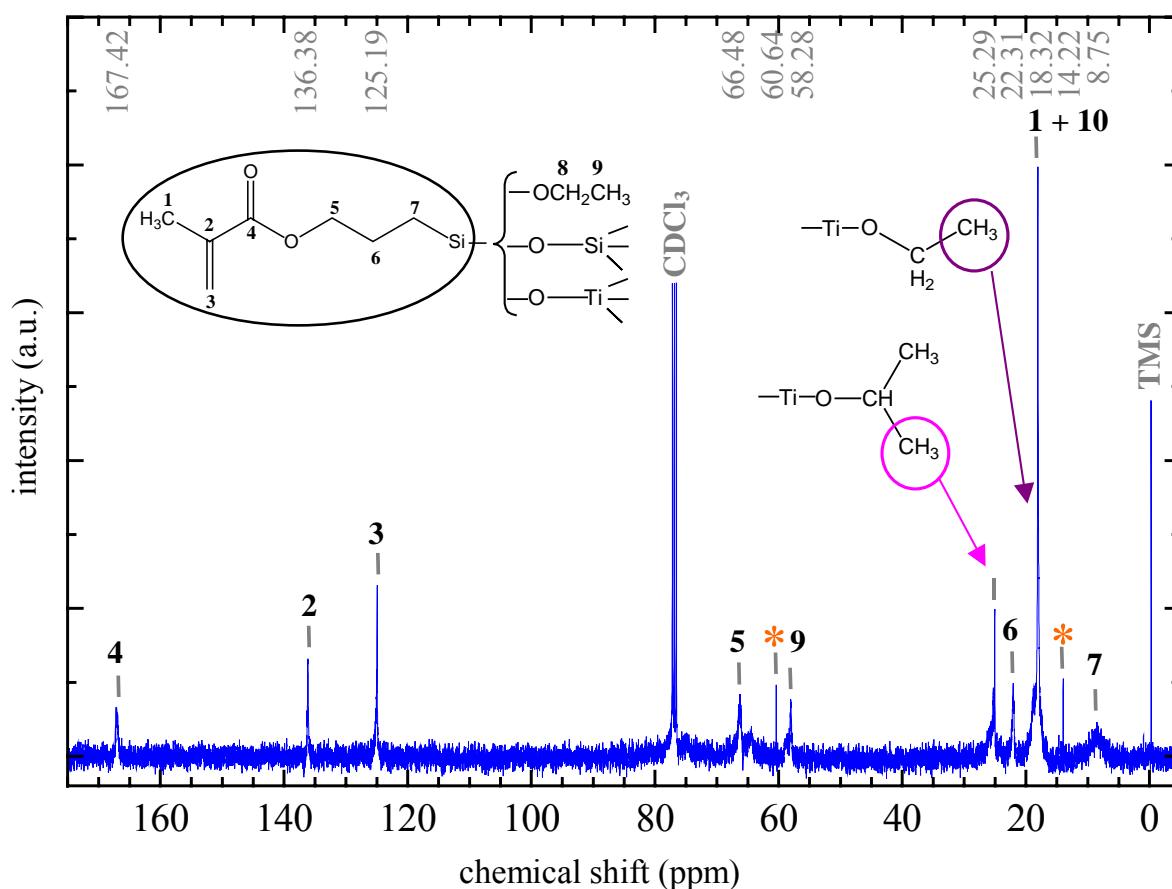
Figure 51: ^{13}C-NMR spectrum of resin PD79, recorded in CDCl$_3$. The different species as well as the carbon atom within these species are labeled.

Resin PD79 was also characterized by ^{29}Si-NMR spectroscopy (Figure 52) in order to obtain more information about the inorganic network. No peak at -42.6 ppm which is characteristic for non-condensed MEMO was detected. MEMO is present as mono-, bi-, and tri-condensed product (T^1, T^2, and T^3) which can be concluded due to three peaks around -53, -61, and -68 ppm, respectively. For the mono- and bi-condensed products, the molecule can contain Si-O-Ti, Si-OR (R = Me or Et), and/or Si-OH groups. It has to be mentioned that the peak width resulting from the different species cannot be reduced by changing the acquisition

parameters of the ^{13}C-NMR spectroscopy measurement. Three peaks at -46.73, -47.02, and -48.30 ppm represent the T^0 species which might also contain Si-O-Ti, Si-OR (R = Me or Et), and/or Si-OH groups.

^{13}C-NMR spectroscopy has proven the absence of Si-OMe groups; thus, MEMO is present as a completely reacted compound in the resin. Also with ^{13}C-NMR spectroscopy, the peaks corresponding to Ti-OEt are still detected in the resin which means that Ti(OEt)$_4$ is not completely hydrolyzed/polycondensed. Thus, the resin will be sensitive to air moisture.
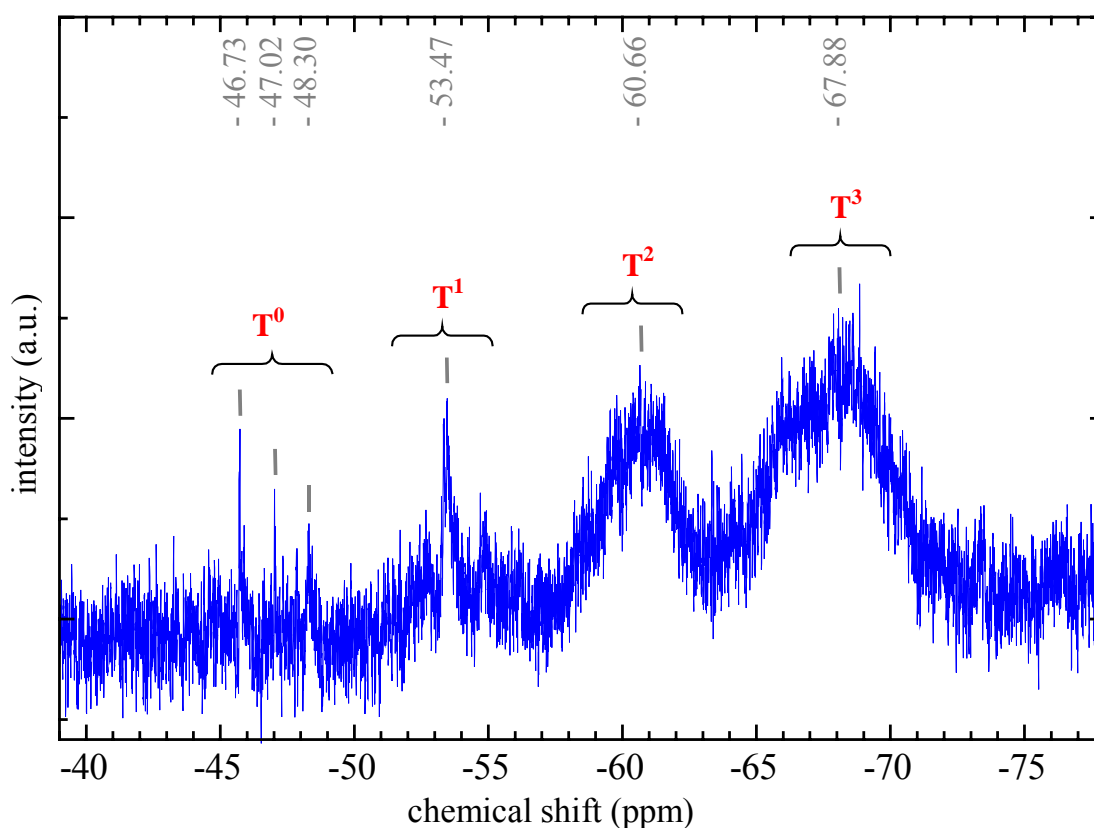
Figure 52: ^{29}Si-NMR spectrum of resin PD79 recorded in CDCl$_3$, with assigned peaks.

In order to assign the two well-defined peaks detected at 14.22 and 60.64 ppm labeled with a red star in the ^{13}C-NMR spectrum of resin PD79 (Figure 51), hydrolysis and polycondensation reactions during the synthesis were investigated at different steps by multi-nuclei NMR spectroscopy. These experiments were performed only for the resin PD113, because the HCl concentration in PD79 and PD49 might be too high in order to follow the hydrolysis and polycondensation reactions. Three specific ^{13}C-NMR spectra were collected (Figures 53 and 54). They are labeled PD113/S40min, PD113/S4h30min and PD113/S24h, and correspond to samples taken from the PD113 synthesis after 40 min, 4h30 min, and 24h after addition of HCl. In order to compare the peak intensities, ^{13}C- and ^{29}Si-NMR spectra (Figure 52, 53, and 54) were normalized using the TMS peak (not shown). The first sample was investigated 40 min after the addition of HCl. This time was chosen, because the mixture MEMO, Ti(OEt)$_4$ led to a milky viscous solution which became a clear dark yellow solution after 4h30min stirring time.
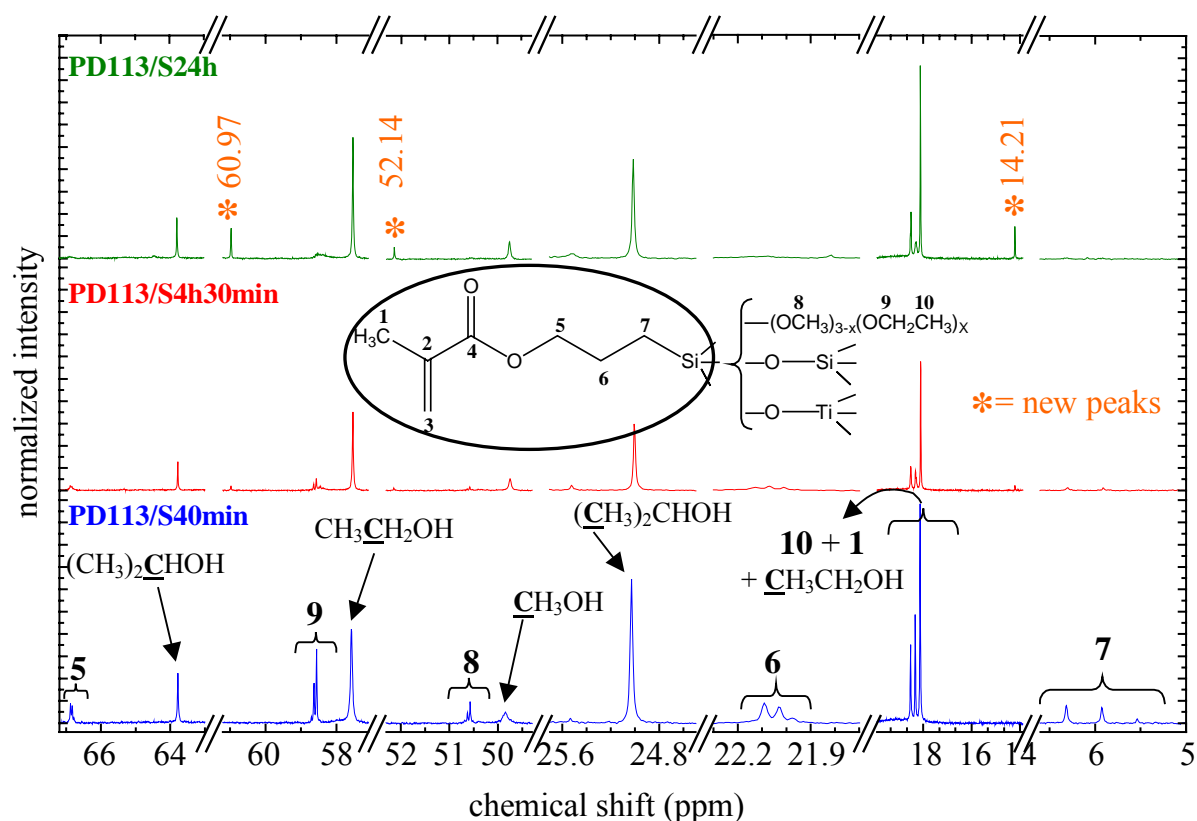
Figure 53: Different zooms (between 5 and 6.6 ppm, 13.9 and 19.9 ppm, 21.7 and 22.3 ppm, 24.5 and 25.7 ppm, 49.3 and 52.3 ppm, 57.1 and 61.2 ppm, and 63 and 67.2 ppm) into the ^{13}C-NMR spectra recorded at different steps during the synthesis of PD113: 40 min (PD113/S40min), 4h30 min (PD113/S4h30min), and 24h (PD113/4h) after the addition of HCl. The TMS peak (not shown) was used to normalize the spectra.

The ^{13}C-NMR spectrum recorded 40 min after the addition of HCl (graph PD113/S40min in Figure 53) shows the presence of peaks from ethanol, isopropanol, and methanol formed by the hydrolysis and polycondensation reactions of MEMO and Ti(OEt)$_4$. The latter contains 10 to 15 % Ti(^{i}PrO)$_4$, and releases ethanol and isopropanol upon hydrolysis. MEMO is not necessarily hydrolyzed, therefore, a direct alkoxy exchange reaction can occur between the methoxy groups of MEMO and ethanol, as already described in chapter 4.1.1.2. Moreover, in the ^{29}Si-NMR spectrum (PD113/S40min in Figure 55), no peak characteristic for hydrolyzed MEMO species was observed. Several carbon peaks which belong to the carbon chain of MEMO (carbon atoms labeled as 5, 6, and 7 in Figure 53) are detected. In addition, carbons of the alkoxy groups of the -Si(OCH$_3$)$_{3-x}$(OCH$_3$CH$_2$)$_x$ units (carbon atoms labeled as 8, 9, and 10 in Figure 53) show multiple signals which prove that an alkoxy exchange reaction between the methoxy groups of MEMO and ethanol took place. After 4h30 min of stirring, the peak intensities of the carbon chain (carbon atoms 5, 6, and 7 in Figure 53) have decreased. In addition, the peaks of the carbon atoms which belong to the methacrylate groups of MEMO (labeled 2, 3, and 4 in Figure 54) became very broad, and their intensities have strongly decreased. The same behavior was observed in the ^{29}Si-NMR spectrum (PD113/S4h30min in Figure 55). These observations indicate that MEMO species have reacted. Moreover, new weak peaks were detected at 14.21, 52.14, and 60.97 ppm (Figure 53) as well as at 126.19, 135.90, and 168.30 ppm (Figure 54) point to the presence of new components formed in a new reaction. It has to be noticed that the new peaks detected at 14.22 and 60.64 ppm in the

^{13}C-NMR spectrum of the resin PD113 (Figure 53) correlate to those detected in the ^{13}C-NMR spectrum of resin PD79 (Figure 51). After 24h stirring, the peak intensities of the peaks recorded at 14.21, 52.14, and 60.97 ppm (Figure 53) as well as at 126.19, 135.90, and 168.30 ppm (Figure 54) have strongly increased, and the peaks characteristic for MEMO species were almost not detected in the ^{13}C- and ^{29}Si-NMR spectra (PD113/S24h in Figures 53 and 54, and PD113/S24h in Figure 55, respectively). On the other hand, the intensities of the peaks at 125.89, 136.19, and 167.86 ppm (Figure 54) increased. This might be attributed to a new component formed during the synthesis of PD113, as already stated above.
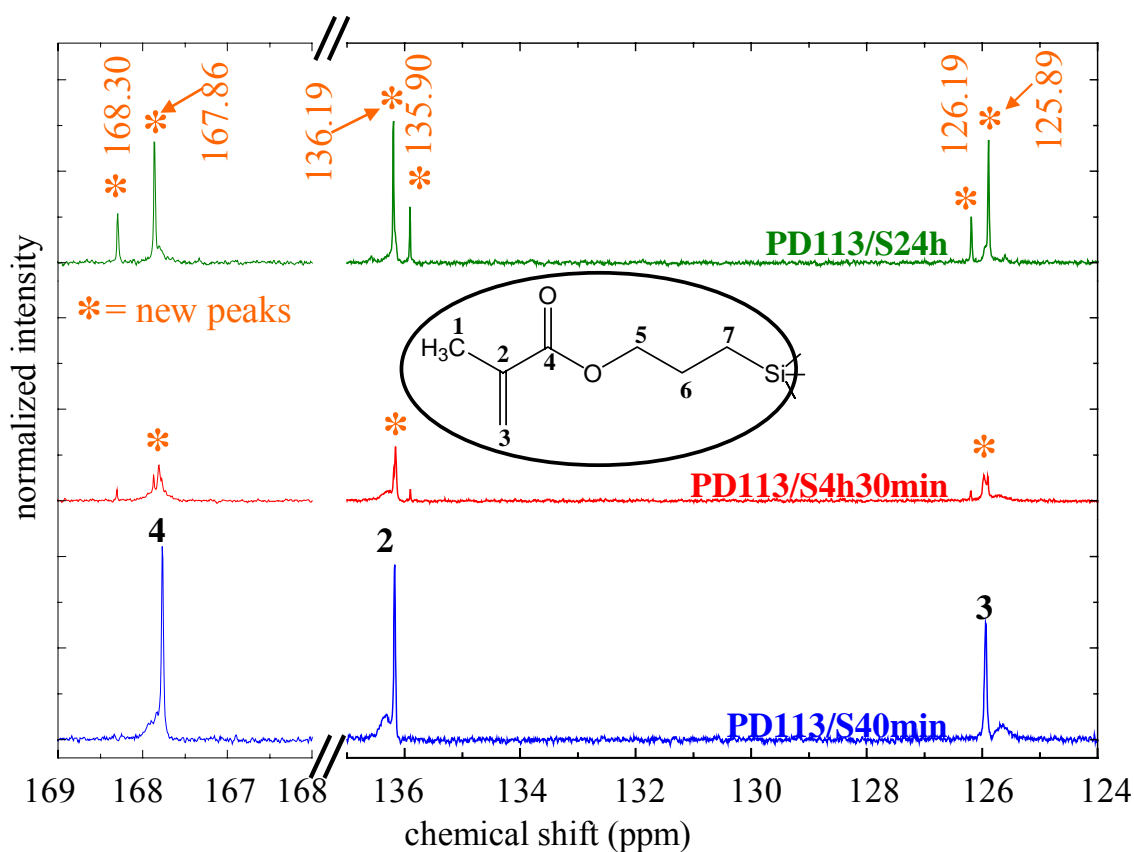
Figure 54: Zooms between 124 ppm and 137 ppm, and 166 and 169 ppm into the ^{13}C-NMR spectra recorded at different steps during the synthesis of PD113: 40 min (PD113/S40min), 4h30 min (PD113/S4h30min), and 24h (PD113/S24h) after the addition of HCl. The TMS peak (not shown) was used to normalize the spectra.
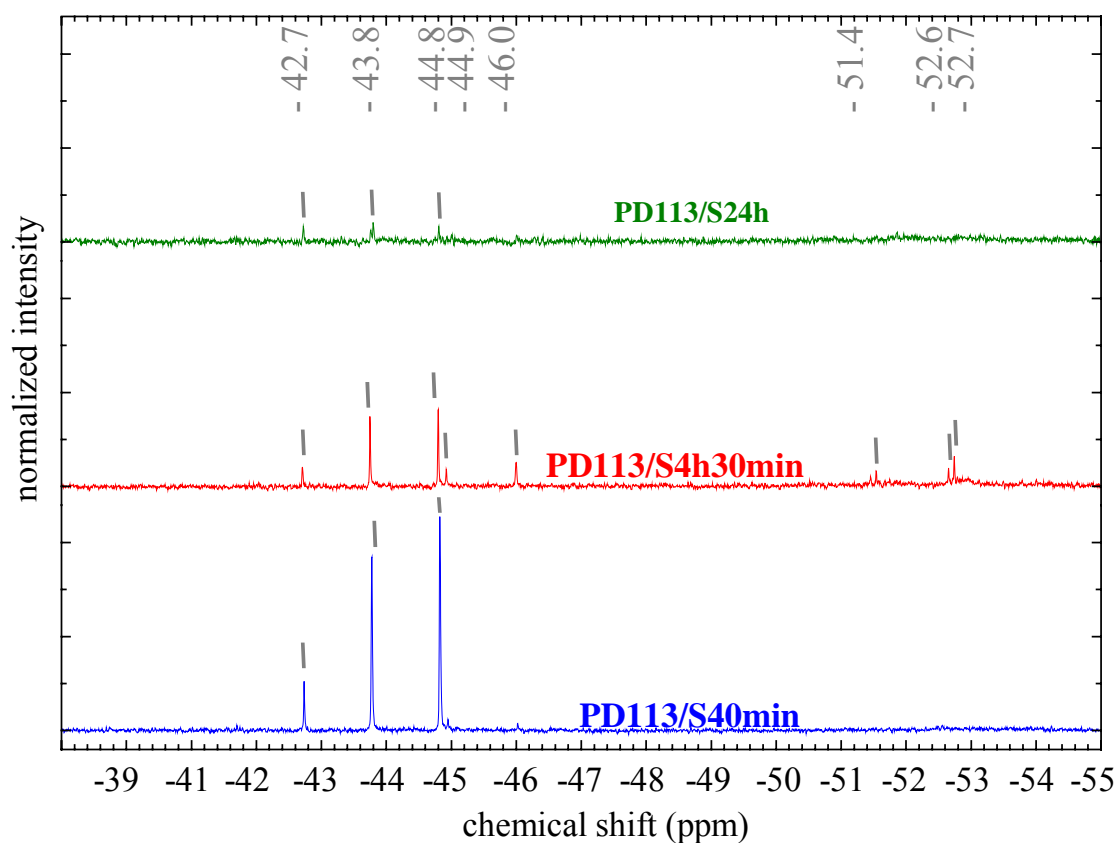
90

Figure 55: ^{29}Si-NMR spectra recorded during the synthesis of PD113: 40 min (PD113/S40min), 4h30 min (PD113S/S4h30min), and 24h (PD113S/24h) after the addition of HCl. The TMS peak (not shown) was used to normalize the spectra.

In order to characterize the products formed during the synthesis of PD113, the volatile species were collected and analyzed by ^{1}H- and ^{13}C-NMR spectroscopy (cf., Figures 56 and 57).
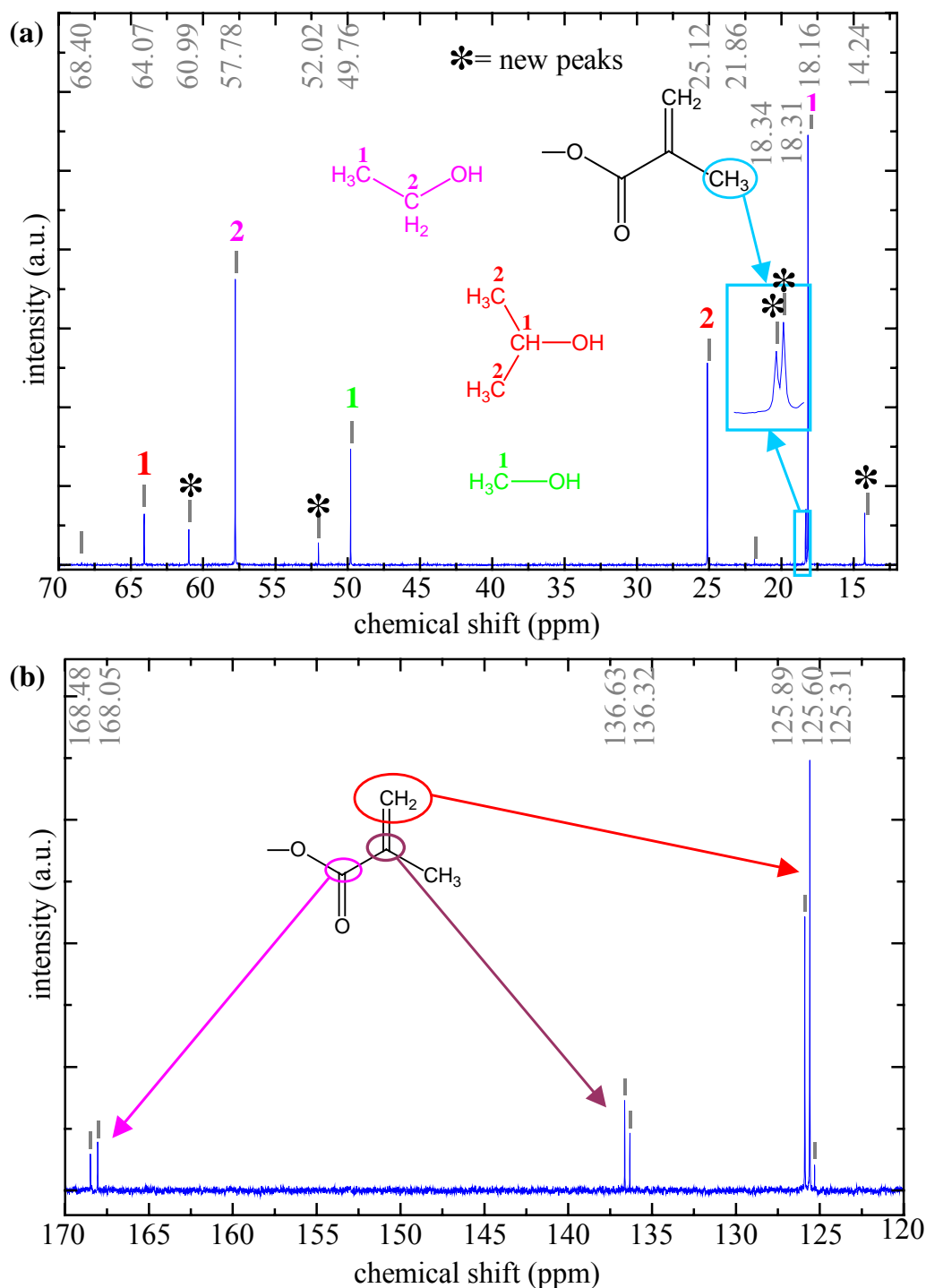
Figure 56: Zooms into the ^{13}C-NMR spectra (in CDCl$_3$) of the components formed during synthesis of PD113, between (a) 14.5 and 70 ppm, and (b) zoom between 120 and 170 ppm. The different peaks are labeled in the spectra.

A zoom into the ^{13}C-NMR spectrum of the volatile species (Figure 56 (a)) shows typical peaks of ethanol at 57.78 and 18.16 ppm, of isopropanol at 25.12 and 64.07 ppm, and of methanol at 49.76 ppm. At 14.24, 52.02, and 60.99 ppm, new peaks were detected. In addition to these three new peaks, eight peaks were attributed to the methacrylate group since

they have nearly the same chemical shift as the methacrylate group of MEMO: two peaks at 168.48 and 168.05 ppm are attributed to C=O, at 136.32 and 136.63 ppm to $\underline{C}$=CH$_2$, at 125.89 and 125.60 ppm to $\underline{CH_2}$=C (Figure 56 b)), and at 18.31 and 18.34 ppm to -CH$_3$ (Figure 56 (a)). One can conclude that MEMO used in the synthesis of PD113 reacted and formed new components containing a methacrylate group.

In the ^{1}H-NMR spectrum of the products formed during the synthesis of PD113 (Figure 57 (b)), signals recorded at 4.20 ppm and at 1.31 ppm reveal the presence of an ethoxy group -O-CH$_2$-CH$_3$.
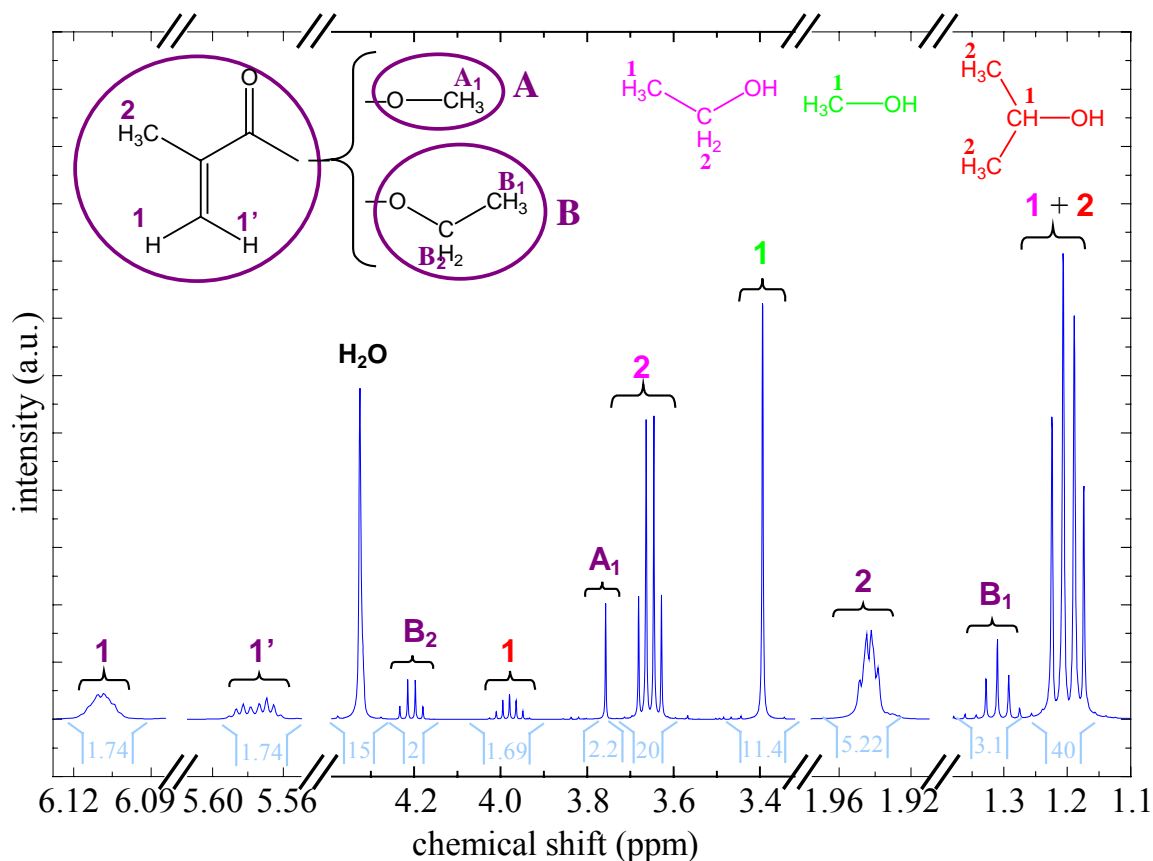

Figure 57: Zooms into the ^{1}H-NMR spectrum (between 1.1 and 1.38 ppm, 4.3 and 4.4 ppm, 5.5 and 5.6 ppm, and 6.08 and 6.13 ppm) of the compounds formed during the synthesis of PD113. The integration of the signals is reported between the graph and the chemical shift axis.

In order to simplify the interpretation of the spectrum, the molecule which is based on this ethoxy group is named B (cf., Figure 57 (b)). The integral of the signal recorded at 4.20 ppm (-O-C$\underline{H}_2$-CH$_3$) is fixed equal to 2, and the integration obtained for the signal at 1.31 ppm is found to be near 3. Thus, the integration of one hydrogen atom of the molecule B corresponds to 1. A single peak at 3.76 ppm with an integration near 2.22 is attributed to the signal of a methoxy group -O-CH$_3$, which belongs to a molecule labeled as A (the integration of one proton of molecule A corresponds to 0.74). In addition, a signal recorded at 3.98 ppm (integration 1.69) attributed to HO-C$\underline{H}$-(CH$_3$)$_2$, is detected. The peaks corresponding to the HO-CH-(C$\underline{H}_3$)$_2$ around 1.2 ppm are overlapped with the signal of the C$\underline{H}_3$-CH$_2$-OH. The integration of the overlapped signal is 40 which corresponds to 10.14 (= 1.69x6H = -O-CH-(C$\underline{H}_3$)$_2$) + 30 (= 10x3H = C$\underline{H}_3$-CH$_2$-OH), and is in good agreement with

the integration of the peaks recorded at 3.62 ppm, corresponding to CH_3-$C\underline{H}_2$-OH. A high peak at 3.39 ppm is attributed to the -OH of ethanol overlapped with $C\underline{H}_3OH$. Another high peak detected at 4.32 ppm is attributed to non-reacted water.

These results are in good agreement with FT-IR spectroscopy, where a broad peak around 3300 cm^{-1} is attributed to the vibrational mode of -OH groups (cf., Figure 50). The two methacrylate units detected in the ^{13}C-NMR spectrum (cf. Figure 56 (b)) are also present with two signals at 6.11 and 5.57 ppm; these are assigned to the -C=CH_2 unit. The integration of each proton of the latter unit is 1.74, which corresponds exactly to the integration of one proton of the molecule A and B (i.e., 1+0.74). Moreover, at 1.94 ppm, a signal corresponding to the -CH_3 unit of the methacrylate group is detected with an integral near 5.22. The latter integration value corresponds to three protons of the molecule A (integration = 1x3) and B (integration = 0.74x3). The combination of the ^{13}C- and ^{1}H-NMR spectra demonstrated that two molecules A and B are based on an ethoxy and a methoxy group as well as a methacrylate group. These two molecules A and B are methylmethacrylate and ethylmethacrylate, which are esters formed during the synthesis of PD113. Thus, the new peaks detected in the ^{13}C-NMR spectrum (cf., Figure 56 (a)) at 14.24 and 60.99 ppm are attributed to -O-CH_2-$C\underline{H}_3$ and -O-$C\underline{H}_2$-CH_3, of ethylmethacrylate (molecule B), and at 52.02 ppm to -O-$C\underline{H}_3$ of methylmethacrylate (molecule A).

For the synthesis of PD113, the hydrolysis and polycondensation reactions of MEMO and Ti(OEt)$_4$ (containing 15 % of Ti(^{i}PrO)$_4$) have led to the formation of methanol, ethanol, and isopropanol. In presence of the acidic catalyst, transesterification reactions took place. MEMO species (containing the characteristic functional unit of an ester) have reacted with methanol and/or ethanol in the presence of 0.01 M HCl which catalyzed the reaction. This corresponds to the conversion of MEMO into methylmethacrylate ((Eq. 18) and/or ethylmethacrylate ((Eq. 19):

$$\text{(Eq. 18)}$$

$$\text{(Eq. 19)}$$
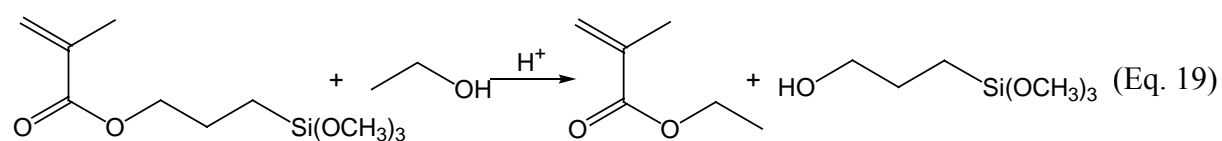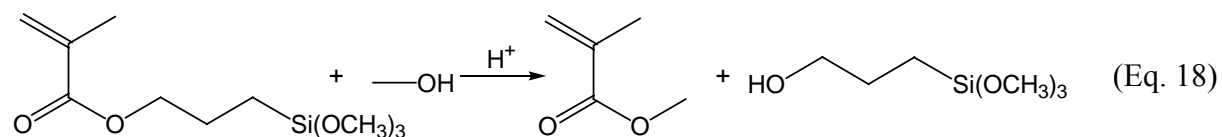
In the resins synthesized with high HCl concentrations (2 M and 12 M for the resin PD49 and PD79), the formation of two new esters also occurred. The transesterification reaction has also led to the formation of a new organo-alkoxysilane component containing an alcohol function. The latter component might be hydrolyzed and condensed with itself, MEMO, or Ti(OEt)$_4$. By means of the NMR or FT-IR spectroscopy, the detection of this new organo-alkoxysilane was not possible due to overlapping peaks. By FT-IR spectroscopy, only a broad peak close to 3300 cm^{-1} which is characteristic of the stretching vibrational modes of -OH groups, shows the presence of the alcohol function and H_2O. The syntheses based on 33 mol-% MEMO and 67 mol-% Ti(OET)$_4$ hydrolyzed with various HCl concentrations (0.01, 2, and 12M, with r = 0.5) have led to transparent coatings. The refractive index of the coatings has increased with the HCl concentration, which might be due to the presence of residual chlorine in the layer. In addition, due to the transesterification reaction of MEMO

with ethanol and/or methanol, new esters (methylmethacrylate and ethylmethacrylate) are also formed during syntheses. As soon as the esters were removed under reduced pressure, the quantity of organic moieties detected in the resins decreased, leading to an increase of the refractive index. The quantity of esters formed might increase with the HCl concentration. Thus, this might explain the large difference of the refractive indices of coatings from resins PD49 and PD79 (n =1.62 at 695 nm and 1.69 at 700 nm, respectively, for coatings cured at 150°C).

Moreover, the refractive indices of the coatings from PD79 increase with the curing temperature. The refractive indices calculated from the transmission spectra (Figure 58) of the coating (labeled as 110105/5, part 3.3.1) cured at 150°C is 1.68 at 1130 nm, and 1.69 at 700 nm (thickness ≈ 500 nm), whereas the refractive indices of the coating cured at 200°C is close to 1.71 at 1090 nm (thickness = 480 nm). Details about the dilution of the resin, and the coating preparation are described in chapter 3.3.1.
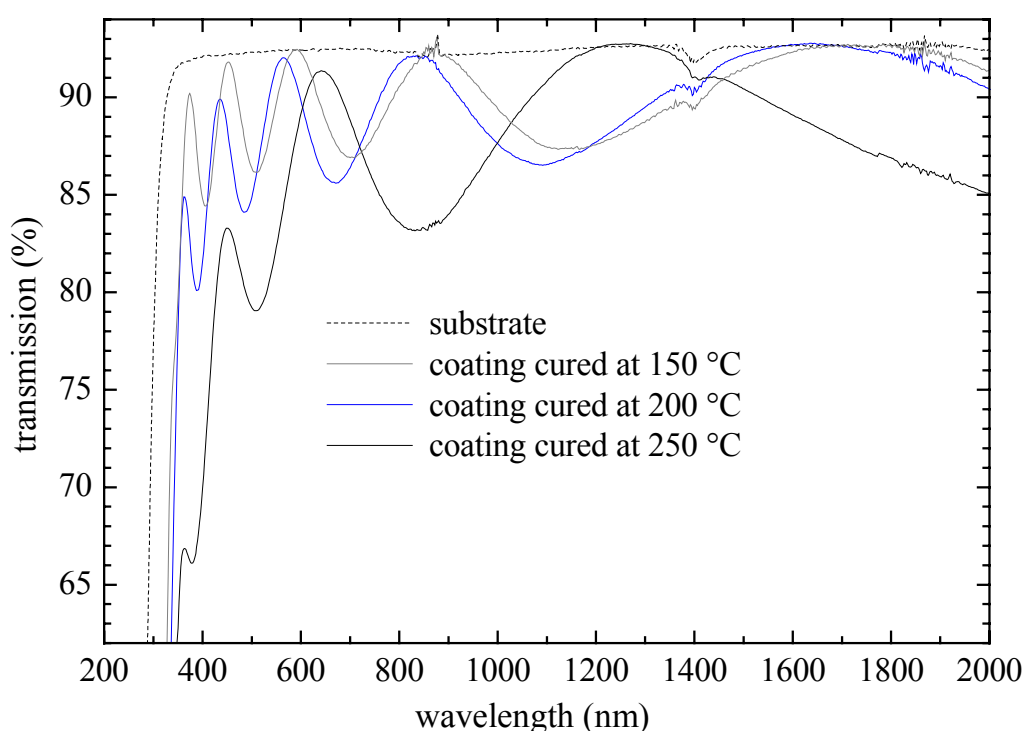

Figure 58: Transmission spectra of a coating prepared from resin PD79 cured up to 250°C (coating labeled 110105/5). The layer thickness was 500 nm after a curing step at 150°C and ≈480 nm after a curing at 200°C. The curing time was 3 hours for each temperature (cf., Table 15, coating 110105/5).

Due to the absorption around 625 nm of the coating cured up to 250°C (Figure 58), the refractive index cannot be calculated by the Swanepoel's technique. On the other hand, the amplitudes of the fringes from the transmission spectra clearly increased between 200 and 250°C, which points to an increase of the refractive index.

4.1.2.1.2 Styrylethyltrimethoxysilane used as organo-alkoxysilane

Based on these results, similar experiments were performed by replacing MEMO by SETMS, which does not have any characteristic functional ester unit. Thus, transesterification reactions like those described in Eqs. 18 and 19 do not take place. Moreover, the refractive index of SETMS is higher than that of MEMO (n_{MEMO}=1.431 and n_{SETMS}= 1.505). Two resins (PD52 and PD60, see section 3.2.2.1) were synthesized from 33 mol-% SETMS and 67 mol-% Ti(OEt)$_4$, with 2M and 12 M HCl as catalyst. The water ratio r_w was fixed to 0.5. In order to study also the influence of the kind of alkoxide in the titanium precursor, Ti(OEt)$_4$ was replaced by Ti(OMe)$_4$ (resin PD77, see section 3.2.2.1). Since Ti(OMe)$_4$ is a solid, the use of a solvent was necessary. However, the choice of solvents was difficult for several reasons. For this synthesis, ketones were avoided due to possible aldol condensation reactions in presence of titanium precursors (cf., section 3.2.2.2). Esters and alcohols were also avoided due to possible transesterification and alkoxy exchange reactions (cf., section 4.1.1.2). THF was used as solvent for the synthesis of resins PD52 and PD60. On the other hand, Ti(OMe)$_4$ was not soluble in THF after three days of stirring, even if the mixture was heated. Thus, acetonitrile was chosen as solvent, and a reflux step was carried out. The optical properties of the resins PD52, PD60, and PD77 are reported in Table 54.

Table 54: Optical properties of the resins PD52, PD60, and PD77, and of their cured ($n_{c\ 150°C}$) and non-cured (n_c) coatings.

Resin n°	Coating n°	n_D^{20} of resin	Optical losses of resin (dB/cm) at 780nm	n_c	$n_{c\ 150°C}$
PD52	1207047/1	1.579	0.520	n.d.	1.71 at 920 nm 1.67 at 1290 nm
PD60	131204/1	1.591	0.044	n.d.	1.70 at 940 nm
PD77	150305/1	----	0.052	1.61 at 1000 nm	1.70 at 930 nm 1.67 at 1200 nm 1.68 at 1680 nm

The refractive indices of the viscous resins PD52 and PD60 were measured with an Abbé refractometer. In addition, the refractive indices were determined according to the Swanepoel's technique (cf., section 2.2.2.4) for coatings prepared from the three resins using their transmission spectra. Figure 59 shows that high transparent coatings are obtained. Details about the dilution of the resins, and the coating preparation are described in chapter 3.3.1.
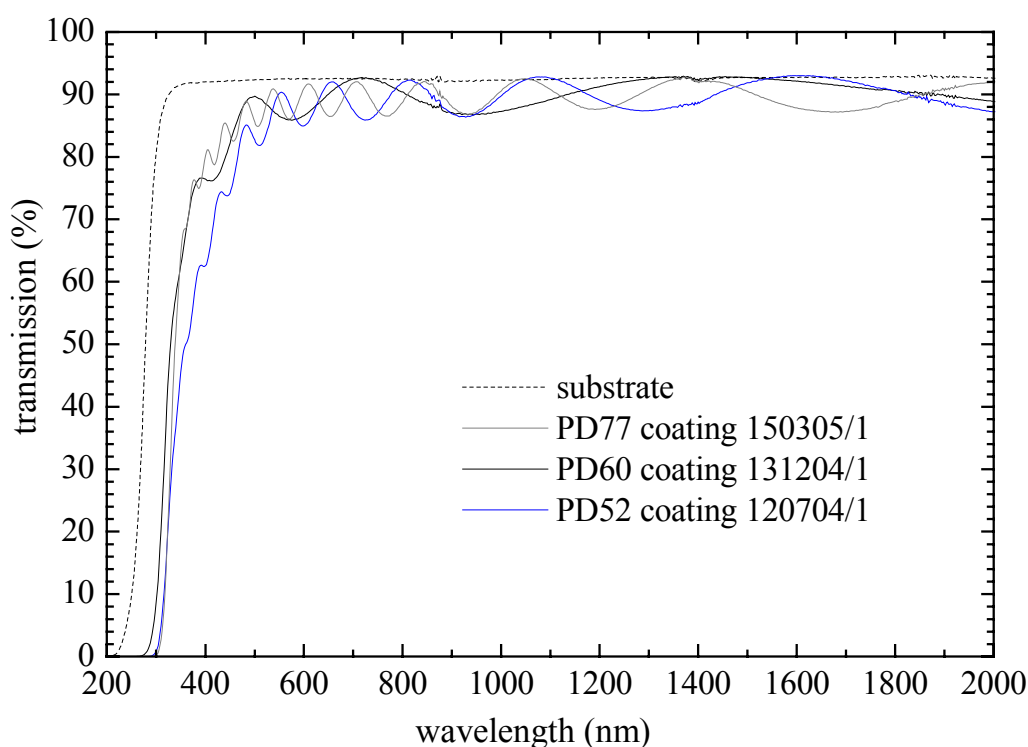
Figure 59: Transmission spectra of a glass substrate and different coatings prepared from resins PD77, PD60, and PD52 on the glass substrates after curing at 150°C for 3 hours.

As already mentioned above, the catalyst concentration in the syntheses is a parameter which affects the optical properties of the resins. The optical losses of the resins are lower for those synthesized with a higher concentration of HCl. For resin PD60 synthesized with 2M HCl, 0.52 dB/cm was measured, whereas for resin PD52 synthesized with 12 M HCl, 0.044 was measured (cf., Table 54). However, for these resins, low optical losses are recorded at the wavelength of the laser used for the 2PP process (Table 54). Thus, they are potentially usable for the 2PP experiments. In section 3.2.2.1, it was reported that the presence of chlorine in inorganic-organic hybrid materials affects their refractive indices. By increasing the concentration of chlorine from 5 mmol to 28 mmol, the refractive index was increased from 1.579 (resin PD52) to 1.591 (resins PD60). It is difficult to conclude of the effect of the titanium alkoxide precursor on the refractive index of the resins since the synthesis of the resin PD77 led to a solid, whereas a viscous material is obtained for resin PD60. Concerning the effect of the titanium alkoxide precursor on the refractive index of the coatings, a direct comparison of the refractive indices measured on the coatings cannot be performed due to the measurement of the refractive index by the Swanepoel's technique which cannot necessarily be performed at the same wavelength. Since, the dispersion curve of the refractive indices of the three resins has to be considered, it is impossible to conclude which resin has a refractive index higher than the other one.

Due to the absorption recorded from the transmission spectra of the non-cured coatings from resins PD52 and PD60, the refractive indices could not be calculated using the Swanepoel's technique. On the other hand, the refractive index of the non-cured coating from resin PD77 was measured, and by curing this coating up to 150°C, the refractive indices of the materials increased from 1.61 at 1000 nm to 1.70 at 930 nm, respectively.

The refractive indices of the coatings cured up to 150°C are higher or equal to 1.70 for wavelengths around 920 to 940 nm. These resins contain organic polymerizable groups, as detected by FT-IR spectroscopy at 1630 cm^{-1} (Figure 61), which can be used for the organic-cross linking by 2PP or UV lithography.

Resin PD77 was also characterized by XRD as synthesized, in order to investigate whether crystalline phases such as anatase or rutile are present in the material. The spectrum shows two large peaks at around 7° and 26° (Figure 60). A peak at 7° cannot be attributed to a crystalline structure. The broad diffraction peak around 26°, present in the non-cured and the cured material was detected. Such broad signal could be attributed to amorphous silica[216].
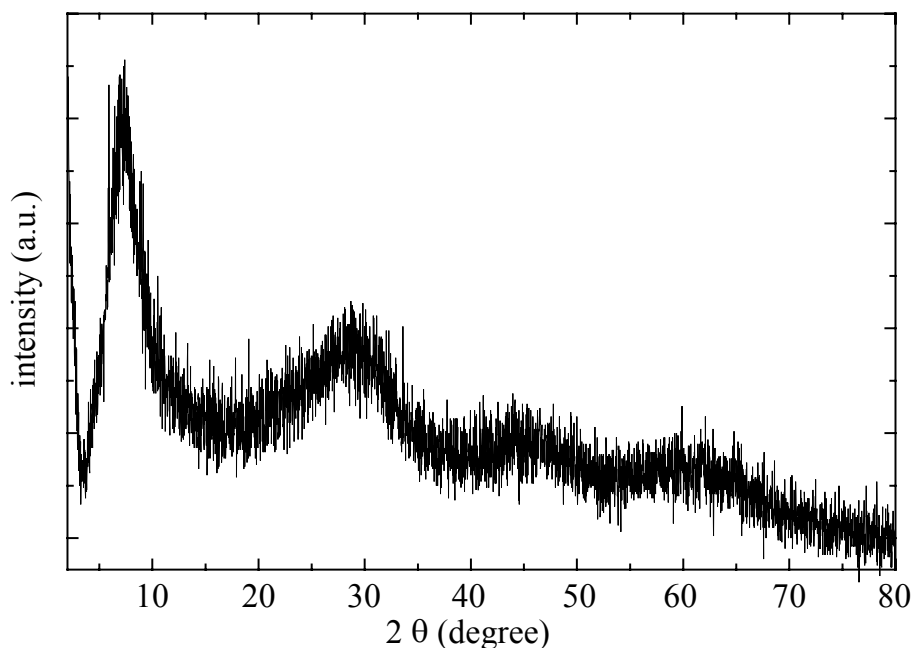

Figure 60: X-ray diffraction pattern of the resin PD77.

The FT-IR spectra of the three resins are very similar (Figure 61). Few -OH groups are detected around 3300 cm^{-1}. As already mentioned for resins PD79 and PD49 in section 4.1.2.1.1, the high HCl concentration used for the syntheses of resins PD77, PD52, and PD60 could inhibit the condensation reactions due to the nucleophilic species (Ti-OH) which can be more or less protonated. The three stretching vibrational modes of C=C corresponding to the aromatic groups of SETMS are detected at 1601, 1581, and 1511 cm^{-1}, respectively. Several broad peaks in the range between 1160 and 1000 cm^{-1} which could correspond to Si-O-Si, Si-O-Ti, Ti-OMe, or/and Si-OMe groups are detected[42,56,105,117,217]. The overlapping of this peaks leads to difficulties in the interpretation of the FT-IR spectra. Thus, multi-nuclei NMR spectroscopy was used in order to better determine the structure of the resins. It has to be noticed that the peaks recorded at 2966, 2819, and 1375 cm^{-1} are detected with a higher intensity in resins PD52 and PD60 than in resin PD77 due to the presence of SiOEt groups. Since these peaks are overlapped to other vibrational modes, a decrease of the intensity in these region is observed in resin PD77 due to the replacement of Ti(OEt)$_4$ from resin PD60 by Ti(OMe)$_4$.
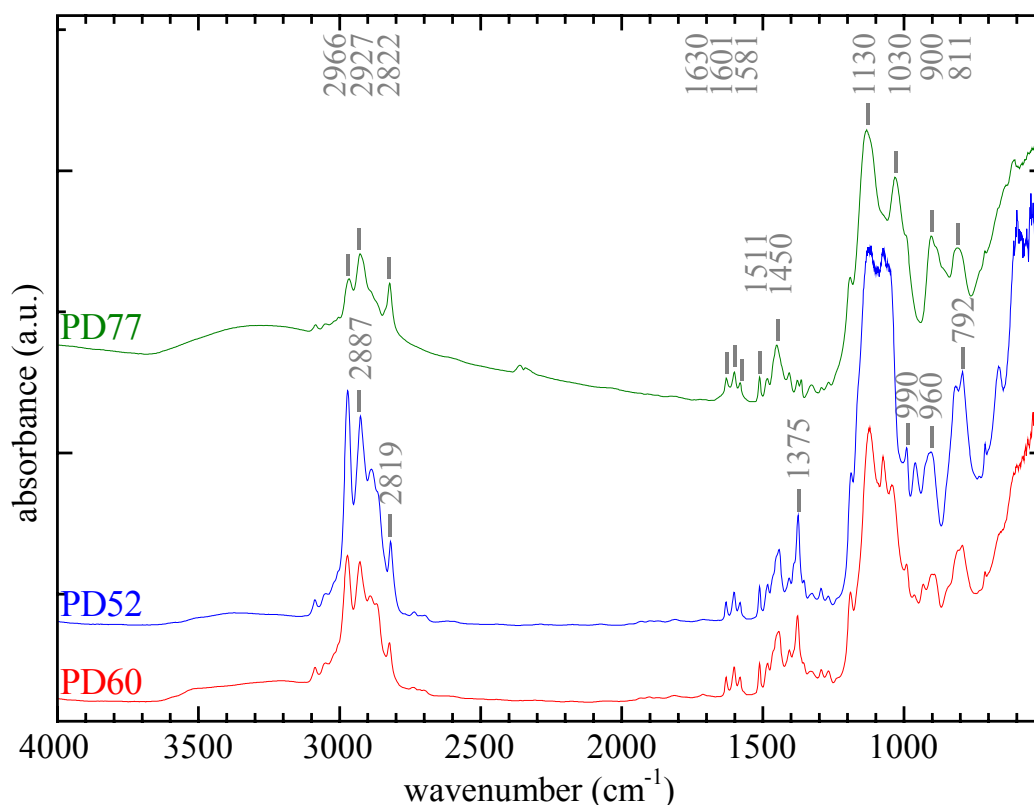
Figure 61: FT-IR spectra of the resins PD52, PD60, and PD77.

The resins PD52, PD60, and PD77 were characterized by multi-nuclei NMR spectroscopy in order to obtain more information about the structure of the resins. Since SETMS is based on a the mixture of the isomers *meta* and *para*, but also on the isomers *a* and *b* (see section 4.1.1.1), overlapped NMR signals were obtained. A **d**istortionless **e**nhancement by **p**olarization **t**ransfer (DEPT) ^{13}C-NMR spectrum of resin PD77 is shown in Figure 62. DEPT spectra give additional information about the number of protons attached to the carbon atoms in the structure. DEPT spectroscopy determines the presence of primary (CH$_3$), secondary (CH$_2$), and tertiary (CH) carbon atoms. On the other hand, quaternary carbon atoms (C) are not detected by DEPT. DEPT spectroscopy has been used complementary to ^{13}C-NMR spectroscopy, because the signals of the carbon atoms from isomers *a* and *b* can be better distinguished. Figure 62 shows the DEPT spectrum of resin PD77, where the peaks pointed upward are attributed to primary and tertiary carbon atoms, whereas those pointed downward are attributed to secondary carbon atoms.

Due to co-condensation reactions of SETMS with itself or with Ti(OMe)$_4$, the signal recorded for the carbon atom linked to the silicon atom (carbon atoms numbered 9a and 10b in Figure 62) were shifted from 25.4 to 25.6 ppm for isomer *a*, and from 11.4 to 14.3 ppm for the isomer *b*, respectively. They are recorded with very broad signals which result from the amount of T species. This is supported by ^{29}Si-NMR spectroscopy (cf., Figure 63).
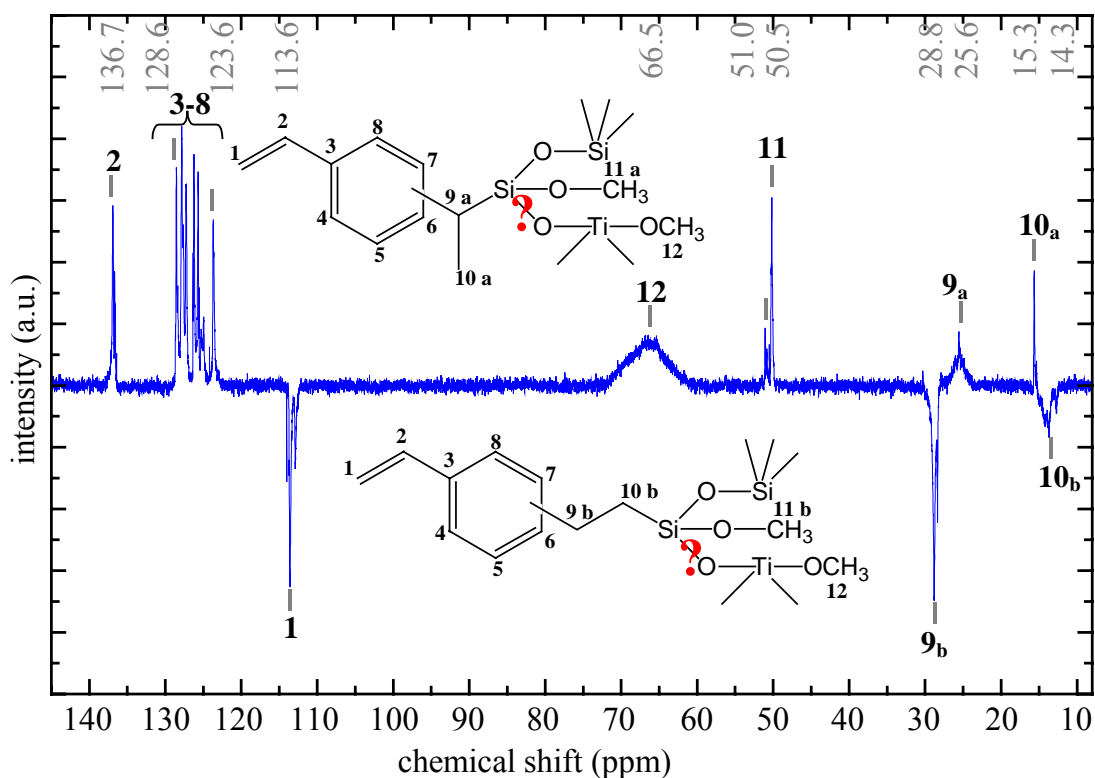
Figure 62: DEPT ^{13}C-NMR spectrum of resin PD77 recorded in CDCl$_3$. The peaks are assigned according to the carbon atoms in the SETMS structures presented as insets.

The signals recorded at 50.5 and 51.0 ppm are attributed to carbon atoms of the methoxy groups of SETMS (carbon atoms numbered 11a and 11b in Figure 62), which shows that the SETMS is not completely condensed. The very large peak around 66.5 ppm belongs to the methoxy group of Ti(OMe)$_4$. The peaks detected between 123.6 and 128.6 ppm are attributed to the carbon atoms belonging to the aromatic groups from the isomer mixture of SETMS. The signals of the carbon atoms resulting from the organic polymerizable groups -CH=CH$_2$ are detected around 113.6 ppm and 136.7 ppm for -CH=$\underline{C}$H$_2$, and -$\underline{C}$H=CH$_2$, respectively.

The ^{13}C-NMR spectra of resins PD52 and PD60 (not shown) are very similar to that of resin PD77. The only difference is due to the titanium precursor used. The signal from carbon atoms from methoxy groups are not detected in resins PD52 and PD60, since Ti(OEt)$_4$ was used as precursor. On the other hand, the signals of the carbon atoms from the -Si(OCH$_2$CH$_3$) unit were detected in resin PD52 and PD60. The latter signals were formed by the alkoxy exchange reaction between the methoxy groups of SETMS and the ethoxy groups of Ti(OEt)$_4$.

^{29}Si-NMR spectra of the resins PD77 and PD52 shown in Figure 63 show some dissimilarities. The ^{29}Si-NMR spectra of resin PD77 shows four main regions. At -42.72 ppm, the T^0$_{(OMe)(OMe)(OMe)}$ species of SETMS is detected, which means that SETMS has not completely reacted. Around -51.2 ppm, T^1 species are recorded, while between -56.5 and -61.5 ppm and -64.0 and -70.5 ppm, T^2 and T^3 species are detected, respectively. The T^2 region recorded in resin PD77 is very broad compared to that detected for the hydrolysis of SETMS (recorded between -58.0 and -60.0 ppm, see section 4.1.1.3). This broad peaks could be attributed to the presence of Ti-O-Si bonds in resins PD77.

The regions detected in the ^{29}Si-NMR spectrum of resin PD52 are not well superposed to those from resin PD77, which shows that the inorganic networks are different. The peak detected around -45.5 ppm is attributed to $T^0_{(OEt)(OEt)(OEt)}$ species, obtained from the alkoxy exchange reaction between the methoxy groups of SETMS and the ethoxy groups of Ti(OEt)$_4$, already found for the ^{13}C-NMR spectrum of resin PD52. The two broad peaks detected around -46.7 and -47.0 ppm cannot be attributed to T^1 species, which were recorded between -50.6 and -48.3 ppm in the hydrolysis of SETMS (cf., chapter 4.1.1.3). They also cannot be attributed to T^0 species due to their too small chemical shifts. On the other hand, they might be attributed to T^0 species containing Si-O-Ti bonds. The latter bonds have been reported to affect chemical shifts in ^{29}Si-NMR spectroscopy[108]. The peak recorded around -52.6 ppm might be attributed to T^1 species containing ethoxide groups such as, for example, $T^1_{(OMe)(OEt)}$ or $T^1_{(OEt)(OEt)}$. On the other hand, the chemical shift of the two peaks detected around -53.9 and -55.3 ppm are too high to be attributed to T^2 species or to low for T^1 species (cf., Figure 46, section 4.1.1.3), unless that the T^1 species are based on Ti-O-Si bonds. At least, the two large peaks recorded around -60.2 and -61.6 ppm could be attributed to T^2 species such as, for example, $T^2_{(OEt)}$ or $T^2_{(OTi)}$. The four peaks around -49.0 ppm were already detected in the SETMS precursor (cf., Figure 40, section 4.1.1.1), and were attributed to T^1 species and/or to impurities within the SETMS precursor. They are detected only in the resins PD77.
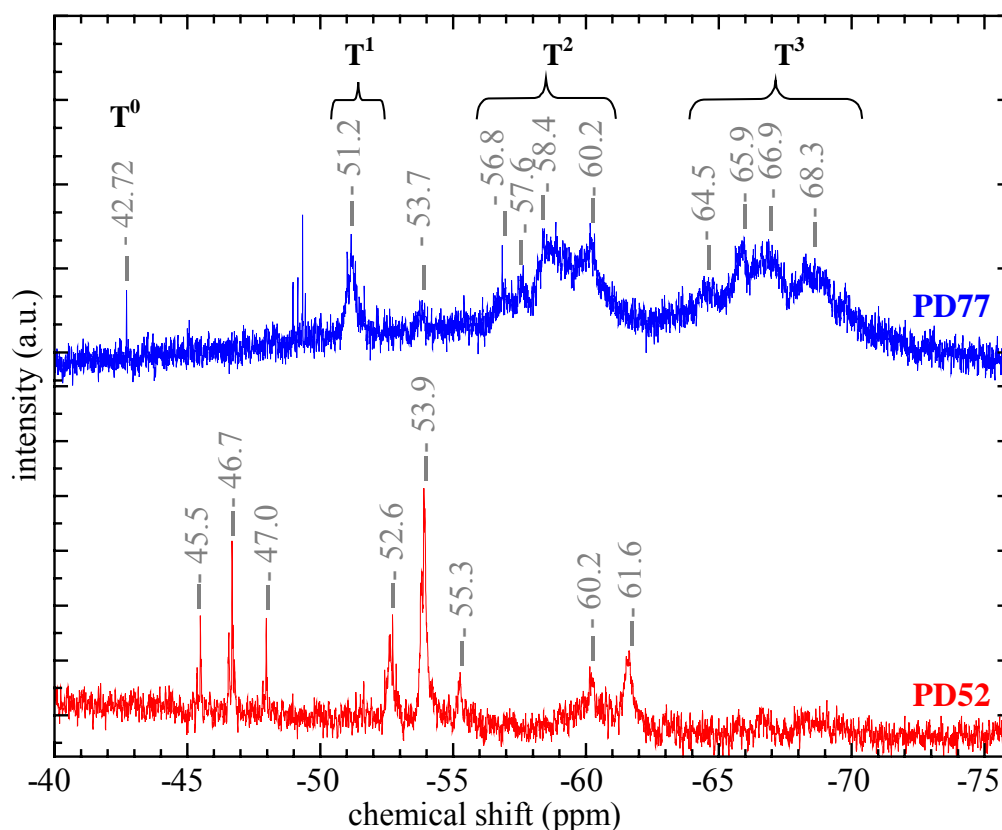

Figure 63: ^{29}Si-NMR spectra of resins PD52 and PD77 recorded in CDCl$_3$. TMS was used as internal reference.

^{29}Si-NMR spectroscopy of resins PD77 and PD52 shows that catalyst concentration as well as the kind of titanium alkoxide precursor are parameters which affect the polycondensation reactions. Since broad signals are obtained for both resins, the attribution of the signals has to

be based on many hypotheses. Particularly, the existence of the Si-O-Ti bonds is assumed, which was reported in the literature from some groups[107-109] (cf., section 2.1.3.2). Thus, the polycondensation reactions between SETMS and Ti(OMe)$_4$ or Ti(OEt)$_4$ cannot be proven for certainty.

On the other hand, due to the presence of organic polymerizable moieties detected by FT-IR and the ^{13}C-NMR spectroscopy which should be used for organic cross-linking (cf., chapter 3.3.1), and due to their high refractive index after a curing at 150°C, these materials present good and promising properties for optical device processing.

Since PD77 is higher condensed than PD52, this resin was chosen for the investigation of its refractive index dependence on the curing temperature and on UV irradiation (cf., chapter 4.2.1.2). The evolution of the refractive index with the curing temperature was investigated for thermally treated coatings. Moreover, resin PD77 possesses highly condensed species detected by ^{29}Si-NMR (cf., Figure 63), which are known from the literature to significantly improve the organic polymerization. Croutxé-Barghorn et al.[178] reported that almost no organic polymerization is achieved with materials presenting a low degree of condensation.

A coating from resin PD77 (coating labeled as 150305/1, part 3.3.1) was cured at different temperatures from 50 to 450°C. The coating preparation and the curing process are described in detail in chapter 3.3.1 (Table 14). Beyond 450°C, crack formation was observed. The transmission spectra collected at each temperature are shown in Figure 64. The strong increase of the amplitude of the fringes with the curing temperature implies an increase of the refractive index of the coating. The strong absorption observed for coating cured up to 350°C is due to annealing of the organic compounds, and thus to an increase of the quantity of titania in the coating. Titania is known to strongly absorb in the UV regim[55,182].
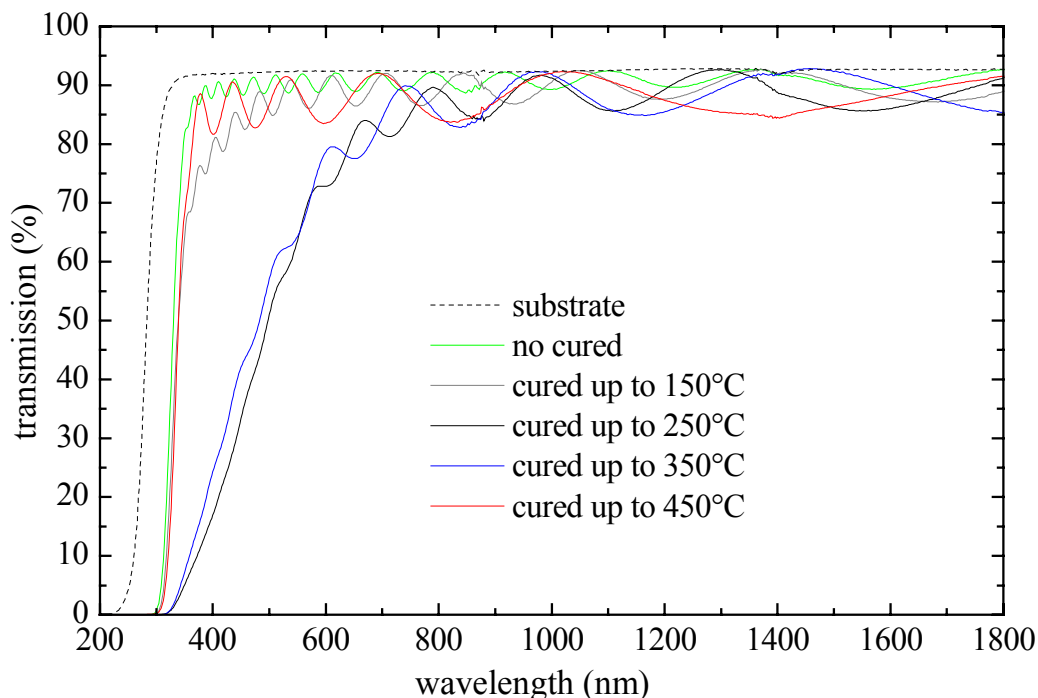

Figure 64: Transmission spectra of the non-coated and coated substrate (coating 150305/1) with resin PD77, non-cured and cured up to 450°C (cf., section 3.3.1, Table 14).

The high transparency of the coating allowed the calculation of the refractive index and the thickness of the coating for each temperature with Swanepoel's technique (cf., section 2.2.2.4). It has to be pointed out that the refractive index of the coating cannot be determined for the same wavelengths in order to allow a direct comparison of the refractive index values of the different materials. The general evolution of refractive index and coating thickness with the curing temperature are reported in Figure 65 (refractive indices, wavelengths, thickness values are reported in more detail in chapter 3.3.1, Table 14). For the non-cured coating, the refractive index is close to 1.61 at 1000 nm, while it continuously increases with temperature and annealing time. It becomes close to 1.75 at 1360 nm for the coating cured up to 450°C, whereas the thickness of the coating decreased from 1700 nm to 580 nm, respectively.
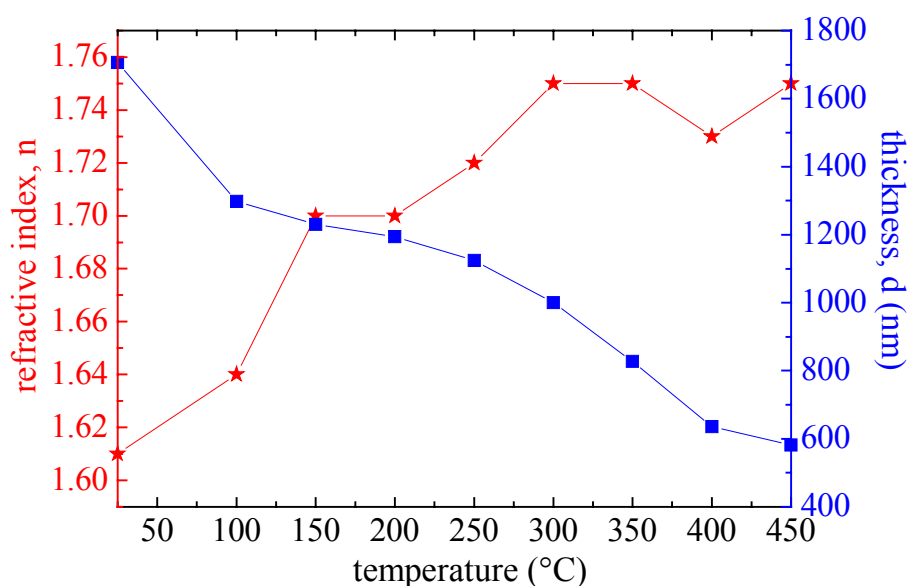

Figure 65: Evolution of the refractive index and the thickness of a PD77 coating (labeled 150305/1, part 3.3.1) on a glass substrate in dependence of the annealing temperature.

In order explain the increase of the refractive index with the annealing temperature, FT-IR spectra were recorded using resin PD77 after different annealing temperatures (Figure 66). It is obvious that the intensities of the stretching vibrational modes of the $\equiv$CH, $=CH_2$, and $-CH_3$ groups around 2900 cm^{-1} decrease with increasing curing temperature pointing to the decomposition of the organic compounds. For samples cured at 400°C, they were no longer detected, i.e. these organic groups were completely removed. On the other hand, vibrational modes around 3430 and 1616 cm^{-1}, corresponding to -OH groups and to H_2O increase with the curing temperature[218]. This indicates that the material absorbs moisture. At 400°C, a broad peak between 420 and 1270 cm^{-1} is detected in the FT-IR spectrum, with three maxima around 430, 925, and 1044 cm^{-1}, and a shoulder around 1178 cm^{-1}. The peak at 430 cm^{-1} is attributed to the vibration of the Ti-O-Ti[219,220] overlapped with the bending vibrational mode of Si-O-Si[103,110,221]. The Si-O-Si stretching vibrational mode is detected at 1044 cm^{-1}[100,155,218-220,222,223]. Due to the presence of the vibration of -OH groups close to 3600 cm^{-1}, it is difficult to confirm that the peak at 925 cm^{-1} is attributed to the Si-O-Ti vibration[7, 10, 21, 24-26, 28-32, 34-38] or to the Si-OH bending vibration[100,155,218,220,223,226], which are reported to be in the same range of wavenumbers.

FT-IR spectroscopy of resin PD77 with the annealing temperature shows that the high increase of the refractive index between the non-cured coating and those cured up to 300°C, reported in Figure 65, is mainly due to the pyrolysis of the organic compounds, leading to a higher densification which also is supported by a significant decrease of the layer thickness.
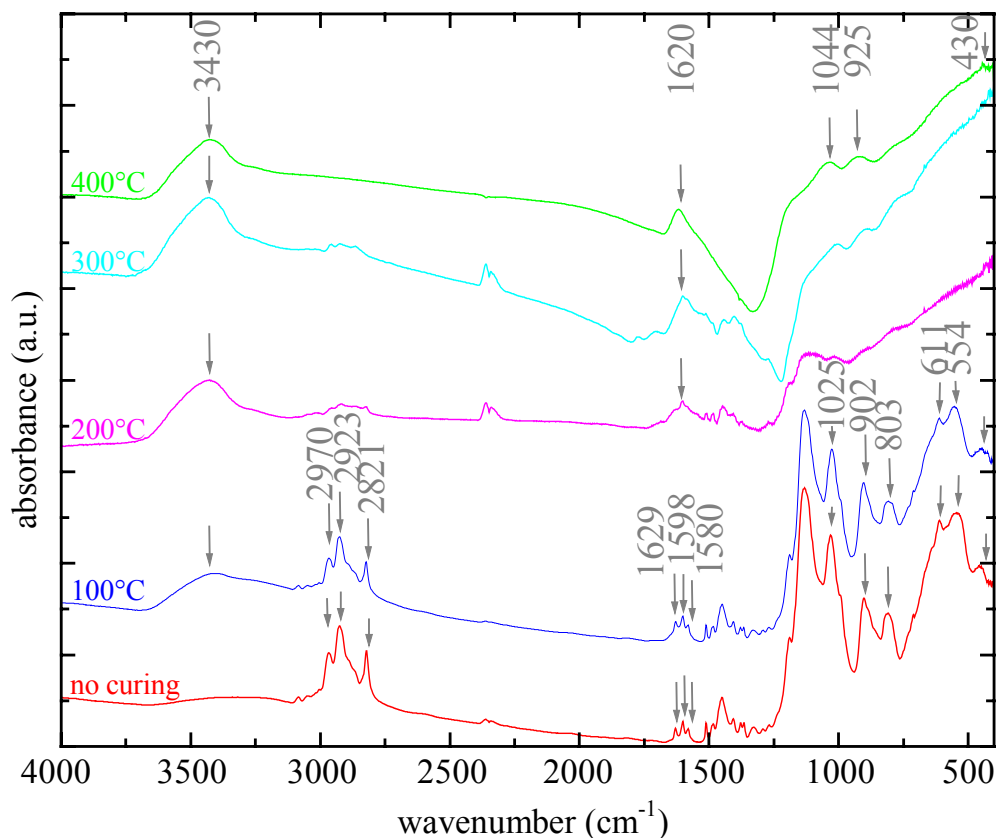

Figure 66: Evolution of the FT-IR spectra of resin PD77 with the curing temperature in comparison to the non-cured resin.

In another synthesis, the Ti content within the inorganic-organic hybrid material was increased up to 90 mol-%, using SETMS (10 mol-%) and Ti(OEt)$_4$ (90 mol-%) (cf. chapter 3.2.2.1) The resulting transparent resin was labeled as PD56.

In Figure 67, an FT-IR spectrum of resin PD56 is presented which has a broad peak around 3250 cm^{-1}, being attributed to the vibrational mode of -OH. This vibrational mode is attributed to Ti-OH or Si-OH bonds, since no water was detected by Karl-Fischer titration. In the range between of 1160 and 1040 cm^{-1}, several broad peaks are observed which could correspond to Si-O-Si, Si-O-Ti, and/or Ti-OEt groups [42,56,105,117,217]. The peaks near 600 cm^{-1} are attributed to Ti-O-Ti bonds[42,217]. No ^{29}Si-NMR spectrum was recorded because of the small quantity of Si within the resin which would lead to a too noisy spectrum. With ^{13}C-NMR measurements (data not shown), no -Si(OCH$_3$) groups were detected, which points to reacted SETMS. Two news peaks recorded at 58.4 and 18.6 ppm were detected which were attributed to signals from carbon atoms of -Si(OCH$_2$CH$_3$) groups. This confirms an alkoxy exchange reaction between SETMS and Ti(OEt)$_4$, as already stated in this section for resin PD77, and also in section 4.1.1.2 in the characterization of the SETMS precursor.
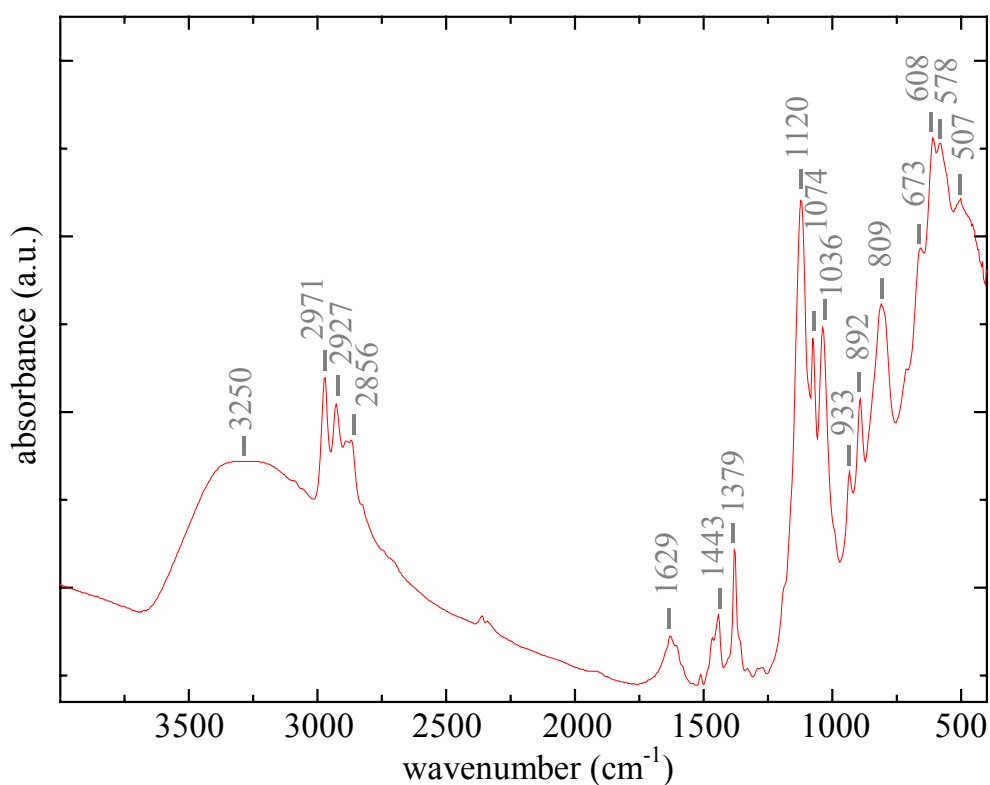
Figure 67: FT-IR spectrum of resin PD56.

The absorption loss of PD56 was determined by UV-VIS spectroscopy to be around 0.38 dB/cm at 780 nm. The coating of a glass substrate was carried out (cf., section 3.3.1, Table 12), and the refractive index of the coating was determined from the transmission spectrum (Figure 68) to be as high as 1.84 at 1820 nm (thickness ≈ 0.25 µm). The increase of concentration of the titanium precursors in the hybrid organic-inorganic material has considerably increased the refractive index. In addition, due to the dispersion behavior of the refractive index, which typically increases by decreasing the wavelength (normal dispersion), a refractive index much higher than 1.84 is expected in the range between 400 and 700 nm. It has to be mentioned, however, that resin and coating are very sensitive to moisture due to the presence of ≡Ti(OEt) groups in the resin, which can further react with moisture. This also results in the observation that the synthesis was found to be poorly reproducible, thus the UV processing of resin PD56 was not investigated in more detail.
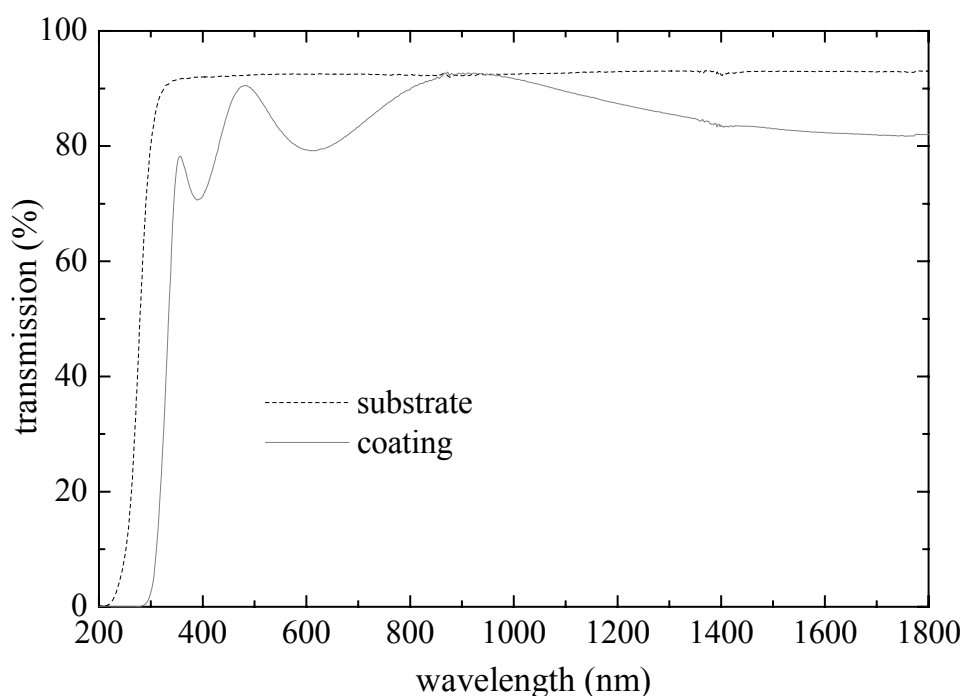
Figure 68: Transmission spectra of a substrate and the coated substrate (labeled as 040804/2, part 3.3.1) from resin PD56, cured at 150°C for three hours.

In order to reduce the sensitivity of the highly inorganic hybrid resin against moisture, a chemical modification of the $Ti(OEt)_4$ precursor with a complexing ligand was carried out (cf., chapter 4.1.3).

4.1.2.2 Resins based on three components

A resin based on MEMO (50 mol-%) and DPD (50 mol-%), commonly referred to as ORMOCER® I[77] in the literature, can be patterned either by conventional UV lithography with a mask aligner[22] or by femtosecond laser pulses making use of a two-photon polymerization (2PP) process[17,19]. Based on ORMOCER® I, new syntheses were developed by replacing part of MEMO by $Ti(OEt)_4$, which should allow to increase the refractive index of the resulting material. For ORMOCER®I, the refractive index is close to 1.55 at 633 nm[17,19].

4.1.2.2.1 [3-(methacryloyloxy)propyl]trimethoxysilane used as polymerizable organo-alkoxysilane

In order to mix MEMO and DPD, the use of a solvent is required to dissolve DPD which is a solid component. The hydrolysis was performed by adding water, where the ratio r_w was fixed to 0.5, and then $Ti(OEt)_4$ was added to the blend. Milky solutions or milky gels were obtained if isobutyl acetate, butanone, cyclopentanone, and/or methyl-isopropylester were used as solvent for syntheses. On the other hand, light yellow transparent solutions were obtained with THF as solvent (PD92). Syntheses performed without water, but with butanone or

cyclopentanone as solvent have yielded milky yellow solutions or dark orange transparent solutions, respectively (PD5). In order to explain this observation, the two syntheses PD92 (performed in THF, with water) and PD5 (in cyclopentanone, without water) were investigated in more detail.

Due to the fact that resin PD92 was a light yellow solid, whereas PD5 was a dark brown and viscous resin, the direct comparison of the refractive indices of the resins was not possible. Thus, the refractive indices of both materials were determined for their coatings. In order to show the influence of Ti(OEt)$_4$ on the refractive index, a new synthesis (PD114) was performed, where TEOS was used instead of Ti(OEt)$_4$. Table 55 summarizes the optical properties of the resins PD5, PD92, and PD114 as well as of their coatings. The attenuation measured at the wavelength of the 2PP laser (780 nm) was determined to be between 0.014 and 0.35 dB/cm which allows one to perform 2PP experiments with these resins.

Table 55: Optical properties of the resins PD5, PD92, and PD114, and their for 3 hours cured ($n_{c\,150°C}$) and non-cured (n_c) coatings.

Resin n°	Coating n°	n_D^{20} of resin	Optical losses of resin (dB/cm) at 780nm	n_c	$n_{c\,150°C}$
PD92	070605/1	solid	0.014	1.60 at 950 nm 1.59 at 1120 nm	1.62 at 960 nm 1.60 at 1170 nm
PD114	---	1.555	0.038	n.d.	n.d.
PD5	241104/1	1.59	0.35	1.58 at 1550 nm	1.60 at 1460 nm

The optical loss at 780 nm of resin PD92 is 20 times lower than for resin PD5. The replacement of 33 mol-% TEOS by 33 mol-% Ti(OEt)$_4$ leads to an increase of the refractive index. The curing step up to 150°C for three hours increased the refractive indices of the coatings of PD5 and PD92 as expected due to the densification of the layers and the evaporation of solvents, which typically have refractive indices close to 1.407 and 1.384 for THF and propylacetate, respectively. In order to follow the refractive index in dependence of the annealing temperature, the samples were heated up to the temperature where crack formation occured. PD92 coatings could be cured up to 200°C. Beyond this temperature, the coatings cracked. The refractive index of the non-cured coating is close to 1.60 at 950 nm and 1.59 at 1120 nm, while it is with 1.61 at 1040 nm slightly increased after the curing step at 200°C. By curing the coating up to 200°C, the thickness decreased about 25% (from 1930 to 1450 nm). This implies a further densification of the material, and thus an increase of its refractive index.

The three resins PD5, PD92, and PD114 were characterized by FT-IR spectroscopy (Figure 69). The spectra are very similar. The three spectra were normalized to the bending vibration (1430 cm^{-1}) of the -CH from the phenyl groups of DPD. The absence of the absorption in the range between 3200 and 3700 cm^{-1} indicates that the materials obviously have a very low -OH content, below the detection limit of the method.
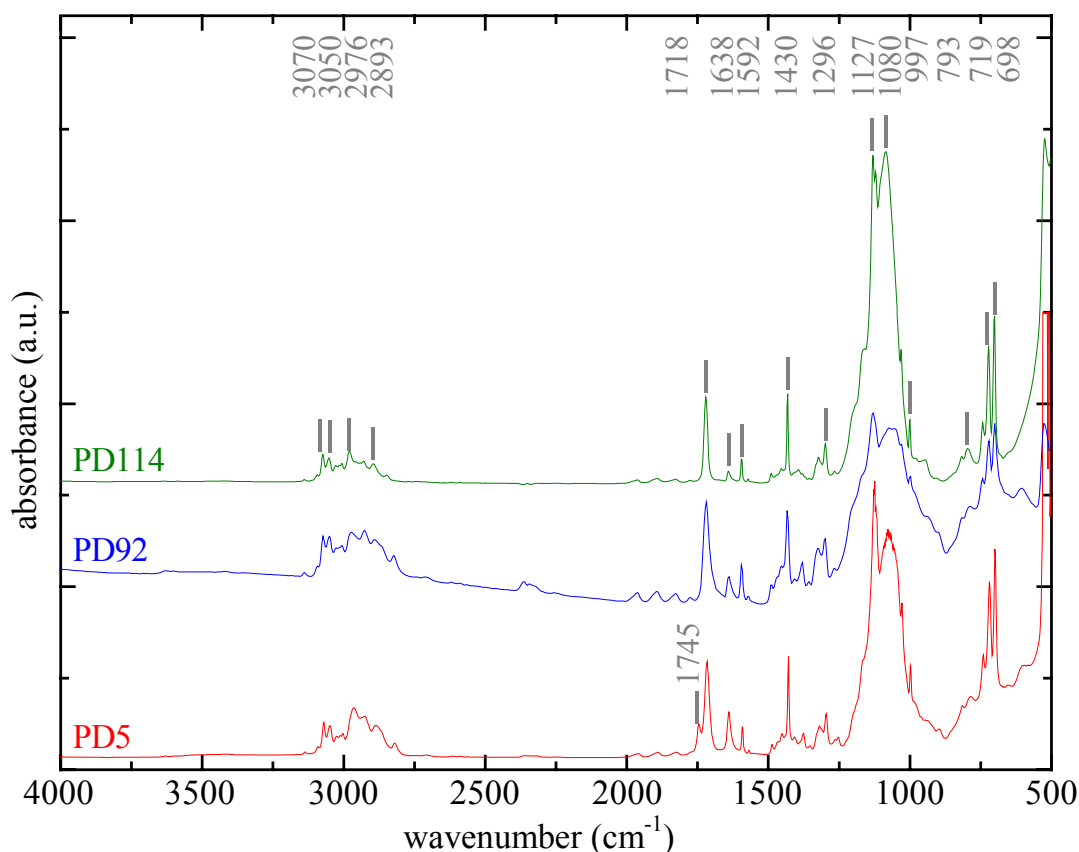
Figure 69: FT-IR spectra of the resins PD92, PD5, and PD114.

Thus, it can be concluded that ≡Si-OH and ≡Ti-OH species are nearly absent. Stretching vibrational modes were detected at 1717 and 1636 cm^{-1} corresponding to the C=O and C=C of MEMO. The latter is typically used for photochemically induced organic polymerization, which is described in more detail in chapter 3.3. The FT-IR spectrum of resin PD5 shows an additional peak at 1745 cm^{-1} which is due to the stretching vibrational mode of C=O from cyclopentanone. The latter component could not be completely removed from resin PD5 even under reduced pressure. A broad peak with a high intensity between 1230 and 900 cm^{-1} was detected for all three resins. This is due to different overlapping vibrational modes, such as an Si-O-Si asymmetric stretching vibration, as reported in the literature between 1040 and 1120 cm^{-1} for the LO (**l**ongitudinal **o**ptical) component, and between 1180 and 1220 cm^{-1} for the TO (**t**ransversal **o**ptical) component[100,101,103,218-220,223,224]. This indicates that an inorganic condensation occurs between the organo-alkoxysilane compounds for these resins. Furthermore, the Si-O-C stretching and bending modes from non-hydrolyzed alkoxides, reported between 940 and 950 cm^{-1} for the bending mode[98,101], and between 1180 and 1000 cm^{-1} for the stretching mode[188,224] contributed to the broad peak between 1230 and 900 cm^{-1}. The latter is also overlapped to the Si-ϕ stretching mode (reported in the literature near 1120 cm^{-1}[227]). The peak between 1230 and 900 cm^{-1} is broader for resins PD92 and PD5 than for PD114, but more intensive for resin PD114. This might be attributed to the resin composition. PD114 is based on organo-alkoxysilanes only, leading to a strong peak between 1000 and 1250 cm^{-1} attributed to the stretching vibration of Si-O-Si and Si-O-C, whereas resins PD5 and PD92 are based on organo-alkoxysilanes and Ti(OEt)$_4$ which may also result in Si-O-Ti bonds. The presence of the Si-O-Ti stretching vibrational mode reported in the

literature to be in the range 900-960 cm⁻¹[100,101,103,154,218-220,223] may be an explanation for the broadening of the peak between 1230 and 900 cm⁻¹. The bending vibration of the Si-OH reported in the literature between 918 and 960 cm⁻¹[100,101,103,154,218-220,223] can overlap the stretching vibration of Ti-O-Si bond. Since the stretching vibrational mode of the -OH groups is nearly absent in the FT-IR spectra of the resins between 3200 and 3700 cm⁻¹, Si-OH groups can be only present in minor quantity.

In order to obtain more information about the structure of the hybrid materials, resins PD5 and PD92 were characterized by ^{29}Si-NMR spectroscopy (Figures 69 and 70). Both spectra show that the inorganic network has dissimilarities. The ^{29}Si-NMR spectrum of the resin PD5 (Figure 70) indicates that DPD and MEMO are present as condensed products with D^1, D^2, and T^3 species.
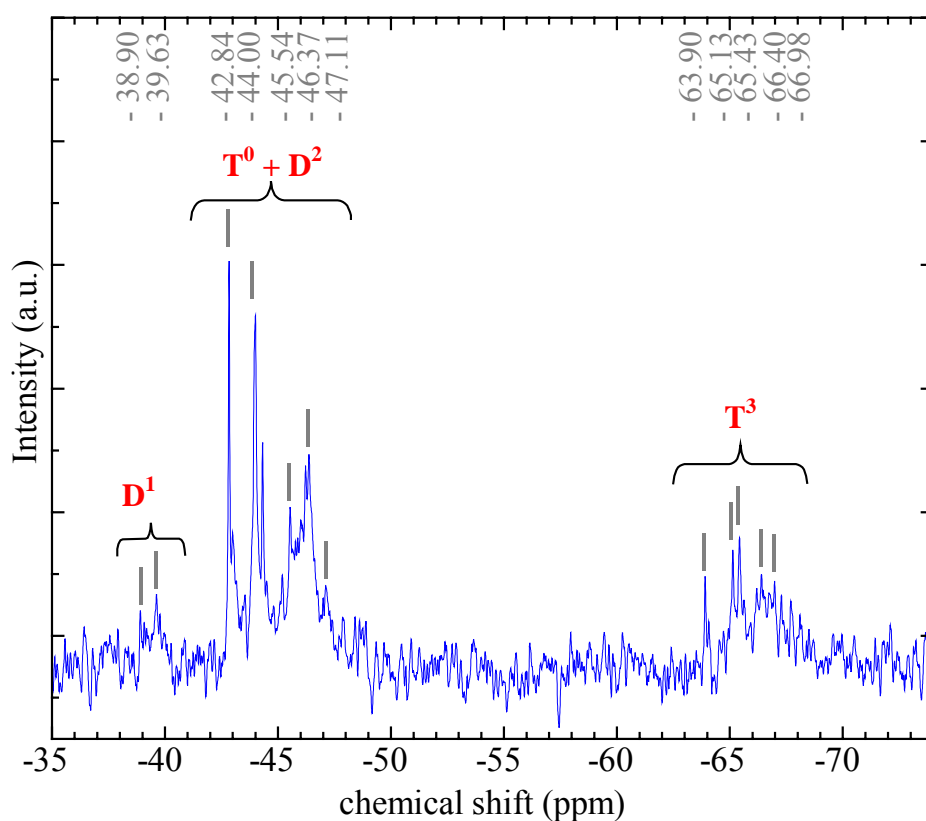

Figure 70: ^{29}Si-NMR spectrum of resin PD5 recorded in acetone-d6. TMS was used as internal reference.

The noise observed in the ^{29}Si-NMR spectrum of resin PD5 could be due to the fact that the spectrum was recorded in aceton-d6. The D^1 region between -38.8 and -39.7 ppm is due to two DPD molecules condensed together, leading to species such as $D^1_{(OH)}$, where a DPD species is condensed with D^2 species or $D^1_{(OH)}$ species. The corresponding chemical shifts have already been reported by Hoebbel et al.[108] to be at -39.44, -39.64, and -39.76 ppm, respectively. This D^1 region can also be attributed to a DPD condensed with a MEMO species. This chemical shift has been reported by Oubaha et al.[2] to be at -38.8 ppm, who studied the co-condensation of MEMO and DPD by ^{29}Si-NMR spectroscopy at different steps of the synthesis. The T^3 region between -63.8 and -67.1 ppm is attributed to a MEMO species condensed with three other MEMO species, and/or to a MEMO species condensed with two

MEMO species and one DPD species[2]. In addition, the T^0 region between -43.3 and -45.6 ppm(cf. Figure 41) may overlap the D^2 region between -42.7 and -47.0 ppm. The peak at -42.8 ppm cannot be attributed to MEMO $T^0_{(OMe)(OMe)(OMe)}$ due to the fact that ^{13}C-NMR spectroscopy cannot detect -Si(OCH$_3$) units (cf., Figure 72). Moreover, as the FT-IR spectrum of resin PD5 (Figure 69) shows no significant -OH vibration, no hydrolyzed MEMO species are detected in the resin. On the other hand, the alkoxy exchange reaction between the ethoxy group of Ti(OEt)$_4$ and the methoxy group of MEMO may occur. In addition, D^1 species can overlap T^0 and D^2 regions, if D^1 species are condensed with titanium alkoxide ($D^1_{(OTi)}$), leading to Si-O-Ti bonds. Hoebbel et al. [108] reported two peaks at -44.26 and -45.86 ppm attributed to Si-O-Ti bonds ($D^1_{(OTi)}$) and Ti-O-Si-O-$\underline{Si}$-O-Si bonds (D^2), respectively, in the spirocyclic titanosiloxane Ti[O$_5$Si$_4$(C$_6$H$_5$)$_8$]$_2$. In the ^{29}Si-NMR spectra of resin PD92, the region detected between -42.7 and -47.0 ppm can be attributed to $D^0_{(OTi)(OTi)}$)species. According to Hoebbel et al.[117] who reported a chemical shift of titanium alkoxides condensed with DPD at -45.31 ppm, assigned to -Ti-O-$\underline{Si}$-O-Ti- bonds ($D^0_{(OTi)(OTi)}$). Thus, it can be concluded that the peaks between -42.7 and -47.0 ppm in Figure 70 are related to T^0 and D^2 species as well as D^1 and D^0 species. The latter two are attributed to DPD condensed with Ti(OEt)$_4$. For resin PD92, the T^2 region and one peak in the region D^0 were detected in addition to the regions recorded in resin PD5 (Figure 71).
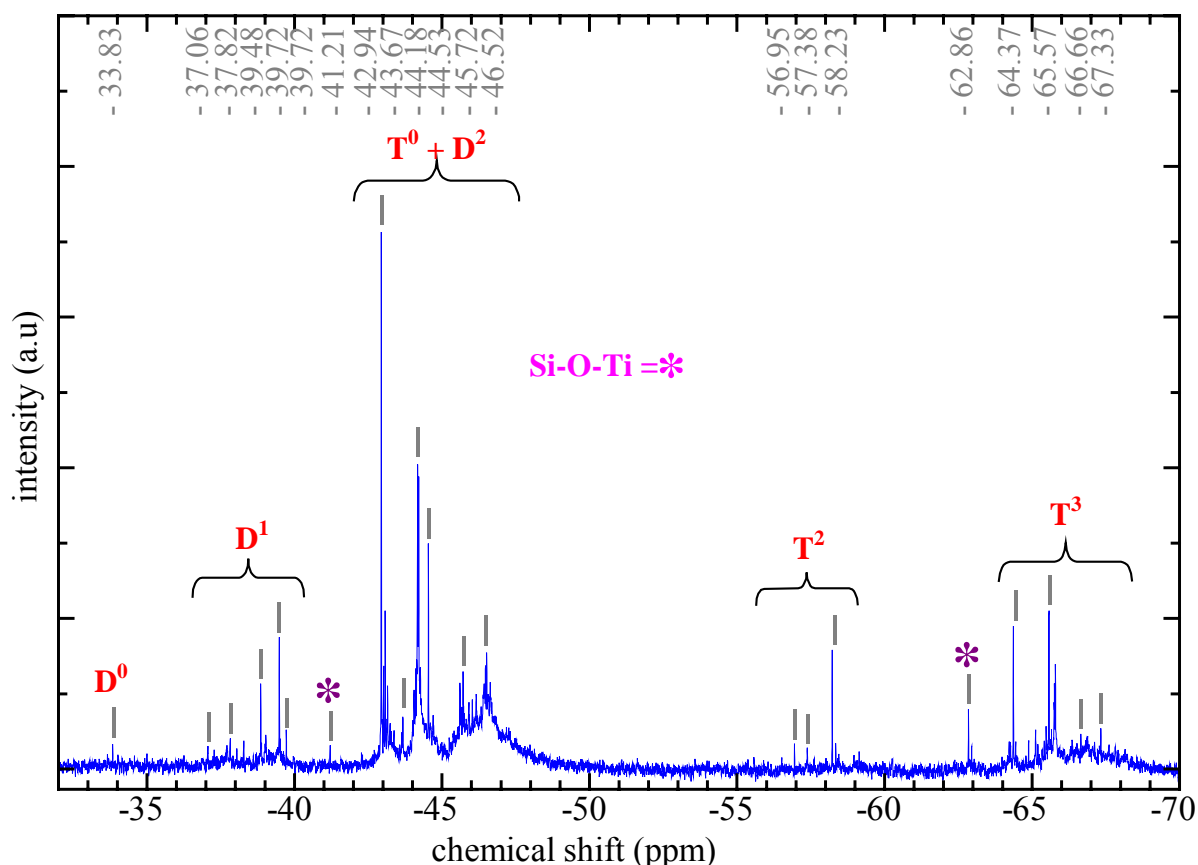

Figure 71: ^{29}Si-NMR spectrum of the resin PD92, performed in CDCl$_3$. TMS was used as internal reference.

The peak at -33.83 ppm in Figure 71 is attributed to DPD $D^0_{(OH)(OH)}$. The area of this peak is negligible compared to the area of the entire spectra. Since in the FT-IR spectrum of resin PD92 no -OH groups were detected (cf., Figure 69), the quantity of non-reacted DPD was

assumed to be negligible. In the T^2 region from -56.5 to -59 ppm, three peaks are detected. One of these can correspond to one MEMO molecule condensed with two other MEMO molecules, as reported previously by Oubaha et al.[2] (-58.5 ppm for $T^2_{(OH)}$ condensed with two T species and -59.1 ppm for $T^2_{(OMe)}$ condensed with two T species). It is also likely that the T^2 species are based on the condensation reaction between a T species with another T species and with a D species. Oubaha et al.[2] reported such chemical shifts close to -59 ppm. Moreover, in the ^{29}Si-NMR spectrum of resin PD92, two peaks at -41.21 and -62.85 ppm are outside the regions previously reported. None of the both peaks were reported by Oubaha et al.[2] Thus, these two peaks may be attributed to Si-O-Ti bonds. According to Hoebbel et al.[117] who reported $D^0_{(OTi)(OTi)}$ species at -41.45 ppm in material based on DPD and titanium alkoxide, the peak detected at -41.21 ppm in Figure 71 is thus attributed to the $D^0_{(OTi)(OTi)}$ species, resulting from the inorganic condensation of a DPD with two Ti(OEt)$_4$. The peak at -62.85 ppm may be attributed to Si-O-Ti bonds resulting from the condensation between MEMO and Ti(OEt)$_4$ molecules.

In order to get a better knowledge of the structure of resins PD92 and PD5, both resins were characterized by ^{13}C-NMR spectroscopy. Zooms of the spectra are shown in Figure 72.

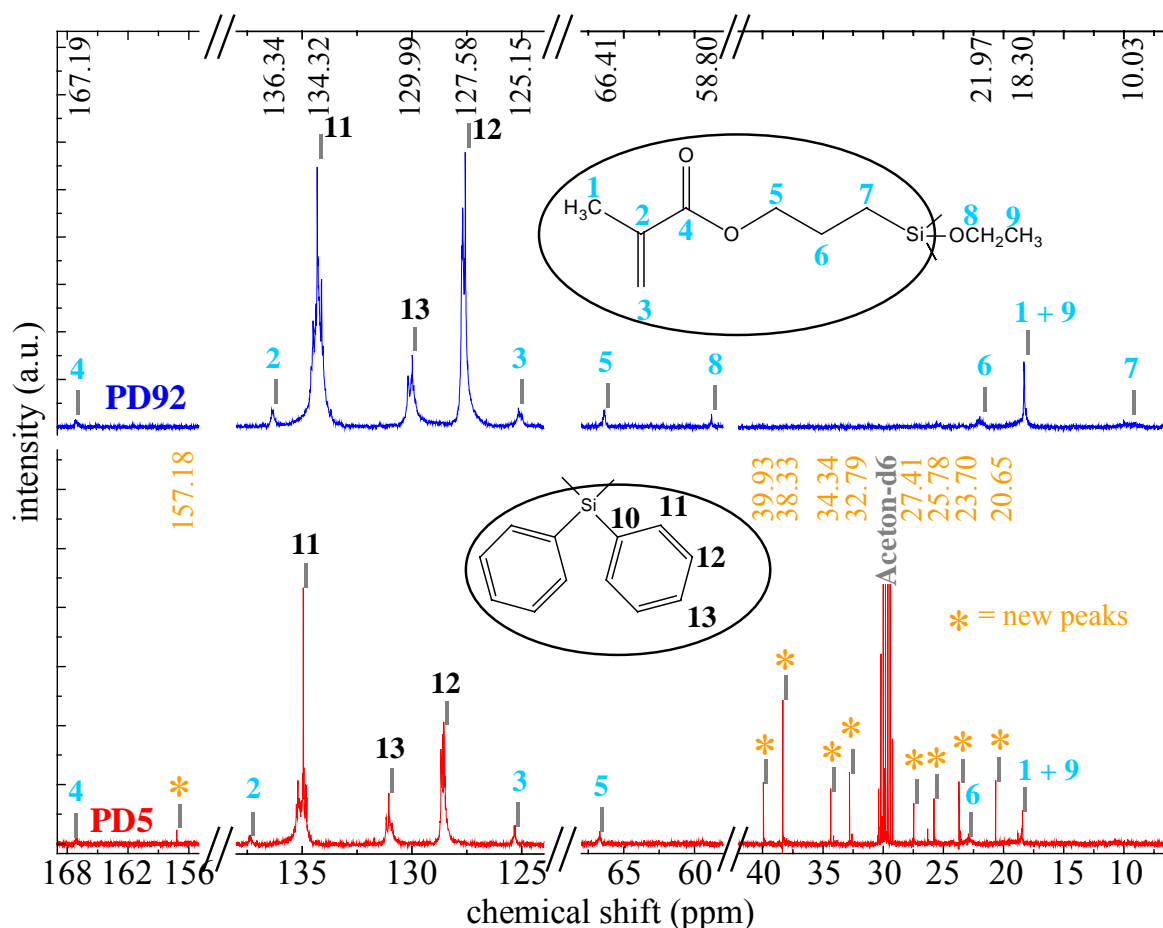Figure 72: Zooms into the ^{13}C-NMR spectra of resins PD5 (recorded in acetone-d$_6$) and PD92 (recorded in CDCl$_3$) between 6 and 42 ppm, 58 and 68 ppm, 124 and 138 ppm, and 155 and 169 ppm, respectively. Carbon atoms relevant for the peak structure are labeled in the structures given in the inset.

In spite of the fact that both resins are based on the same composition (33 mol-% Ti(OEt)$_4$,

50 mol-% DPD, and 17 mol-% MEMO), differences were observed in the same spectra. In both resins, the peaks characteristic for the organic units of MEMO (peaks numbered 1 to 7) and DPD (peaks numbered 11 to 13) were detected, where their positions were slightly shifted due to the two different deuterated solvents used in the measurements (acetone-d6 and CDCl$_3$ for PD5 and PD92, respectively).

In the DPD molecule, the carbon directly bonded to the silicon atom is detected at 138.03 ppm (NMR spectra of DPD collected in acetone-d6, TMS was used as internal reference). In the resins PD5 and PD92, the chemical shift of this carbon (peak number 10) in the organic unit of DPD can be shifted due to the inorganic condensation, thus being overlapped with carbon 11 recorded around 134 ppm. In the MEMO precursor molecule, the carbon directly bonded to the silicon atom (carbon atom number 7) is detected at 4.46 ppm. Due to condensation and alkoxy exchange reactions, this carbon is detected around 10 ppm with a broad and very weak peak (peak number 7).

Concerning Ti(OEt)$_4$, only little information can be extracted from ^{13}C-NMR spectroscopy. The two characteristic peaks of the initial Ti(OEt)$_4$, which are located at 19.4 and 70.6 ppm for -CH$_3$ and -CH$_2$- groups, respectively, were not detected in both resins. Thus, it has to be concluded that Ti(OEt)$_4$ is present in the resin as hydrolyzed or condensed component. Since no significant vibration of -OH groups was detected in the FT-IR spectrum of resin PD92 (Figure 50), it can be concluded that Ti(OEt)$_4$ is present as condensed component which contains -Ti-O-Ti- and/or -Ti-O-Si- bonds. A peak at 58.80 ppm, detected only in resin PD92, is attributed to the chemical shift of the -CH$_2$- in the -Si(O$\underline{C}$H$_2$CH$_3$) unit obtained by an alkoxy exchange reaction between the methoxy group of MEMO and the ethoxy group of Ti(OEt)$_4$ (cf., chapter 4.1.1.2). The chemical shift of the -CH$_3$ of the -Si(OCH$_2$CH$_3$) unit is overlapped with carbon 1 of MEMO at 18.30 ppm. The formation of -Si(OCH$_2$CH$_3$) confirms that Ti(OEt)$_4$ has reacted, and that it is present in the resin as condensed component.

However, some dissimilarities can be noticed in the ^{13}C-NMR spectra of resins PD92 and PD5. In resin PD5, additional peaks are detected compared to the spectra of resin PD92. Peaks of cyclopentanone (solvent used in PD5 synthesis) are detected at 23.70, 38.3, and 220.16 ppm, which might be due to the fact that the solvent was not completely removed under reduced pressure (the peak at 220.16 ppm is not shown in Figure 72). This result correlates with FT-IR measurements carried out with resin PD5 (cf., Figure 69), for which the stretching vibration of the C=O of cyclopentanone was detected at 1745 cm^{-1}. In addition to the three peaks of cyclopentanone detected in the ^{13}C-NMR spectrum, seven new peaks with similar intensities were recorded. In order to assign these peaks, a ^{13}C-DEPT experiment (**D**istorsionless **E**nhancement by **P**olarization **T**ransfer) was performed. This allows one to distinguish primary (-CH$_3$), secondary (-CH$_2$-), and tertiary (=CH-) carbon atoms. Six peaks corresponding to -CH$_2$- units from a new molecule were detected at 20.65, 25.78, 27.41, 32.79, 34.34, and 39.93 ppm, respectively. Due to the fact that the quaternary carbons are not detected by DEPT, the remaining peak at 157.2 ppm was attributed to a quaternary carbon.

In order to assign these peaks, a complementary synthesis was performed: 0.02 mol Ti(OEt)$_4$ was mixed with 0.2 mol cyclopentanone leading to a clear yellow blend which became clear orange. After 15h, the solution was brownish and milky. After a decantation step, the bottom phase remained milky, whereas the top phase was clear and brown. The ^{13}C-NMR spectrum of the latter (not shown) recorded in CDCl$_3$ reveals three strong peaks detected at 23.3, 38.35, and 220.54 ppm, which can be assigned to cyclopentanone. Additionally, 10 peaks at 20.17, 25.32, 27.02, 29.58, 32.58, 34.33, 39.81, 127.99, 158.56, and 207.29 ppm were detected which belong to a new molecule formed during the synthesis. The ^{13}C-NMR DEPT spectrum indicated that all peaks correspond to -CH$_2$- groups except for the peaks at 127.99, 158.56,

and 207.29 ppm. The three latter peaks are attributed to quaternary carbons. The chemical shift at 207.29 ppm is attributed to the C=O function, and peaks at 127.99 and 158.56 ppm are attributed to the C=C function. These assumptions were confirmed by FT-IR spectroscopy measurements. Two peaks were detected at 1738 cm^{-1} and 1640 cm^{-1}, which are attributed to C=O and C=C vibrations, respectively. Thus, from NMR and FT-IR spectroscopy it can be concluded that a Ti-induced reaction of the cyclopentanone took place resulting in the formation of a compound containing ten carbon atoms with seven -CH$_2$- groups, one C=O, and one C=C function. Two cyclopentanone molecules reacted together via an aldol condensation and led to the new molecule 2-cyclopentylidenecyclopentanone with the co-production of water (Eq. 20). In this reaction, Ti(OEt)$_4$ is used as catalyst, and the hydrolysis of the catalyst from the released water produces the milky phase.

$$2 \quad \xrightarrow{\text{Ti(OEt)}_4} \quad + \ H_2O \qquad \text{(Eq. 20)}$$
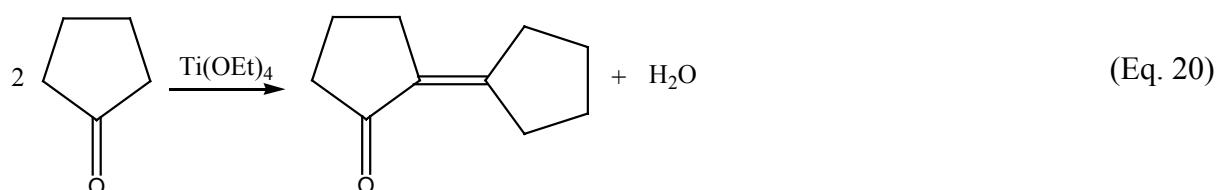
The advantage of this reaction is that no water is needed for the hydrolysis reaction, because it is produced in situ and slowly. Thus, it suppresses the possible macromolecular phase segregation. Such an aldol condensation reaction has already been used by Barkley et al.[228] with acetone as solvent, who made use of the slow water production in order to synthesize titanium clusters. However, the main disadvantage of an aldol condensation is that the quantity of produced water cannot be controlled. Even if the synthesis is reproduced under the same conditions, as soon as cyclopentanone remains in the resin, the release of water may significantly disturb the potential Ti-O-Si bonds.

4.1.2.2.2 Styrylethyltrimethoxysilane used as polymerizable organo-alkoxysilane

In order to determine the influence of the organo-alkoxysilane on the structure of the resin and thus on the refractive index, the same syntheses as performed for PD5 and PD92 were carried out by replacing MEMO by SETMS, leading to two new materials, PD51 and PD109, respectively. Due to the different refractive indices of the two organo-alkoxysilane precursors (1.51 for SETMS and 1.43 for MEMO, cf., chapter 2.2.1.3), the replacement of MEMO by SETMS should significantly influence the refractive index of the resulting materials. After removing the volatile compounds under reduced pressure, a viscous clear orange resin was obtained for PD51, whereas a light clear solid is obtained for resin PD109. The optical properties of the resins and the coatings are summarized in Table 56.

Table 56: Optical properties of PD51 and PD109 and their cured ($n_{c\ 150°C}$) and non-cured (n_c) coatings.

Resin	n_D^{20}	Optical losses of resins (dB/cm) at 780nm	Coating n°	n_c	$n_{c\ 150°C}$
PD51	1.595	0.142	070704/3	n.d.	1.61 at 950 nm 1.60 at 1070 nm
PD109	solid	0.031	190106/1	1.61 at 940 nm 1.60 at 1110 nm	1.63 at 930 nm 1.62 at 1240 nm

The refractive index of resin PD51 is close to 1.595, while those of the resin PD109 measured on coatings (coating 190106/1, see chapter 3.3.1) is close to 1.61 at 940 nm for the non-cured coating, and increased up to 1.63 at 930 nm for the coating cured up to 150°C. Due to the dispersion behavior of the refractive index, higher refractive indices than 1.63 can be expected for wavelengths lower than 930 nm. The refractive index of a PD51 coating (coating 070704/3) cured up to 150°C is close to 1.61 at 950 nm. The optical loss measured at the wavelength of the 2PP laser (780 nm) is 4.6 times higher for the resin synthesized in cyclopentanone than for those synthesized in THF, and may be explained by the presence of the cyclopentanone which is still detected by FT-IR in the resin (Figure 73).

The FT-IR spectra of the resins PD109 and PD51 (Figure 73) are normalized to the vibrational mode of the C=C bond from the aromatic group of DPD, detected at 1591 cm^{-1}. In both spectra, no significant vibrational mode around 3600 cm^{-1} corresponding to -OH groups is recorded. The stretching vibrational mode of the C=O of cyclopentanone is detected at 1745 cm^{-1}. This was also confirmed by ^{13}C-NMR spectroscopy (not shown) by the presence of the three peaks at 23.63, 38.28, and 218.71 ppm which are attributed to the cyclopentanone molecule. In addition, in the FT-IR spectrum of resin PD51, the vibrational mode recorded at 1708 cm^{-1} is attributed to the stretching vibrational mode of the C=O from the 2-cyclopentylidenecyclopentanone molecule. This latter is formed by an aldol condensation already reported in chapter 3.2.2.2 for the synthesis of resin PD5. The ^{13}C-NMR spectrum of resin PD51 (not shown) confirms the formation of 2-cyclopentylidenecyclopentanone with the presence of eight new peaks recorded at 20.59, 25.72, 27.40, 29.84, 32.74, 34.29, 39.89, and 209.83 ppm. The latter peaks were also detected in resin PD5.
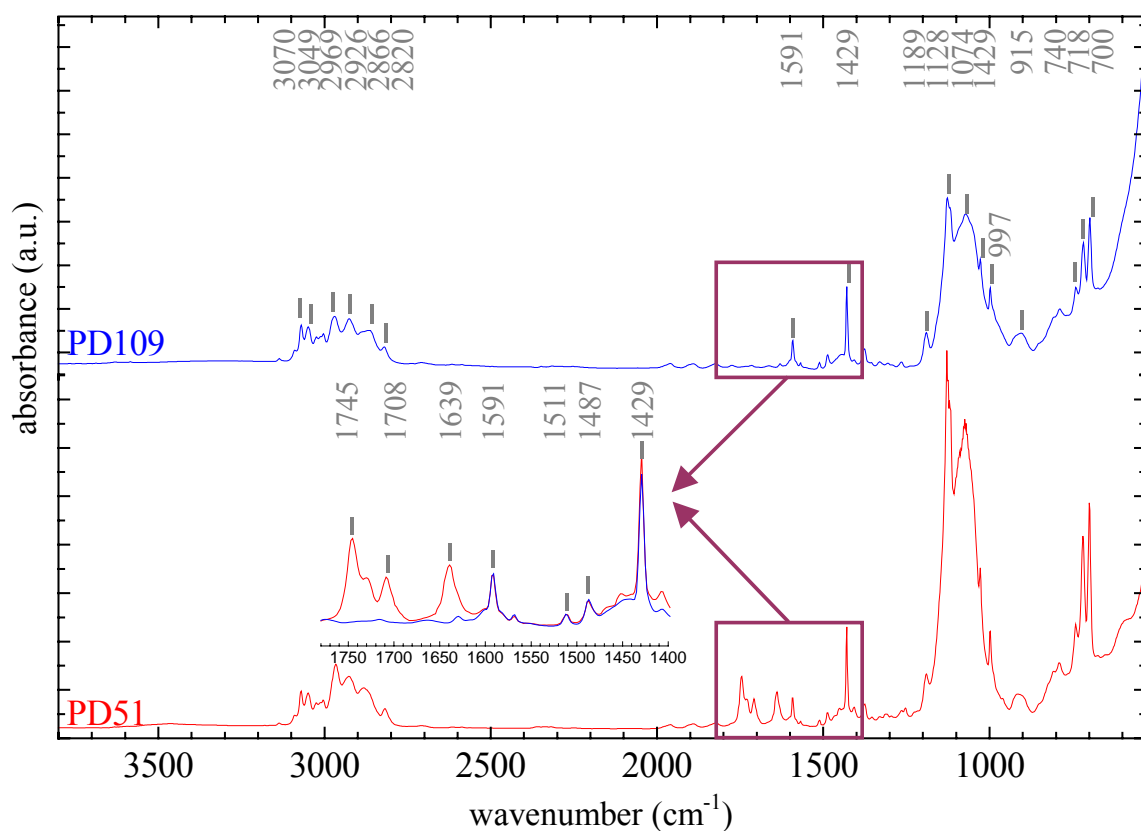

Figure 73: FT-IR spectra of resins PD109 and PD51 recorded on KBr and NaCl pellet, respectively. A superposition of both spectra is shown in the inset, marked by the two arrows.

The FT-IR spectra of both resins also show another difference. A large peak at 1639 cm^{-1} is detected for resin PD51 (zoom in Figure 73), whereas a very weak peak at 1629 cm^{-1} is recorded for resin PD109. These peaks are attributed to the stretching vibrational mode of the organic polymerizable C=C bond of SETMS. In resin PD51, this vibrational mode is overlapped with the stretching vibrational mode of the C=C bonds from 2-cyclopentylidenecyclopentanone (reported in the literature[229] to be at 1640 cm^{-1}), and with the stretching vibrational mode of the C=C bonds from the enol form of cyclopentanone (reported to be at 1622 cm^{-1}[229]). The overlapping peaks between 1213 and 938 cm^{-1} are mainly attributed to the siloxane network. The intensity of the peak recorded at 1189 cm^{-1} is higher for resin PD51 than for resin PD109 due to the C=C stretching vibrational mode of the cyclopentanone and 2-cyclopentylidenecyclopentanone, detected at 1153 and 1170 cm^{-1}, respectively[229].

Since the FT-IR and ^{13}C-NMR spectra only give poor information about the inorganic network, ^{29}Si-NMR spectroscopy measurements of resins PD51 and PD109 were carried out. ^{29}Si-NMR spectra of resins PD51 and PD109 (not shown) are very similar to the ^{29}Si-NMR spectrum of resin PD92, although resin PD92 is synthesized using MEMO, and PD51 and PD109 are synthesized with SETMS.

4.1.3 Resins with complexing ligand

In order to moderate the reactivity of titanium alkoxide, the use of complexing ligands is very often reported in the literature [42-55]. Acetic acid and **ac**etyl**ac**etone (ACAC) are mainly used for this purpose. When a metal alkoxide reacts with acetic acid or acetylacetone, part of the alkoxide group is substituted by acetate or acetylacetonate groups. The resulting bonded ligands are less easily hydrolyzed than the remaining alkoxide groups[35,43]. In order to decrease the number of non-reacted alkoxide groups in the final hybrid material, the use of such bonded ligands as precursor seems to be very promising. On the other hand, due to the increase of the organic content, the refractive index of the final material might be affected. Acetic acid or methacrylic acid are very often used as **c**omplexing **l**igands (CL) in the literature[39], their refractive indices are 1.37 and 1.43, respectively[138]. However, carboxylic acids[37,43,230] with higher refractive index could be used as well.

Two different ways to synthesize the inorganic-organic polymerizable material were chosen. First, the modification of the PD56 synthesis by the complexation of the titanium ethoxide precursor with ACAC is carried out. The second way of synthesis is to use polycondensation reactions of organo-alkoxysilanes with titanium oxo-clusters as precursors. All materials synthesized with CL were labeled as "PD-CL resins". These materials will be discussed in the following chapters.

4.1.3.1 Synthesis based on titanium precursor chelated with acetylacetone

It was already shown in chapter 4.1.2.1.2 that, by increasing the concentration of Ti(OEt)$_4$ up to 90 mol-% in resin PD56, the refractive index increased up to 1.84 at 1820 nm. On the other hand, the resin was found to be very sensitive to moisture due to the presence of non-reacted ethoxy groups from the Ti(OEt)$_4$ precursor, and also to its coordination number which can reach 6[28]. Thus, in order to decrease the reactivity of the resin PD56, a chemical modification of Ti(OEt)$_4$ was performed by using ACAC leading to resin PD-CL76, which is based on 10 mol-% SETMS, 45 mol-% Ti(OEt)$_4$, and 45 mol-% ACAC.

Since the resulting resin was solid, the refractive index of the resin could not be determined by Abbé refractometry, but was determined on a coating. Figure 74 shows the transmission spectra of a non-cured and cured coating (sample 101104/3, part 3.3.1). The refractive indices calculated from Swanepoel's technique is close to 1.63 at 1450 nm for the non-cured coating, and increased up to 1.75 at 902 nm for the coating cured at 150°C. In comparison to resin PD56, the refractive index of coatings from resin PD-CL76 has considerably decreased due to the presence of the organic groups from ACAC. The optical loss of the resin at the wavelength of the 2PP laser (780 nm) is close to 0.336 dB/cm which is in the same order than for resin PD56, and remains very high compared to the values obtained with resins PD92 or PD77.
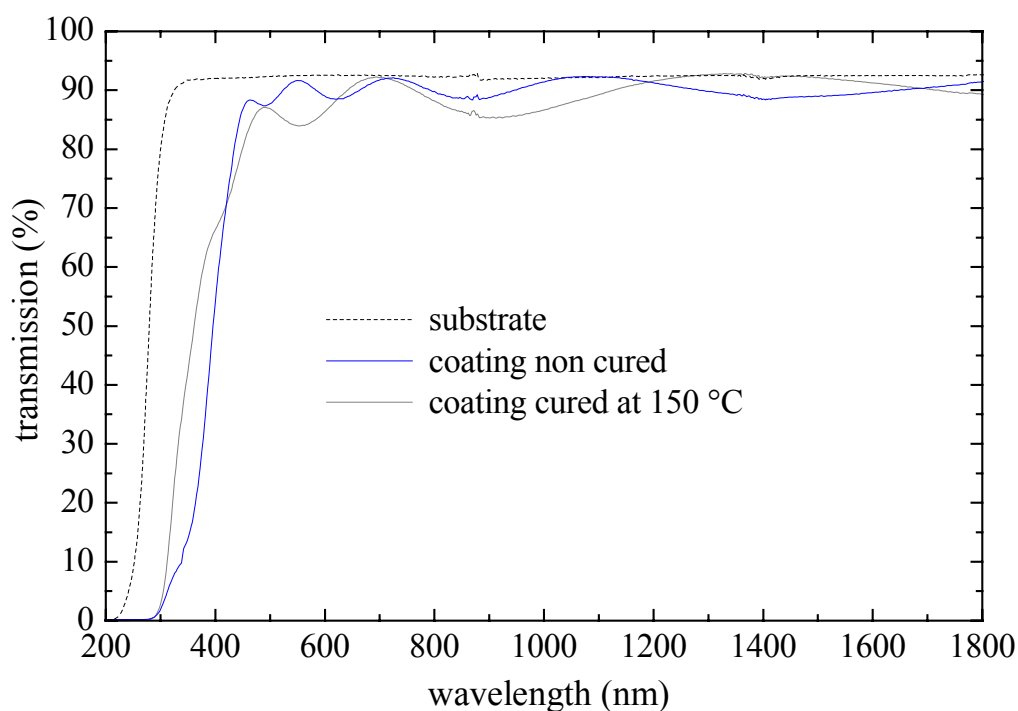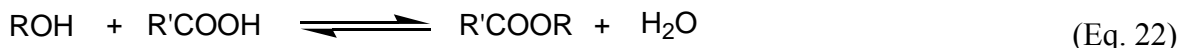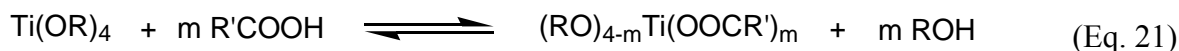

Figure 74 : Transmission spectra of a glass substrate, and of PD-CL76 non-cured and cured coatings. The curing temperature was 150°C (sample 101104/3, part 3.3.1).

The UV irradiation of the PD-CL76 coatings were studied by FT-IR spectroscopy which is presented in chapter 4.2.1.3.

4.1.3.2 Synthesis based on titanium oxo-cluster used as precursor

The reaction between titanium alkoxide and carboxylic acid leads to alcohol formation (Eq. 21). In addition, water as well as esters can be produced upon reaction (Eq. 22). The resulting water may hydrolyze the remaining alkoxide groups. Due to the very slow and continuous in-situ production of water, the formation of titanium oxo-clusters ($Ti_wO_x(OR)_y(OOCR')_m$) is very often observed[39].

116

$$Ti(OR)_4 \ + \ m \ R'COOH \ \rightleftharpoons \ (RO)_{4-m}Ti(OOCR')_m \ + \ m \ ROH \qquad \text{(Eq. 21)}$$

$$ROH \ + \ R'COOH \ \rightleftharpoons \ R'COOR \ + \ H_2O \qquad \text{(Eq. 22)}$$

Well-defined titanium oxo-clusters[231] were used as precursors for condensation reactions with organo-alkoxysilanes. The oxo-clusters were synthesized from titanium propoxide and benzoic acid leading to $Ti_6O_4(C_6H_5COO)_8(OPr)_8$. Benzoic acid has the advantage to have a better electronic polarizability compared to carboxylic or methacrylic acid, leading to a higher refractive index[118].

These clusters have been well characterized by NMR and FT-IR spectroscopy as well as by single crystal X-ray diffraction[231]. However, these clusters are still sensitive against moisture. Compared to titanium propoxide, the number of propoxide groups per titanium atom was decreased, and therefore the reactivity of the titanium against moisture was decreased as well. The titanium oxo-clusters $Ti_6O_4(C_6H_5COO)_8(OPr)_8$ were condensed with organo-alkoxysilane precursors.

The composition of the resin was chosen in order to maintain the symmetrical structure of the cluster. A resin labeled as PD-CL1 was synthesized from 25 mol-% titanium oxo-cluster $Ti_6O_4(C_6H_5COO)_8(OPr)_8$, 20 mol-% MEMO and 55 mol-% DPD. By assuming that MEMO (60 -OMe groups) will react completely with DPD (110 -OH groups), the residual DPD (50 -OH groups) will react with $Ti_6O_4(C_6H_5COO)_8(OPr)_8$ (200 -OPr groups), and the symmetry of the titanium oxo-cluster might be kept.

The resulting resin was a solid, thus the refractive index was determined on coatings (cf., chapter 3.3.1). The coating was moderately cured, and beyond 100°C crack formation was observed.

The refractive index and the thickness of the coating were calculated using the coating's transmission spectra (Figure 75). The refractive index is close to 1.60 at 1520 nm (d=1.60 μm) for the non-cured coating, and 1.63 at 1050 nm for the cured coating at 100°C (d=1.5 μm). The decrease in thickness was about 100 nm between non-cured and cured coating.
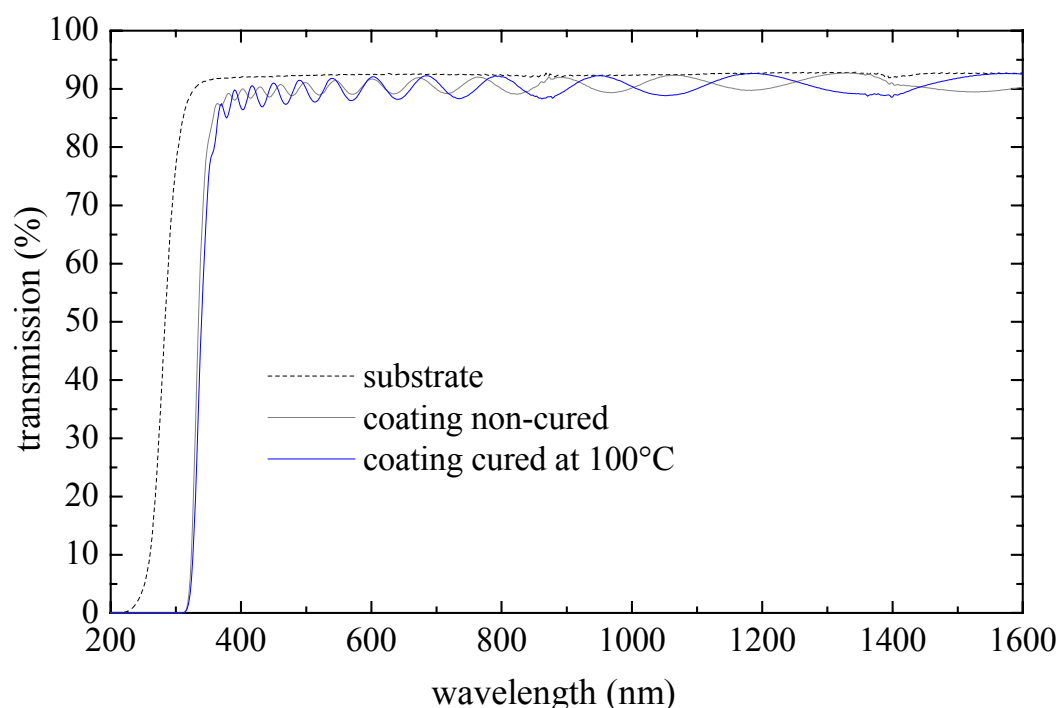
Figure 75: Transmission spectra of a non-coated and a coated substrate (labeled 160805/1) from resin PD-CL1, and for non-cured and cured coatings at 100 °C.

The refractive index of the non-cured coating is not very high compared to those of the previously described resins based on titanium alkoxide precursors (PD#n resins, such as e.g., PD5, PD92, ...), despite the high titanium content per cluster (1 mol cluster contains 6 mol Ti). The organic content in the resin is higher than that in the PD#n resins, particularly due to the benzoate group from the cluster. Thus, this increase of the organic content in resins decreases the refractive index of the coating.

Resin PD-CL1 was characterized by FT-IR and multi-nuclei NMR spectroscopy. In the FT-IR spectrum (Figure 76), no vibrational mode around 3600 cm^{-1} corresponding to -OH groups was detected. The stretching vibrational mode of the C=O bond from MEMO was detected at 1718 cm^{-1}. In addition, the stretching vibration of the C=C bond from MEMO, present at 1637 cm^{-1}, is overlapped with a peak near 1689 cm^{-1}. The latter can be attributed to the stretching vibrational of the C=O from free benzoic acid.
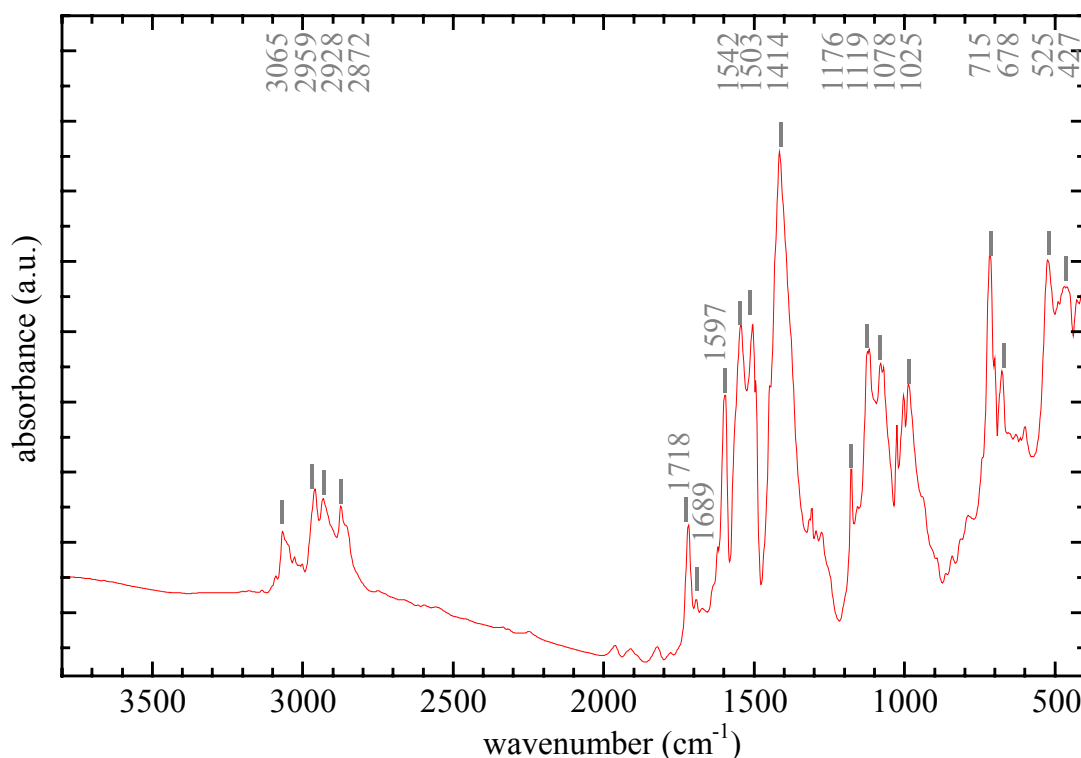
Figure 76: FT-IR spectrum of resin PD-CL1.

The presence of the organically polymerizable C=C bond is confirmed by ^{13}C-NMR spectroscopy (Figure 77) with two peaks at 125.20 and 136.38 ppm, attributed to the CH_2=**C**- and the -**C**H$_3$ of MEMO. As it was already noticed for resin PD92, a shift of the -**C**H$_2$-Si(OMe)$_3$ of MEMO from 5.5 to 10.3 ppm is observed due to the condensation reaction. The peaks attributed to **C**H$_3$-C=, -CH$_2$-**C**H$_2$-CH$_2$-, -**C**H$_2$-CH$_2$-O are recorded at 18.28, 22.08, and 66.48 ppm, respectively. It is important to notice that no peak from the methoxide group of MEMO was detected, which means that MEMO is present in the resin as completely reacted compound. It cannot be excluded that an alkoxide exchange reaction between the propoxide group from the cluster Ti$_6$O$_4$(C$_6$H$_5$COO)$_8$(OPr)$_8$ and the methoxide group from MEMO occurs, leading to the formation of an -Si(OCH$_2$CH$_2$CH$_3$) group (peaks at 10.63, 25.69, and 64.78 ppm). Many peaks between 125 and 136 ppm can be correlated to aromatic carbons of DPD and the clusters. The propoxide groups of the clusters were detected around 10.6, 25.7, and 80.6 ppm for the **C**H$_3$-, -**C**H$_2$- and -**C**H$_2$-O-, respectively. In addition, the C=O bonds of the clusters were detected around 174 ppm.
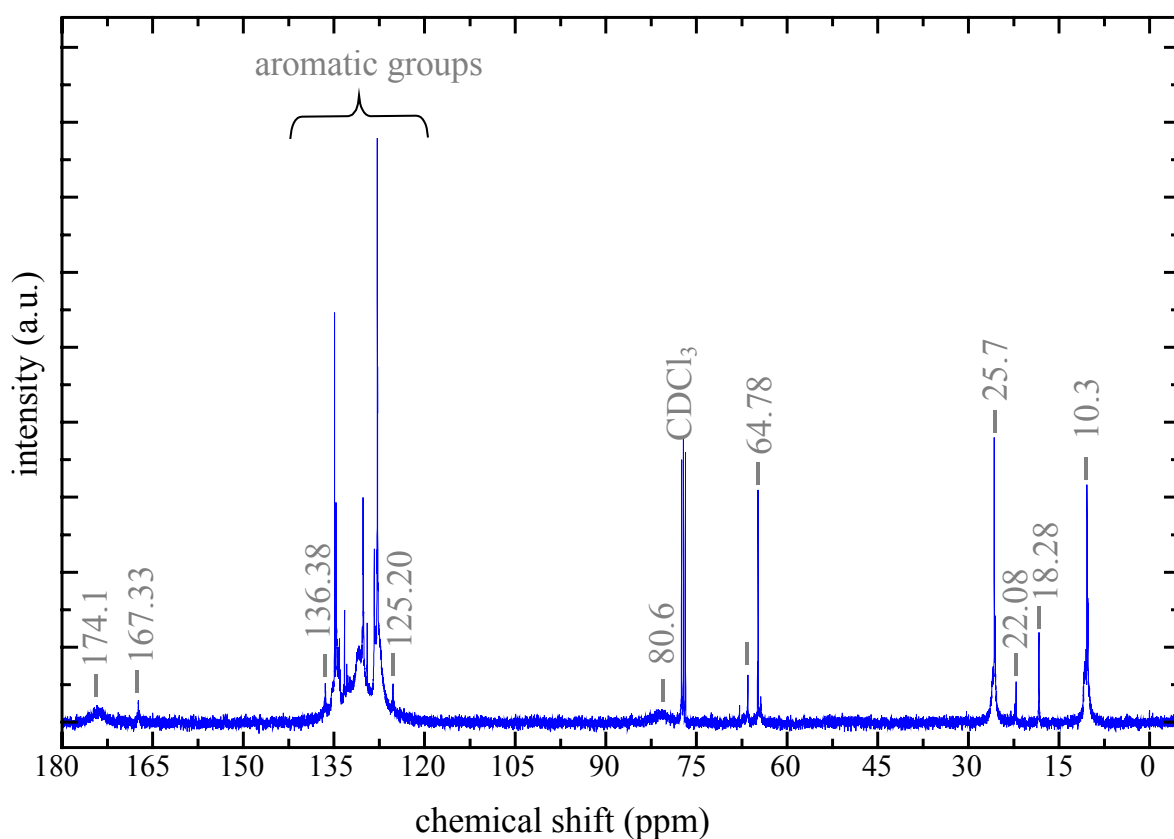
Figure 77: ^{13}C-NMR spectrum of resin PD-CL1, recorded in CDCl₃.

The XRD pattern of resin PD-CL1 (Figure 78 (a)) shows very broad peaks at around 7° and 18°. The broad diffraction peak near 24° could be due to amorphous silica [216]. However, not all peaks of the original cluster are found in the XRD spectrum of PD-CL1 (Figure 78 (b)) which points to the fact that the cluster has reacted with the alkoxysilanes, and has lost its original structure.
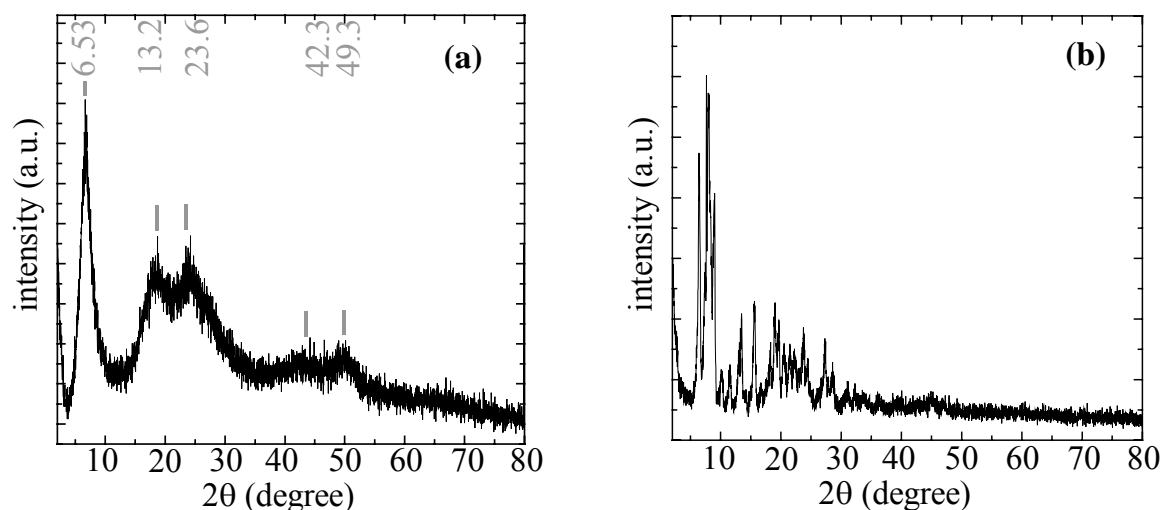
Figure 78: XRD pattern of (a) resin PD-CL1. (b) titanium oxo-clusters $Ti_6O_4(C_6H_5COO)_8(OPr)_8$[87]. Peaks resulting from the cluster are unlabeled in (b).

In summary, a hybrid organic-inorganic resin (PD-CL1) was synthesized by polycondensation reactions of organo-alkoxysilanes (MEMO and DPD) and titanium oxo-clusters ($Ti_6O_4(C_6H_5COO)_8(OPr)_8$). This resin possesses the organically cross-linkable moieties from MEMO which can be used for UV lithography and/or the 2PP process, as for the resins described in the previous chapters. Coatings prepared from this resin were highly transparent. The calculated refractive index is 1.60 (1523 nm) for non-cured coatings and 1.63 (1050 nm) for coatings cured at 100°C, respectively. For T > 100°C, the coatings show crack formation. Despite of the higher titanium concentration in resin PD-CL1 than in resin PD92, the refractive index did not increase significantly. Since higher refractive indices were obtained with resins PD#n, the polymerization process of resin PD-CL1 was not investigated.

4.1.4 Resins containing organophosphorus precursors

In order to introduce an organic polymerizable moiety into the hybrid inorganic-organic materials, organo-alkoxysilane precursors were described in the previous chapters, leading to the resins PD#n and PD-CL#n. This was performed by hydrolysis and co-condensation reactions of titanium alkoxide with organo-alkoxysilanes, leading to Si-O-Si, Ti-O-Si and Ti-O-Ti bonds. In the same way, organic moieties can be also bonded to titanium species with organophosphorus components in a homocondensation reaction, leading to the formation of Ti-O-P bonds which have been reported by Mutin et al.[57,58,232]. However, no refractive index values were reported up to now. The substitution of organo-alkoxysilanes by organophosphorus compounds in the resins PD#n can lead to completely different networks than reported in the previous chapters, and may affect the refractive index of the materials. This will be investigated in the following. An important advantage of the homocondensation of P-O-H is that the formation of P-O-P bonds takes place only under high temperature dehydrating conditions[57]. Principally, phenyl phosphonic acid (PPA) and diphenylphosphinic acid (DPPA) have been used as reported in the literature, but these precursors do not contain organic polymerizable moieties (Figure 79). Only few organophosphorus components having an organic cross-linkable moiety are commercially

available. Sigma-Aldrich sells 2-(methacryloyloxy)ethyl-phosphate (MEPA) and vinylphosphonic acid (Figure 79). MEPA possesses a methacrylate function. On the other hand, the latter component has the disadvantage to have a functional ester unit, which reacts via transesterification reactions, leading to the decrease or the elimination of the organic polymerizable moiety (cf., chapter 4.1.2.2).

p-vinylbenzylphosphonic acid (p-VBPA, , Figure 79) as a new organophosphorus precursor was synthesized[2], and further used for the syntheses of novel photo-patternable hybrid organic-inorganic materials. This precursor was preferably used compared to the commercially available vinylphosphonic acid precursors, due to their aromatic groups which are known to increase the refractive index (cf., section 2.2.1.2). p-VBPA was employed in order to study the influence of the organophosphorus component on the refractive index. Thus, the composition of resin PD92 (33 mol-% Ti(OEt)$_4$, 17 mol-% MEMO, and 50 mol-% DPD) was used as model system, and the organosilicon precursors were partially replaced by organophosphorus precursors, leading to new inorganic-organic hybrid resins labeled PD-P#n. In resins PD-P#n, no water was added, since hydroxyl functions are present in the organophosphorus components, which were used for an in-situ water production.

diphenylphosphinic acid (DPPA)   2-(methacryloyloxy)ethyl phosphate (MEPA)

phenylphosphonic acid (PPA)   p-vinylbenzylphosphonic acid (p-VBPA)
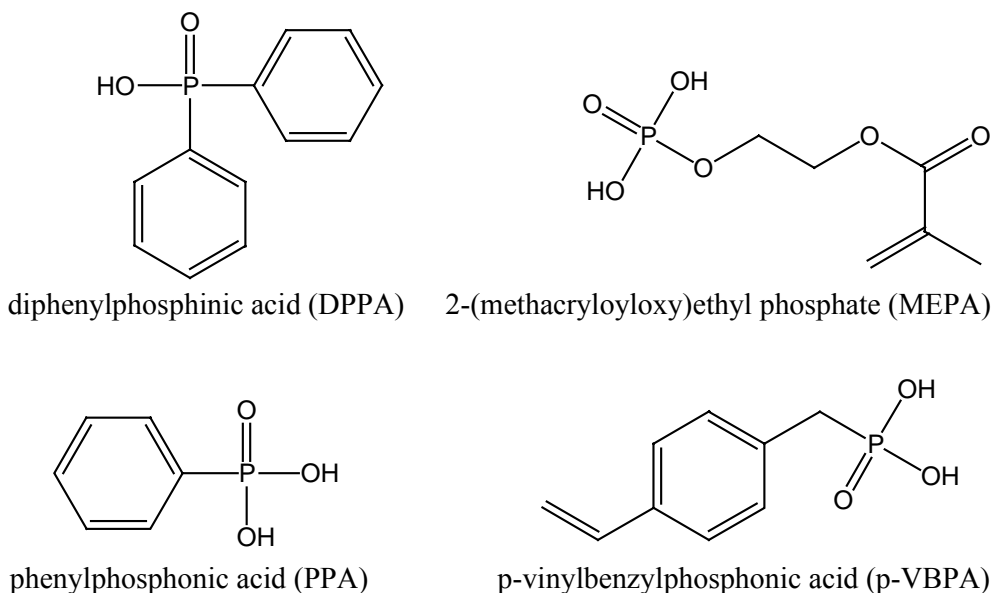
Figure 79: Chemical structures of the organophosphorous precursors used for the syntheses of PD-P#n resins.

Resin PD-P1 was synthesized using the composition of resin PD92, but by replacing MEMO with PPA (i.e., a composition of 17 mol-% PPA, 33 mol-% Ti(OEt)$_4$, and 50 mol-% DPD). PPA does not contain any polymerizable group and was only used for preliminary syntheses. By mixing PPA and Ti(OEt)$_4$ in THF during the synthesis of PD-P1, a nearly solid milky gel was obtained which was not possible to dissolve neither by stirring nor heating up to 60°C. In the following syntheses PPA, was replaced by p-VBPA for introduction of organically polymerizable moiety. This strategy was chosen, because only a small quantity of p-VBPA

---

[2] synthesis was performed in the framework of a collaboration with the University of Montpellier, in France (Dr H. Mutin and Dr. G. Guerrero).

was available due to the weak yield of its synthesis (44%).

A similar synthesis like PD-P1 was performed by replacing $Ti(OEt)_4$ by $Ti(OPr^i)_4$, leading to resin PD-P4 (17 mol-% PPA, 33 mol-% $Ti(OPr^i)_4$, and 50 mol-% DPD). Resin PD-P4 could be processed by dissolving it in THF (cf., chapter 3.3.1 for the coating process).

The transmission spectrum of the PD-P4 coating (Figure 80) shows that a transparent film is obtained. The maxima of the interference fringes of the coating do not reach the transmission spectrum of the substrate, having 0.26% difference, which points to scattering within the material. The refractive index and the thickness of the coating calculated from the transmission spectrum of the coating was close to 1.61 at 980 μm (d = 1370 nm) which is very similar to the refractive index value obtained for a coating prepared with resin PD92 (n= 1.60 at 950 nm for the coating 070605/1, section 3.3.1).
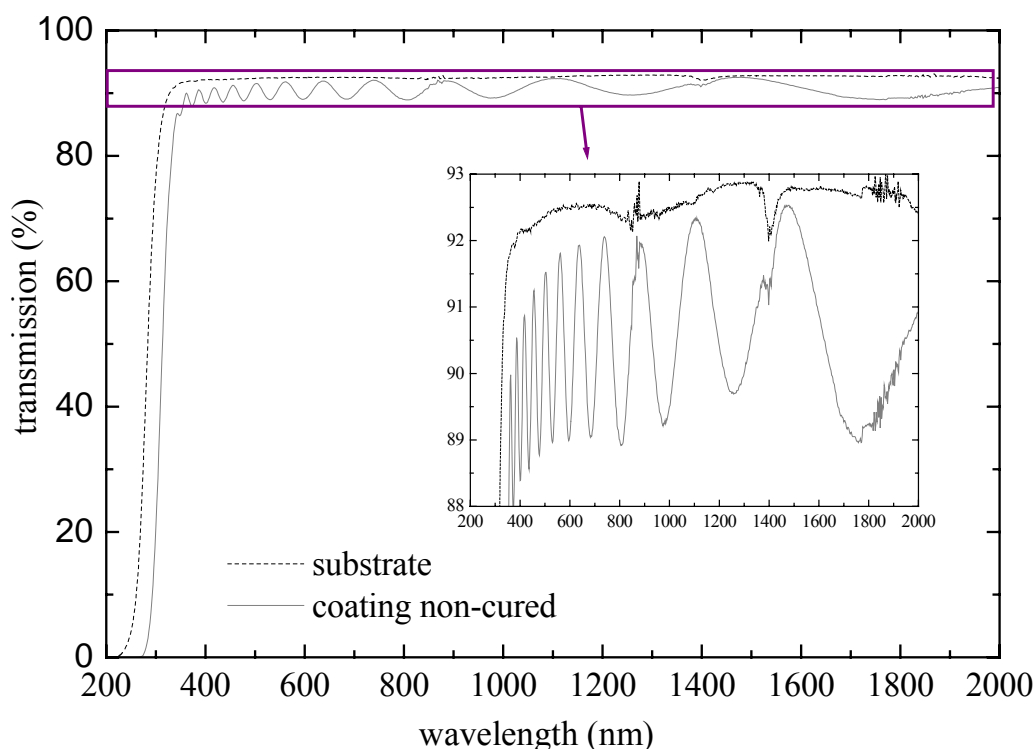
Figure 80: Transmission spectrum of substrate and coated substrate (270306/1, part 3.3.1) from resin PD-P4.

It has to be pointed out that the transparency in the blue and UV range of the coating from resin PD-P4 is higher compared to the PD#n coatings. Since the replacement of MEMO by PPA has led to a transparent coating with a high refractive index, resin PD-P4 was reproduced, but by replacing DPD with DPPA. This leads to resin PD-P6 based on 17 mol-% PPA, 33 mol-% $Ti(OPr^i)_4$, and 50 mol-% DPPA. Resin PD-P6 was processed also by diluting it in THF, and by spin-coating on a glass substrate. The resulting coating was transparent, fuzzy, and blurred (coating 280306/2, section 3.3.1), whose refractive index could not be determined due to too strong light scattering.

Based on the composition of resin PD-P4, PPA was replaced by p-VBPA, which contains an organic cross-linking moiety. The resulting resin (PD-P7) was synthesized using 17 mol-% p-VBPA, 33 mol-% $Ti(OPr^i)_4$, and 50 mol-% DPDA. Resin PD-P7 was diluted in THF and coated onto a glass substrate. The transmission spectrum of the coating (labeled as 040406/1,

section 3.3.1) is highly transparent (Figure 81). The refractive index determined with Swanepoel's technique (cf., chapter 2.2.2.4) was close to 1.64 at 580 and 680 nm, and 1.62 at 1065 nm, with a thickness of 1.150 μm. Due to the method used to measure the refractive index, a direct comparison of the refractive indices of PD-P7 coatings with those from PD92 and PD51 is not directly possible.

But taking the material dispersion relation into account, i.e., an increase of the refractive index for decreasing wavelengths, one could conclude that the refractive index of a PD-P7 coating close to 1.62 at 1065 nm is higher for lower wavelengths than those of coating from PD92 (070605/1, section 3.3.1) determined to be close to 1.60 and 1.59 at 950 and 1120 nm, respectively. This increase of the refractive index is attributed to the fact that PD92 is based on 17 mol-% MEMO, which has methacrylate groups, whereas PD-P7 is based on 17 mol-% p-VBPA which has styryl groups. Styryl groups have been reported to possess a better electron density packing leading to a higher refractive index (cf., chapter 2.2.1.2). On the other hand, the refractive index of coatings from resin PD51 which also have styryl groups is close to 1.61 at 950 nm, and is lower than that of PD-P7. Moreover, the use of $Ti(OPr^i)_4$ instead of $Ti(OEt)_4$ may affect the refractive index of the resin, since the refractive index of $Ti(OEt)_4$ is higher than that of $Ti(OPr^i)_4$ (1.464 compared to 1.505, respectively).
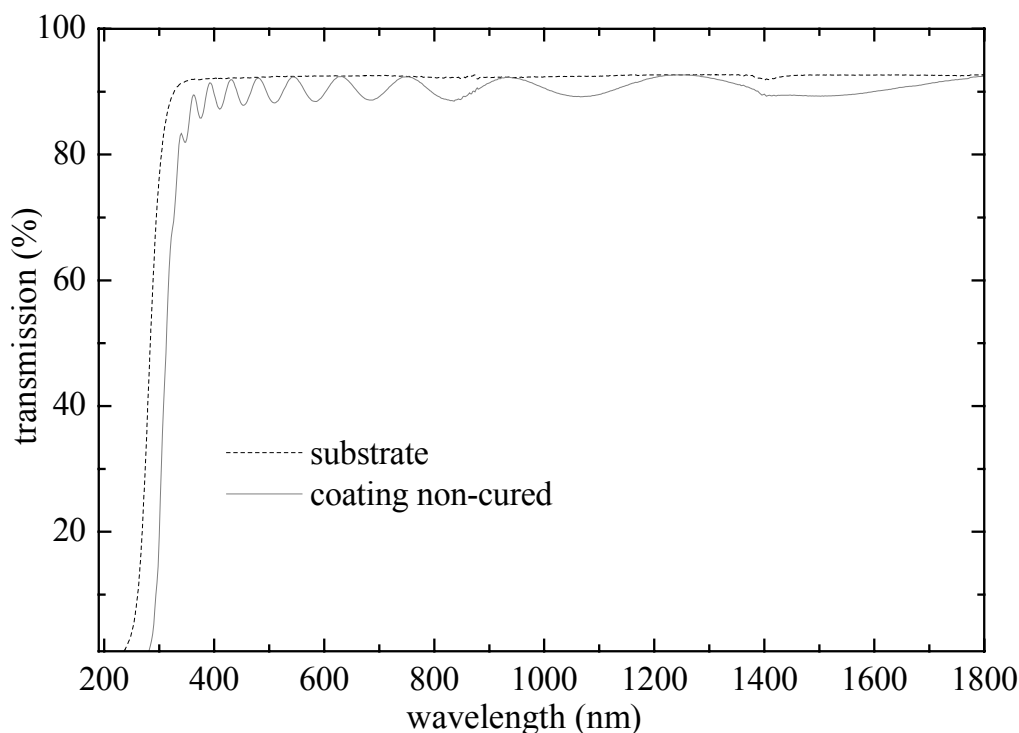
Figure 81: Transmission spectrum of non-coated and coated glass substrate from resin PD-P7 (040406/1, setion 3.3.1).

PD-P4 and PD-P7 were characterized by FT-IR spectroscopy. Their spectra are very similar (Figure 82), and show a large peak around 3400 cm^{-1} characteristic for the vibrational mode of -OH groups. No peaks corresponding D^0 and D^1 species containing hydroxyl groups (i.e., $D^0_{(OH)(OH)}$, $D^0_{(OH)(OPri)}$, or $D^1_{(OH)}$) were detected by ^{29}Si-NMR spectroscopy of resins PD-P4 and PD-P7 (Figure 85). Hoebbel et al.[108] reported these peaks to be close to -33.12, -34.84, -36.40 ppm for $D^0_{(OH)(OH)}$, $D^0_{(OH)(OPri)}$, or $D^1_{(OH)}$ species, and between -39.44

124

and -39.76 ppm for D[1] species, respectively. Thus, it can be concluded that the -OH groups detected by FT-IR spectroscopy result from PPA and p-VBPA in resins PD-P4 and PD-P7, and from hydrolyzed Ti(OPr^i)$_4$. In resin PD-P7, p-VBPA, the organic cross-linking is detected by the presence of the C-H bending vibrational mode at 1511 and 1408 cm^{-1}, due to the para substitution[227], and the C=C stretching frequency of the polymerizable group is detected at 1628 cm^{-1}.

Figure 82: FT-IR spectra of resins PD-P4 and PD-P7. The inset shows a zoom into the spectra marked by the rectangle.
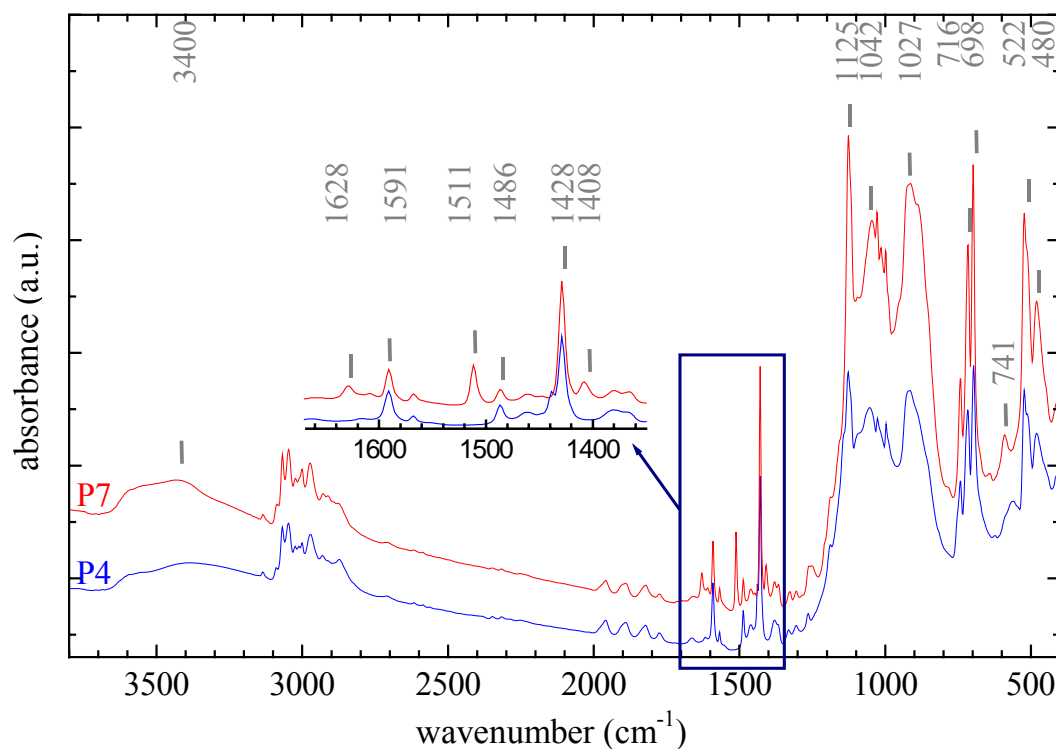
The organically polymerizable group of p-VBPA was also detected by ^{13}C-NMR spectroscopy (Figure 83), at 136.38 and 125.90 ppm for the CH$_2$=**C**- and **C**H$_2$=C- groups, respectively. In both spectra, the peaks recorded between 135 and 126 ppm are attributed to the signals of carbons of the phenyl groups from p-VBPA, PPA, and DPD. Moreover, the carbon atoms of the signals detected at 24.97 and 24.89 ppm in resins PD-P4 and PD-P7 are attributed to -CH(**C**H$_3$)$_2$ from Ti(OPr^i)$_4$. The peak corresponding to the signal of -**C**H(CH$_3$)$_2$ is detected in resin PD-P4 at 64.66 ppm, and might be present around 65 ppm with a very weak and large signal in resin PD-P7. Two other peaks found in both resins, are detected at 68.17 and 68.29 ppm and at 25.33 and 25.41 ppm. DEPT-NMR spectra of both resins (not shown) show that these signals are attributed to -CH$_2$- groups, and their chemical shifts are attributed to those of THF, which was used as solvent in the syntheses of the resins. In spite of the removal of the volatile compounds under reduced pressure, THF is still detected in both resins. It can act as a potential coordinating solvent, and may block the coordination site of the titanium atom[38,57,117,233]. In resin PD-P7, the signal of the -CH$_2$- entity, which is bonded to the phenyl group might be weak, and can be superposed with the signal of the THF at 25.33 ppm.
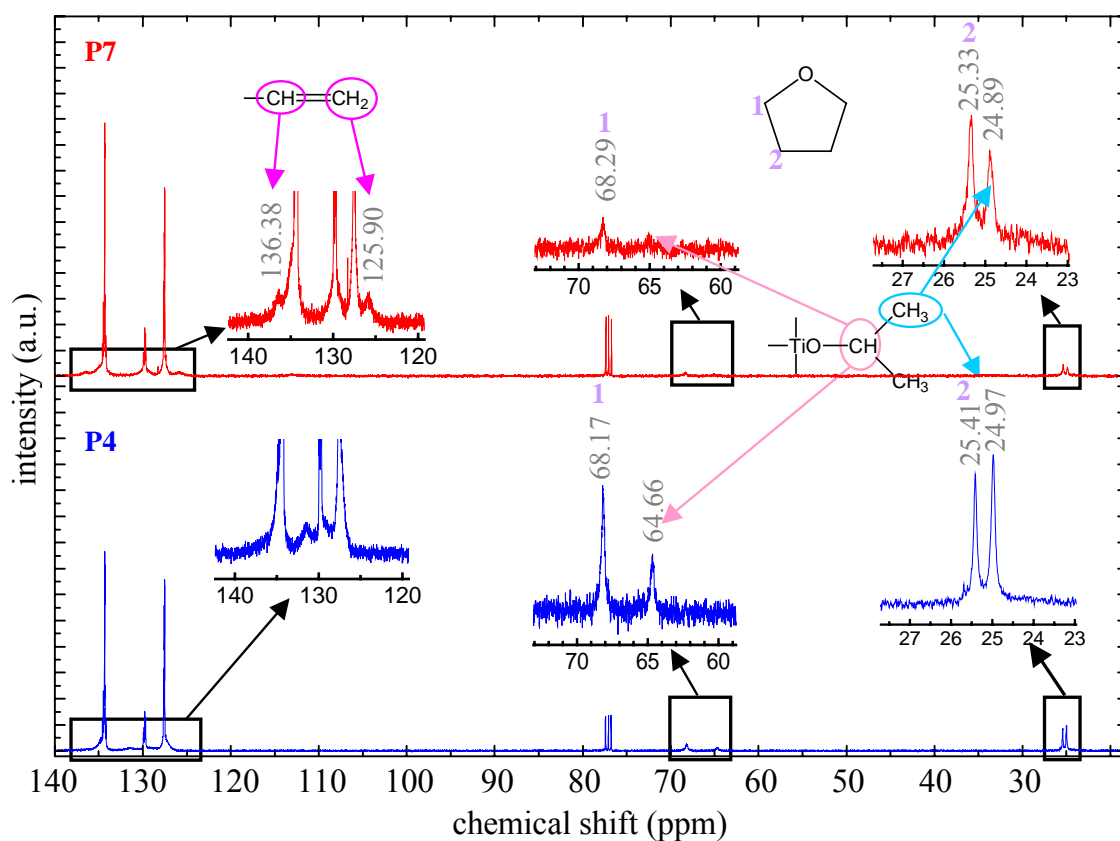
Figure 83: ^{13}C-NMR spectra of resins PD-P4 and PD-P7 recorded in CDCl$_3$. The insets show zooms into the individual spectra, marked by the rectangles.

The solid-state ^{31}P-MAS NMR spectrum of resin PD-P7 (Figure 84) shows only one broad peak around 14.8 ppm which indicates the formation of Ti-O-P bonds by a condensation reaction between Ti(OPr^i)$_4$ and PPA[233]. Thus, the presence of Si-O-P bonds, which have been reported under particular conditions[57], is excluded.
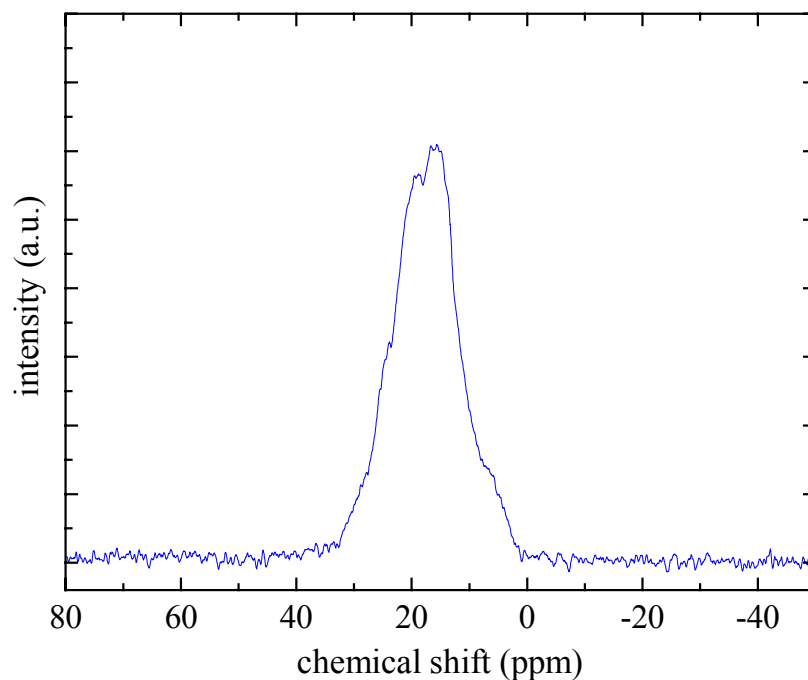
Figure 84: ^{31}P-MAS NMR spectrum of resin PD-P7.

The ^{29}Si-NMR spectra of resins PD-P4 and PD-P7 are identical in spite of the different composition of the resins (Figure 85). Both resins are based on 33 mol-% Ti(OPr^i)$_4$ and 50 mol-% DPD, but different organically polymerizable groups were used (17 mol-% PPA and 17 mol-% p-VPA, respectively). Thus, the absence of the Si-O-P bonds found by ^{31}P-MAS NMR spectroscopy of resin PD-P7 is confirmed by ^{29}Si-NMR spectroscopy. Since Si-O-P bonds have been reported to be very sensitive to hydrolysis[57], their absence in the two resins might be an advantage for the stability of the resin against moisture. Three regions are detected in the ^{29}Si-NMR spectra.

In the region between -40.8 and -41.5 ppm, a strong peak at -41.06 and -41.04 ppm is found for resins PD-P7 and PD-P4, respectively. The chemical shift of the latter one is too weak to be attributed to D^0 species, and too strong to be attributed to D^1 species, if one supposes that DPD is condensed only with itself. Thus, as soon as Si-O-P bonds are excluded, this peak can be only attributed to $D^0_{(OTi)}$ species which contains Ti-O-Si bonds, resulting from the condensation reaction between Ti(OPr^i)$_4$ and DPD. Hoebbel et al.[108] have reported four chemical shifts at -40.68, -41.45, -41.52, and -41.67 ppm in solutions based on Ti(OPr^i)$_4$ and DPD. These are attributed to Si atoms bonded via oxygen directly or indirectly to titanium. The difference in the chemical shifts reported by Hoebbel et al.[108] and the peaks detected for resins PD-P7 and PD-P4 can result from the presence of PPA and p-VBPA which are condensed with Ti(OPr^i)$_4$, and can affect the chemical shift in the -Si-O-Ti-O-P- species. The second region between -43.3 and -44.8 ppm presents three peaks detected at -43.38, -43.49, and -43.96 ppm for resin PD-P4 and three peaks detected at -43.41, -43.51, and -43.98 ppm for resin PD-P7. The peaks at -43.96 ppm for resin PD-P4 and -43.98 ppm for resin PD-P7 can be attributed to -Ti-O-**Si**-O-Si- ($D^1_{(OTi)}$) in the spirocyclic titanophenylsiloxane. (cf., Figure 20 (c), chapter 2.1.3.2 [108,117]). The two other peaks recorded at -43.38 and -43.49 ppm for resin PD-P4 and at -43.41 and -43.51 ppm for resin PD-P7 have not been found by Hoebbel et al.[108,117], who reported chemical shifts of -Ti-O-Si- units in polycondensation

reactions of dimethyldimethoxysilane and Ti(OPr^i)$_4$ by ^{29}Si NMR spectroscopy. These shifts may be attributed to -P-O-Ti-O-**Si**- units. The third region between -45.3 and -46.4 ppm is composed of two strong signals. The signals detected at -45.66 ppm for resin PD-P4 and -45.70 ppm for resin PD-P7 are attributed to -Ti-O-Si-O-**Si**-O-Si (D^2) units, and have been already reported by Hoebbel et al.[108,117] in the spirocyclic titanophenylsiloxane. The signals recorded at -45.38 ppm for resin PD-P4 and at -45.40 ppm for resin PD-P7 might be attributed to -Ti-O-**Si**-O-Ti- units, already reported to be at the same chemical shift[108,117].
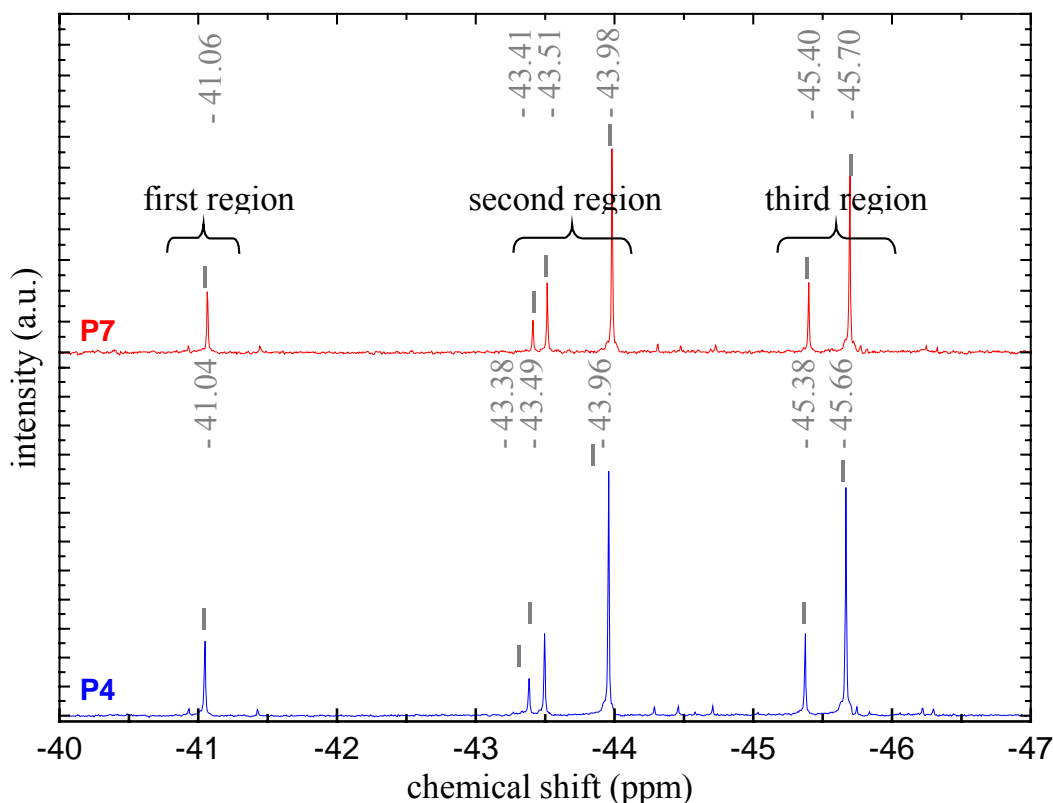
Figure 85: ^{29}Si-NMR spectra of resins PD-P4 and PD-P7, recorded in chloroform-d6.

4.1.5 Discussion of the synthesized resins

In the previous chapters, it has been shown that class II hybrid organic-inorganic resins were synthesized by hydrolysis and/or condensations reactions from different organo-alkoxysilanes precursors (MEMO, SETMS, and DPD) and titanium precursors (titanium alkoxides, and titanium oxo-clusters). The use of organophosphorus precursors was also investigated.

The partial substitution of MEMO in ORMOCER® syntheses with titanium precursors has led to highly transparent coatings and to a significant increase of the refractive index. For example, in an ORMOCER® based on 50 mol-% MEMO and 50 mol-% DPD, the refractive index of the resin was determined to be 1.538 (at 633 nm)[22]. By substituting 33 mol-% MEMO with 33 mol-% titanium ethoxide, the refractive index of the resin was increased up to 1.59 (at 633nm). Another example is the replacement of TEOS (resin PD114) by Ti(OEt)$_4$ (resin PD5) which has increased the refractive index from 1.55 to 1.59. This means that the incorporation of titanium alkoxide by hydrolysis and condensation reactions notably influences the refractive index of the resulting material.

In the case of resin PD5, not only the titanium incorporation modifies the refractive index, but also the solvent used for the syntheses. Cyclopentanone was used and has reacted by an aldol condensation producing water. The resulting compounds have a high molecular weight, and could not be removed by a vacuum step. The refractive index of these compounds could be higher than those of cyclopentanone (n=1.437). This is due to the fact that the condensation reaction of two cyclopentanone molecules leads to the formation of [bicyclopentyliden]-2-one which has a higher refractive index than the original compound (n=1.522)[234]. The comparison of the refractive indices of resins PD5 and PD92 (same composition, only different type of solvent) provides information on the influence of the solvents on the synthesis of hybrid polymer resins. Since a solid was obtained for resin PD92, the comparison can only be performed by comparing the refractive indices calculated from the transmission spectra of coatings. PD5 coatings which were cured at 150°C have refractive indices close to 1.60 at 1460 nm, whereas those of resin PD92 are close to 1.60 at 950 nm and 1.59 at 1120 nm, respectively. Unfortunately, the refractive indices of the coatings from resins PD5 and PD92 are difficult to compare since the determination could only be carried out at different wavelengths (cf., chapter 2.2.2.4). Thus, it is very difficult to draw conclusions on the effect of the solvent onto the network solely on the basis of refractive index values. On the other hand, the dipole moments of the two different solvents, which are μ = 2.89 D for cyclopentanone and μ = 1.75 D for THF can notably affect the final inorganic network[28]. Therefore, the refractive index of the final material is also affected.

The replacement of MEMO by SETMS in resins PD92 and PD109 altered the refractive index of the coatings. For example, the refractive indices of PD92 coatings cured at 150°C are close to 1.62 at 960 nm, whereas those of PD109 are close to 1.63 at 950 nm. This is attributed to the difference of refractive index of the two organo-alkoxysilane precursors SETMS and MEMO, reported to be close to 1.505 and 1.431, respectively[153]. Since SETMS possesses a higher electronic mobility than MEMO, its refractive index is higher[118].

Coatings from other resins based on 33 mol-% organo-alkoxysilane (MEMO or SETMS) and 67 mol-% titanium alkoxide were also found to be highly transparent. The kind of organo-alkoxysilane and the catalyst concentration seem also to influence the material's refractive index. For resins synthesized with MEMO with three different catalyst concentrations (0.2, 2, and 12 M HCl), the refractive indices are close to 1.61 (at 1080 nm) and 1.67 (at 1170 nm), both cured at 150°C for three hours. A higher HCl catalyst concentration seems to increase the refractive index of the final coating. On the other hand, NMR and FT-IR spectroscopy measurements show that in presence of an acid, MEMO reacts with ethanol or methanol, and ethylmethacrylate or methylmethacrylate are produced, respectively. This reaction is influenced by the catalyst concentration which leads to two different materials, having different refractive indices. In any case, resins synthesized with a higher catalyst concentration yielded a higher refractive index. This can be explained as follows. By increasing the catalyst concentration, the concentration of the residual chlorine is increased. This is known to improve the refractive index due to its high electronegativity. In addition, transesterification reactions occurring in presence of acidic media between MEMO and alcohol, lead to the formation of ester compounds, which are further removed from the resins under reduced pressure. The concentration of esters may be increased by increasing the catalyst concentration. By using SETMS as organo-alkoxysilane with different catalyst concentrations, the refractive indices of the coatings cured at 150 °C from the resins synthesized with 2 M or 12 M HCl are close to 1.67 (at 1290 nm, PD52) or 1.70 (at 940 nm), respectively. One is able to compare the refractive indices of the resins directly at more or less around the same wavelength, for refractive indices measured at the same wavelength. The alkoxide groups from the titanium alkoxide precursor also influences the refractive index

of the resulting materials. For example, $Si(OEt)_4$ has a higher refractive index (n = 1.382) than $Si(OMe)_4$ (n = 1.369). No data from the refractive index of $Ti(OMe)_4$ were found in the literature. The refractive indices of resins PD77 and PD60 which were synthesized with the two different titanium alkoxides, $Ti(OMe)_4$ and $Ti(OEt)_4$, are close to 1.7 (at 930 nm, PD77) and 1.7 (at 957 nm, PD60), for both coatings cured at 150 °C for three hours. Thus, it can be concluded that the alkoxide groups from the titanium precursors have not a direct influence on the refractive index of the final material. By increasing the concentration of $Ti(OEt)_4$ up to 90 mol-%, the refractive index of the coating has increased significantly. For example, the refractive index of the resin PD56 coating, based on 90 mol-% $Ti(OEt)_4$ and 10 mol-% SETMS, is close to 1.84 at 1820 nm, and could be much higher at lower wavelengths due to its dispersion behavior. However, resin and coating were very sensitive to moisture. In addition, the material was found to be poorly reproducible due to the high content of non-reacted alkoxide groups from the titanium precursors. Thus, a chemical modification of the titanium alkoxide precursor with CL was performed, leading to resin PD-CL76.

Two different ways to synthesize the inorganic-organic polymerizable material based on titanium alkoxide precursors and CL were tested. The first one is a complexation of 45 mol-% titanium ethoxide with 45 mol-% ACAC, followed by a condensation reaction with 10 mol-% SETMS, leading to resin PD-CL76. The refractive indices of the highly transparent coatings were close to 1.65 at 1450 nm for the non-cured coating, and close to 1.75 at 902 nm for coating cured at 150°C. The second way to synthesize hybrid organic-inorganic materials based on titanium precursors and CL was the use of titanium oxo-clusters, $Ti_6O_4(C_6H_5COO)_8(OPr)_8$, leading to resin PD-CL1. The refractive indices are close to 1.60 at 1520 nm for non-cured coatings. Since beyond 100°C cracking of the coating was observed, refractive indices were determined only for layers cured at this temperature, having values close to 1.63 at 1050 nm. Despite of the high titanium content per cluster, the refractive indices of these materials are not so high compared to those of resins synthesized with organo-alkoxysilanes and titanium alkoxide precursors. This can be attributed to the high content of organic groups in the titanium oxo-clusters.

Other new syntheses based on organo-alkoxysilanes, titanium alkoxides, and also organophosphorus precursors were performed. The replacement of MEMO by p-VBPA has led to an increase of the refractive index of about 1.9 % (at comparable wavelengths). The refractive indices measured on non-cured coatings were close to 1.60 at 950 nm and 1.59 at 1120 nm, whereas those of the phosphorous-containing materials were 1.64 at 580 and 680 nm, and 1.62 at 1065 nm, respectively. This increase can be attributed to the presence of aromatic groups in the p-VBPA. On the other hand, in resins, where SETMS was replaced by the same quantity of p-VBPA, the refractive indices of non-cured coatings are close to 1.61 (at 940 nm) and 1.60 at (1100 nm), being considerably lower than those determined from coatings containing phosphorous precursors.

By curing coatings thermally, their refractive indices were always increased compared to the liquid resins due to a structural densification by removing solvents which, in addition, also have a lower refractive index. The variation of the refractive index with the curing temperature is also dependent on the concentration of titanium precursor. The refractive index of PD92 coatings (based on 33 mol-% titanium alkoxide) is close to 1.60 (at 950 nm, non-cured) and 1.62 (at 960 nm, cured at 150 °C for three hours), respectively. On the other hand, the refractive index of PD77 coatings (based on 67 mol-% titanium alkoxide) is close to 1.61 (at 1000 nm, non-cured) and 1.67 (at 1200 nm, cured at 150 °C for three hours), respectively. The higher increase of the refractive index with temperature might be attributed to the formation of Ti-O-Ti bonds in the final coatings. It has to be mentioned, however, that for

resins synthesized with a high amount of organo-alkoxysilanes (67 mol-%), crack-free coatings were only obtained up to 200°C, whereas for lower organo-alkoxysilane content (33 mol-%), curing up to 450°C was possible without cracks. By increasing the curing temperature up to 450°C, the refractive index of PD77 coatings is close to 1.78 (at 824 nm).

4.2 Patterning of the resins

It was shown that many parameters influence the refractive index of a final coating such as the synthesis parameters (amount and type of organo-alkoxysilane, kind and amount of catalyst and its concentration, solvents). However, beside syntheses, also the technological processing influences the refractive index such as, for example, the thermal curing of the coatings. The influence of the UV processing on the refractive index for some selected resins is discussed in the following chapters, and also first results of the 2PP polymerization from some selected resins are reported.

The following chapter reports the patterning process of the resins tested firstly by UV lithography processing from some selected resins, in order to evaluate the cross-linking behavior of the synthesized resins (cf., 4.2.1). After patterning of structures with a mask aligner, some resins were polymerized by 2PP processing (section 4.2.2).

A sketch of the different steps of the UV lithography process is shown in chapter 2.3. Since the degree of conversion (i.e., the percentage of vinyl moieties converted to aliphatic groups, chapter 3.1.4) affects the refractive index of the material, μ-Raman spectroscopy analysis was used to investigate the UV lithography process of patterned coatings. The refractive indices of coatings were determined by ellipsometry measurements[3].

Since the presence of titanium has been reported to affect the organic polymerization[99,100,188] (cf., chapter 2.3.1), the Ti concentration present in the resins has to be taken into account. Thus, in the following chapter, the UV lithography process of the resins synthesized during this work is divided into four parts: resins based on a low titanium concentration (33 mol-%), resins based on higher titanium content (67 mol-%), resins containing CL, and resins based on organophosphorus precursors.

4.2.1 The UV lithography process

As already reported, the resolution of the UV lithography process depends on many parameters such as kind and concentration of UV initiator introduced into the resins, pre-and post- exposure bake steps, nature of the polymerizable group, or UV dose. In addition, the use of hetero-elements in the syntheses of resins notably affects the polymerization process. Thus, in order to investigate the patterning process of the novel organic-inorganic hybrid materials reported in the previous chapters, preliminary experiments were performed with the resins PD5 and PD92, synthesized with a low Ti content and MEMO as polymerizable moiety. Based on these results, the UV processing was carried out on resins having nearly the same

---

[3] Ellipsometry measurement which was carried out at at the Joanneum Research Institute for Nanostructured Materials and Photonics (Austria).

composition, but containing different polymerizable moieties, i.e., resins with SETMS as polymerizable moieties (PD51 and PD109). Then, the polymerization process as well as the resulting refractive indices after UV exposure of a resin with a higher titanium content was investigated. Finally, the polymerization a phosphorous-based resin was investigated. It has to be noticed that only preliminary work could be performed on the processing, since the optimization of a processing process requires much more investigations, and was not scope of this thesis.

4.2.1.1 Resins based on low titanium content

The polymerization process of ORMOCER®I, based on 50 mol-% MEMO and 50 mol-% DPD, has been used as reference process for the resins PD5 and PD92, in which 33 mol-% MEMO was replaced by 33 mol-% Ti(OEt)$_4$. A typical polymerization process of ORMOCER®I with 1wt.-% Irgacure®369 and diluted with propylacetate for waveguide application is summarized in Table 57. After a filtration step, the solution is spin-coated on a silicon wafer substrate without any surface treatment.

Well-resolved patterned structures are obtained by applying a 1 min prebake step at 80°C, followed by 30 s UV exposure, and 1 min post-exposure bake at 80°C. The development is performed by dipping the sample into a mixture of MP and isopropanol for approximately 30 s.

Table 57: Typical processing parameters of ORMOCER®I for waveguide applications. W, t: spin speed, Δ_1, t: temperature and duration of the pre-exposure bake, t_{UV}: UV exposure time, Δ_2, t: temperature and duration of the post-exposure bake.

Substrate preparation	W, t	Δ_1, t	t_{UV}	Δ_2, t	Development
no pre-treatment	2000 rpm, 40 s	80°C, 1 min	30 s	80°C, 1 min	MP:isopropanol

Typically, for a dilution ratio of ORMOCER®I:PA = 10:1 (in wt.) a 20 μm thick coating of the radically initiated polymerization is obtained after the spin-coating. After the development step, a 12 μm thick coating is obtained.

First polymerization experiments were performed with resin PD5. As for ORMOCER®I, Irgacure®369 was chosen as photo-initiator, but its quantity was increased to 1.5 wt.-% due to the lower content of MEMO in PD5 compared to its content in ORMOCER®I. As for the technological processing of ORMOCER®I (Table 57), the same processing was applied to resin PD5. Compared to the results of ORMOCER®I processing, some differences were observed. Firstly, it was not possible to obtain thick coatings with PD5. With ORMOCER®I by varying parameters such as the spinning speed and the dilution rate, different coatings thickness can be obtained. For example, homogeneous 12 μm thick coatings were obtained with ORMOCER®I with a dilution rate of ORMOCER®I:PA = 10:1, whereas homogeneous coatings from resin PD5 were obtained only with highly diluted solution (dilution rate PD5:PA = 0.9:1), and a speed spinning of 4000 rpm, leading to thicknesses lower than 10 μm. The replacement of 33 mol-% of MEMO by 33 mol-% of Ti(OEt)$_4$ has led to a significant decrease of the organic content in the material, and an increase of metal-oxygen-metal bonds. Moreover, it is known from the literature that thick films based on inorganic compounds are

difficult to obtain, and typically for 1 μm thick titania-based coating multilayers coating processes are needed[103]. Furthermore, the development step performed in the mixture (MP:isopropanol), which is typically used for ORMOCER® resins, has led to white coatings, which this was not observed if only MP was used as developer. Thus, MP was further used in the development step. The temperature of the pre- and post-exposure bake, which were optimized to be 80°C for ORMOCER®I was found to be too low for resin PD5. At this temperature, the structures were completely delaminated. Thus, higher pre- and post-exposure bake temperatures were investigated.

Series of experiments were carried out with resin PD5 (c.f., chapter 3.3.2). These show that a prebake step at 110°C for 1 min is required in order to improve the adhesion of the coating to the substrate. Below this temperature, the coating delaminated upon development. In addition, those parts of the coatings which were not exposed to UV light could not be removed in the development step for samples handled with a post-exposure bake step at 110°C for 1 min. Toluene and MP were investigated as developer, and MP has led to better results. Structures were achieved for samples which were prebaked at 110°C for 1 min, and without post-exposure bake. With the same conditions, the exposure time was increased from 30 to 600 s, leading to an increase in thickness from 170 to 1150 nm. Figure 86 shows optical microscopy images of patterned PD5 layers, which were UV-irradiated for 60 and 240 s, respectively. Squares of 5x5 μm^2 were easily obtained by processing resin PD5 which point to a potential for high resolution.
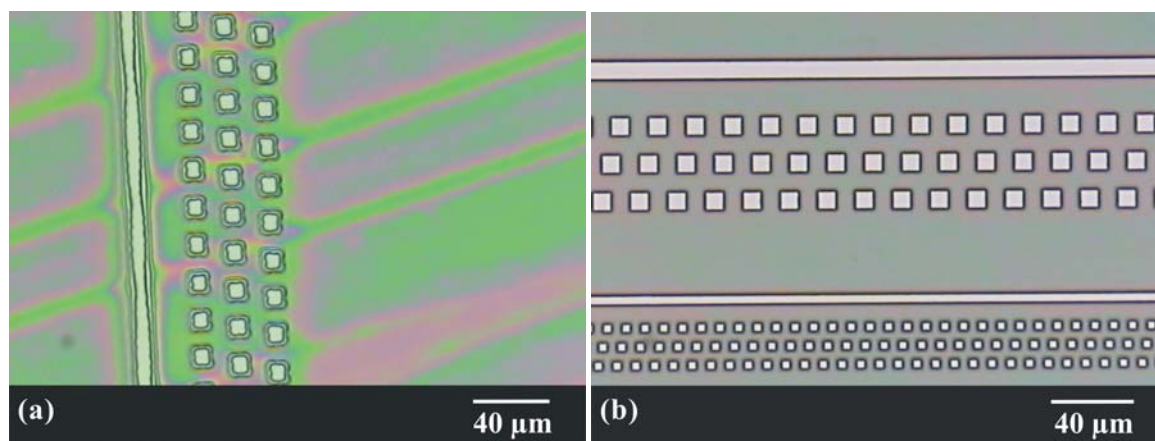
Figure 86: Optical microscopy images of patterned PD5 coatings processed on p-Si(100) wafers (white) at different exposure times. (a) 60 s (sample 220104/2a, thickness 540 nm, part 0), and (b) 240 s (sample 230104/4, thickness 970 nm, part 0).

The refractive indices of the patterned PD5 coatings which were UV-cured but not thermally cured in order to compare their refractive indices with those of the non-processed coatings was calculated from transmission spectra (Figure 87). The transmission spectrum of a UV-processed coating shows a high transmittance above 500 nm, and a strong absorption around 400 nm, which is attributed to the presence of titania in the hybrid film[46,235], and also to the presence of the phenyl groups from DPD. After the development step, the thickness of the coating was 1100 nm and the refractive index close to 1.63 (at 1550 nm) and 1.65 (at 810 nm). Comparison to the refractive index measured on the non-processed coatings (i.e., without initiator and not thermally cured), which was close to 1.58 at 1550 nm (sample 241104/1), revealed an increase of the refractive index of about 3%. This is attributed to the

densification of the coating with the organic cross-linking of the methacrylate group from MEMO. It has to be noticed that the addition of the photo-initiator, which contains phenyl groups (cf., chapter 2.3.1) may also contribute to this increase.
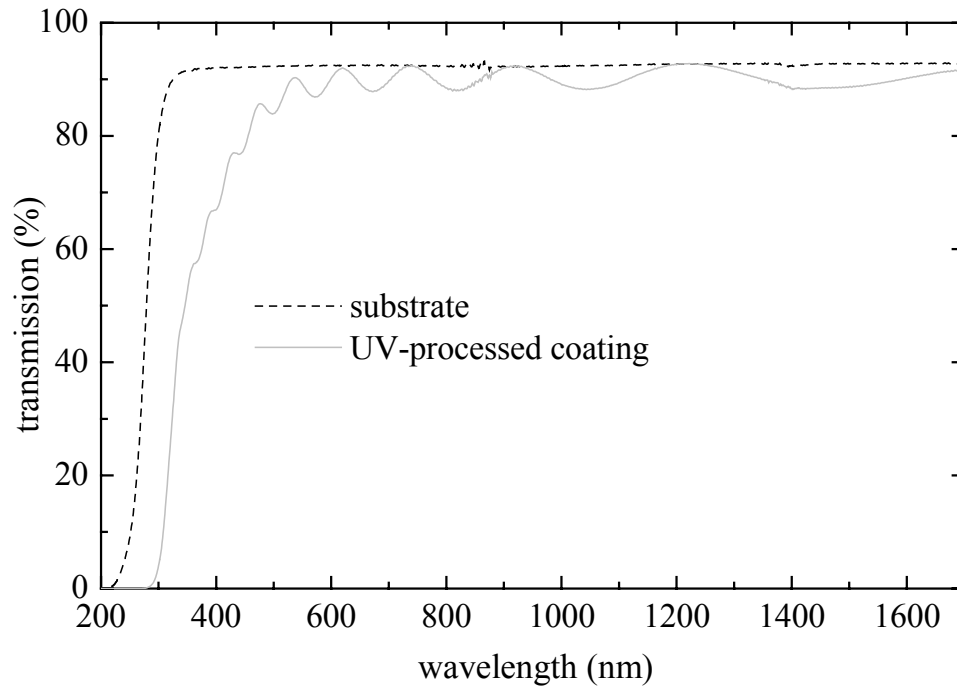
Figure 87: Transmission spectra of a Borofloat® glass substrate, and a UV-processed coating not thermally cured (sample 090204/2, part 0) from resin PD5.

In order to study the reproducibility of the polymerization process, the organic cross-linking was performed with different PD5 batches. Based on the preliminary process for resin PD5 (batch b, cf., Table 57), the same process was applied to batch j. The optical microscopy images in Figure 88(a) show that the non-exposed part could not be removed in the development step. By decreasing the pre-bake temperature to 80°C (Figure 88 (b)), the material could be completely removed from the non-exposed areas, i.e., via opening was achieved. Thus, the UV lithography process of resin PD5 seems to be not reproducible. This is discussed in the following.

Figure 88: Optical microscopy images of patterned PD5 coatings on p-Si(100) wafers with a pre-bake step at (a) 110°C (sample 251104/1, part 0), and (b) 80°C (sample 251104/2, part 0), clearly showing via opening.

In order to explain the non-reproducibility of the PD5 patterning process, characterizations by FT-IR and multi-nuclei NMR spectroscopy of different resin batches of PD5 were carried out. By NMR spectroscopy, no differences between the individual batches could be detected, i.e. the batches sh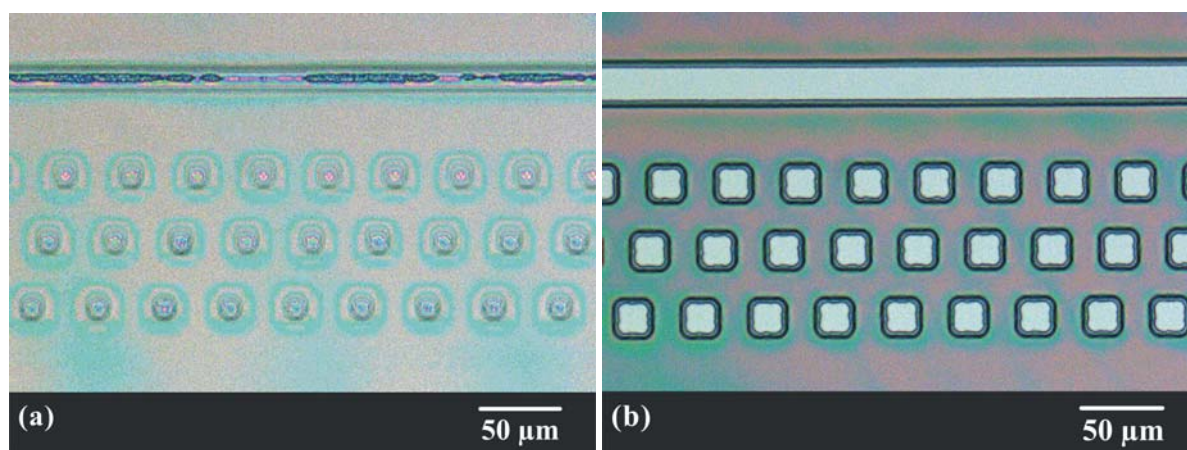owed no deviation from each other. On the other hand, it was found that the PD5 batches still contain cyclopentanone and also 2-cyclopentylidenecyclopentanone. The latter compound is formed by aldol condensation reactions between two cyclopentanone molecules by releasing water (cf., chapter 4.1.2.2.1). During the storage time of the resin, this reaction can proceed with the remaining cyclopentanone content in the resin, and/or it can be proceeded between one cyclopentanone molecule and one 2-cyclopentylidenecyclopentanone molecule, also by releasing water upon the aldol condensation reactions. Since this water may react with the inorganic network of the resin, the titanate and silicate backbone of the resin could be notably affected.

Croutxé-Barghorn et al.[178] have reported that the degree of the condensation of the silicate backbone significantly affects the photopolymerization process. They reported an efficient degree of conversion (DC) upon UV irradiation for condensed systems. For example, a DC value of 5% and more than 30% were notified for non-hydrolyzed MEMO (i.e., containing only T^0 species) and condensed MEMO species (containing T^1 and T^2 species), respectively. These observations were attributed to the change of the viscosity of the material with the DC of the silicate backbone. They reported that a high viscosity favors the propagation reaction rather than the termination step, thus allowing to achieve a higher DC value with the photo-polymerization process. Thus, as soon as water from the aldol condensation reaction can be produced in resin PD5 upon storage, modifications in the inorganic network may occur, which affect the organic polymerization reaction.

In resin PD5, the formation of 2-cyclopentylidenecyclopentanone by an aldol condensation may change the viscosity of the resin during storage time, and can notably affect the reproducibility of the polymerization process. After one month storage time of the diluted resin PD5 containing the photo-initiator, a gel was obtained which shows the increase of the viscosity with the storage time.

In order to avoid gel formation of the resin upon storage by water released from the aldol condensation, the same synthesis was performed by replacing cyclopentanone by THF as solvent, but by defined addition of water for the hydrolysis and condensation reactions. The resin was labeled as PD92 (chapter 3.2.2.2). The processing of resin PD92 was carried out

using the same conditions as for PD5. This process has led to a very thin coating below 40 nm. It was found that the pre-bake step at 110°C for 1 min was essential to achieve good coatings. Below this temperature, the adhesion of the coating was poor, resulting in the removal of the coating upon development. In order to even more improve the adhesion of coatings on the substrates, a titania-primer coating was introduced in processing (cf., chapter 3.3.2) which considerably improved the adhesion between the substrate and the PD92 coating. Figure 89 shows two optical microscopy images of coatings, which were prepared by the same polymerization process, but using two different substrate treatments. The coatings applied on the titania-primed Si wafer are considerably better than those applied on a bare Si wafer surface. More cracks were observed around the structures for the coating applied on the non-primed Si wafer compared to those applied on the titania primed Si wafer. The cracks seem to occur by delamination of the coating during the development step (exemplary arrows in Figure 89(a)). A reduction of this phenomenon was observed for coatings applied on titania primed Si substrates.
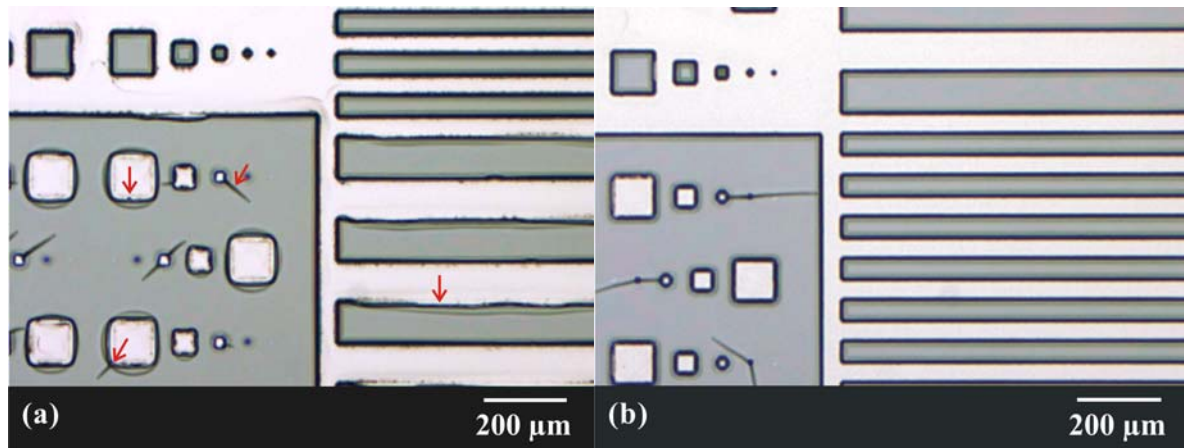
Figure 89: Optical microscopy images of patterned PD92 coatings on p-Si(100) wafers. These substrates were (a) non-primed, and (b) titania-primed using the same processing conditions. The arrows mark exemplary delamination points.

Finally, cracks typically occurring around the structure disappeared completely by decreasing the UV exposure time from 120 to 30 s (cf., Figure 90), corresponding to a decrease of the UV exposure dose of 66%. This points to the fact that a reduction of the exposure dose has led to less densification of the material.

The duration of the development step also considerably affected the appearance of the coatings. For development steps longer than 1 minute, cracks around the non-exposed parts were observed (cf., Figure 90 (c)). For short development durations (cf., see Figures 89 (a) and (b)), no cracks were observed. Based on the same patterning process, a decrease of the UV exposure time from 30 to 10 s has led to a worse thickness homogeneity of the coating (cf., Figure 90 (d)). The coating thickness of a 30 s exposed sample was about 2 μm, whereas a thickness variation between 1 and 3 μm was found for 10 s UV exposure.
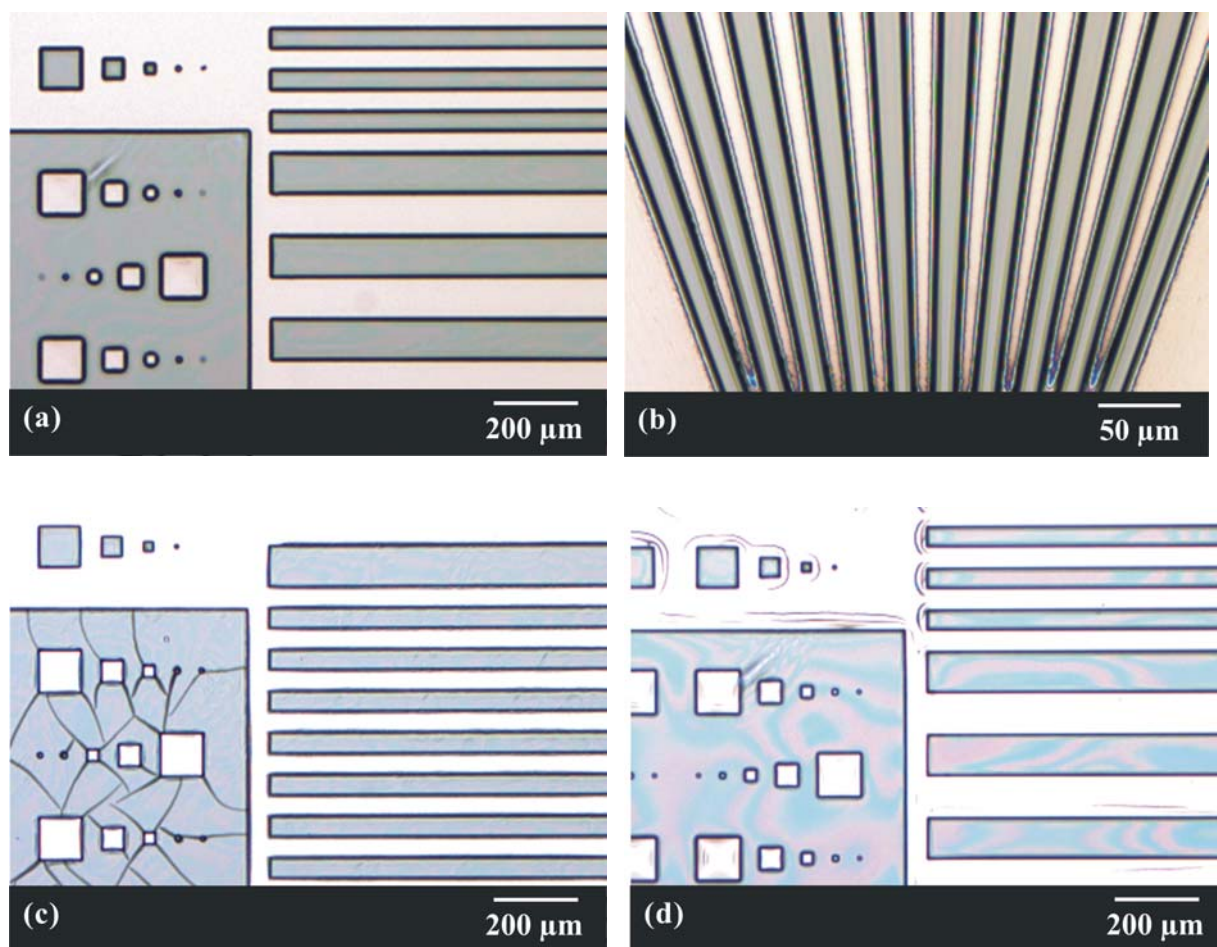
Figure 90: Optical microscopy images of patterned PD92 coatings on titania-primed p-Si(100) wafers. The samples were UV-exposed for 30 s [(a) to (c)], and were developed for (a) and (b) 30 s, (c) for 1 min, whereas (d) was UV-exposed for 10 s and developed for 1 min.

The processing of resin PD92 has led to well-patterned coatings, where 8 μm structures could be dissolved. Below 8 μm, the materials were not completely dissolved. The resolution of the structure is typically well below 5 μm for an ORMOCER® synthesized without any titanium precursors[76]. Thus, resin PD92 is promising, but can be possibly improved by better adapting the processing parameters, such as for example the quantity and/or the kind of UV initiator, the UV exposure dose, the developer solvent, and the temperature treatment. To our knowledge, it is the first time that patterned structures are obtained with materials containing a such high titanium content (33 mol-%). Thus, due to the successful patterning process of resin PD92, this material was chosen for the 2PP process in order to write 3D structures (cf., chapter 4.2.2).

The optical properties of the organic-inorganic PD92 coating were measured by ellipsometry[4]. The dispersion curve of the refractive index of the PD92 coating obtained after

---

[4] Ellipsometry measurement which was carried out at at the Joanneum Research Institute for Nanostructured Materials and Photonics (Austria).

the micro-patterning process is shown in Figure 91. In order to compare the influence of UV irradiation on the refractive index, the refractive indices of the non-UV-exposed coating, which were determined from the transmission spectrum are also shown in Figure 91.
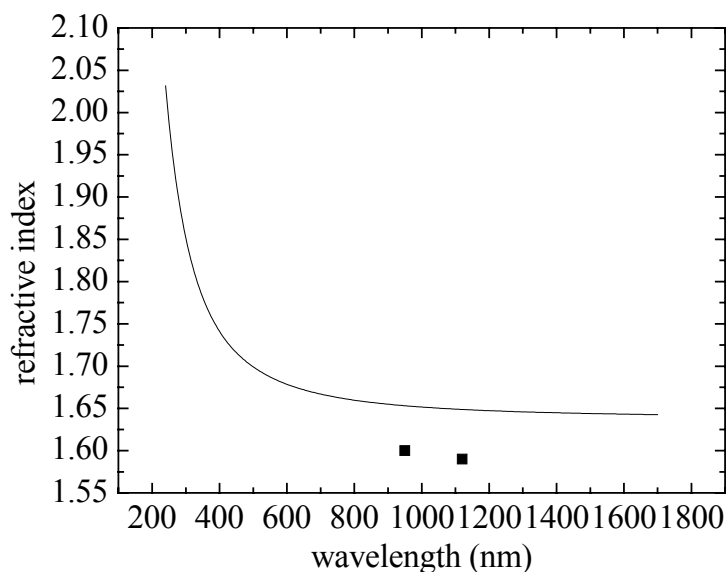

Figure 91: Dispersion curve of a patterned PD92 coating. The two values determined from the transmission spectrum of the non-UV-exposed coating are marked by the two squares.

At 950 nm, the refractive index of non-processed coating is 1.60, whereas a value of 1.65 was measured for the patterned coating due to a densification of the material upon processing, for example by an organic cross-linking of the layer, which is known to increase the refractive index due to the densification of the material[180,236]. Moreover, the addition of the photochemical initiator can also contribute to the increase of the refractive index due to the presence of aromatic groups which are known to improve the refractive index due their better electronic polarizability[118]. In order to study the effect of the UV exposure on the coatings, the cross linking (determined by DC) and refractive indices values were calculated from μ-Raman spectra of non-UV-exposed and UV-exposed coatings recorded for different UV irradiation times. The calculation of the DC values is described in chapter 3.1.4 (Eq. 16). Since the measurements were performed just after the UV exposure, no development step has been carried out. Thus, an oxygen inhibition layer is present at the surface (i.e., a non-cross-linked area at the coating's surface[175]) which is formed by the reaction of the excited photo-initiator reacted with molecular oxygen. In order to minimize the signal of the inhibition layer, the μ-Raman spectra were recorded near the surface of the silicon wafer.

Moreover, since the DC values have been reported to be affected by the initiator concentration[178,183], μ-Raman spectra were recorded for samples prepared with two concentrations of Irgacure®369 (1.5 and 3 wt.-%).

Figure 92 shows three μ-Raman spectra after different irradiation times, for coatings prepared from a formulation based on 1.5 wt.-% of Irgacure®369. Four peaks are clearly visible, whereas their intensity differs slightly for 1638 and 1715 cm^{-1}, respectively. The peaks at 1567 cm^{-1} are attributed to the antisymmetric stretching vibration of the C=C from the phenyl group from DPD. Since their position and intensity does not change upon processing, they are

used as standard internal reference. The symmetric stretching vibration of the C=C from the phenyl group from DPD is recorded at 1591 cm^{-1}.

The peak recorded at 1638 cm^{-1} is attributed to the organic polymerizable moiety (C=C) of the methacrylate group of MEMO. The decrease of its area with the increasing UV irradiation time could be attributed to a UV-induced organic cross-linking of the methacrylate group. In addition, due to the strong absorption of titania and its photocatalytic properties, a degradation of the organic groups may also occur[99,100,190]. A slight decrease of the intensity of the C=O stretching mode at 1715 cm^{-1} can be also observed. This is probably due to the conjugation of the carbonyl bond with the C=C bond. This phenomenon has been reported to be more important FT-IR spectroscopy than in Raman spectroscopy[208].
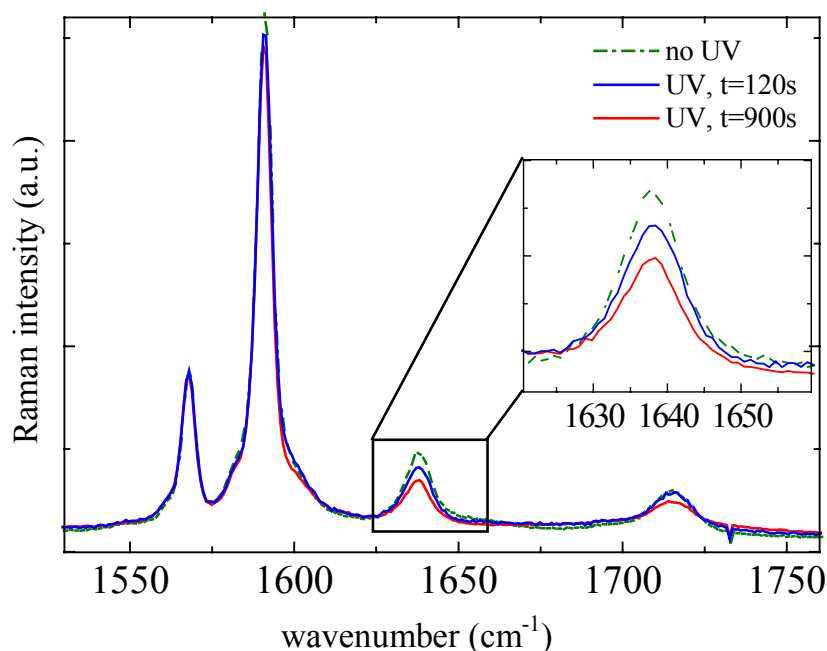
Figure 92: Evolution of µ-Raman spectra of PD92 (prepared from a formulation with 1.5 wt.-% Irgacure 369) coatings in dependence of the UV exposure time for no UV irradiation (0 s, sample 260106/1), 120 s (sample 260106/2), and 900 s (sample 260106/4). Sample preparation is describe in section 0.

Similar spectra were detected on coatings prepared with 3 wt.-% photoinitiator, which are not shown here. The only difference in the spectra compared to spectra shown in Figure 91 is the increase of the intensity of the very weak shoulder around 1604 cm^{-1}. This shoulder is attributed to the presence of the UV initiator. The resulting DC values for both coatings are displayed in Figure 93.
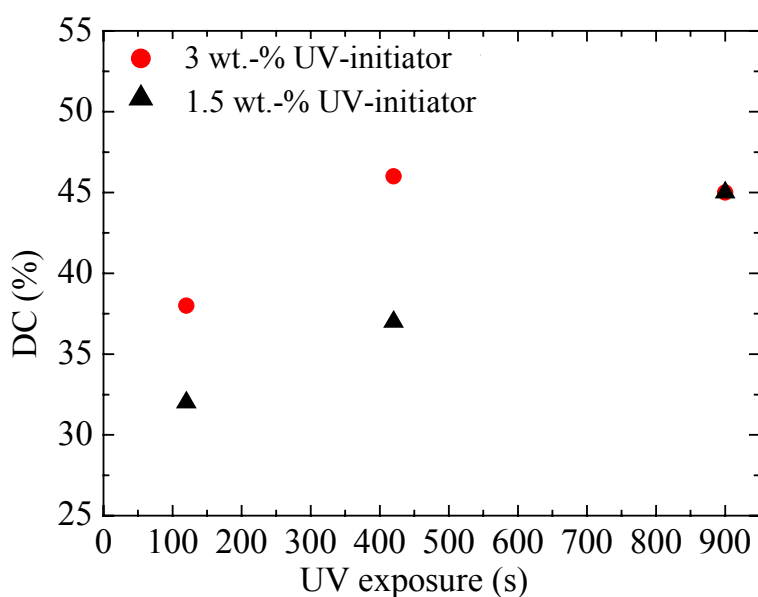
Figure 93: Influence of the UV exposure time and the UV initiator (Irgacure®369) concentration on the DC for a non-developed coating.

For long UV exposure times (900 s), no significant difference of the DC values with the photo-initiator concentration is observed. For 120 s UV exposure times, the DC values are between 32 and 37%. These DC values are very low compared to those reported in the literature. For example, on completely processed coating based on 50 mol-% DPD and 50 mol-% MEMO, DC values have been reported by Houbertz et al.[183] to be approximately between 62 and 78 %, for UV initiator concentrations ranging between 0.25 and 3 wt.-%. This difference can be attributed to the presence of titania, which strongly absorbs in the UV regime[237], i.e., in the same wavelength range than the photo-initiator, and thus might absorb a part of the energy needed to initiate the polymerization process. As already mentioned, the DC value is referred to the degree of conversion or polymerization, i.e., the percentage of vinyl moieties converted to aliphatic groups. However, due to the strong absorption of the titania in the UV regime, and its potential photocatalytic activity[99,186,189-191], a degradation of the organic groups may also occur. Thus, the DC values given in Figure 93 should be understood as the degree of organic polymerization and degree of organic degradation, since one cannot distinguish between both using μ-Raman measurements.

Since the μ-Raman measurements are performed on non-developed coatings within a depth of 3 μm, the possibility of a partial measurement in the inhibition layer should be considered, and this can also contribute to the low DC values in the resin PD92. Croutxé-Barghorn et al.[178] also reported DC values around only 45%, for materials based on MEMO. They attributed these low values to the presence of the inhibition layer.

In addition, the effect of the UV irradiation time (and thus the UV exposure dose) on the refractive index values was investigated by ellipsometry on coatings exposed to various irradiation times. The dispersion curves are displayed in Figure 94, showing a significant increase of the refractive index from 1.62 to 1.64 measured at 633 nm, for exposure times close to 120 and 900 s, respectively. This corresponds to an increase in density of the

140

coatings, and correlates well to the higher DC values from the μ-Raman data (Figure 93). It must be pointed out that the ellipsometry measurements were carried out on non-developed coatings, which means that the inhibition layer, i.e., the non-cross-linked layer remains present at the surface. Thus, the refractive indices are expected to be much higher than 1.64 for completely processed layers (developed and thermally treated to remove solvents which lower the refractive index). For patterned and developed coatings, refractive indices of about 1.67 at 633 nm were achieved (cf., Figure 91), whereas the layers are still not completely processed, i.e., a final thermal curing was not employed. This, however, would even result in a higher density due to further cross-linking and removal of residual solvents from the layers which are known to reduce the refractive index.
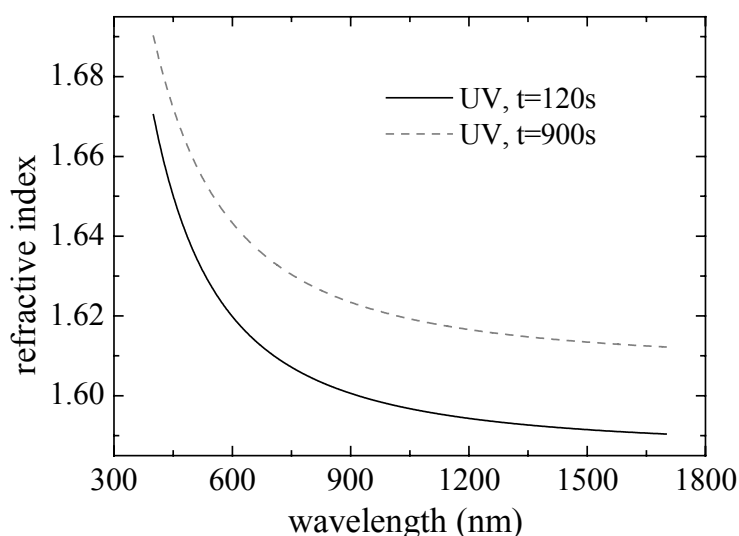
Figure 94: Dispersion curves of the refractive indices of PD92 coatings UV-exposed for 120 and 900 s (samples 231105/1b and 231105/1d, part 0).

The DC values were also investigated on developed coatings. Based on the optimization of the polymerization process of resin PD92, μ-Raman measurements were performed after the pre-bake step and after the development step. The DC value was calculated to be close to 25% on a developed coating which was UV-exposed for 30s. This value, however, is much lower than those obtained for the non-developed coatings (cf., Figure 93), which results from the shorter UV exposure time.

The organic cross-linking of the hybrid organic inorganic materials PD5 and PD92, based on the same precursors (33 mol-% Ti(OEt)$_4$, 17 mol-% MEMO, and 50 mol-% DPD), but synthesized with different solvents was investigated. The polymerization process of resin PD5 was not reproducible. Solutions based on resin PD5 became gels after one month storage time, whereas no gel was obtained even after one year storage time for resin PD92.

Since the processing of PD5 was not very reducible as described above, more investigations were carried out on the organic cross-linking of resin PD92, for whivh well-patterned coatings were obtained. The surface preparation of the Si substrate by applying a titania primer layer has significantly improved the adhesion between the substrate and the coating. The DC values and thus the refractive indices of the coatings have increased with the UV exposure time. Moreover, the DC values which correspond to the percentage of vinyl groups converted into alkyl groups, and the contribution of a possible degradation of the organic

groups have to be considered. The latter contribution can notably affect the refractive index. Finally, the refractive index of the completely processed coating, but without thermal curing, is close to 1.67 at 633 nm. In comparison to the non-UV-exposed coating, an increase of the refractive index from 1.60 to 1.65 at 950 nm, i.e., of more than 3%, was observed upon UV processing. This increase in n is significant compared to ORMOCER$^{®}$I, whose refractive index increased only from 1.538[77] to 1.552[180,183] at 633 nm, i.e. 0.9 %, upon UV-processing and thermal curing. The degradation of the organic groups in presence of titania in resin PD92 might justify this huge increase of the refractive index during the UV lithography process. Since a high refractive index was reproducibly obtained after the UV lithography process, this resin was selected as model system for further 2PP experiments.

PD51 and PD109 belong to resins based on a low titanium content (33 mol-% Ti(OEt)$_4$, 17 mol-% SETMS, and 50 mol-% DPD) synthesized with SETMS. However, the kind of solvent and the quantity of water were different in the syntheses. PD51 was synthesized in cyclopentanone without additional water, whereas PD109 was synthesized in THF and water was added (ratio equal to 0.5). Like for resin PD5, the presence of cyclopentanone and 2-cyclopentylidenecyclopentanone was also detected in resin PD51. Due to the presence of the latter components, resin PD51 was not stable with the storage time. Thus, the polymerization process of resin PD51 was not detailed investigated.

The influence of the UV exposure time on the C=C conversion was investigated by μ-Raman spectroscopy for resin PD109. Coatings containing 1.5 wt.-% Irgacure$^{®}$369 were UV-exposed for different exposure times (cf., chapter 3.3.2). μ-Raman spectra were recorded near the surface of the wafer in order to avoid a measurement in the inhibition layer still being present at the surface. The μ-Raman spectra (Figure 95) are normalized to the peaks at 1567 cm^{-1}. This peak is attributed to the antisymmetric stretching vibrational mode of the C=C bonds in DPD. The symmetric vibrational mode of the C=C bonds in DPD is close to 1590 cm^{-1}. The latter peak is overlapped with the peaks from the antisymmetric and symmetric stretching vibrational modes from the C=C bonds in the phenyl group from the SETMS moieties, detected at 1598 and 1606 cm^{-1}, respectively. The spectra of UV-irradiated coatings from resin PD109 (cf., Figure 95) show a decrease of the area of the stretching frequency of the polymerizable C=C moiety of SETMS detected at 1629 cm^{-1} by increasing the UV irradiation time. This is attributed to the organic cross-linking or/and to an organic degradation of the resin. The DC values are close to 38% after 120 s UV exposure time, and increased up to 48 and 58% with increasing the UV exposure time to 420 and 900 s, respectively. As for resin PD92, these values are still very low compared to those from materials whose syntheses are based only on organo-alkoxysilanes[183]. This difference is attributed to the presence of a titania backbone, which absorbs in the UV range. Thus, a competition between the UV absorption from the titania backbone and from the photoinitiator can occur. Moreover, as already mentioned for the polymerization of resin PD92, a potential degradation of the organic groups has also to be considered[99,100,188].
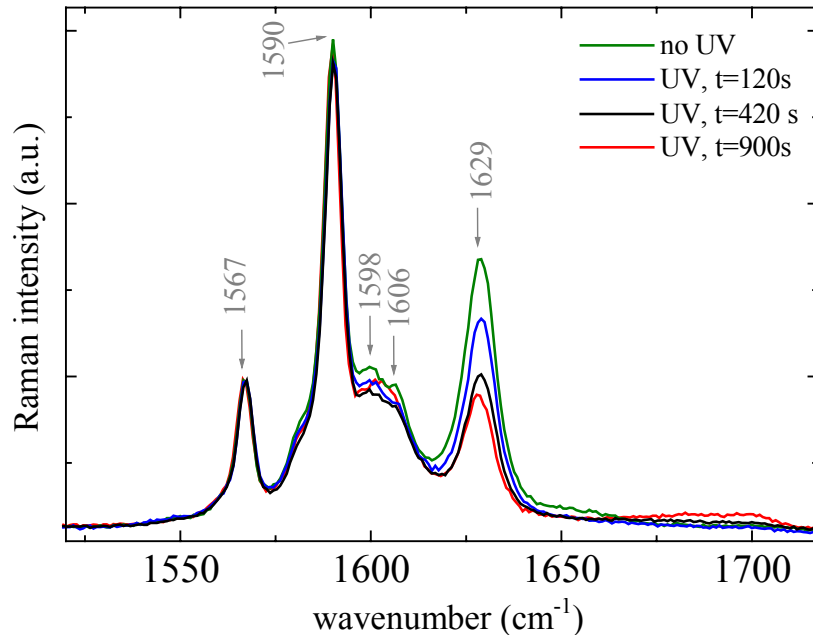
Figure 95: µ-Raman spectra of PD109 coatings for a non-UV-irradiated sample (sample 240106/1), and samples UV-irradiated for 120, 420, and 900 s (samples 240106/2, 240106/3, and 240106/4). Details of sample preparation are given in section 0)

Based on the polymerization process of resin PD92, the UV exposure time was fixed to 30 s for resin PD109. Due to the replacement of MEMO by SETMS and due to a different reactivity of methacrylate and styryl groups with UV exposure, a new process has to be investigated.

First tests show that the pre- and post- exposure bake which were optimized to be around 110°C for resin PD92 have to be decreased for the processing of resin PD109 due to an insolubility of the non-UV-exposed areas after UV irradiation. This insolubility can result from the pre- and post- exposure treatment, or can be related to the solvent used as developer. Thus, some pre- and post exposure-bake tests were performed at temperatures between 40 and 60°C. Figure 96 shows optical microscopy images of some patterning tests from PD109 coatings after applying different pre- and post-exposure temperatures.
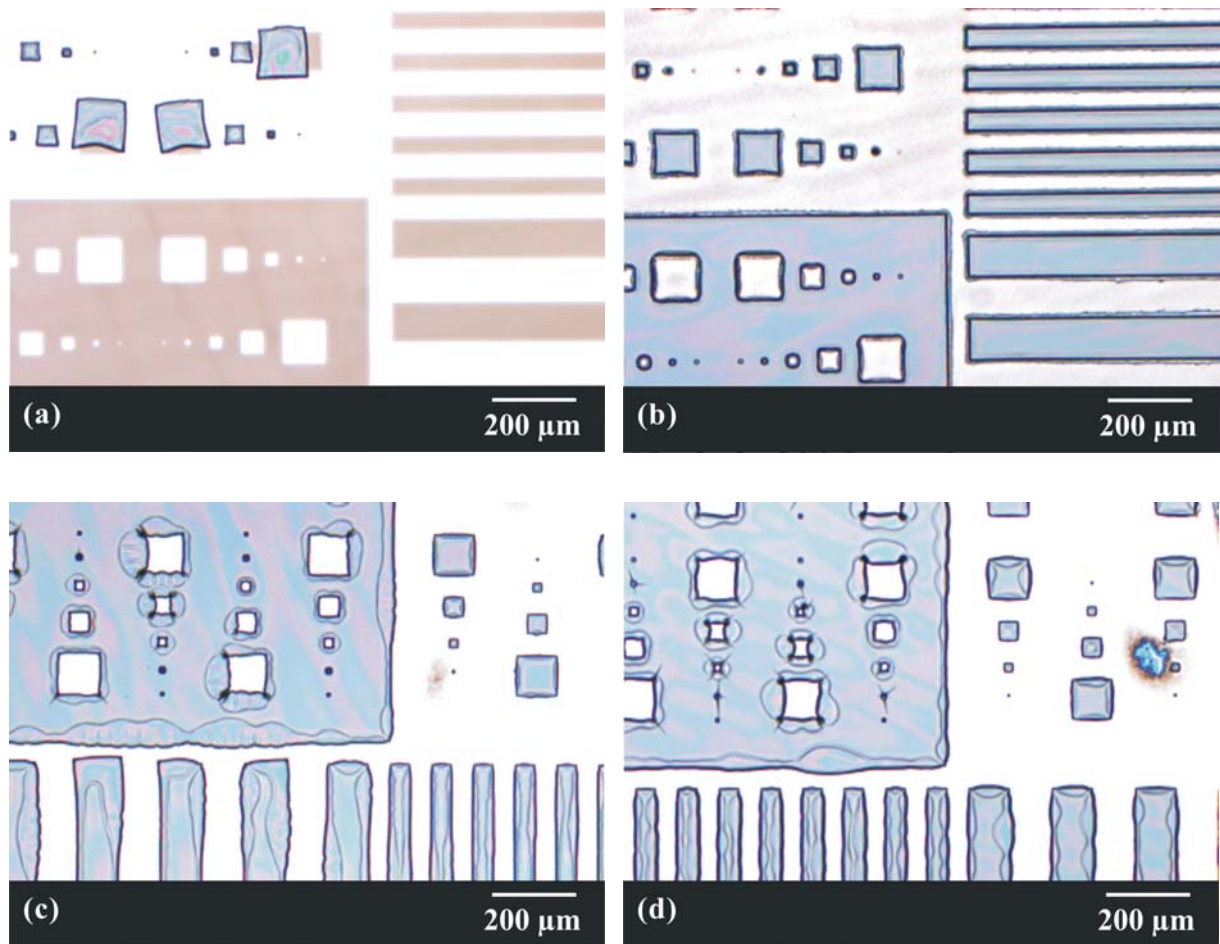
Figure 96: Optical microscopy images of patterned PD109 coatings after 30s UV exposure and 30s development in MP. Pre- and post-exposure bake were carried out at (a) 40 °C for 1 min, (b) 60 °C for 1 min, (c) 50 °C for 1 min, and (d) 40 °C for 3 min (samples 190706/1, 190706/2, 190706/3, and 190706/4, part 0).

Coatings treated at 40°C delaminate (Figure 96 (a)). A better adhesion was obtained with a pre- and post- exposure bake temperature of 50 °C, where a delamination around the non-exposed parts of the sample is observed (Figure 96 (c)). The same effect, but less pronounced was also observed for the coating thermally treated at 40°C for 3 min (Figure 96 (d)). On the other hand, from Figure 96 (b) one can conclude that a good adhesion is achieved for a temperature treatment at 60°C. Figure 97 shows a zoom into Figure 96 (b), where one clearly sees that 25 µm open vias are obtained. However, the material is not well dissolved around the structures. A rending between the non- and UV- exposed parts is observed.

144
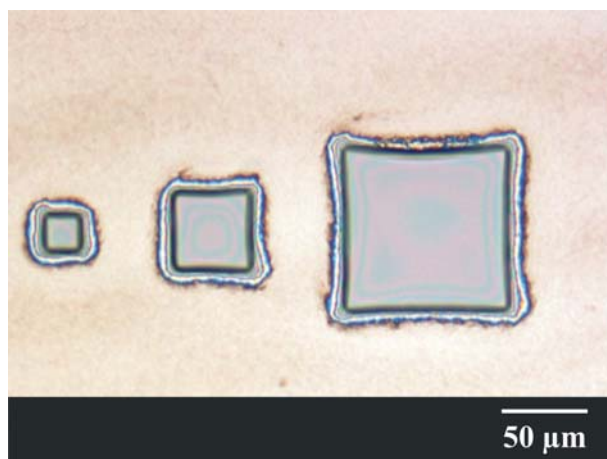
Figure 97: Zoom into the optical microscopy image of patterned PD109 coatings from Figure 96 (b) (sample 190706/2, part 0). Square areas correspond to UV-exposed regions.

It can be concluded that the DC values of resins based on SETMS are slightly higher than those based on MEMO. The temperature of the pre- and post-exposure bake step was completely different depending on the polymerizable organo-alkoxysilane used for the synthesis of the resins. Besides, the pattern resolution appears to be lower, but much more process optimization as well as a more detailed understanding of the underlying process would be necessary, which was not the scope of this work. Thus, resin PD109 was not selected for the 2PP experiments.

4.2.1.2 Resins based on high titanium content

The polymerization process of resins PD109 and PD92 has been reported to be different due to the kind of organo-alkoxysilanes used for syntheses. Thus, for the polymerization process of resins based on 67 mol-% titanium alkoxide, a distinction between resins based on MEMO (PD49, PD79, and PD113) and SETMS (PD52, PD60, and PD77) was carried out. Moreover, due to the addition of the catalyst HCl, transesterification reactions occurred (cf., chapter 3.2.2.1). These reactions have reduced the presence of the polymerizable groups in resins based on MEMO. Thus, more attention was put on the polymerization processes of resins PD52, PD60, and PD77, based on SETMS, particularly on the polymerization process of resin PD77. PD77 as chosen because of the evolution of its refractive index with the curing temperature. Since the quality of the processed coating depends on many parameters as described above, many tests were performed. Thus, in order to evaluate the feasibility of the polymerization process, investigations of the UV irradiation time of PD77 coatings on the DC values were studied first. Then, processing tests on the polymerization process were done by varying parameters such as the initiator concentration, the UV irradiation time, the pre and post-exposure bake as well as the developer.

The influence of the exposure time on PD77 coatings was studied by μ-Raman spectroscopy. Since the samples were not developed, the μ-Raman spectra were recorded near the surface of the wafer in order to avoid measurements in the oxygen inhibition layer. Figure 98 shows the evolution of the μ-Raman spectra with the UV exposure time of the coating. In order to compare the spectra, the peaks recorded at 1584 and 1604 cm^{-1}, corresponding to the antisymmetric and symmetric vibrational modes of the C=C of the aromatic groups from

SETMS were taken as internal reference. As expected, the area of the vibrational mode of the polymerizable moiety detected at 1630 cm^{-1} decreases with increasing the UV exposure time. Even after a very long exposure such as 15 min, the polymerizable moiety C=C from SETMS is still detected. By increasing the UV exposure time from 120 to 900 s, the DC values increased from 31 to 66%, respectively. The impact of the concentration of initiator on the DC was also investigated by μ-Raman spectroscopy. For a UV initiator concentration close to 2.5 wt.-%, the DC value was found to be 54 and 66% for 120 and 900 s UV exposure, respectively.
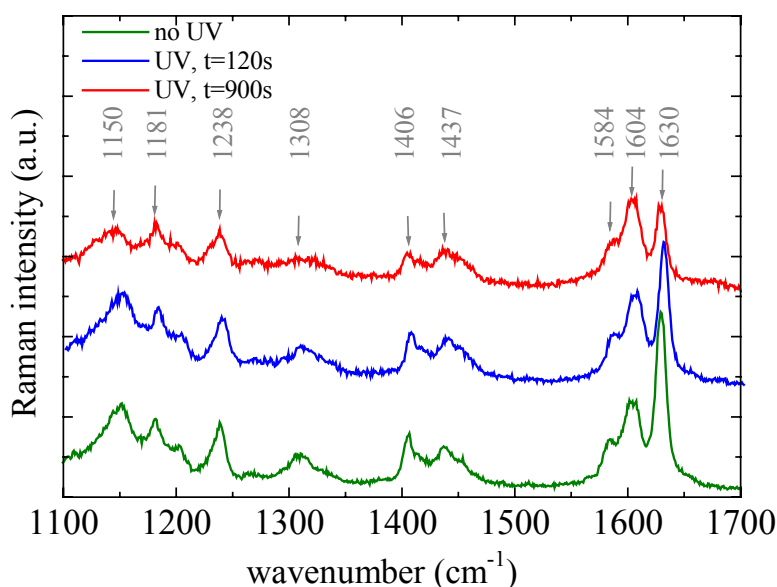
Figure 98: μ-Raman spectra of PD77 coatings for samples being non-UV-irradiated (sample 260405/1a), and UV-irradiated for 120 and 900 s (sample 260405/1b and -/1c). Details of the sample preparation are given in section 0)

The development step was investigated with different solvents. The UV initiator concentration and the UV exposure time were fixed and differents solvent, or mixtures of solvents were tested.

Resin PD77 was diluted in THF, and Irgacure®369 was used as photo-initiator. Three initiator concentrations 3.5, 1.5, and 0.5 wt. %, were investigated. The diluted resins were spin-coated on p-Si(001) wafer substrates. The UV exposure time and the temperature of the pre- and post-exposure bake were adjusted depending on the quality of the coating obtained after the development step. The details of the solution preparation and processing of the PD77 coatings are given in chapter 3.3.2. Two examples of optical microscopy images of processed PD77 coatings based on 3.5 wt.-% initiator are shown in Figure 99. Both coatings were UV-irradiated for 120 s and developed for 30 s in MP. However, the pre- and post-exposure bake temperatures lead to difference patterning results. The non-UV exposed part could only be dissolved for the coating which was not thermally treated, and delamination near the open vias is observed (Figure 99 (b)). In fact, by increasing the development time to 1 min instead of 30 s, the coating completely delaminated in MP due to the poor adhesion between the coating and the substrate, and/or due to a poor DC value. The samples presented in Figure 99 (b) developed for 30 s led to 990 nm thick coatings, without thermal pre-treatment, but thermally cured at 150°C curing for 3 hours.

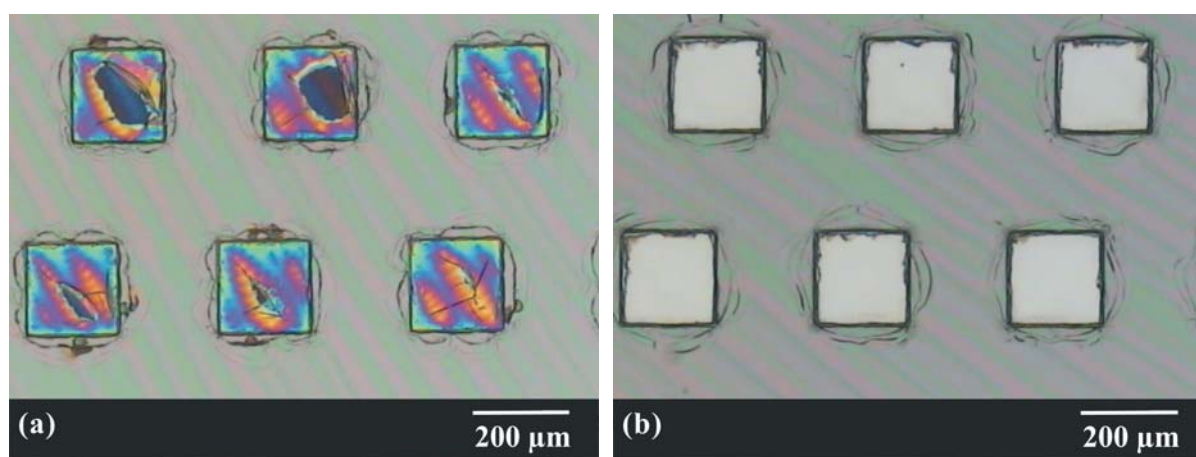Figure 99: Optical microscopy images of PD77 coatings based on 3.5 wt.-% initiator. The samples were exposed to UV for 120 s and were developed for 30 s in MP. The prebake was varied: (a) 1 min at 60°C (sample 291104/1), and (b) no pre-bake (sample 291104/3). Square areas correspond to non-UV-exposed regions, i.e., the substrate is visible.

The patterning process was also investigated with a very low photo-initiator concentration of 0.5 wt.-%. No matter which exposure dose or temperatures were used for pre- and post-exposure bake, very thin coatings below 30 nm were obtained. This might be due to a low DC value related to the low initiator concentration. Thus, the change of the solubility between the non-exposed and UV-exposed part may not be different enough in order to differentiate them. Since the rate of dissolution for a polymer decreases with an increase of the molecular weight[176], the molecular weight of the polymer from resin PD77 may be not sufficient enough, and the DC value is too low.

The concentration of the initiator was increased up to 1.5 wt.-%, the UV exposure time was fixed to 120 s, and the temperature of the pre- and post-exposure bake was varied. Figure 100 shows optical microscopy images of PD77 coatings for different pre- and post-exposure temperatures. For a coating which was treated at 40°C with a pre- and post-exposure bake (Figure 100 (a)), the non-exposed part was partially delaminated (arrow in Figure 100 (b)), and a very thin coating was obtained (~ 30 nm) with cracks around the opened vias. For a coating thermally treated at 70°C, the difference in solubility between the non- and UV-exposed parts still was not high enough, and a delamination of the non-UV-exposed part can be observed (Figure 100 (b)). Finally, further increase of the pre- and post-exposure temperature up to 80°C yielded samples without delamination (Figure 100 (c)). When the development was done in an ultrasonic bad of MP (Figure 100 (d)), the non-exposure part was partly dissolved leading to a very thin brown coating.
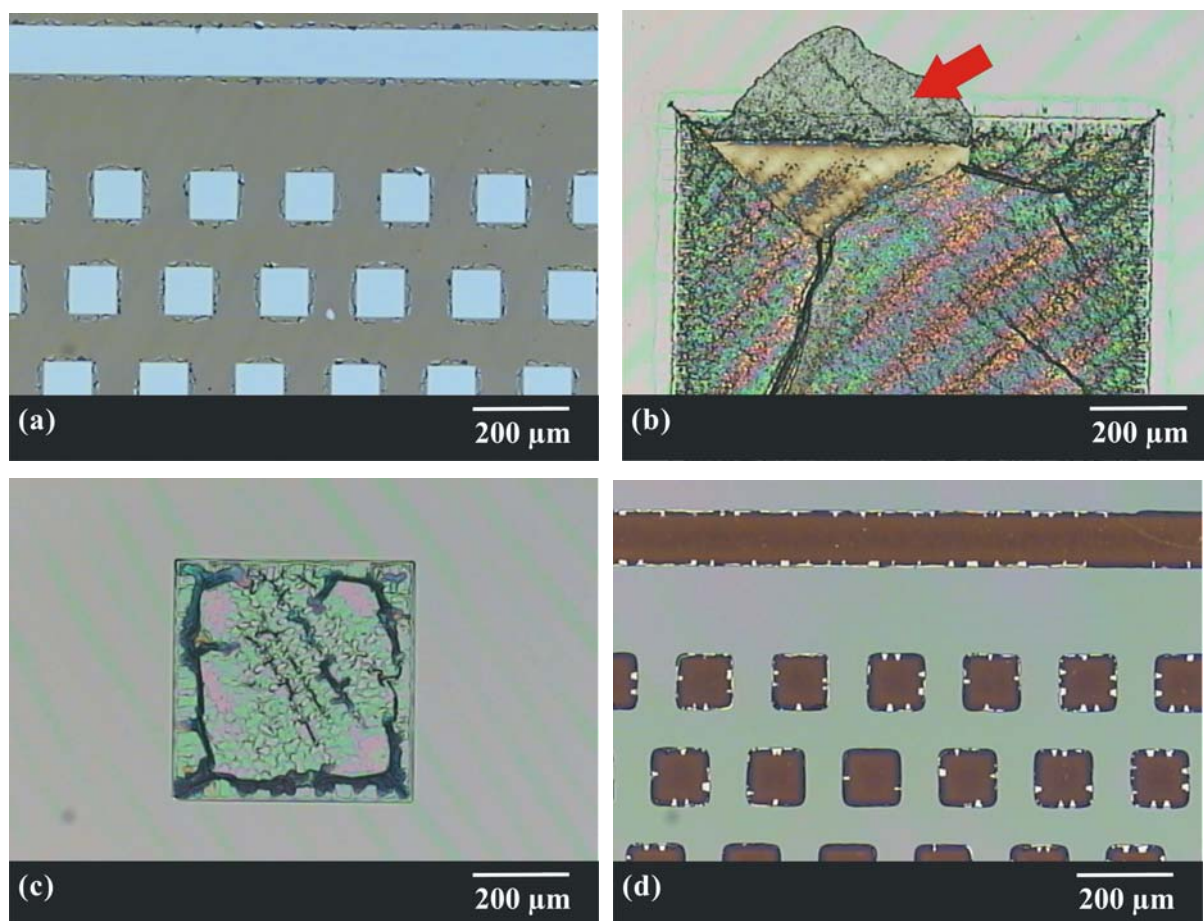
Figure 100: Optical microscopy images of PD77 coatings on p-Si(100), based on 1.5 wt.-% initiator, a UV exposure time of 120 s, a development in MP for 30 s, and with a pre- and post-exposure bake for 1 min at (a) 40°C, (b) 70°C, and (c) 80°C. (d) Post exposure bakeoff 80°C, but developed in an ultrasonic bath (samples 210305/2-, -/5, -/3, and 180305/2). Squared areas correspond to non-UV-exposed regions.

For a low initiator concentration (0.5 wt.-%), very thin coatings are obtained independently of the pre- and post-exposure temperature. For a high initiator concentration (3.5 wt.-%), the non-exposed areas can be removed during the development step only for coatings which were thermally not treated. On the other hand, non-UV-exposed areas for samples prepared with an initiator concentration of 1.5 wt.-% were removed during the development step, if coatings were thermally treated at 40°C. Rising the pre- and post-exposure temperature up to 70°C still yielded no significant difference of exposed and non-exposed areas, and the non-exposed areas still could not be dissolved. Even if the temperature was increased to 80°C, the non-exposed parts could not be dissolved, except if the development was carried out in an ultrasonic bath. In that case, the non-exposed areas led to a very thin brown coating. Thus, the development process is also a step which has to be investigated in more detail particularly, for example the kind of employed developer.

Therfore, different solvents and also mixtures thereof were investigated as developers which will be described in the following. Two PD77 solutions were prepared (PD280405/1, and PD030505/4 cf., chapter 3.3.2), based on an initiator concentration of 1.5 wt.-%. Since the μ-Raman measurements from PD77 coatings (Figure 98) showed a higher DC value for a UV

148

exposure time of 900 s, the latter one was chosen for investigations on the development solutions.

In order to make sure that the coating which was exposed to UV light 900 s shows the same behavior during the development step in MP than the coatings which were UV-exposed for 120 s, a test with MP with and without an ultrasonic bath was carried out. The corresponding optical microscopy images (Figure 101) correlate very well to those of samples which were UV-exposed for 120 s (Figure 100 (c) and (d)). The non-exposed areas were removed only with the ultrasonic bath, and a 1.7 µm thick coating was obtained. However, it has to be mentioned that the edges of the structures were very damaged due to the development process. In addition, residues are observed within the structures.
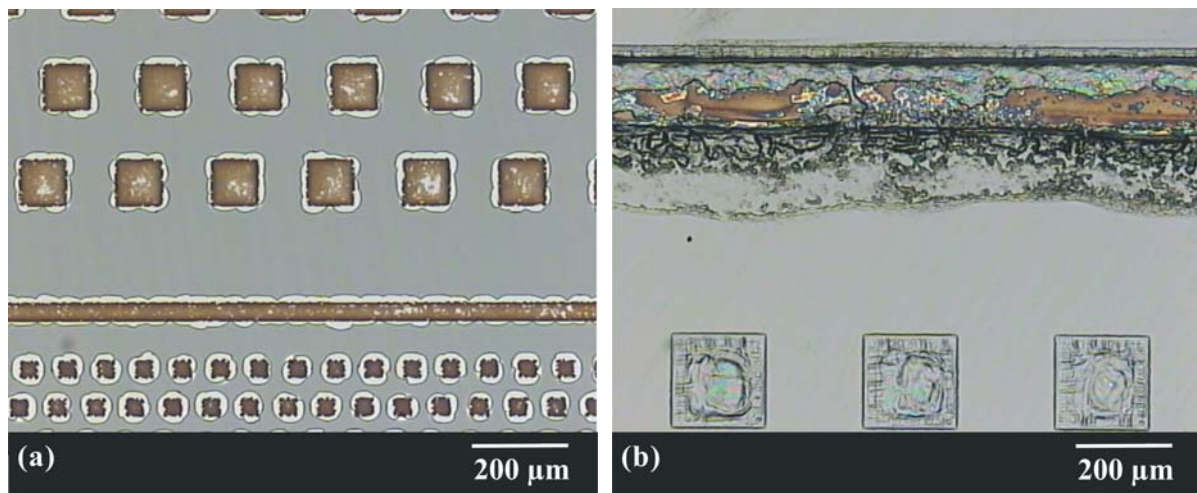
Figure 101: Optical microscopy images of patterned PD77 coatings on p-Si(100) substrates developed in MP (a) with and (b) without ultrasonic bath (sample 280405/2 and -/3, section 0).

The side walls of the structures were investigated by SEM (Figure 102), and EDX spectroscopy was performed at different locations: on top of the coating (position 1 in Figure 102(a)), and at different locations of the structure's side walls (positions 2 and 3 in Figure 102(a)) as well as in the developed via structures (position 4 in Figure 102(a)), where no PD77 material should be present.

149
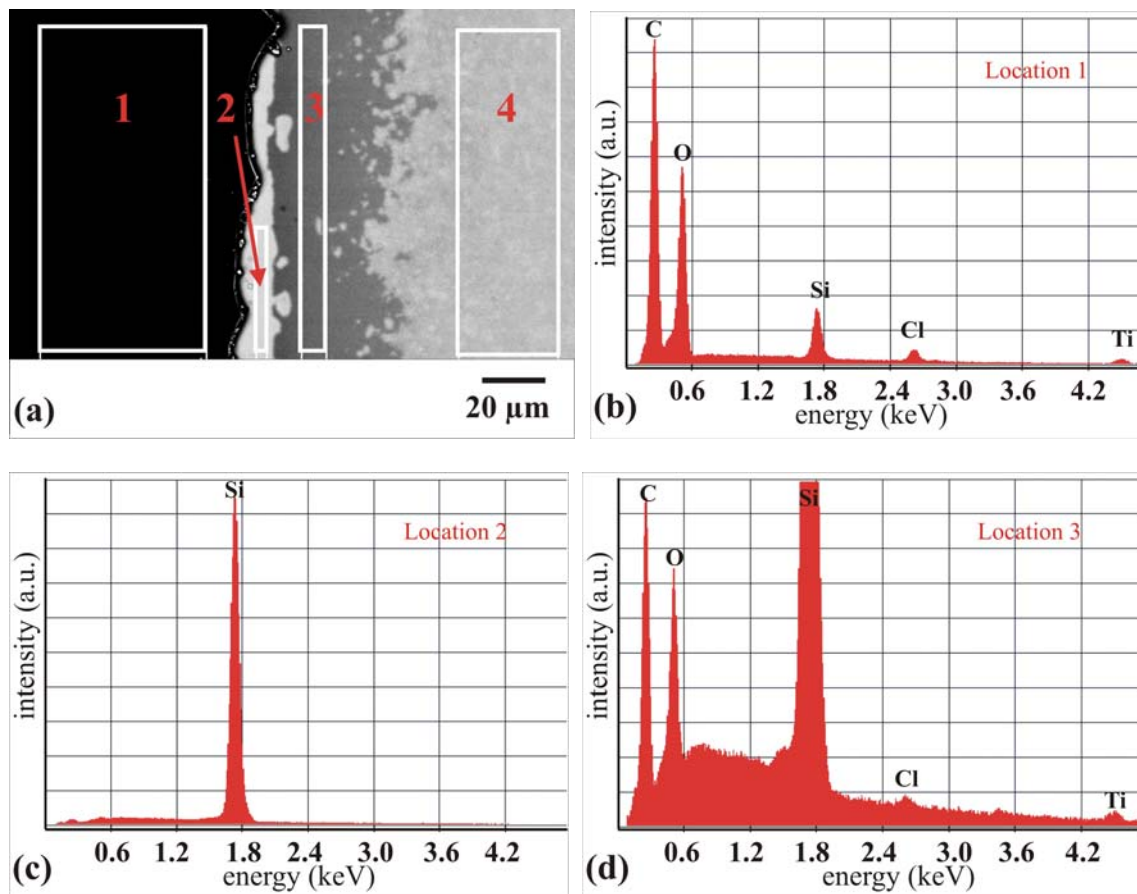
Figure 102: (a) SEM image of a patterned coating of PD77 (sample 280405/3, part 0). EDX spectra recorded in (b) location 1, (c) location 2, and (d) location 3, marked by the white rectangles in (a). Position 4 is not shown due to its similarity to the position 3.

As elements, C, O, Si, Cl, and Ti were detected at the positions 1, 3, and 4 (position 4 not shown). At position 3, a very intense Si peak was found. This is related to the coating thickness: it is so thin that mainly a signal of the Si wafer was detected. At position 2, no Ti was detected.

In order to optimize the development step, other solvents were investigated as developer. Figure 103 (a) to (h) shows optical microscopy images of patterned PD77 coatings developed in acetonitrile, toluene, chloroform, heptane, THF, tert.-butyl-methyl ether, xylene, and acetone, respectively. The non-UV-exposed part was not dissolved if acetonitrile, toluene, heptan, and xylene were used as developer solutions. On the other hand, chloroform dissolved the exposed part, whereas THF, tert.-butyl-methyl ether, and acetone also dissolved the non-UV-exposed part. Figure 103 (e) shows a delamination of the coating at the side wall of the structure, resulting from high mechanical stress and thus, leading to cracks, if THF is used as developer. The use of this solvent is thus too aggressive for the coating. The non-UV-exposed part was partially removed, if tert.-butyl-methyl ether and acetone (Figure 103 (f), and (f)) were used as developer, however, residues are still present in the structure.
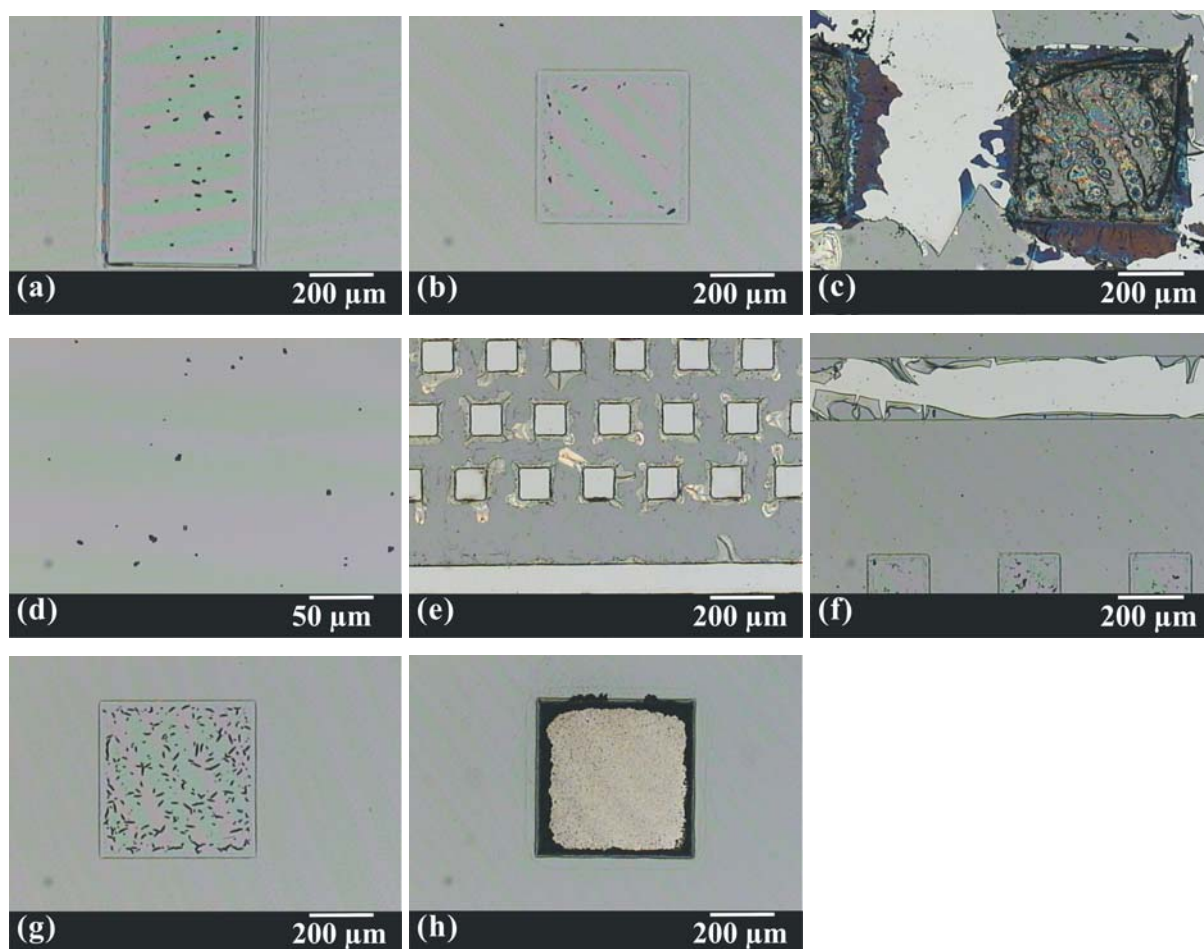
Figure 103: Optical microscopy images of patterned PD77 coatings on p-Si(100) substrates. The samples were exposed to UV light for 900s, and were subsequently developed in (a) acetonitrile, (b) toluene, (c) chloroform, (d) heptane, (e) THF, (f) tert.-butyl-methyl ether, (g) xylene, and (h) acetone (samples 130505/1a, -/1b, -/1c, -/1d, -/2a, -2/b, -2/c, and -/2d, section 0).

Since the best development results were found for THF despite the delamination at the side walls of the structures (Figure 102), mixtures of THF-based solvents were further investigated (Figure 104). The non-UV-exposed part was not soluble, if a mixture of (THF:Xylene)=(1:1) was used (cf., Figure 104 (a)). On the other hand, by increasing the volume of THF (THF:Xylene = 2:1), the non-UV-exposed part was partially dissolved leading to brown residues, beside the formation of cracks at the side walls of the structures (Figure 104 (b)). Similar observations were made for THF:toluene mixtures (1:1) where, in addition some of the cracked coatings areas were partially removed (Figure 104 (c)). By using a mixture of THF and heptane with a ratio of (1:1) or (2:1), the non-UV-exposed part could not be dissolved (Figures 102 (d) and (e)). A mixture of (THF: tert.-butyl-methyl ether)=(1:3) dissolved the exposed part, instead of the non-UV-exposed part (Figure 104 (f)).
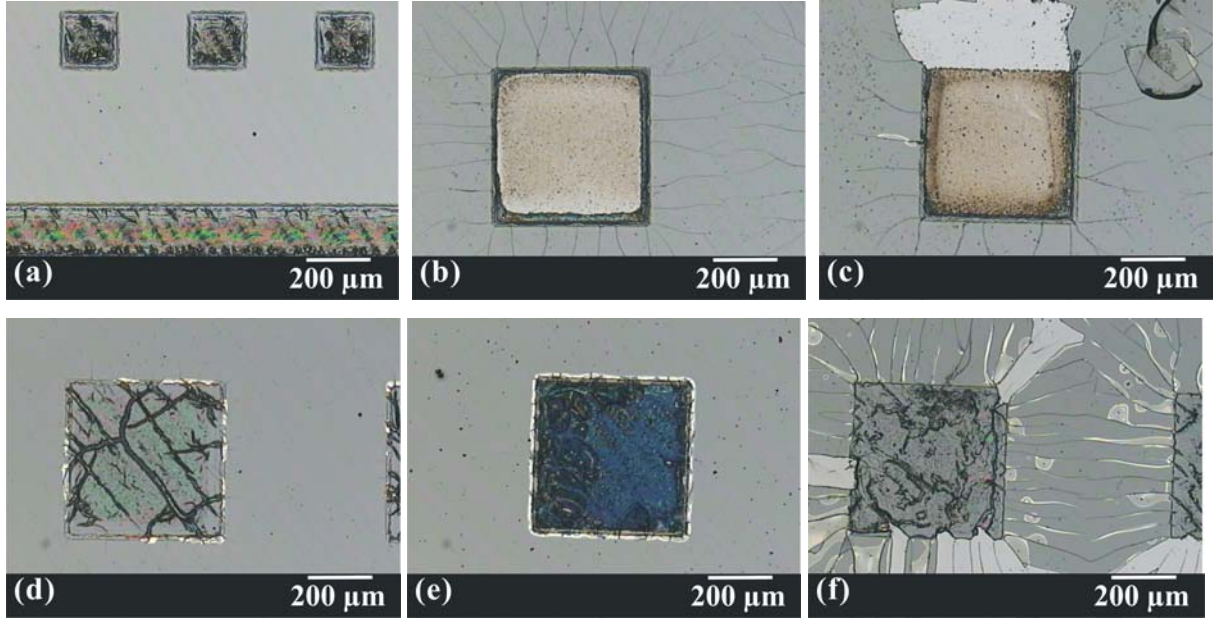
Figure 104: Optical microscopy images of patterned PD77 coatings on p-Si(100) substrates. The development was carried out in (a) THF:xylene = 1:1, (b) THF:xylene = 2:1, (c) THF:toluene = 1:1, (d) THF:heptane = 1:1, and (e) THF:heptane = 2:1 and (f) THF: tert.-butyl-methyl ether = 1:3 (samples 180505/1a, -/1b, -/2a, -/2b, -/2d, and -/1c, section 0).

From a thermodynamic point of view, two substances are mutually soluble, if the Gibbs free energy of mixing ΔG_M is negative (Eq. 23):

$$\Delta G_M = \Delta H_M - T \Delta S_M , \qquad (Eq.\ 23)$$

where ΔH_M and ΔS_M are the enthalpy and entropy of mixing, respectively. As ΔS_M is generally positive, the enthalpy determines the sign of ΔG_M. The enthalpy of mixing (ΔH_M) has been correlated to the solubility parameter (δ), introduced in 1916 by Hildebrand[238], as follows:
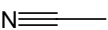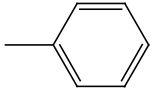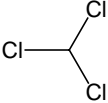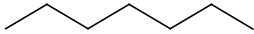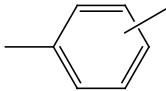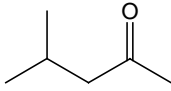
$$\Delta H_M = \phi_1\ \phi_2\ V\ (\delta_1 - \delta_2) , \qquad (Eq.\ 24)$$

where δ_1 and δ_2 are the solubility parameters of component 1 and 2, V is the molar volume of the mixture, and ϕ_1 and ϕ_2 are the volume fractions of component 1 and 2. In order to ensure a possible dissolution, ΔH_M has to be reduced as much as possible. Thus, (Eq. 24) predicts that $\Delta H_M = 0$, if $\delta_1 = \delta_2$, so that two substances with equal solubility parameters should be mutually soluble. This is in good accordance with the general rule that chemical and structural similarity favor solubility. However, a single parameter cannot describe the solubility behavior, if polar and hydrogen-bonding solvents are included in the system. The Hansen solubility parameters (HSP), defined in (Eq. 25), take the type of interaction forces into account. The total solubility parameter δ is a function of the solubility parameters δ_d, δ_P, and δ_H, which are the contribution of dispersive forces, polar forces, and hydrogen bonding, respectively

$$HSP = \delta^2 = \delta_d^2 + \delta_P^2 + \delta_H^2 . \qquad (Eq.\ 25)$$

152

Values of δ_d, δ_P, and δ_H for some solvents which were used as developer are listed in Table 58[238].

Table 58: Hansen solubility parameters of selected processing solvents[238].

solvent	structure	δ_d $(J^{1/2}/cm^{3/2})$	δ_P $(J^{1/2}/cm^{3/2})$	δ_H $(J^{1/2}/cm^{3/2})$	δ $(J^{1/2}/cm^{3/2})$
acetonitrile		15.4	18.0	6.1	24.5
toluene		17.3-18.1	1.4	2	17.5-18.3
chloroform		17.7-18.1	3.1	5.7	18.9-19.2
heptane		15.5	0	0	15.5
THF		16.8-18.9	5.7	8.0	19.5-21.3
xylene (o-, m-, p-)		16.6-18.1	1.0	1.0	16.7-18.1
acetone		15.5	10.4	7.0	19.9
MP		15.3	6.1	4.1	17.0

The values of δ_d, δ_P, and δ_H for the mixtures solvents which were used as developers are given in Table 59[238].

Table 59: Hansen solubility parameters of selected mixtures of processing solvents.

mixture composition	δ_d (J$^{1/2}$/cm$^{3/2}$)	δ_P (J$^{1/2}$/cm$^{3/2}$)	δ_H (J$^{1/2}$/cm$^{3/2}$)	δ (J$^{1/2}$/cm$^{3/2}$)
(THF:xylene) =(1:1)	17.7	4.09	5.7	19.0
(THF:xylene) =(2:1)	17.7	4.7	6.6	19.5
(THF:toluene) =(1:1)	17.8	5.4	7.1	19.9
(THF:heptane) =(1:1)	16.7	4.0	5.7	18.1
(THF:heptane) =(2:1)	17.10	4.65	6.53	18.9

Several solvents were investigated as developer in order to find the suitable one, which can dissolve the non-UV-exposed parts without the removing of the UV-exposed part. From the Tables 59 and 60, it is difficult to find a general trend for the coating solubility due to the fact that only some solvents were investigated. However, it seems to be likely that the non-UV-exposed part can be dissolved, if $\delta_d \sim 17.7$, $\delta_P \sim 4.7$-5.7, and $\delta_H \sim 6.6$-8 J$^{1/2}$/cm$^{3/2}$. On the other hand, with such solubility parameters, the UV-exposed part is damaged and cracks, more or less pronounced, are observed. Such cracks are not present, if acetone is used as developer. Since the solubility parameters of acetone are $\delta_d \sim 15.5$, $\delta_P \sim 10.4$, and $\delta_H \sim 7.0$ J$^{1/2}$/cm$^{3/2}$, it seems likely that δ_d and δ_P parameters may contribute to the improvement of the UV-exposed part.

From the Hansen solubility parameters, it was shown that other solvents have to be investigated in order to establish a direct trend between the solubility parameters and the development step, which was not the scope of this work. However, the coating has to be processed in order to measure the refractive index of the final coating.

The refractive index of a sample of PD77 completely processed on a p-Si(100) substrate was measured by ellipsometry (sample 280405/3). The sample was exposed to UV light for 900 s, and the coating was developed in an ultrasonic bath of MP. The use of the Cauchy function for the modeling process did not yield a good correlation to the measurement. Thus, a modified Cauchy and Urbach function (Eq. 26) was used to model the measurement, and a much better agreement of theory and measurements was obtained:

$$n(\lambda) = a + \frac{b}{\lambda^2} + \frac{c}{\lambda^4} + d\lambda^3 , \qquad\qquad\qquad (Eq.\ 26)$$

where λ is the wavelength of the light, and a, b, c, and d are fitparameter.

The coating thickness which was obtained using this model (d=1690 nm) was in good agreement with those measured using profilometry (d=1700 nm). The corresponding dispersion curve is shown in Figure 105.
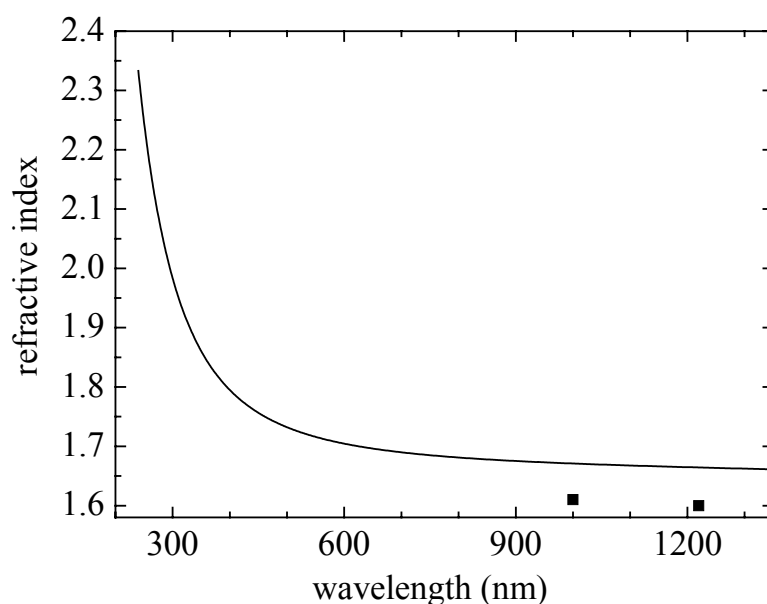
Figure 105: Dispersion curve of (─) a non-polymerized coating, and a (■) UV-exposed coating for 900s from resin PD77 (sample 150305/1 and 280405/3, section 3.3.2). No thermal treatment was carried out.

At 1000 nm, the refractive index of the non-processed coating is close to 1.61, whereas 1.67 was measured for the patterned coating (i.e., after UV exposure and development). As it has already reported for the resin PD92, this increase can be attributed to the processing of the materials.

However, although a large variety of experiments were carried out on the patterning process of resin PD77, the processing could not be further optimized in the framework of this thesis, which is related to the huge parameter space. Moreover, in order to further optimize the patterning process, further investigations have to be done in order to improve the patterning process.

4.2.1.3 Resins containing complexing ligands

The influence of the UV exposure dose on coatings prepared from resin PD-CL76 was investigated by FT-IR spectroscopy (Figure 106). The resin was diluted in butan-2-one, and spin-coated onto a p-Si(100) wafer (cf., chapter 3.3.2). The coating was UV-exposed for different exposure times, i.e., between 2 and 15 min corresponding to different energy doses, and FT-IR spectra were recorded just after the UV-exposure step (Figure 106). In the spectrum of the non-UV-exposed coating, the absence of the vibrational mode at 1711 cm^{-1} which characterizes the stretching vibrational mode of the C=O bond from free ACAC, shows that ACAC is complexed to Ti(OEt)$_4$. The two peaks recorded at 1529 and 1585 cm^{-1} are attributed to the stretching vibrational modes of the C=C bonds of the aromatic groups and to the polymerizable moiety of SETMS, respectively. In addition, these peaks are overlapped to the stretching vibrational modes of C=O and C=C bonds from the complex formed between Ti(OEt)$_4$ and ACAC, which are reported in the literature to be at 1529 and 1600 cm^{-1}, respectively[28].
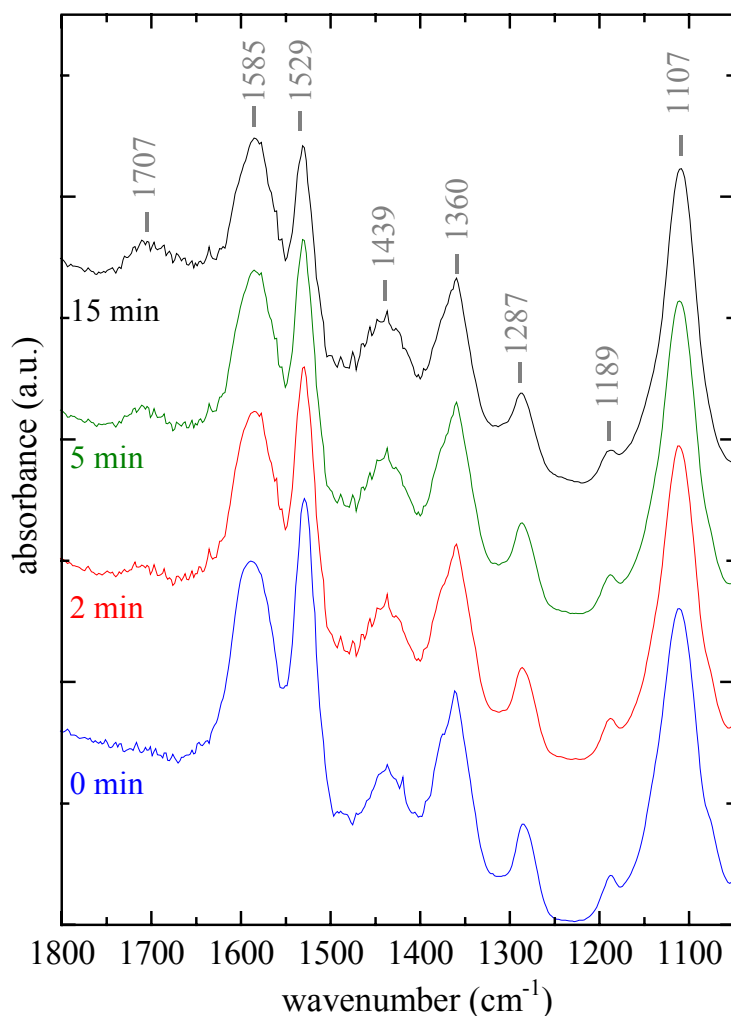
Figure 106: Evolution of the FT-IR spectra of PD-CL76 coatings in dependence on the UV exposure time (sample 291104/6, part 0). The spectra were normalized to the vibrational mode recorded at 1107 cm^{-1}.

After 2 minutes UV exposure, a broad peak around 1710 cm^{-1} is evolving, which was not observed for the non-UV-exposed coating. By increasing the UV exposure time and thus the energy dose, the intensity of this peak increased, while the intensity of the peak detected at 1529 cm^{-1} slightly decreased. The decrease of the intensity of the latter peak detected and the intensity increase of the broad peak around 1710 cm^{-1} are due to the dissociation of ACAC from the titanium precursor. The intensity of the peaks attributed to the enolic form of ACAC decreased, whereas the intensity of the peaks attributed to free ACAC, detected around 1660 cm^{-1} for the stretching vibrational mode of C=O and C=C, increased. Such dissociation by UV irradiation has also been reported by Tohge et al.[46,187]. Moreover, the decrease of the peak intensity at 1529 cm^{-1} can be also due to the contribution of the organic polymerization of the C=C bonds from SETMS.

ACAC was used in the synthesis of resin PD-CL76 in order to decrease the reactivity of Ti(OEt)$_4$ precursors resin PD-CL76. The dissociation of the chelate is obtained after UV exposure and thus, the organic polymerization of resin PD-CL76 was not further investigated.

4.2.1.4 Resins containing organo-phosphorus precursors

The patterning process of phosphorus containing resins was investigated in the same way as for resins PD92 and PD77 in order to show the feasibility to process the material. The coatings were removed upon development, no matter what UV exposure dose or temperature of pre- or/and post-exposure-bake steps were employed. In order to understand the influence of the UV exposure dose on the resins based on organophosphorus precursors, μ-Raman spectra were recorded on non- and UV-exposed coatings. For different depths within the layers, coatings from resin PD-P7 were UV exposed for 420 and 900 s (Figures 105).
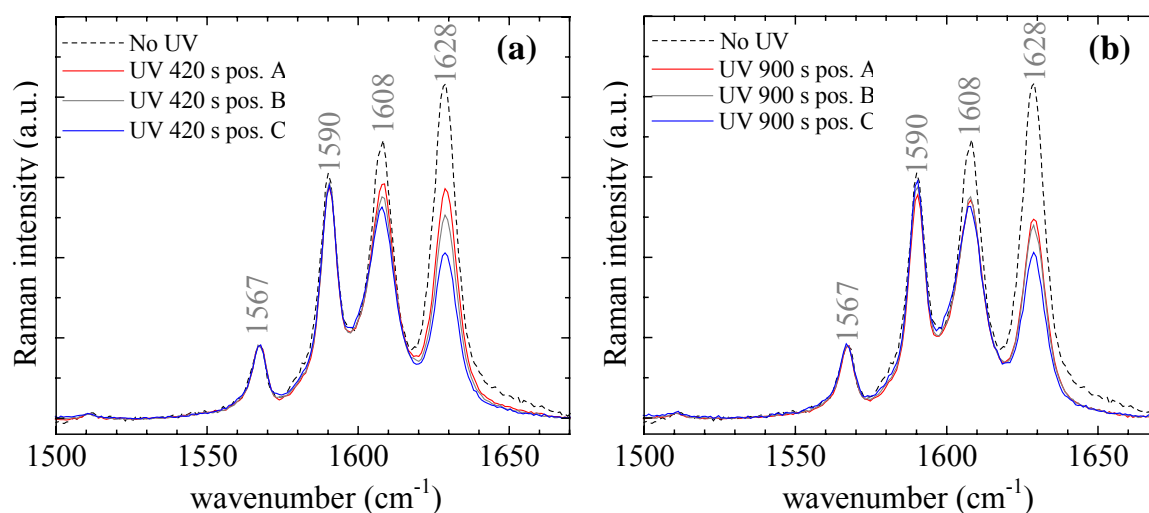
Figure 107 : μ-Raman spectra of PD-P7 coatings on Si p-(001) wafers for different UV exposure times. (a) 420 (060406/1b), and (b) 900 s (060406/1c). The spectra were compared to non-UV-exposed coatings (060406/1a). Position A: location close to the surface, position C: close to the interface wafer/coating, position B: in the bulk of the coating.

Four peaks are clearly resolved between 1500 and 1670 cm^{-1}. Two peaks recorded at 1567 and 1590 cm^{-1} are attributed to the antisymmetric and symmetric stretching vibration of the C=C of the aromatic group from DPD. The two remaining peaks recorded at 1608 and 1628 cm^{-1} are attributed to stretching modes of the C=C bonds from the aromatic group and the polymerizable C=C bond of the p-VBPA units. For both UV doses, the intensity of the peaks recorded at 1608 and 1628 cm^{-1} decreases with the UV exposure dose. The decrease in intensity of the peak at 1628 cm^{-1} can be attributed to an organic polymerization. This also affects the peak intensity at 1608 cm^{-1} due to the delocalization of π-electrons in the styrene group, which is modified by the organic polymerization reaction.

Moreover, the intensity of the two peaks at 1608 and 1628 cm^{-1} for spectra recorded at different depth positions are not similar. This is due to the presence of an inhibition layer (i.e., the reaction between oxygen and the excited photoinitiator, cf., chapter 2.3.1), since the coatings were investigated without a development step. The intensity of the peak at 1628 cm^{-1} is stronger for the spectra recorded at position A, i.e., near the coating's surface, than the spectra recorded at the position C, i.e., near the wafer's surface. At position A, the inhibition layer may have also been recorded. The DC values calculated from (Eq. 16) (cf., chapter 3.1.4) are shown in Table 60 for the spectra presented in Figure 107.

Table 60 : Influence of the UV exposure dose and the location within the PD-P7 coatings on the DC values.

Sample n°	UV exposure time (s)	Location	DC (%)
060406/1b	420	A_{420}	37
		B_{420}	47
		C_{420}	58
060406/1c	900	A_{900}	44
		B_{900}	48
		C_{900}	58

The DC values are higher for the spectra recorded close to the wafer surface, where DC values up to 58% were obtained, independently of the UV exposure dose. On the other hand, influenced by the presence of the inhibition layer, the spectra recorded at the coating's surface have lower DC values. However, a direct comparison of this values is not possible since the spectra could not be recorded at the same depth.

The results of the μ-Raman investigation on the organic polymerization of resin PD-P7 have shown the possibility to pattern these resins. High DC values were achieved at the surface of the wafer. Since crack-free coatings were obtained for thickness below 2 μm, the polymerized part of the coating may have been too thin in order to established a good patterning process.

4.2.2 The two-photon absorption process

The experimental set-up and the general features of the 2PP process are described in chapter 2.3.2. For a standard ORMOCER® (no heteroelements used upon the synthesis), a droplet of material was sandwiched between two glass substrates. By using the same method with the novel inorganic-organic hybrid PD materials, cracks were always observed. Thus, these materials were spin-coated onto glass substrates, and subsequently exposed to the femtosecond laser beam. Since the 2PP experiments were performed at the Laser Zentrum in Hannover, only two resins could be investigated: resins PD77 and PD92. These were chosen, because they could be patterned by UV lithography. Due to their low attenuation at the femtosecond laser's wavelength of 780 nm, which was determined to be around 0.014 and 0.052 dB/cm for resins PD92 and PD77, respectively, 2PP patterning could be carried out to these materials.

In addition to the parameters of the UV polymerization process, for 2PP other parameters such as the writing speed related to the 3D movement of the sample, the average laser power, the beam profil and also the repetition rate have to be adjusted and optimized in order to obtained well-defined 3D structures.

In order to evaluate the average laser power which can be supported by the materials, voxels (volume pixels) were written by 2PP at two different powers in resin PD77 (Figure 108). Since the development performed with MP was not successful, further investigations were not carried out.
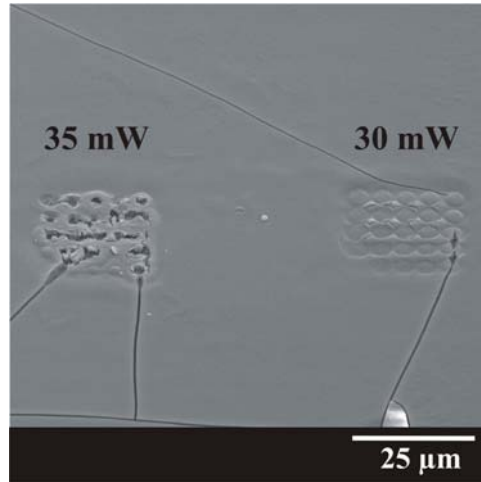
Figure 108: SEM image of voxels written by 2PP in resin PD77 material at different average laser powers.

Further experiments were carried out using resin PD92. Beside variation of the laser power, voxels were also written with multiple exposure (Figure 109). The first written voxel has the position $(X_1;Y_1)$, then $(X_1;Y_2)$, $(X_1;Y_3)$, etc. Moreover, each voxel was written with different laser exposure dose, which are defined by equation (Eq. 27), where the laser exposure time in ms was fixed with the position of the voxel, $(Xi;Yi)$, as followed:

$$\text{time (ms)} = 100 + (Y_i - 1) \times 400 + (X_i - 1) \times 2000, \qquad \text{(Eq. 27)}$$

where Xi and Yi are numbers ranging from 1 to 5.

For multiple exposure, the laser restarted to expose the positions $(X_1;Y_1)$, then $(X_1;Y_2)$, $(X_1;Y_3)$, etc. (Figure 109 (b) shows three exposure modes).
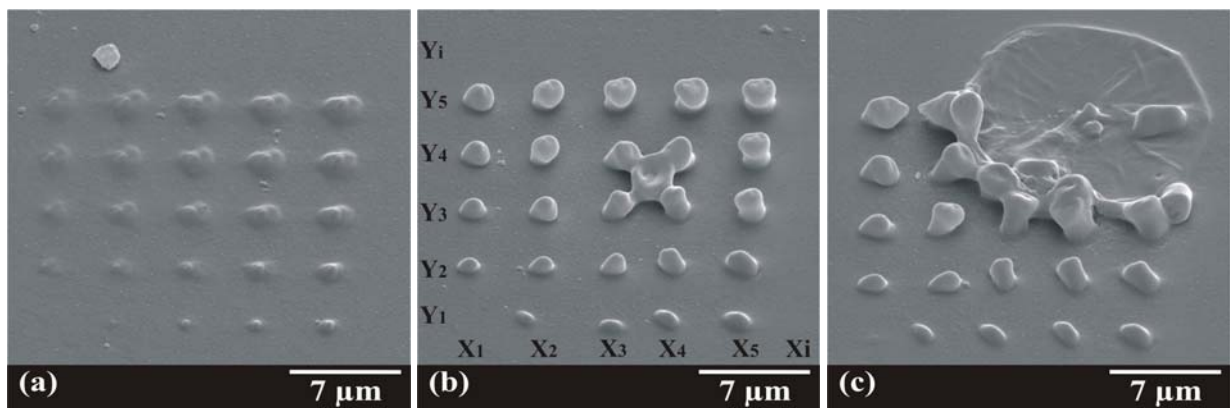
Figure 109: SEM images of voxels written by 2PP in resin PD92 with different laser exposure times at (a) 35 mW (one exposure), (b) 35 mW (three times exposed), and (c) 45 mW (one exposure).

Thus, by increasing the laser exposure time, the voxel size increases. This can be seen in Figure 109 (b), where the voxel diameter has increased from 0.9 to 2 µm, for laser exposure times ranging from 500 $(X_2;Y_1)$ to 9700 $(X_5;Y_5)$ ms, respectively. Moreover, by increasing the number of exposure "modes" the voxel size also increased. For example, for one exposure mode, an average power of 35 mW and an exposure time close to 500 ms (position $X_2;Y_1$,

159

Figure 109 (a)), a small voxel (0.5 µm diameter) is written, whereas for three exposure modes a 0.9 µm voxel diameter is written (Figure 109 (b)). By increasing the power of the laser, the voxel size also increased (see Figure 109 (a) and (c)). On the other hand, for high exposure time of the laser the material "exploded" (see Figure 109 (c)), which could be due to a too fast reaction from the high power of the laser. Thus, the voxels size can be modulated with the laser exposure dose, the average laser power as well as with the number of exposure times of the laser.

In order to improve the 2PP processing of resin PD92, lines were written by varying the number of exposures on an individual structure, the average power of the laser, and also the writing speed related to the 3D movement of the sample. The latter one is directly correlated to the exposure dose of the laser defined in the fabrication of the voxels. The material was first spin-coated on glass, and structures were subsequently written with the femtosecond laser followed by a development step in MP, whereas the energy was varied. SEM images of written PD92 lines are shown in Figure 110. Typically, for ORMOCER® resins such as ORMOCER®I, well-defined structures can be written with one exposure. For the 2PP experiment, it has to be evaluated how structures which will enable further optical characterization can be processed using a high refractive index material. A set of lines was written by 2PP, where the first line was written by exposing the material one time. For the following lines, the number of exposures on the sample structure was incrementally carried out with increment 1. Therefore, the last line corresponds to 10 exposures. SEM images (Figure 110) show that a slow writing speed related to the 3D movement of the sample, a low average laser power, and multiple exposures are needed in order to obtain well-defined structures.
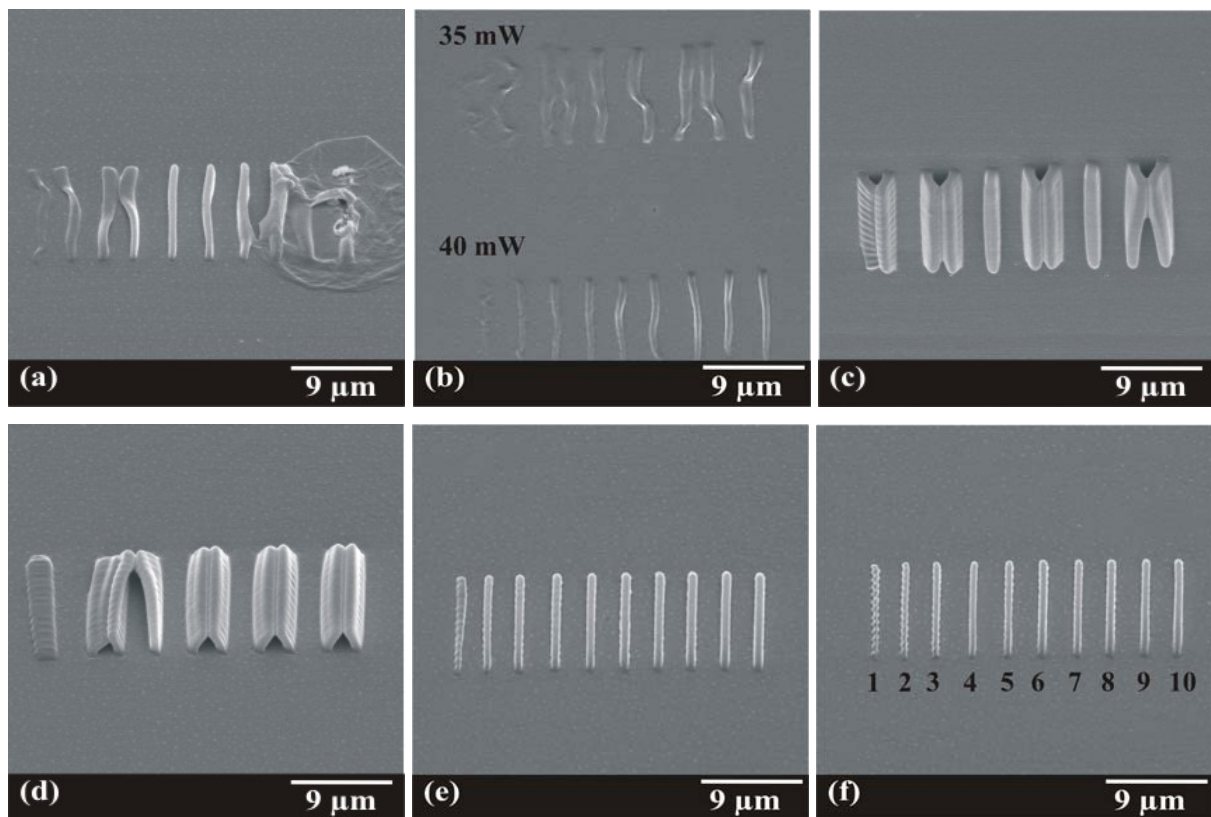
Figure 110: SEM images of lines written with by 2PP in resin PD92. From the right to the left, from one to ten times exposures were carried out. The parameters were (a) 50 mW, 200 µm/s, (b) 35 mW and 40 mW, both are 200µm/s. At 20 µm/s, structures were written at (c) 40 mW, (d) 20 mW, (e) 15 mW, and (f) 10 mW.

First attempts were carried out in order to investigate the possibility to write 3D photonic crystal structures in PD92 by means of 2PP. The writing speed was fixed to 20 µm/s, and few 3D photonic crystal structures were written with different average laser powers between 7 and 32 mW (Figure 111 (a)). The typical structural dimensions range between approx. 400 nm and 1 µm line width with a period of about 2 µm (Figure 111 (b)). It has to be mentioned, however, that neither the process is optimized so far, nor the quality of the generated structures is good enough to account for optical characterization. Besides, the photo-initiator used for radical initiation (Irgacure$^{®}$369) has a very low two-photon absorption cross-section which limits the possibilities of the 2PP method (cf., chapter 2.3.2). Cumpston et al.[203] demonstrated that using π-conjugated components as photo-initiators, the two-photon absorption cross-section can be significantly increased, i.e., absorption cross-sections of up to 1.25×10^{-47} (cm^{4}s/photon) were achieved, compared to 3×10^{-55} (cm^{4}s/photon) for Irgacure 369[17].
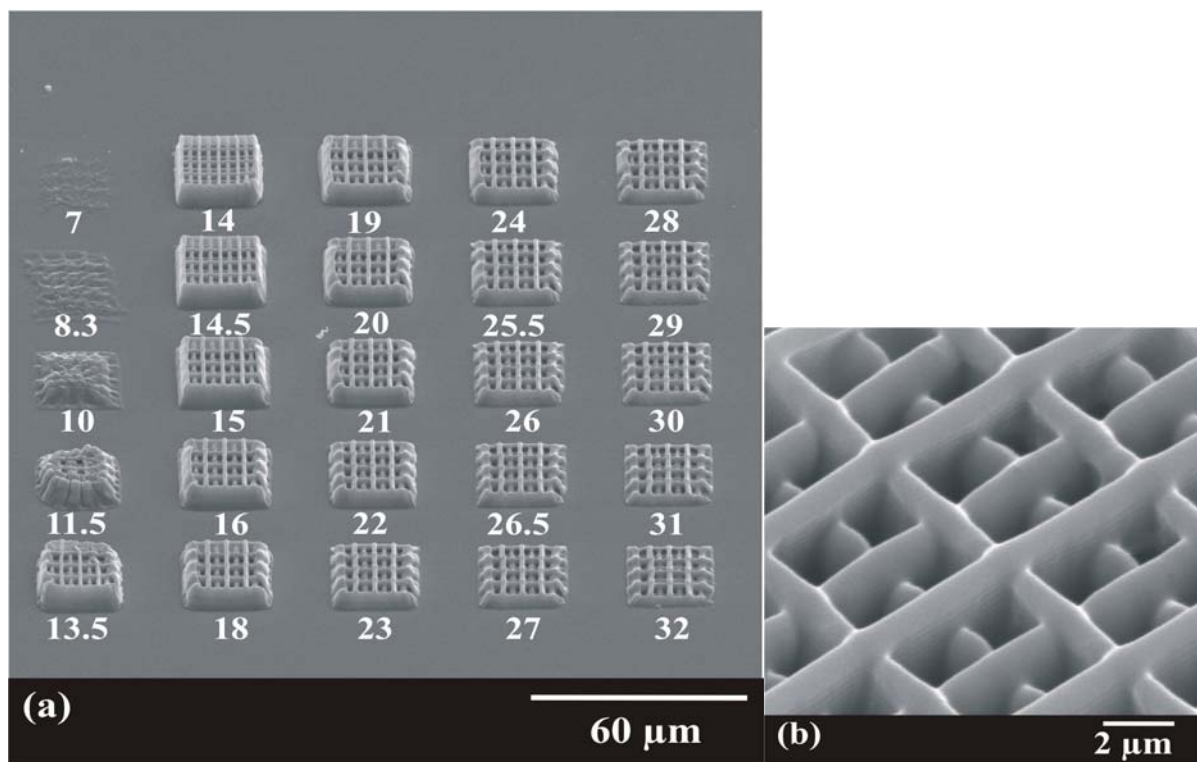
Figure 111: (a) First 3D photonic crystal structures, produced in resin PD92. The average laser power was varied between 7 and 32 mW (from the upper left to the lower right), and five exposure times were used. (b) Zoom into a structure written with an average laser power of 14 mW.

Further optimization of the 2PP process and deeper understanding of the light-material interaction will enable structures which could be optically characterized. For example, the structure size and precision can be optimized by adapting the optical component to the high refractive index material. In addition, parameters which are more related to a general processing such as the adhesion between the crystal and the glass substrate, the development step, and also the material's shrinkage have to be optimized. These experiments have also revealed that resins based on titanium compounds require 2PP processing parameters

completely different those of the standard ORMOCER® materials as reported in the literature[17]. This is also supported by the low percentage of organic cross-linking determined from μ-Raman spectroscopy (cf., chapter 4.2.1.1).

For the first time 3D PC structures were written by 2PP with a hybrid organic-inorganic material based on 33 mol-% Ti(OEt)$_4$, 50 mol-% DPD, and 17 mol-% MEMO. Typically, 3D photonic crystal structures were obtained in about 5 min for the entire process. Slower speed, lower energy, and also continuous multiple exposure of the same structure have to be applied with resin PD92 in order to obtain photonic crystal structures. Comparing to the processing parameters used to write PC structures in ORMOCER® the new Ti-containing resin PD92 requires more time (approximately 40 min). This might be related to the high absorption of titania as a competitive process to the light-initiated organic cross-linking. In addition, the structural feature sizes are much broader than for the ORMOCER® [17] which is a result of the non-optimized optics for high refractive index materials within the 2PP experiment.

5. Summary

In the framework of this thesis, new UV-patternable organic-inorganic hybrid polymers with higher refractive indices than reported in the literature for photonic applications were developed and studied with respect to their chemical structure, their optical properties, and their ability of being patterned by 1PP and 2PP. Particularly with 2PP, one could create 3D structures using the novel hybrid materials. The materials were prepared from hydrolysis and polycondensation reactions of

- organo-alkoxysilanes and titanium alkoxide precursors, modified with and without CL and organo-alkoxysilanes precursors, and

- organo-alkoxysilanes, titanium alkoxide and organophosphorus precursors.

The major scope of this work was to increase the refractive index of ORMCER® materials based on only organo-alkoxysilanes. Thus, the parameters which influence the refractive index were investigated thoroughly. In particular, the synthesis parameters such as the introduction of titanium alkoxide and its concentration, the organo-alkoxysilanes, the catalyst concentration, the solvent used, but, also the processing parameters such as, the UV exposure dose, initiator concentration, and developer were investigated.

The introduction of titanium alkoxide by hydrolysis and condensation reactions has significantly increased the refractive index of the resulting resins. For example, in ORMOCER®I based on 50 mol-% MEMO and 50 mol-% DPD, the replacement of 33 mol-% of MEMO by 33 mol-% of titanium alkoxide has increased the refractive index of the resin from 1.538 to 1.590 (at 587 nm). Another example is the replacement of TEOS by titanium alkoxide which has increased the refractive index from 1.55 to 1.59. In addition, it could be shown by NMR spectroscopy that the choice of the solvent used for the syntheses affects the condensation degree of the inorganic network. The kind of organo-alkoxysilanes changes the refractive index of materials. For example, organo-alkoxysilanes containing aromatic groups have a higher refractive index than aliphatic ones. Thus, the replacement of MEMO by SETMS has increased the refractive index of coatings up to 1.63 (at 950 nm). For the resins based on 33 mol-% organo-alkoxysilanes, the kind of organo-alkoxysilanes and the catalyst concentration modify the refractive index of the material. For resins based on MEMO, the use of acidic media led to transesterification reactions, independently of the acidic concentration. Thus, in the latter resins, a decrease of the polymerizable groups was observed. For resins based on 33 mol-% SETMS, the increase of the catalyst concentration lead to a change of the refractive index from 1.67 (at 1290 nm) to 1.70 (at 940 nm). However, due to the dispersion relation n(λ) and due to the method used during this work to determine the refractive index, the effect of the catalyst concentration cannot be determined. The concentration of titanium alkoxide precursors was found to increase the refractive index up to 1.84 at 1820 nm for a resin based on 90 mol-% titanium alkoxide. However, due to the high content of unreacted alkoxide groups from the titanium precursor, the resins was poorly reproducible, and unstable, as expected. Thus, chemical modifications of the titanium alkoxide with CL have been done in order to reduce the reactivity of the titanium precursor. On the other hand, the use of CL has increased the organic quantity in the resin, which reduced its refractive index. Other new resins synthesized from organo-alkoxysilane, titanium alkoxide, and organo-phosphorus were developed as well in order to investigate the influence of the organo-phosphorus precursors on the refractive index. The replacement of MEMO or SETMS by p-VBPA has increased the refractive index slightly. Moreover, the main advantage for the characterization of resins based on organo-phosphorus precursors is that the

Ti-O-P bonds can be very well characterized by ^{31}P-NMR spectroscopy compared to Si-O-Ti bonds which cannot be well characterized by ^{29}Si NMR spectroscopy.

For some selected resins, the UV lithography process was developed. Classical ORMOCER®s without titanium alkoxides were chosen as model systems for the organic polymerization of new materials synthesized during this work. However, the polymerization process needed a complete reassessment. The resins based on titanium precursors needed a long UV exposure time, in order to achieve a high degree of conversion of the C=C bond. Despite of very long exposure time which is 300 times higher for the Ti-modified materials, the C=C bond conversion remained below 60%. The latter values are very low in comparison to those reported for ORMOCER®I for a UV exposure time of 30 s. For the same UV exposure time in case of the Ti-containing hybrid materials, the conversion degree of the resins does not exceed 30%. This is related to the high absorption of titania in the UV regime. Since the titania absorbs in the same wavelength than the photoinitiator, a part of the energy needed to initiate the polymerization is absorbed from the titania. Moreover, the potential photocatalytic effect of titania leading to a degradation of the organic groups can occur and affect the conversion degree.More attention was focused on the correlation between the UV exposure time and the refractive indices of the coatings. Ellipsometry measurements also showed an increase of the refractive index. For example, for a completely processed coating, the refractive index measured was close to 1.65, whereas at the same wavelength, was close to 1.60 for a non-processed coating.

The introduction of 1.5 wt.-% of photo-initiator, which contains phenyl groups can participate to the refractive index increase. Moreover, the organic cross-linking contributed to the increase of the refractive index. In addition, a final thermal curing of the coating leads to a densification of the layer due to further cross-linking and removal of residual solvent. On non developed coatings, ellipsometer measurements were recorded for different exposure times, and were correlated to the conversion degree. It is obvious that the refractive index measured is attributed to the polymerized part of the coating, but also to the part which reacts with oxygen, i.e., the inhibition layer, since this layer was not removed for some samples. In any case, an increase of the refractive index from 1.62 to 1.64, by increasing the UV exposure time from 120 to 900 s was reported, whereas the conversion degree increased from 32 to 45 %. The effect of the initiator concentration on the conversion degree values has also investigated during this work. However, no significant effect was found. Additional UV exposure on a completely processed coating was also investigated. The conversion degree of the completely processed coating was close to 25%, whereas with 900 s additional UV exposure time of the completely processed coating, the conversion degree increased up to 47 %. This high increase was attributed to the degradation of the organic part from the organo-alkoxysilanes, due to the presence of titania units ($\equiv$Ti-O-Ti$\equiv$). This might be correlated to the photocatalytic degradation of the organic molecules in presence of TiO_2. The UV lithography process of selected resins has led to patterned structures with 8x8 μm^2 resolutions for resins based on 17 mol-% MEMO, 33 mol-% titanium alkoxide 50 mol-% DPD. The replacement of MEMO by SETMS led to a decrease of the patterned resolution, where only 25x25 μm^2 bright structures have been dissolved. For resins, based on a lower organo-alkoxysilane concentration of 33 mol-%, a polymerization process was developed, but not completely optimized which was not the aim of this wok.

Two resins were selected for the 2PP process:

- a resin based on 17 mol-% MEMO, 33 mol-% titanium alkoxide, and 50 mol-% DPD, and

- a resin based on 33 mol-% SETMS and 67 mol-% titanium alkoxide.

The resin based on SETMS was difficult to develop, and no further investigations were performed. Voxels, lines, and photonic crystal-like structures have been written by 2PP process with the resin based on 17 mol-% MEMO, 33 mol-% titanium alkoxide, and 50 mol-% DPD. The average laser power and the number of passages of the laser have been reported to be vital parameters in order to write reliable structures. With a writing speed fixed at 20 µm/s, and an average laser power between 7 and 32 mW, typical structural dimensions ranged between 0.4 and 1 µm, having a periodicity of 2 µm. Until now, no optical characterization of the PC structure was possible due to the fact that the structure size precision, the adhesion of the PC structure to the substrate, as well as the material shrinkage need to be further optimized. Beside that, an optimization of the optics of the 2PP apparatus could allow to achieve a PC structure which can be used for optical characterization.

6.   Summary in German

Im Rahmen dieser Doktorarbeit wurden neue UV-strukturierbare organisch-anorganische hybride Polymere für photonische Anwendungen mit einem hohem Brechungsindex und der Möglichkeit, sie durch Ein- bzw. Zwei-Photonen-Polymerisation zu strukturieren, entwickelt. Die Materialien wurden in Bezug auf ihre chemische Struktur, ihre optischen Eigenschaften, und ihrer Fähigkeit, durch 1PP und 2PP strukturierbar zu sein, untersucht. Besonders mit 2PP konnte man mit diesen neuartigen hybriden Materialien 3D-Strukturen erzeugen. ie Hydrolyse und Polykondensationsreaktionen wurden mit

- Organo-Alkoxysilanen und Titanalkoxiden, modifiziert mit und ohne komplexierende Liganden und

- Organo-Alkoxysilanen, Titanalkoxiden und Organophosphorsäure

als Precrusoren durchgeführt.

Primäres Ziel dieser Arbeit war es, den Brechungsindex von ORMOCER®en, die auf der Basis von Organo-Alkoxysilan-Precursoren ohne Heteroelemente synthetisiert werden, zu vergrößern. Die chemische Struktur der synthetisierten Materialien und somit mit ihr die Parameter, die den Brechungsindex beeinflussen, wurden eingehend untersucht. Insbesondere die Synthese-Parameter, wie das Einsetzen der Titanalkoxide und ihrer Konzentration, der Organo-Alkoxysilane, die Katalysator-Konzentration, die verwendeten Lösungsmittel und auch die Verfahrensparameter für eine spätere Strukturierung durch lithographische Verfahren, wie die UV-Bestrahlungsdosis, die Initiator-Konzentration und der Entwickler, wurden untersucht.

Einbringen von Titanalkoxiden während der Hydrolyse und Kondensationsreaktionen hat den Brechungsindex der resultierenden hybriden Harze signifikant erhöht. Als ein Beispiel sei ein ORMOCER®, basierend auf 50 mol-% MEMO und 50 mol-% DPD genannt, bei dessen Synthese 33 mol-% des verwendeten MEMO durch 33 mol-% eines Titanalkoxids ersetzt wurde. Die Brechzahl des resultierenden Harzes konnte so von 1.538 für das ORMOCER® auf 1.590 (beide bestimmt bei 587 nm) angestiegen. Ein anderes Beispiel ist der Ersatz von TEOS durch das Titanalkoxid, der Brechungsindex wird dadurch von 1.55 auf 1.59 vergrößert. Außerdem wurde durch NMR-Spektroskopie gezeigt, dass die Wahl des Lösungsmittels, das bei den Synthesen eingesetzt wird, den Kondensationsgrad des anorganischen Netzwerkes beeinflusst. Darüber hinaus ändert auch die Art des Organo-Alkoxysilans den Brechungsindex von Materialien. Zum Beispiel haben Organo-Alkoxysilane, die aromatische Gruppen enthalten, einen höheren Brechungsindex als Aliphatische. Daher konnte der Brechungsindex an Schichten durch den Ersatz von MEMO durch SETMS auf 1.63 (gemessen bei 950 nm) erhöht werden. Harze mit MEMO unter Verwendung eines sauren Katalysators synthetisiert, fand eine Umesterungsreaktion, statt, unabhängig von der gewählten Säurekonzentration. Dabei wurde eine Abnahme der polymerisierbaren Gruppen beobachtet. Hybride Harze, die mit 33 mol-% SETMS synthetisiert wurden, zeigten bei Erhöhung der Katalysator-Konzentration eine Änderung des Brechungsindex von 1.67 (bestimmt bei 1290 nm) auf 1.70 (bestimmt bei 940 nm). Da es jedoch im Rahmen dieser Arbeit keine Möglichkeit gab, die Brechzahlen exakt bei der gleichen Wellenlänge zu bestimmen, kann die Wirkung der Katalysator-Konzentration aufgrund der Dispersionsrelation $n(\lambda)$ der Materialien nicht eindeutig abgeleitet werden. Eine Erhöhung der Konzentration des Titaniumalkoxid-Precursors auf 90 mol-% Titanalkoxid vergrößert den Brechungsindex bis zu 1.84 (bestimmt bei 1820 nm), wobei aufgrund der Dispersionsrelation im sichtbaren Wellenlängenbereich eine erheblich höhere Brechzahl

erwartet werden kann. Wegen des hohen Gehalts an unreagierten Titanalkoxid-Gruppen waren die Harze jedoch erwartungsgemäß schlecht reproduzierbar und nicht stabil. Daher wurde der Titanalkoxid-Precursor chemisch mit komplexierenden Liganden modifiziert, um die Reaktionsfähigkeit des Titan-Precursors zu reduzieren. Andererseits führte die Verwendung dieser Liganden dazu, den Anteil an Organik im Harz zu vergrößern und so den Brechungsindex wieder zu reduzieren. Darüber hinaus wurden weitere neue Harze, die mit Organo-Alkoxysilanen, Titanalkoxiden und Organophosphorsäure als Precursoren entwickelt, um die Beeinflussung des Brechungsindexes durch synthetisiertes Material mit Organophosphorsäure, zu untersuchen. Der Ersatz des MEMO oder des SETMS durch p-VBPA hat den Brechungsindex erhöht. Ein wichtiger Vorteil der Harze, die mit Organophosphorsäure synthetisiert wurden ist, dass die Ti-O-P- Bindungen sehr gut durch die ^{31}P-NMR Spektroskopie charakterisiert werden können. Im Vergleich dazu können Si-O-Ti-Verbindungen nicht annähernd so gut durch ^{29}Si NMR-Spektroskopie charakterisiert werden.

Für einige ausgewählte Harze wurde ein UV Lithographie-Prozess entwickelt, um erste Strukturierungserfahrungen zu sammeln, die im Hinblick auf die Verwendung dieser Harze im Zwei-Photonen-Prozess nützlich sind. Ziel dieser Voruntersuchungen war daher nicht die Entwicklung eines Anwendungsprozesses, sondern der Schwerpunkt wurde auf die Wechselbeziehung zwischen der UV-Belichtungszeit und den Brechungsindices der Schichten gelegt. Klassische ORMOCER® ohne Titanalkoxide wurden während dieser Arbeit als Modellsysteme für die organische Polymerisation der C=C Bindungen der neuen synthetisierten Materialien gewählt. Da sich die Ti-haltigen Materialien jedoch deutlich von denen der sonst in der Mikrosystemtechnik verwendeten ORMOCER®e unterscheiden, musste der gesamte Strukturierungsprozess komplett untersucht werden. Aufgrund der hohen Absorption von Ti-Oxiden im UV-Bereich musste die UV-Belichtungszeit signifikant erhöht werden, um das Material organisch zu polymerisieren. Trotz der sehr langen UV-Belichtungszeit, die 300 mal länger für die Titan-modifizierten Hybridpolymere als für die unmodifizierten Materialien ist, bleibt der Umsetzungsgrad der C=C- Bande unter 60 %. Dieser Wert ist deutlich niedriger als der Umsatz, der an optischen Hybridmaterialien, die lediglich für 30 s belichtet wurden, bestimmt wurde. Wird das Ti-haltige Material nur für 30 s belichtet, überschreitet der Umsetzungsgrad der Harze 30 % nicht. Da das im Material enthaltene Titanoxid bei der gleichen Wellenlänge absorbiert wie der Photoinitiator, wird ein Teil der benötigten Energie zur Initiierung der Polymerisation vom Titanoxid absorbiert. Außerdem kann die potenzielle photokatalytische Wirkung des Titanoxids zu einer Degradierung der organischen Gruppen führen und den Umsetzungsgrad beeinflussen. Da sich jedoch durch UV-Belichtung in einem Maskenbelichter stabile Schichten und insbesondere stabile Strukturen durch einen Entwicklungsprozess erzeugen lassen. Durch die Prozessierung (UV-Belichtung und thermische Härtung) konnte die Brechzahl beispielsweise von 1.6 (für das unprozessierte Harz) auf 1.65 (prozessierte Schicht), beide bei der gleichen Wellenlänge mithilfe eines Ellipsometers gemessen, erhöht werden.

Die Einführung des Photoinitiators, der Phenylgruppen enthält, kann ebenfalls zu einer Zunahme des Brechungsindex führen. Daneben hat die photochemisch initiierte organische Vernetzung einen signifikanten Einfluss auf die Zunahme des Brechungsindexes. Zusätzlich führt eine Endhärtung der Beschichtung zu einer Verdichtung innerhalb der Schicht auf Grund weiterer Vernetzung sowie auch zur vollständigen Entfernung von Lösemittelresten, die durch die Prozessierung noch im Material vorhanden sein können und die üblicherweise, je nach Gehalt in der Schicht, die Brechzahl etwas verringern können. Es wurden an belichteten, jedoch nicht entwickelten Beschichtungen Ellipsometer-Messungen an Proben durchgeführt, die mit verschiedenen UV-Belichtungszeiten präpariert wurden. Die erhaltenen Ergebnisse wurden mit dem Umsetzungsgrad der C=C-Bindungen korreliert. In allen Fällen

wurde eine Zunahme des Brechungsindexes von 1.62 auf 1.64 festgestellt, bei gleichzeitiger Verlängerung der UV-Belichtungszeit von 120 bis 900 s. Der Umsetzungsgrad stieg von 32 auf 45%. Auch die Wirkung der Initiator-Konzentration auf die Umsetzungsgradswerte wurde untersucht. Falls es einen Einfluss des Initiators auf die Brechzahl gibt, muss dieser deutlich unterhalb der Nachweisgrenze der Messverfahren liegen, da im Rahmen dieser Arbeit keine Abhängigkeit beobachtet wurde. Zusätzliche UV-Belichtung auf eine völlig prozessierten Beschichtung wurde auch untersucht. Der Umsetzungsgrad der völlig prozessierten Beschichtung war 25 %. Bei zusätzlicher UV Beleuchtungszeit der völlig prozessierten Beschichtung mit 900 s wurde der Umsetzungsgrad bis zu 47 % vergrößert. Diese hohe Zunahme wurde zur Degradierung des organischen Teils vom Organo-Alkoxysilan gerechnet, wegen der Anwesenheit der Titania Anteile ($\equiv$Ti-O-Ti$\equiv$). Das könnte zur photokatalytischen Degradierung der organischen Moleküle in der Anwesenheit von TiO_2 bezogen werden. Der UV Lithographie Prozess von ausgewählten Harzen hat für Harze beruhend auf 17 mol-% MEMO, 33 mol-% Titanium Alkoxide 50 mol-% DPD zu Strukturen mit 8x8 μm^2 Auflösung geführt. Der Ersatz des MEMO durch SETMS führte zu einer Abnahme der Strukturauflösung, bei der nur 25x25 μm^2 Strukturen sind aufgelöst worden sind. Für Harze beruhend auf eine niedrigere Organo-Alkoxysilan-Konzentration von 33 mol-%, wurde ein Polymerization Prozess entwickelt, aber nicht völlig optimiert, da es nicht das Ziel dieses Arbeit war. Zwei Harze wurden für 2PP Prozess ausgewählt:

- ein Harz beruhend auf 17 mol-% MEMO, 33 mol-% Titanium Alkoxide, und

50 mol-% DPD und

- ein Harz basiert auf 33 mol-% SETMS und 67 mol-% Titanium Alkoxide.

Das Harz beruhend auf SETMS war schwierig zu entwickeln, es wurde aber keine weiteren Untersuchungen durchgeführt. Voxels, Linien, und photonic Kristallstrukturen sind per 2PP Prozess mit dem Harz, beruhend auf 17 mol-% MEMO, 33 mol-% Titanium Alkoxide und 50 mol-% DPD, geschrieben worden. Die durchschnittliche Leistung des Lasers und die Zahl von Durchgängen des Lasers sind vital Parameter um zuverlässige Strukturen zu schreiben. Mit einer Schreiben-Geschwindigkeit gesetzt auf 20 $\mu m/s$, und eine durchschnittliche Leistung des Lasers zwischen 7 und 32 mW, wurden typische Strukturdimensionen zwischen 0.4 und 1 μm mit einer Periodizität von 2 μm hergestellt. Bis jetzt war keine optische Charakterisierung der PC-Struktur möglich, weil die Genauigkeit der Strukturgröße, das Anhaften der PC-Struktur zum Substrat, sowie das materielle Zusammenschrumpfen weiter optimiert werden müssen. Mit einer Optimierung der 2PP Apparate Optik könnte eine PC-Struktur, die für die optische Charakterisierung verwendet werden kann, erreicht werden.

7. References

[1] Y. Sugahara, S. Okada, K. Kuroda, and C. Kato, *J. Non-Cryst. Solids* **139**, 25 (1991).

[2] M. Oubaha, M. Dubois, and P. Etienne, *J. Sol-Gel Sci. Technol.* **38**, 111 (2006).

[3] R. G. Peall, J. W. Parker, and P. M. Harrison, *IEEE Advances in Interconnection Technology* 8/1-8/6 (1991).

[4] H. J. R. Dutton, *Understanding Optical Communications*, Prentice-Hall, Upper Saddle River NJ, (1998).

[5] J. D. Joannopoulos, P. R. Villeneuve, and S. Fan, *Nature* **386**, 143 (1997).

[6] P. N. Prasad, *Nanophotonics*, Wiley Interscience, Hoboken, New Jersey, (2004).

[7] E. Yablonovitch, *Phys. Rev. Lett.* **58**, 2486 (1987).

[8] S. John, *Phys. Rev. Lett.* **53**, 2169 (1987).

[9] http://ab-initio.mit.edu/photons/tutorial/.

[10] M. E. Yanik, S. Fan, M. Soljacic, and J. D. Joannopoulos, *Opt. Lett.* **28**, 2506-2508 (2003).

[11] J. D. Joannopoulos, R. D. Meade, and J. N. Winn, *Photonic Crystals*, New Jersey, (1995).

[12] M. Deubel, G. von Freymann, M. Wegener, S. Pereira, K. Busch, and C. M. Soukoulis, *Nature Material* **3**, 444 (2004).

[13] S. Wong, M. Deubel, F. Pérez-Willard, S. John, G. A. Ozin, M. Wegener, and G. Von Freymann, *Adv. Mater.* **18**, 265-269 (2006).

[14] A. Blanco, *Nature* **405**, 437 (2000).

[15] Y. A. Vlasov, X. Z. Bo, J. C. Sturm, and D. J. Norris, *Nature* **414**, 289 (2001).

[16] W. Dong, H. Bongard, B. Tesche, and F. Marlow, *Adv. Mater.* **14**, 1457 (2002).

[17] J. Serbin, A. Egbert, A. Ostendorf, B. N. Chichkov, R. Houbertz, G. Domann, J. Schulz, C. Cronauer, L. Fröhlich, and M. Popall, *Opt. Lett.* **28**, 301 (2003).

[18] S. Steenhusen, Mikrostrukturierung von Hybridpolymeren mit Zwei-Photonen-Absorption, University of Würzburg, Diplomarbeit (2008).

[19] R. Houbertz, J. Schulz, L. Fröhlich, G. Domann, M. Popall, J. Serbin, and B. N. Chichkov, *Mater. Res. Soc. Symp. Proc.* **780**, 175 (2003).

[20] A. Jitianu, M. Gartner, M. Zaharescu, D. Cristea, and E. Manea, *Mater. Sci. Eng., C* **23**, 301-306 (2003).

[21] H. Wolter, W. Storch, and H. Ott, *Mater. Res. Soc.* **346**, 143 (1994).

[22] R. Houbertz, G. Domann, C. Cronauer, A. Schmitt, H. Martin, J.-U. Park, L. Fröhlich, R. Buestrich, M. Popall, U. Streppel, P. Dannberg, C. Wächter, and A. Bräuer, *Thin Solid Films* **442**, 194 (2003).

[23] R. Houbertz, Private communication (2008).

[24] S. Kawata, H.-B. Sun, T. Tanaka, and K. Takada, *Nature* **412**, 697-698 (2001).

[25] C. Sanchez, and F. Ribot, *New J. Chem.* **18**, 1007 (1994).

[26] K.-H. Haas, and H. Wolter, *Curr. Opin. Solid State Mater. Sci.* **4**, 571-580 (1999).

[27] U. Schubert, and N. Hüsing, *Synthesis of inorganic materials*, Wiley-VCH, Weinheim, Germany, (2000).

[28] C. J. Brinker, and G. W. Scherer, *Sol-Gel Science*, Academic Press, San Diego, CA, (1990).

[29] P. Judeinstein, and C. Sanchez, *J. Mater. Chem.* **6**, 511 (1996).

[30] D. C. Bradlay, *Coord. Chem. Rev.* **2**, 299 (1967).

[31] F. Ribot, P. Toledano, and C. Sanchez, *Chem. Mater.* **3**, 759 (1991).

[32] B. E. Yoldas, *J. Mater. Sci.* **21**, 1087 (1986).

[33] M. Kallala, C. Sanchez, and B. Cabane, *J. Non-Cryst. Solids* **147-148**, 189 (1992).

[34] M. Kallala, C. Sanchez, and B. Cabane, *Phys. Rev. E: Stat. Phys., Plasmas, Fluids* **48**, 3692 (1993).

[35] U. Schubert, *J. Sol-Gel Sci. Technol.* **26**, 47 (2003).

[36] M. Camail, M. Humbert, A. Margaillan, A. Riondel, and J. L. Vernet, *Polymer* **39**, 6525 (1998).

[37] D. P. Birnie, and N. J. Bendzko, *Mater. Chem. Phys.* **59**, 26 (1999).

[38] G. Kickelbick, M. P. Feth, H. Bertagnolli, M. Puchberger, D. Holzinger, and S. Gross, *J. Chem. Soc., Dalton Trans.* **20**, 3892 (2002).

[39] B. Moraru, N. Hüsing, G. Kickelbick, U. Schubert, P. Fratzl, and H. Peterlik, *Chem. Mater.* **14**, 2732 (2002).

[40] J. Méndez-Vivar, P. Bosch, V. H. Lara, and R. Mendoza-Serna, *J. Sol-Gel Sci. Technol.* **25**, 249 (2002).

[41] A. Kayan, *J. Inorg. Organomet. Polym.* **13**, 29 (2003).

[42] F. Babonneau, A. Leaustic, and J. Livage, *Mater. Res. Soc. Symp. Proc.* **121**, 317 (1988).

[43] N. Steunou, F. Robert, K. Boubekeur, F. Ribot, and C. Sanchez, *Inorg. Chim. Acta* **279**, 144 (1998).

[44] P. Löbmann, and P. Röhlen, *Glass Sci. Technol.* **76**, 1 (2003).

[45] J. Blanchard, F. Ribot, C. Sanchez, V. Bellot, and A. Trokiner, *J. Non-Cryst. Solids* **265**, 83 (2000).

[46] N. Tohge, K. Shinmou, and T. Minami, *J. Sol-Gel Sci. Technol.* **2**, 581 (1994).

[47] C. Sanchez, M. In, P. Toledano, and P. Griesmar, *Mater. Res. Soc. Symp. Proc.* **271**, 669 (1992).

[48] J. Livage, C. Sanchez, M. Henry, and S. Doeuff, *Solide State Ionics* **32/33**, 633-638 (1989).

[49] C. Sanchez, J. Livage, M. Henry, and F. Babonneau, *J. Non-Cryst. Solids* **100**, 65 (1988).

[50] N. Miele-Pajot, L. G. Hubert-Pfalzgraf, R. Papiernik, J. Vaissermann, and R. Collier, *J. Mater. Chem.* **9**, 3027 (1999).

[51] A. C. Jones, P. A. Williams, J. F. Bickle, A. Steiner, H. O. Davies, T. J. Leedham, A. Awaluddin, M. E. Pemble, and G. W. Critchlow, *J. Mater. Chem.* **11**, 1428 (2001).

[52] M. Mehring, G. Guerrero, F. Dahan, H. Mutin, and A. Vioux, *Inorg. Chem.* **39**, 3325 (2000).

[53] C. Sanchez, and M. In, *J. Non-Cryst. Solids* **147**, 1 (1992).

[54] U. Gbureck, J. Probst, and R. Thull, *J. Sol-Gel Sci. Technol.* **27**, 157 (2003).

[55] S. Doeuff, Y. Dromzee, F. Taulelle, and C. Sanchez, *Inorg. Chem.* **28**, 4439 (1989).

[56] U. Schubert, E. Arpac, W. Glaubitt, A. Helmerich, and C. Chau, *Chem. Mater.* **4**, 291 (1992).

[57] H. Mutin, G. Guerrero, and A. Vioux, *J. Mater. Chem.* **15**, 3761 (2005).

[58] V. Lafond, C. Gervais, J. Maquet, D. Prochnow, F. Babonneau, and H. Mutin, *Chem. Mater.* **15**, 4098 (2003).

[59] J. D. Mackenzie, and D. R. Ulrich, Sol-gel optics, (1990).

[60] J. D. Mackenzie, Sol-Gel Optics III, (1994).

[61] J. D. Mackenzie, Sol-Gel Optics II, (1992).

[62] D. Avnir, V. R. Kaufman, and R. Reisfeld, *J. Non-Cryst. Solids* **74**, 395 (1985).

[63] Y. Kobayashi, Y. Kurokawa, and H. Imai, *J. Non-Cryst. Solids* **105**, 198 (1988).

[64] J. C. Pouxviel, B. Dunn, and J. I. Zink, *J. Phys. Chem.* **93**, 2134 (1989).

[65] J. C. Pouxviel, S. Parvaneh, E. T. Knobble, and B. Dunn, *Solid State Ionics* **32-33**, 646 (1989).

[66] E. J. A. Pope, M. Asami, and J. D. Mackenzie, *Mater. Res. Soc.* **4**, 1018 (1989).

[67] D. Levy, S. Einhorn, and D. Avnir, *J. Non-Cryst. Solids* **113**, 137 (1989).

[68] A. Morikawa, Y. Iyoku, M.-K. Kakimoto, and H. Imai, *J. Mater. Chem.* **2**, 679 (1992).

[69] M. Toki, T. Y. Chow, T. Ohnaka, H. Samura, and T. Saegusa, *Polym. Bull.* **29**, 653 (1992).

[70] M. W. Ellsworth, and B. M. Novak, *Chem. Mater.* **5**, 839 (1993).

[71] B. M. Novak, and C. Davies, *Macromolecules* **24**, 5481 (1991).

[72] C. Sanchez, B. Julián, P. Belleville, and M. Popall, *J. Mater. Chem.* **15**, 3559 (2005).

[73] M. Popall, A. Dabek, M. E. Robertsson, G. Gustafsson, O.-J. Hagel, B. Olsowski, R. Buestrich, L. Cergel, M. Lebby, P. Kiely, J. Joly, D. Lambert, M. Schaub, and H. Reichl, in: *Proc of Electronic Components and Technology Conference, 48th IEEE,* Seattle, WA, (1998). pp. 1018.

[74] R. Buestrich, F. Kahlenberg, M. Popall, P. Dannberg, R. Müller-Fiedler, and O. Rösch, *J. Sol-Gel Sci. Technol.* **20**, 181 (2001).

[75] R. Houbertz, L. Fröhlich, J. Schulz, and M. Popall, *Mater. Res. Soc. Symp. Proc.* **665**, C8.16 (2001).

[76] U. Streppel, P. Dannberg, C. Wächter, A. Bräuer, L. Fröhlich, R. Houbertz, and M. Popall, *Opt. Mater.* **21**, 475 (2002).

[77] R. Houbertz, L. Fröhlich, M. Popall, U. Streppel, P. Dannberg, A. Bräuer, J. Serbin, and B. N. Chichkov, *Adv. Eng. Mater.* **5**, 551 (2003).

[78] K. J. Shea, D. A. Loy, and O. Webster, *J. Am. Chem. Soc.* **114**, 6700 (1992).

[79] R. J. P. Corriu, J. J. E. Moreau, P. Thepot, and M. Wong Chi Man, *Chem. Mater.* **4**, 1217 (1992).

[80] G. M. Jamison, D. A. Loy, and K. J. Shea, *J. Mater. Chem.* **5**, 1193 (1993).

[81] D. E. Rodrigues , A. B. Brennan, C. Betrabet, B. Wang, and G. L. Wilkes, *Chem. Mater.* **4**, 1437-1446 (1992).

[82] H. Schmidt in: *Ultrastructure Processing of Advances Materials,* (D. R. Uhlmann eds), Wiley, New York, 1992.

[83] S. Diré, F. Babonneau, C. Sanchez, and J. Livage, *J. Mater. Chem.* **2**, 239-244 (1992).

[84] H. Kim, N. C. Pramanik, B. Y. Ahn, and S. I. Seok, *Phys. Status Solidi A* **203**, 1962-1970 (2006).

[85] D. Hoebbel, K. Endres, T. Reinert, and H. Schmidt, *Mater. Res. Soc. Symp. Proc.* **346**, 863 (1994).

[86] S. Cochet, L. Rozes, M. Popall, and C. Sanchez, *Mater. Sci. Eng., C* in press (2006).

[87] S. Cochet, L. Rozes, and M. Popall, in: *European Mater. Res. Soc., Spring Meeting, poster session,* Strasbourg, France, (2005).

[88] F. Kahlenberg, PhD thesis, Bayerische Julius-Maximilians-Universität Würzburg (Germany), **2004**.

[89] http://www.top-coating.de./.

[90] R. Houbertz, J. Schulz, L. Fröhlich, G. Domann, and M. Popall, *Mater. Res. Soc. Symp. Proc.* **769**, H7.4.1 (2003).

[91] H. Wolter, and W. Storch, *J. Sol-Gel Sci. Technol.* **2**, 93 (1994).

[92] M. T. Firla, *Dental Spiegel* **8**, 48 (1999).

[93] http://www.voco.de.

[94] K.-H. Haas, *Adv. Eng. Mater.* **2**, 571-582 (2000).

[95] BMWI Leitprojekt, "Energieminimierte Systemintegration", 1.10.99-30.9.2004.

[96] B. Lintner, N. Arfsten, H. Dislich, H. Schmidt, N. Philipp, and B. Seiferling, *J. Non-Cryst. Solids* **100**, 378 (1988).

[97] H. Schmidt, and B. Seiferling, *Mater. Res. Soc. Symp. Proc.* **73**, 739 (1986).

[98] O. Soppera, C. Croutxé-Barghorn, C. Carré, and D. Blanc, *Appl. Surf. Sci.* **186**, 91 (2002).

[99] M. Langlet, *Thin Solid Films* **472**, 253 (2005).

[100] X. Luo, C. Zha, and B. Luther-Davies, *J. Non-Cryst. Solids* **351**, 29 (2005).

[101] M. Trejo-Vàldez, P. Jenouvrier, J. Fick, and M. Langlet, *J. Mater. Sci.* **39**, 2801 (2004).

[102] W. Bao-Ling, and H. Li-Li, *Chin. Phys.* **13**, 1887 (2004).

[103] F. Del Monte, P. Cheben, C. P. Grover, and J. D. Mackenzie, *J. Sol-Gel Sci. Technol.* **15**, 73 (1999).

[104] B. E. Yoldas, *J. Non-Cryst. Solids* **39-38**, 81 (1980).

[105] T. Hayashi, T. Yamaha, and H. Saito, *J. Mater. Sci.* **18**, 3137 (1983).

[106] Z. Liu, and R. J. Davis, *J. Phys. Chem.* **98**, 1253 (1994).

[107] F. Babonneau, *Mater. Res. Soc. Symp. Proc.* **346**, 949 (1994).

[108] D. Hoebbel, T. Reinert, and H. Schmidt, *J. Sol-Gel Sci. Technol.* **6**, 139 (1996).

[109] D. Hoebbel, T. Reinert, and H. Schmidt, *J. Sol-Gel Sci. Technol.* **7**, 217 (1996).

[110] A. Matsuda, T. Kogure, Y. Matsuno, S. Katayama, T. Tsuno, N. Tohge, and T. Minami, *J. Am. Ceram. Soc.* **76**, 2899 (1993).

[111] H. Imai, H. Morimoto, A. Tominaga, and H. Hirashima, *J. Sol-Gel Sci. Technol.* **10**, 45 (1997).

[112] J. D. Basil, and C.-C. Lin, *Mater. Res. Soc. Symp. Proc.* **121**, 49 (1988).

[113] M. Aizawa, Y. Nosaka, and Y. Fujii, *J. Non-Cryst. Solids* **128**, 77 (1991).

[114] D. Hoebbel, M. Nacken, and H. Schmidt, *J. Sol-Gel Sci. Technol.* **13**, 37 (1998).

[115] R. M. Almeida, X. M. Du, D. Barbier, and X. Orignac, *J. Sol-Gel Sci. Technol.* **14**, 209 (1999).

[116] A. M. Seco, M. C. Goncalves, and R. M. Almeida, *Mater. Sci. Eng., B* **76**, 193 (2000).

[117] D. Hoebbel, M. Nacken, H. Schmidt, V. Huch, and M. Veith, *J. Mater. Chem.* **8**, 171 (1998).

[118] H. Ma, A. K.-Y. Jen, and L. R. Dalton, *Adv. Mater.* **14**, 1339 (2002).

[119] S. Musikant in: *Optical Materials: An Introduction to Selection and Application*, Vol. 6 (B. J. Thompson, W. F. May and Provost eds), 1985.

[120] G. Wedler, *Lehrbuch der Physikalischen Chemie*, Wiley-VCH, Weinheim, (1997).

[121] *Handbook of chemistry and physics, 57th edition*, CRC Press, (1976).

[122] M. J. Weber, *Handbook of Optical Materials*, CRC Press, (2003).

[123] G. Hougham, G. Tesoro, A. Viehbeck, and J. D. Chapple-Sokol, *Macromolecules* **27**, 5964 (1994).

[124] T. Matsuda, Y. Funae, M. Yoshida, T. Yamamoto, and T. Takaya, *J. Appl. Polym. Sci.* **76**, 50 (2000).

[125] G. Hougham, G. Tesoro, and A. Viehbeck, *Macromolecules* **29**, 3453 (1996).

[126] J. P. Jolivet, M. Henry, and J. Livage, *De la solution à l'oxyde*, (CNRS eds), Paris, France, (1994).

[127] K. P. C. Vollhardt, and N. E. Schore, *Organic Chemistry, Structure and Function*, (Freeman, ed), (2002).

[128] L. Eldada, *Opt. Eng.* **40**, 1165 (2001).

[129] N. Kawatsuki, and M. Uetsuki in: *Microoptical Grating Elements*, (L. A. Hornak eds), Dekker, New York, 1992.

[130] T. Flaim, Y. Wang, and R. Mercado, *Proc. SPIE* **5250**, 423 (2003).

[131] H. Franke in: *Polyimide Lightguides*, (L. A. Hornak eds), Dekker, New York, 1992.

[132] R. Mercado, and W. L. DiMenna, US 7192999, Brewer Science Inc., Rolla MO (US), **2007**.

[133] T. Kaino in: *Polymer Optical Fibers*, (L. A. Hornak eds), Dekker, New York, 1992.

[134] W. F. X. Frank, B. Knödler, A. Schösser, T. K. Strempel, F. Tschudi, F. Linke, D.

Muschert, A. Stelmaszyk, and H. Strack, *Proc. SPIE* **2290**, 125 (1994).

[135] A. Schösser, B. Knödler, T. Tschudi, W. F. X. Frank, A. Stelmaszyk, D. Muschert, D. Rück, S. Brunner, F. Pozzi, S. Morasca, and C. de Bernardi, *Proc. SPIE* **2540**, 110 (1995).

[136] http://www2.dupont.com/DuPont_Home/en_US/.

[137] G. Odian, *Principles of Polymerization*, Wiley, Canada, (1981).

[138] http://www.sigmaaldrich.com/.

[139] *Polymer Handbook, Second Edition*, John Wiley & Sons, (1975).

[140] L. Eldada, A. Nahata, and J. T. Yardley, *Proc. SPIE* **3288**, 175 (1988).

[141] L. Eldada, K. Beeson, D. Pant, R. Blomquist, L. W. Shacklette, and M. R. McFarland, *Proc. SPIE* **3950**, 78 (2000).

[142] J.-G. Liu, and M. Ueda, *J. Mater. Chem.* **19**, 8907-8919 (2009).

[143] L. Robitaille, C. L. Callender, J. P. Noad, F. Gouin, and R. M. Almeida, *Opt. Eng.* **37**, 1157 (1998).

[144] M. Hasegawa, and K. Horie, *Prog. Polym. Sci.* **26**, 259 (2001).

[145] http://www2.dupont.com/Kapton/en_US/assets/downloads/pdf/Gen_Specs.pdf.

[146] C.-C. Chang, and W.-C. Chen, *Chem. Mater.* **14**, 4242 (2002).

[147] A. E. Eichstadt, T. C. Ward, M. D. Bagwell, I. V. Farr, D. L. Dunson, and J. E. McGrath, *Macromolecules* **35**, 7561 (2002).

[148] T. Nakayama, A. Mochizuki, and M. Ueda, *Reactive & Functional Polymers* **30**, 109 (1996).

[149] H. Han, J. Seo, S. M. Pyo, and C. C. Gryte, *Polymer* **39**, 2963 (1998).

[150] H. Hou, J. Jiang, and M. Ding, *European Polymer Journal* **35**, 1993 (1999).

[151] http://www.fujifilm-ffem.com/Products/Polyimides.aspx.

[152] M. Popall, J. Kappel, J. Schulz, and H. Wolter, in: *4th International Conference on Micro Electro, Opto, Mechanical Systems and Components,* Berlin, (1994). 271.

[153] http://www.abcr.de/.

[154] X. Min Du, and R. M. Almeida, *J. Mater. Res.* **11**, 353 (1995).

[155] M. Trejo-Valdez, P. Jenouvrier, J. Fick, and M. Langlet, *J. Mater. Sci.* **39**, 2801-2810 (2004).

[156] D. Blanc, S. Pelissier, K. Saravanamutu, S. I. Najafi, and M. P. Andrews, *Adv. Mater.* **11**, 1508 (1999).

[157] Y. Liu, C. Lü, M. Li, L. Zhang, and Y. Bai, *Colloids and Surfaces A: Physicochem. Eng. Aspects* **328**, 67-72 (2008).

[158] C.-M. Chang, C.-L. Chang, and C.-C. Chang, *Macromol. Mater. Eng.* **291**, 1521-1528 (2006).

[159] H.-W. Su, and W.-C. Chen, *J. Mater. Chem.* **18**, 1139-1145 (2008).

[160] http://www.u.arizona.edu/~sborota.

[161] http://www2.ups.edu/faculty/hanson/labtechniques/refractometry/intro.htm.

[162] M. Born, and E. Wolf, *Principles of optics electromagnetic theory of propagation, interference and diffraction of light*, Cambridge Univ. Press, (1999).

[163] R. Ulrich, and R. Torge, *Appl. Opt.* **12**, 2901 (1973).

[164] H. G. Tompkins, and W. A. McGahan, *Spectroscopic ellipsometry and reflectometry*, Wiley, Canada, (1999).

[165] R. M. Azzam, and N. M. Bashara, *Ellipsometry and polarized light*, North-Holland, Amsterdam, (1992).

[166] http://www.uta.edu/optics/research/ellipsometry/ellipsometry.htm.

[167] http://academic.brooklyn.cuny.edu/physics/holden/ellipsometry.htm.

[168] http://www.jawoollam.com/index.html.

[169] J. D. Klein, A. Yen, and S. F. Cogan, *J. Appl. Phys.* **68**, 1825 (1990).

[170] J. C. Manifacier, J. Gasiot, and J. P. Fillard, *J. Phys. E: Sci. Instrum.* **9**, 1002 (1976).

[171] J. Shamir, and P. Gräff, *Appl. Opt.* **14**, 3053 (1975).

[172] R. Swanepoel, *J. Phys. E: Sci. Instrum.* **16**, 1214 (1983).

[173] E. D. Palik, *Handbook of Optical Constants of Solids*, Harcourt Brace Jovanovich, Orlando, (1985).

[174] W. C. Tuan, K. Koughia, J. Singh, and S. O. Kasap in: *Fundamental Optical Properties of Materials I*, (J. Singh eds), Wiley, 2006.

[175] C. Croutxé-Barghorn, O. Soppera, L. Simonin, and D. J. Lougnot, *Adv. Mater. Opt. Electron.* **10**, 25 (2000).

[176] C. G. Roffray, *Photogeneration of reactive species for UV curing*, John Wiley, New York, (1997).

[177] C. Croutxé-Barghorn, M. Feuillade, and D. J. Lougnot, in: *RadTech Europe Conference 2005: Exhibition & Conference for Radiation Curing,* Barcelona, Spain, (2005). 303.

[178] C. Croutxé-Barghorn, O. Soppera, and C. Carré, *J. Sol-Gel Sci. Technol.* **41**, 93 (2007).

[179] O. Soppera, and C. Croutxé-Barghorn, *J. Polym. Sci., Part A: Polym. Chem.* **41**, 716 (2003).

[180] U. Streppel, P. Dannberg, C. Wächter, A. Bräuer, and R. Kowarchik, *Appl. Opt.* **42**, 3570 (2003).

[181] O. Soppera, and C. Croutxé-Barghorn, *J. Polym. Sci., Part A: Polym. Chem.* **41**, 831 (2003).

[182] O. Soppera, C. Croutxé-Barghorn, and D. J. Lougnot, *New J. Chem.* **25**, 1006 (2001).

[183] R. Houbertz, G. Domann, J. Schulz, B. Olsowski, L. Fröhlich, and W.-S. Kim, *Appl. Phys. Lett.* **87**, 1105 (2004).

[184] W.-S. Kim, R. Houbertz, T.-H. Lee, and B.-S. Bae, *J. Polym. Sci., Part B: Polym. Phys.* **42**, 1979 (2004).

[185] E. Scolan, C. Magnenet, D. Massiot, and C. Sanchez, *J. Mater. Chem.* **9**, 2467 (1999).

[186] F. N. Castellano, J. M. Stipkala, L. A. Friedman, and G. Meyer, *Chem. Mater.* **6**, 2123 (1994).

[187] N. Tohge, K. Shinmou, and T. Minami, *Proc. SPIE* **2288**, 589 (1994).

[188] X. Luo, C. Zha, and B. Luther-Davies, *Opt. Mater.* **27**, 1661 (2005).

[189] J.-M. Herrmann, *Top. Catal.* **34**, 1 (2005).

[190] A. Fujishima, T. N. Rao, and D. A. Tryk, *J. Photochem. Photobiol. C: Photochem. Rev.* **1**, 1 (2000).

[191] A. Fujishima, K. Hashimoto, and T. Watanabe, *TiO₂ photocatalysis Fundamentals and Applications*, BKC Inc., (1999).

[192] O. Carp, C. L. Huisman, and A. Reller, *Prog. Solid State Chem.* **32**, 33 (2004).

[193] J. Serbin, PhD thesis, Universität Hannover (Germany), **2004**.

[194] A. Ovsianikov, S. Passinger, R. Houbertz, and B. N. Chichkov in: *Three dimensional material processing with femtosecond lasers*, Vol. 129 (C. R. Phipps eds), Springer series in optical science, 2007.

[195] M. Drobizhev, A. Karotki, A. Rebane, and C. W. Spangler, *Optics Letters* **26**, 1081 (2001).

[196] R. Houbertz, P. Declerck, S. Passinger, A. Ovsianikov, J. Serbin, and B. N. Chichkov, *Phys. Stat. Sol. (a)* **204**, 3662 (2007).

[197] R. Houbertz, J. Schulz, J. Serbin, and B. N. Chichkov, *Phys. in unserer Zeit* **36**, 278 (2005).

[198] L. Cerami, E. Mazur, S. Nolte, and C. B. Schaffer in: *Femtosecond laser micromachining*, (R. Trebino and J. Squier eds), Trafford Publishing, Victoria, Canada, 2007.

[199] C. Martineau, R. Anémian, C. Andraud, I. Wang, M. Bouriau, and P. L. Baldeck, *Chem. Phys. Lett.* **362**, 291 (2002).

[200] W. Haske, V. C. Chen, W. Dong, S. Barlow, S. R. Marder, and W. Perry, *Optics express* **15**, 3426 (2007).

[201] D. Yang, J. Jhaveri, and C. K. Ober, *Mater. Res. Bull.* **30**, 976 (2005).

[202] K. J. Schafer, J. M. Hales, M. Balu, K. D. Befield, E. W. Van Stryland, and D. J. Hagan, *J. Photochem. Photobiol. A: Chem.* **162**, 497 (2004).

[203] B. H. Cumpston, S. P. Ananthavel, S. Barlow, D. L. Dyer, E. Ehrlich, L. L. Erskine, A. A. Heikal, M. Kuebler, I.-Y. S. Lee, D. McCord-Maughon, J. Qin, H. Röckel, M. Rumi, X.-L. Wu, S. R. Marder, and J. W. Perry, *Nature* **398**, 51 (1999).

[204] M. Albota, D. Beljonne, J.-L. Brédas, J. E. Ehrlich, J.-Y. Fu, A. A. Heikal, S. E. Hess, T. Kogej, M. D. Levin, S. R. Marder, D. McCord-Maughon, J. W. Perry, H. Röckel, M. Rumi, M. Rumi, G. Subramaniam, W. W. Webb, X.-L. Wu, and C. Xu, *Science* **281**, 1653 (1998).

[205] C. Martineau, G. Lemercier, C. Andraud, I. Wang, M. Bouriau, and P. L. Baldeck, *Synth. Met.* **138**, 353-356 (2003).

[206] H. Guo, H. Jiang, L. Luo, C. Wu, H. Guo, X. Wang, H. Yang, Q. Gong, F. Wu, T. Wang, and M. Shi, *Chem. Phys. Lett.* **374**, 381 (2003).

[207] W. S. Shin, X. F. Li, B. Schwartz, S. L. Wunder, and G. R. Baran, *Dent. Mater.* **9**, 317-324 (1993).

[208] C. Pianelli, J. Devaux, S. Bebelman, and G. Leloup, *J. Biomed. Mater. Res.* **48**, 675 (1999).

[209] https://www.cibasc.com/.

[210] J. Livage, M. Henry, and C. Sanchez, *Prog. Solid State Chem.* **18**, 259 (1988).

[211] J. C. Pouxviel, J. P. Boilot, J. C. Beloeil, and J. Y. Lallemand, *J. Non-Cryst. Solids* **89**, 345 (1987).

[212] S. Diré, and F. Babonneau, *J. Non-Cryst. Solids* **167**, 29 (1994).

[213] B. L. Bischoff, and M. A. Anderson, *Chem. Mater.* **7**, 1772 (1995).

[214] C. Barbé, F. Arendse, P. Comte, M. Jirousek, F. Lenzmann, V. Shklover, and M. Grätzel, *J. Am. Ceram. Soc.* **80**, 3157 (1997).

[215] T. Lopez, R. Gomez, C. Sanchez, F. Tzompantzi, and L. Vera, *J. Sol-Gel Sci. Technol.* **22**, 99 (2001).

[216] W. B. Kim, S. H. Choi, and J. S. Lee, *J. Phys. Chem. B* **104**, 8670 (2000).

[217] Y. Matsuura, K. Kumon, N. Tohge, H. Inoue, and K. Matsukawa, *Thin Solid Films* **422**, 4 (2002).

[218] M. A. Holland, D. M. Pickup, G. Mountjoy, E. S. C. Tsang, G. W. Wallidge, R. J. Newport, and M. E. Smith, *J. Mater. Chem.* **10**, 2495 (2000).

[219] S. K. Samantaray, and K. Parida, *J. Mater. Sci.* **39**, 3549 (2004).

[220] H. J. Lee, S. H. Hahn, E. J. Kim, and Y. Z. You, *J. Mater. Sci.* **39**, 3683 (2004).

[221] X. Gao, S. R. Bare, J. L. G. Fierro, M. A. Banares, and I. E. Wachs, *J. Phys. Chem. B* **102**, 5653 (1998).

[222] B.-S. Lee, D.-J. Kang, and S.-G. Kim, *J. Mater. Sci.* **38**, 3545 (2003).

[223] O. Martins, and R. M. Almeida, *J. Sol-Gel Sci. Technol.* **19**, 651 (2000).

[224] H. Imai, H. Hirashima, and K. Awazu, *Thin Solid Films* **351**, 91-94 (1999).

[225] *Infrared analysis of organosilicon compounds: spectra-structure correlation*, ABCR catalogue ,Geleste Incorporation (2004).

[226] W. Du, H. Wang, W. Zhong, L. Shen, and Q. Du, *J. Sol-Gel Sci. Technol.* **34**, 227 (2005).

[227] D. Lin-Vien, N. B. Colthup, W. G. Fateley, and J. G. Grasselli, *The handbook of Infrared and Raman Characteristic Frequencies of Organic Molecules*, Academic press, San Diego, California, (1991).

[228] J. V. Barkley, J. C. Cannadine, I. Hannaford, M. M. Harding, A. Steiner, J. Tallon, and R. Whyman, *Chem. Commun.* 1653 (1997).

[229] http://www.aist.go.jp/RIODB/SDBS/.

[230] A. Rammal, F. Brisach, and M. Henry, *C. R. Chimie* **5**, 59 (2002).

[231] S. Cochet, PhD thesis, Université Paris 6 (France), **2007**.

[232] H. Mutin, V. Lafond, A. F. Popa, M. Granier, L. Markey, and A. Dereux, *Chem. Mater.* **16**, 5670 (2004).

[233] H. Mutin, G. Guerrero, and A. Vioux, *C. R. Chimie* **6**, 1153 (2003).

[234] http://www.chem007.com,

[235] N. Yamada, I. Yoshinaga, and S. Katayama, *J. Appl. Phys.* **85**, 2423 (1999).

[236] K. D. Dorkenoo, H. Bulo, H. Leblond, and A. Fort, *J. Phys. IV France* **119**, 173 (2004).

[237] C.-H. Chang, A. Mar, A. Tiefenthaler, and D. Wostratzky in: *Photoinitiators: Mechanisms and Applications*, 2 (L. J. Calbo eds), Dekker, M., 1992.

[238] D. W. Van Krevelen, *Properties of polymers*, Elsevier, Amsterdam, (1990).

8. Annex

8.1 Annex 1: Other resins synthesized during this work

Table 61: Other resins synthesized during this work.

Resin name	Composition of resins (mol-%)			Solvent	n_D^{20} of resin	n_c	Remark
PD54	SMDES, 10	Ti(OEt)$_4$, 90		___	n.d.	n.d.	absorbing coating
PD18	MEMO, 17	DPD, 50	Ti(OEt)$_4$, 33	PA	1.576	1.61 at 1608 nm	no patterning tested
PD20	MEMO, 17	DPD, 50	Ti(OEt)$_4$, 33	BU	1.585	1.61 at 1480 nm	no patterning tested
PD21	MEMO, 17	DPD, 50	Ti(OEt)$_4$, 33	acetone	1.566	1.62 at 1720 nm	no patterning tested
PD22	MEMO, 17	DPD, 50	Ti(OEt)$_4$, 33	ethylacetate	1.578	1.62 at 1520 nm	no patterning tested
PD88	MEMO, 40	DPD, 50	Ti(OEt)$_4$, 10	THF	1.556	1.54 at 1360 nm	coatings not homogeneous, agglomeration (20 μm)
PD23	MEMO, 17	DPD, 50	Zr(OEt)$_4$, 33	cyclopentanone	n.d.	n.d.	brown milky resin
PD108	MEMO, 17	DPD, 50	Zr(OEt)$_4$, 33	THF	n.d.	n.d.	brown milky resin
PD110	MEMO, 17	DPD, 50	Zr(OPr)$_4$, 33	THF	n.d.	1.58 at 900 nm	no patterning tested
PD35	MEMO, 20	DPDMS, 25	Cu(OH)$_2$, 55	toluene	n.d.	n.d.	black milky resin
PD42	MEMO, 20	DPD, 25	Cu(OH)$_2$, 30 / DPDMS, 25	BU	1.535	1.54 at 1720 nm	no patterning tested

Sequel from Table 61: Other resins synthesized during this work.

Resin name	Composition of resins (mol-%)			Solvent	n_D^{20} of resin	n_c	Remark
PD36	MEMO, 20	DPD, 55	Ni(OOCCH$_3$)$_2$, 25	toluene	n.d.	n.d.	milky resin
PD84	SETMS, 33	Fe(OEt)$_3$, 67		acetonitrile	n.d.	n.d.	coatings not homogeneous, agglomeration
PD89	MEMO, 40	DPD, 50	Fe(OEt)$_3$, 10	THF	1.558	1.51 at 1400 nm	small agglomeration (10 μm) on the coating
PD37	MEMO, 50	Co(OOCCH$_3$)$_2$, 4 H$_2$O, 50		ethanol	n.d.	n.d.	absorbing coating and agglomeration observed
PD38	MEMO, 20	Co(OOCCH$_3$)$_2$, 4 H$_2$O, 50	DPD, 30	ethanol	n.d.	n.d.	absorbing coating and agglomeration observed
PD27	DPD, 25	MA, 50	Ti(OEt)$_4$, 25	___	n.d.	1.60 at 1190 nm	no patterning tested
PD15	MA, 20	Zr(PrO)$_4$, 80		propanol	1.482	n.d.	coating too thin
PD102	DPD, 25	MAEAA, 50	Ti(OEt)$_4$, 25	toluene	1.566	n.d.	absorbing coating
PD103	DPD, 25	MAEAA, 50	Ti(OPr^i)$_4$, 25	toluene	1.537	1.64 at 690 nm 1.61 at 1600 nm	no patterning tested
PD104	MAEAA, 50	Ti(OEt)$_4$, 50		ethanol	1.541	n.d.	absorbing coating
PD106	MAEAA, 33	Ti(OEt)$_4$, 34	MA, 33	toluene	1.562	n.d.	absorbing coating
PD95	MAEAA, 66	Ti(OPr^i)$_4$, 34		toluene	n.d.	n.d.	yellow resin used for other syntheses

Sequel from Table 61: Other resins synthesized during this work.

Resin name	Composition of resins (mol-%)			Solvent	n_D^{20} of resin	n_c	Remark
PD98	PD95, 30	MEMO, 20	DPD, 50	___	n.d.	n.d.	a gel is obtained
PD99	PD95, 30	DPD, 50	Memo, 20	___	1.566		absorbing coating
PD94	Ti(OPri)$_4$, 50		Cis-2- butene-1,4-diol, 50	toluene	n.d.	n.d.	solid used for other syntheses
PD97	PD94, 27	MEMO, 17	DPD, 56	toluene	n.d.	n.d.	absorbing coating

8.2 Annex 2: Calculation of k and k'

λ_1 and λ_2 correspond to particular wavelengths such as minima or maxima of the transmission spectrum of the coating, with $\lambda_1 > \lambda_2$. The ratio between two maxima or minima, λ_1/λ_2 is reported in Table 62. This Ratio allows the determination of k and k' defined in chapter 2.2.2.4 (Eq. 13) and (Eq. 14).

Table 62: Ratio between two maxima or minima, the values of λ_1 or λ_2.

λ_2 \ λ_1	$\lambda_0/4$	$\lambda_0/2$	$3\lambda_0/4$	λ	$5\lambda_0/4$	$3\lambda_0/2$	$7\lambda_0/4$	$2\lambda_0$	$9\lambda_0/4$	$5\lambda_0/2$	$11\lambda_0/4$
$\lambda_0/2$	2										
$3\lambda_0/4$	3	3/2									
λ	4	2	4/3								
$5\lambda_0/4$	5	5/2	5/3	5/4							
$3\lambda_0/2$	6	3	2	3/2	6/5						
$7\lambda_0/4$	7	7/2	7/3	7/4	7/5	7/6					
$2\lambda_0$	8	4	8/3	2	8/5	8/6	8/7				
$9\lambda_0/4$	9	9/2	3	9/4	9/5	3/2	9/7	9/8			
$5\lambda_0/2$	10	5	10/3	5/2	2	10/6	10/7	5/4	10/9		
$11\lambda_0/4$	11	11/2	11/3	11/4	11/5	11/6	11/7	11/8	11/9	11/10	
$3\lambda_0$	12	6	4	3	15/5	2	12/7	3/2	4/3	6/5	12/11
$13\lambda_0/4$	13	13/2	13/3	13/4	13/5	13/6	13/7	13/8	13/9	13/10	13/11
$7\lambda_0/2$	14	7	14/3	7/2	14/5	7/3	2	7/4	14/9	7/5	14/11
$15\lambda_0/4$	15	15/2	5	15/4	3	5/2	15/7	15/8	5/3	3/2	15/11

8.3 Annex 3: Emission spectra of the lamp from the mask aligner

Spectrum MA6